Anionic microgels for colorful smart materials

Inauguraldissertation

zur

Erlangung der Würde eines Doktors der Philosophie

vorgelegt der

Philosophisch-Naturwissenschaftlichen Fakultät

der Universität Basel

von

Vittoria Chimisso

Originaldokument gespeichert
auf dem Dokumentenserver der Universität Basel
edoc.unibas.ch

Basel 2023

Genehmigt von der Philosophisch-Naturwissenschaftlichen Fakultät auf Antrag von

Prof. Dr. Cornelia Palivan (Universität Basel)
Erstbetreuerin

Prof. Dr. Jonathan de Roo (Universität Basel)
Zweitbetreuer

Prof. Dr. Eric Dufresne (ETH Zürich)
Externer Experte

Basel, 21.06.2022
Prof. Dr. Marcel Mayor
Dekan

In memory of Prof. Wolfgang Meier.

Abstract

Microgels are a class of soft materials that have been used in almost all fields, including drug delivery, food science, biocatalyis, and formulation. The wide range of possible application relies on their hybrid nature, bridging linear macromolecules, hard colloids, and surfactants. One of the most well-studied characteristics of microgels is their rapid response to external stimuli. Depending on their chemical design, microgels can be responsive to temperature, pH, ionic strength, light, electrochemical potential, or molecular cues. Microgels responsive to multiple stimuli exist, *e.g.* thermoresponsive anionic microgels decorated with COOH which are responsive to changes in both temperature and pH. While the phase behaviour of such microgels in response to these stimuli has been well characterized, an additional mode of responsiveness inherent to the same chemical formulations has barely been investigated: Their response to the presence of divalent cations that can enter metal-ligand interactions with COOH groups. Moreover, previous studies regarding these fascinating and versatile microgels have been limited to studying their responsiveness, but have yet to explore their use as soft composites for macroscopic applications.

This thesis presents some applications that thermoresponsive anionic microgels can offer beyond merely swelling/deswelling in response to changes in temperature or pH. The microgels presented were chemically tailored to fit the application presented for each chapter. Briefly, this thesis presents in Chapters 2 and 3, poly(vinylcaprolactam-*co*-itaconic acid) P(VCL-*co*-IA) microgels and their interactions with biologically-relevant divalent cations. Detailing the investigation of swelling behaviour, uptake, release, and ion selectivity to produce biocompatible ion delivery systems for biomedical and synthetic biology applications. Chapter 4 describes the use of poly(N-isopropylacrylamide-*co*-methacrylic acid) (P(NIPAm-*co*-MAAc)) microgels as building blocks for granular double-network hydrogels, which are mechano- and thermochromic. This simple, yet effective approach to make structurally-colored gels inspired attempts to shape the same gels via additive manufacturing, outlined in Chapter 5. Microgels can be used not only as building blocks for large composite materials but also as models for soft and compartmentalized reactions in synthetic cells. Chapter 6 presents their encapsulation in synthetic, block copolymer-based membrane compartments, and

describes their behaviour in crowded environments, with potential applications in synthetic biology.

Declaration

I hereby declare that except where specific reference is made to the work of others, the contents of this dissertation are original and have not been submitted in whole or in part for consideration for any other degree or qualification in this, or any other university. This dissertation is my own work and contains nothing which is the outcome of work done in collaboration with others, except as specified in the text and Acknowledgements.

Vittoria Chimisso
2023

First, I would like to thank my late supervisor Prof Wolfgang Meier for assigning me to this thesis project, and giving me the freedom to choose my own path. The challenge to work through this project that took a wholly unexpected direction made me grow as a scientist and as a person.

A big thank you goes also to my current supervisor and mentor Prof. Cornelia Palivan, who with infinite patience has supported me (through any means) through the PhD, especially in the last year, where times and research have been, to say the least, challenging. She shaped me into a more cautious, mature, and less impulsive me, which made me the woman and the scientist I am really proud of.

A thank you also goes to my last-minute second supervisor Prof. Jonathan de Roo, who accepted the role with no hesitation.

Many thanks also go to my external supervisor Prof Eric Dufresne, who took the time to read my work and evaluate my thesis.

Speaking of people who contributed to this work, I would like to acknowledge a couple of key helpers within the realization of this thesis. The post docs that followed my work, supported it and tolerated with kindness and empathy my dramatic existence in the lab: Dr. Csaba Fodor, Dr. Daniel Messmer, Dr. Elena dos Santos, Dr. Phally Kong, and Dr. Olivia Eggenberger. Especially to Daniel, I want to express a deep-rooted gratitude, not only for the little tricks and suggestions in the lab (without you, both me and my students would have spent a lot more time crying over failed experiments than we already did), but for the time, effort and empathy in guiding me through the last stages of my PhD, and for teaching me invaluable lessons on "how to science". Also, thank you for supporting me, emotionally and strategically through the last stretch of my PhD, your help (and sassy thesis corrections) have been precious. You are an example of curiosity, creativity and patience, from which I can only keep learning. Thank you Csaba for always challenging me and for flooding me with literature and more ideas. You taught me what it means to learn to anticipate questions and how to be perfectly prepared. Thanks to all of you, you had my back. I have learned a great deal from you, especially how to stand up for myself and go for what I want, and for this I will always be grateful.

I would like to acknowledge Ms. Judith Kobler Waldis for the great help with ion chromatography measurements and Ms Susanne Erpel for the help with TEM and SEM measurements.

Most of this thesis would also not be here if it wasn't for my students: Dr. Simona Conti, Theresa Emt and Hendrik Wested, who made a real difference for my projects by being fantastic collaborators.

Last but not least, Magic Matteo Hirsch, who, by collaborating with me on the printing of microgels opened me up to a completely new and exciting world, and got me rolling again after a period of scientific stagnation.

I am sad to be leaving behind some great colleagues and friends, who I had the pleasure to work with during these years. So, a big "I will miss you a lot" goes to Lukas Heuberger for making me laugh when I really needed it and for providing me with gossip, plant care and snacks when necessary. Similarly, "I will miss you" go to Dimitri, Daniel, Cora, and Viviana, who never fail to be there when I needed the most (as in, the 10 am coffee break). Thank you to Ricco and Ale for the ice cream and car trips, my first year would have been not as nice without you. I would also like to acknowledge the rest of the Meier-Palivan group, who are a funky bunch, and contributed to entertaining times in the lab. Especially Maria and Olivia for the last-minute aperos. The student association I have been part of for more than three years, the PCC also deserves a heartfelt thank you, because I have never before had the pleasure to work with such proactive, collaborative and dynamic group of people, this made my PCC president role quite easy.

To my friends, which had the persistence to be at my side during these 4 years of academic adventures and perils: these 4 years would have not been nearly as interesting and packed with adventures and emotions without you. Thus, thank you Rocio, Ivan, Shanta, Jaime, Sthefany, Miguel, Andrea, and Agi for being by my side, and giving me motivation, support, hugs, and lunch breaks (and breakdowns), you're all a source of inspiration for me to do better. Special note goes to Sam (Pooh.D.), who is an amazing scientist, arancini maker and cat dad, and never failed to encourage me from a distance.

Un grazie di cuore va alla mia famiglia, che negli anni mi ha spinto sempre a fare sempre meglio, con coraggio. Grazie. Grazie per l'incoraggiamento, la fiducia, i pacchi da giü e le cose dette con franchezza.

Last but not least, I would not be where I am without Martijn, who is a wonderful partner and he never gave me slack in complaining, and always pushed me to give my best, and accept that the limit is my own, personal, best. Simplicity is key, and you taught me that. Thank you.

Ad maiora.

Publications related to this thesis

1. **Chimisso, V.**, Fodor, C., Meier, W. (2019). Effect of divalent cation on swelling behavior of anionic microgels: Quantification and dynamics of ion uptake and release. Langmuir, 35(41), 13413-13420.

2. **Chimisso, V.**, Conti, S., Kong, P., Fodor, C., Meier, W. P. (2021). Metal cation responsive anionic microgels: behaviour towards biologically relevant divalent and trivalent ions. Soft Matter, 17(3), 715-723.

Publications produced during research period

1. **Chimisso, V.**, Maffeis, V., Hürlimann, D., Palivan, C. G., Meier, W. (2020). Self-Assembled Polymeric Membranes and Nanoassemblies on Surfaces: Preparation, Characterization, and Current Applications. Macromolecular bioscience, 20(1), 1900257.

2. **Chimisso, V.**, Aleman Garcia, M. A., Yorulmaz Avsar, S., Dinu, I. A., Palivan, C. G. (2020). Design of Bio-Conjugated Hydrogels for Regenerative Medicine Applications: From Polymer Scaffold to Biomolecule Choice. Molecules, 25(18), 4090.

3. Wehr, R., Dos Santos, E. C., Muthwill, M. S., **Chimisso, V.**, Gaitzsch, J., Meier, W. (2021). Fully amorphous atactic and isotactic block copolymers and their self-assembly into nano-and microscopic vesicles. Polymer chemistry, 12(37), 5377-5389.

List of figures

1.1 Microgels position themselves in between three classes of materials: surfactants, hard colloids and polymers.[1] 2

1.2 Simplified schematic of dispersion precipitation polymerization: (1) oligoradicals start growing from monomers, then they reach a critical molecular weight (2) and form small unstable particles which keep growing (3) staying collapsed as the reaction temperature is higher than the volume phase transition temperature (VPTT). When the temperature is decreased to below the VPTT and the polymer chains become soluble again, the particles swell and swollen microgels are formed (4). 3

1.3 Chemical structures of monomers that produce temperature responsive polymers. From left to right: NIPAm, NIPMAm, DEAm, TBAm and VCL. . . . 6

1.4 Chemical structures of monomers that produce pH responsive polymers. From left to right: AAc, MAAc, VIm, APMA and DMAPMA 6

1.5 Schematic representation of the spiropyran isomerization between its closed hydrophobic SP form and open zwitterionic MC form. 9

2.1 Schematic representation of chapter content. 20

2.2 ^{1}H NMR spectra ($CDCl_3$, 400 MHz, 256 scans) of PVCL (purple, 100:0) with no signal at 3.64 ppm, P(VCL-*co*-IADME) 5 mol% (blue, 95:5), 10 mol% (turquoise, 90:10), 15 mol% (green, 85:15), 20 mol% (lime, 80:20) and 30 mol% (red, 70:30). Methyl ester peaks are highlighted in blue. . . . 25

2.3 ATR-FTIR normalized spectra of P(VCL-*co*-IADME) microgels; (a) full spectra and (b) the relevant characteristic peaks. 26

2.4 TEM images acquired of (a) N0 homopolymeric PVCL microgels and (b) N5 (20 mol% IADME),(c) N10 (10 mol% IADME) (d) N15 (15 mol% IADME) (e) N20 (20 mol% IADME) and (f) N30 (30 mol% IADME) microgels, all stained with uranyl acetate. 26

2.5 ^{1}H NMR spectra of hydrolyzed microgels M8 to M30 in D_2O (400 MHz, 256 scan, room temperature (RT)). Highlighted in blue, the absence of the methyl ester protons (compare in Figure 2.2). 27
2.6 Normalized IR spectra of P(VCL-*co*-IA) microgels; (a) full spectra and (b) the relevant characteristic peaks. 28
2.7 TEM images recorded of P(VCL-*co*-IA) M8, M14, M22, M26 and M30 microgels by stained with PTA and imaged at an acceleration voltage of 80k mV. 30
2.8 D_H of P(VCL-*co*-IADME) (N*n*) and P(VCL-*co*-IA) (M*m*) microgels in water at T= 20 °C according to the IADME mol% (N micro-gels) and COOH moieties (M microgels) measured by DLS at pH=7. 31
2.9 D_H, as determined by DLS, of (a) P(VCL-*co*-IADME) (N*n* samples) and (b) D_H of P(VCL-*co*-IA) (M*m* samples) as functions of temperature, both measured by DLS in pure water at pH=7. 32
2.10 D_H, as determined by DLS, of P(VCL-*co*-IA) (M*m*) microgel samples against time, at a Ca^{2+} concentration of 10 mM and T= 40 °C at neutral pH. 34
2.11 D_H, as determined by DLS, of P(VCL-*co*-IADME) (N*n*) microgels (orange) and P(VCL-*co*-IA) (M*m*) microgels (purple) as determined by DLS, recorded in MilliQ water at pH=7 (hollow symbols) or in 10 mM $CaCl_2$ solution (filled symbols), all at T= 10 °C. For simplicity, the monomer % for the ionic gels is counted as each IADME that has been hydrolyzed has turned into a itaconic acid methyl ester. 35
2.12 D_H of P(VCL-*co*-IA) (M*m*) microgels determined by DLS at T = 10 °C in water at different $CaCl_2$ concentrations at neutral pH. 36
2.13 D_H of M6 (6 mol% COOH), M10 (10 mol% COOH) and M19 (19 mol% COOH) at different concentrations of a) $MgCl_2$ b) $SrCl_2$ c) $CuCl_2$ d) $FeCl_3$ determined by DLS at T = 10 °C at neutral pH in MilliQ water. 37
2.14 . Hydrodynamic diameter D_H of M10 (10 mol% COOH) measured via DLS in the presence of Mg^{2+} (purple) and Na^{+} (red) in MilliQ water, at neutral pH and RT. 40

3.1 Schematic representation of the metal uptake and release of the microgel system. 43

3.2 The number of Ca^{2+} ions retained by a solution of 0.1 wt% P(VCL-*co*-IA) according to the COOH concentration of each microgel, performed at different initial Ca^{2+} concentrations (mM). Samples were soaked at a given concentration of $CaCl_2$ at room temperature and neutral pH, and then spin filtrated. The retained number of ions was determined by ion chromatography of the filtrate. 44

3.3 Concentration of Mg^{2+}, Sr^{2+}, Cu^{2+} and Fe^{3+} bonded by a 0.1 wt% microgel solution with different COOH concentrations per gel: N0 (0 mol% COOH), M6 (6 mol% COOH), M10 (10 mol% COOH) and M19 (19 mol% COOH) at RT and neutral pH. The samples were soaked at an initial MCl_x concentration, filtered, and the concentration of the filtered ions was determined by ion chromatography. 46

3.4 Concentration of Ca^{2+} retained overtime at pH 7 and T= 20 °C of a 0.1 wt% solution of P(VCL-*co*-IA) microgel (Mm microgels). Each datapoint represents a washing cycle, where the gels are diluted in MilliQ water, centrifuged and filtered, and the ions present in the filtrate are determined by ion chromatography. 49

3.5 The concentration of (a) Mg^{2+} , (b) Sr^{2+} ,(c) Cu^{2+} and (d) Fe^{3} retained for a 0.1 wt% microgel solution at neutral pH and RT when subjected to consecutive cycles of centrifugation and dispersion in MilliQ water. The sampels were initially soaked in 1 mM of (a) $MgCl_2$, (b) $SrCl_2$, (c) $CuCl_2$ and (d) $FeCl_3$, washed by centrifugation and redispersion in MilliQ water 2 times, and then subjected to the cycled. The concentration of leached ions is determined from the filtrate by ion chromatography. 50

3.6 Concentrations of Ca^{2+} ions released by a 0.1 wt% P(VCL-*co*-IA) (Mm) microgel samples solution at different pH in pure water at room temperature. Concentrations were determined from the filtrate of the centrifuged-filtered microgel samples *via* ion chromatography. 51

3.7 Percentage of released (a) Mg^{2+} (b) Sr^{2+} (c) Cu^{2+} and (d) Fe^{3+} for a 0.1 wt% solution of M6 (6 mol% COOH), M10 (10 mol% COOH) and M19 (19 mol% COOH) at different pH values, RT, values measured after an equilibration time of 2 h after pH switch from pH 7. 52

3.8 Mg^{2+} concentration of M6 (6 mol% COOH), M10 (10 mol% COOH) and M19 (19 mol% COOH) 0.1 wt% microgel solutions at room temperature. Odd data points on the x-axis represent the loaded concentrations of Mg^{2+} within the total amount of microgels (1,3,5) and the even data points refer to the Mg^{2+} concentration left within the microgel sample after pH trigger (2, 4, 6). 53
3.9 Absorbance intensity (700 nm wavelength) measured of a 0.1% wt/V microgel dispersion as a function of time, measured with a scanning rate of 1 measurement per second; (a),(c),(e),(g),(i): measurements were made at T= 20 °C and pH= 7, (b),(d),(f) and (j): measurements were performed in the same cuvette at T= 20 °C, with a starting pH= 7. 55
3.10 Uptake and release times: (a) bonding and (b) release time of Ca^{2+} of a 0.1 wt% P(VCL-*co*-IA) (Mn) microgel samples at RT. Concentrations are final calcium concentrations. 56
3.11 . Percentage of coordinated ions with respect to its competitor for each microgel, M6, M10 and M19 at pH 7 and room temperature. Colour coding: yellow represents Cu^{2+}, red represents Sr^{2+} and green represents Mg^{2+}. The microgels used are M6 (6 mol% COOH), M10 (10 mol% COOH) and M19 (19 mol% COOH). 58
3.12 Percentage of Fe^{3+} (in orange) bonded by a 0.1 wt% microgel solution at pH 7 and room temperature in the presence of Mg^{2+} (not visible, first 3 data sets for M6, M10 and M30), Cu^{2+} in green and Sr^{2+} in red. The microgels used are M6 (6 mol% COOH), M10 (10 mol% COOH) and M19 (19 mol% COOH). 59
3.13 Percentage of Ca^{2+} (in blue) bonded by a 0.1 wt% M10 microgel solution at pH 7 and room temperature in the presence of Mg^{2+} in red, Sr^{2+} in green, Cu^{2+} in yellow and Fe^{3+} in orange. 59

4.1 Schematic representation of P(NIPAm-co-MAAc) microgel synthesis, where SDS concentration was varied to obtain anionic microgels in a range of sizes. 66
4.2 D_H values at neutral pH measured by DLS; PNIPAm-350, PNIPAm-400, and PNIPAm-450 (a), (c), (e) in water and (b), (d), (f) in 10% wt/V AAm from 10 °C to 50 °C. 68
4.3 TEM images of P(NIPAm-*co*-MAAc microgels stained with PTA at neutral pH. The microgels here represent an overview of PNIPAM-400 at (a) 0.1% wt/V concentration, (b) 0.1% wt/V, close up, (c) at 0.01% wt/V and (d) a close-up of PNIPAm-400 microgels. The darker shadow behind the microgels belongs to the grid, and is a staining effect fromthe PTA stain. 69

4.4 SEM images of (a) NIPAm-450, (b) NIPAm-400, and (c) NIPAm-350, aquired with an accelertion of 5 kV. 70
4.5 P(NIPAM-*co*-MAAc) microgels compressed by ultracentrifugation at 282k RCF for 2 h at RT. (a) NIPAm-350 in blue (b) NIPAm-400 in green (c) NIPAm-450 in pink. Images are taken under diffused natural light. 70
4.6 (a) PNIPam-450, (c) PNIPAm-400, and (e) PNIPAm-350 compressed by ultracentrifugation at 282k RCF for 2 h, before photocuring. (b) PNIPam-450, (d) PNIPAm-400, and (f) PNIPAm-350 after being exposed to 15 min UV light (2 mW/cm^2). 71
4.7 PNIPAm-400 in 10wt/V% Aam double networks, imaged *via* SEM, as (a) close up of smooth surface, (b) and (c) overview of ripped surface and (d) close-up of ripped surface. Smooth surface was imaged on a non-ripped specimen, while the ruptured surface image was taken at the interface of a torn specimen. 73
4.8 DNGH of PNIPAm-350 in 10% wt/V of AAm in its (a) neutral position, (b) extended and (c) compressed, at RT. 74
4.9 Schematic representation of crystalline plane modification in a microgel-based photonic crystal. (a) represents the effect on the interplane spacing upon uniaxial extension and (b) upon compression. D_1 is the distance between the planes at rest, D_2 is the interplane distance during extension and D_3 during compression.The scheme is not to scale. 75
4.10 Strain-dependent reflectance spectra of PNIPAm-350 DNGH (10% AAm), after being soaked overnight, taken at RT from a cylindrical specimen and measured with a light incidence perpendicular to the sample. Spectra (which overlap) are taken at angles (20-90 °in 10 °intervals. The size of the illuminated spot varied from ≈3 mm to ≈2 mm to increase the resolution of the spectrum. Spectra of the vertically-mounted specimen are recorded (a) at rest with an aperture of ≈3 mm,(b) with 35% compression an aperture of ≈3 mm, (c) with 43% compression and an aperture of ≈2 mm. Spectra of the horizontally measured specimen (d) was recorded. 76
4.11 PNIPAm-400 double network, crosslinked in 10 wt/V% of AAm and molded into 1 cm *d* cylinder, in its (a) neutral position, (b) extended and (c) compressed, at RT. 77

4.12 The PNIPAm-350 double network, crosslinked in 10 wt/V% of AAm and embedded in a PDMS slab. The object is (a) in its neutral position, (b) compressed form above, (c) compressed from the sides with medium force and (d) compressed from the sides with high force, at RT. 78
4.13 The PNIPAm-350 DNGH, crosslinked in 10 wt/V% of AAm and molded into a PDMS slab, compressed into an oblique form from the sides by hand. (a) The DNGH in neutral position, (b) under medium compression and (c) under stronger compression. 79
4.14 The PNIPAm-350 double network, crosslinked in 10 wt/V% of AAm and embedded in a PDMS slab. The object is (a) bent up, (b) bent down at RT. Pictures are taken under diffused light from a 90 °angle. 80
4.15 PNIPAm-350 double network, crosslinked in 10% wt/V of AAm. The object is (a) kept at RT, (b) submerged in a t= 60 °C water bath. Pictures are taken under diffused light from a 90 °angle. 81

5.1 Stress recovery tests of compressed PVCL microgels with a D_H of (a) 333 nm and (b) 450 nm soaked in 10% wt/V of AAm. G' (black) and G" (red) of the pellet at 1% oscillation strain (filled circles) and at 10% oscillation strain (hollow circles). 95
5.2 VCL-450 double networks composed of PVCL-450 in 10% wt/V AAm, extruded with a pressure of 70 kPa and 10 mm/s printing speed. (a) view from the side and (b) from the top. 96
5.3 single-layer printed and crosslinked (a) VCL-IA-5-560, (b) VCL-IA-15-490 and (c) VCL-IA-15-500, P(VCL*co*-IA) microgels, obtained from P(VCL-*co*-IADME) hydrolysis. The inks were obtained from 2h ultracentrifugation at 232k RCF at RT and neutral pH in 10% wt/V of AAm, extruded with a pressure of 70 kPa and a speed of 10 mm/s. 97
5.4 Shear recovery tests of (a) VCL-IA-5-450 and (b) VCL-IA-5-560, (c) PVCL-IA-10-466, (d) VCL-IA-15-460, and (e) PVCL-IA-15-490 pellets taken at RT, centrifuged at 282k RCF at RT and neutral pH. G' (in black) and G" (pink) are plotted against time, at 10% strain (filled dots) and 1% strain (hollow dots). 99
5.5 GMA Microgels compressed by ultracentrifugation for 2 h at 232k RCF in 10% wt/V AAm. (a) VCL-GMA-350 against a black background, (b) VCL-GMA-350 stained with 0.1% nigrosine solution. 100

5.6 Shear recovery tests of (a) NIPAm-350, (b) NIPAm-400, and (c) NIPAm-450, redispersed in 10% wt/V AAm solution, and centrifuged at 82k RCF for 2 h. G' (in black) and G" (pink) are plotted against time, at 10% strain (filled dots) and 1% strain (hollow dots). 100
5.7 PNIPAm-400 printed into a 2 wt% PAAc granular hydrogel, obtained from cryo-milling a macroscopic PAAc hydrogel. The grid has been printed at RT, with a printing pressure of 70 KPa and a printing speed of 7 mm/s. The PAAc granular hydrogel only contained water. 101
5.8 Shear recovery plots of (a) PVCL-IA-15-500 and (c) PVCL-IA-15-550, (e) PVCL-IA-15-600 containing 0.01 M $CaCl_2$ and (b), (d), and (f) 0.05 M $CaCl_2$, from dispersions centrifuged at 282k RCF at RT and neutral pH. G' (in black) and G" (in pink) are plotted against time, at 10% strain (filled dots) and 1% strain (hollow dots). 104
5.9 Microgels compressed by ultracentrifugation for 2 h at 232k RCF in 10 wt/C% AAm and 0.05 M $CaCl_2$ concentration, then extruded by hand and crosslinked uner UV light. Figure (a) VCL-IA-15-500, (b) VCL-IA-15-550 and (c) VCL-IA-15-650. 105
5.10 Temperature-induced aggregation of 1% wt/V NIPAM-*co*-MAAc, with [Ca^{2+}] decreasing from left to right (0.5 M - 0.01 M);(a) side view of microgels kept at 80 °C for 1 h in the oven, (b) top view of microgels kept at 80 °C for 1 h and (c) top view of microgels 5 min after removal from the oven, when allowed to cool down to RT. 106
5.11 Shear recovery tests of PVCL-based microgels redispersed in 1% wt/V CMC (M_W = 90 kDa) in MilliQ water. Microgels used for the inks are (a) VCL-333, (b) VCL-450, and (c) VCL-600. G' (in black) and G" (pink) are plotted against time, at 10% strain (filled dots) and 1% strain (hollow dots). 107
5.12 3D-printed and crosslinked alginate networks containing P(NIPAm-*co*-AlAm) microgels. (a) PNIPAm-AlAm-350 microgels printed as a 2-layer grid with a pressure of 140 kPa and 10 mm/s printing speed, (b) PNIPAm-AlAm-250 microgels and (c) PNIPAm-AlAm-200 microgels printed as a 2-layer grid with a pressure of 70 kPa and 5 mm/s printing speed. The microgel pellets were printed at RT and neutral pH, and then crosslinked with 0.1 M $CaCl_2$. 109
5.13 NIPAm-AlAm-400 microgels resuspended in 10% wt/V AAm at RT, at (a) (from left to right) 10, 8, 6, and 5% wt/V microgel solutions. (b) Close-up of the 6% suspension, where the opalescent crystal can be seen, as sparkles at the bottom of the vial. 109

5.14 Shear recovery tests of NIPAm-AlAm-400 microgels redispersed in 10% wt/V AAm at RT, at (a) 10% wt/V and (b) 11% wt/V in 10% wt/V AAm, at RT and neutral pH. G' (in black) and G" (pink) are plotted against time, at 10% strain (filled dots) and 1% strain (hollow dots). 110
5.15 NIPAm-AlAm-400 in 10% AAm, 3D printed into a three-layer grid. The specimen was cured under UV light and kept at RT. 111
5.16 VCL-IA-15-460 microgels crosslinked in 10 wt/V% AAm under UV light, at RT and neutral pH. The sample was prepared by ultracentrifugation and molding into a cylindrical specimen. Images are taken when the angle between incident light and observation is at approximately (a) 30 °, (b) 90 °and (c) 120 °. 112
5.17 VCL-IA-15-460 microgels crosslinked in 10% wt/V AAm under UV light, at RT and neutral pH. The sample was prepared by ultracentrifugation and molding into a cylindrical specimem. Images are taken when the incident light is at approximately (a) 30 °, (b) 90 °, where and the sample is at RT, and (c) 30 °incidence after having been placed in a 60 °C water bath. 113
5.18 VCL-IA-15-460 microgels crosslinked in 10% wt/V AAm under UV light, at RT and neutral pH. The specimen was printed in a 2-layer grid with a printing pressure of 70 kPa and 10 mm/s printing speed. The sample is (a) at RT and (b) right having been submerged in a 60 °C water bath. 113
5.19 NIPAm-AlAm-400 microgels in 10% wt/V of AAm, cured under UV light, at RT and neutral pH. The sample was prepared from redispersion of the microgels, centrifugation and 3D printing into a two-layer grid. Images are taken under diffused natural light. (a) A sample at RT, (b) a sample as it is being placed under a 60 °C water jet, which causes the sample to immediately turn white, and (c) when hot water is spread over the rest of the sample. . . 115

6.1 Chemical structures of the A_9B_{26} and $A_8B_{104}A_8$ block copolymers used in this study. 124
6.2 Schematic representation of the "solvent switch" method. (a) PDMS-*b*-PMOxa is initially dissolved in a water-miscible organic solvent, (b) rehydration buffer is added to the mixture until (c) polarity of the solvent induces the self-assembly into polymersomes. 126
6.3 TEM images of self-assembly between ABA and P(NIPAm-*co*-MAAc) microgels performed in PBS buffer and dialyzed against MilliQ water, stained with PTA at neutral pH. (a), (b), (c), and (d) are taken from the same sample. 128

6.4 TEM images of self-assembly between ABA and P(NIPAm-*co*-MAAc) microgels performed in bicarbonate buffer and dialysed against MilliQ water, stained with PTA at neutral pH. 129
6.5 TEM images taken of the self-assembly of ABA with P(NIPMAm-*co*-MAAc) microgels in boric acid buffer, and then dialysed against MilliQ water. Samples have been stained with PTA at neutral pH, and images are taken from several locations in the same TEM grid. 130
6.6 TEM images of self assembly between ABA and P(NIPAm-*co*-MAAc) microgels performed at RT with the "solvent switch" method in (a) and (b) PBS buffer and dialyzed against PBS buffer and in (c) and (d) boric acid buffer and dialyzed against boric acid buffer. 131
6.7 Schematic representation of the "film rehydration" method. (a) polymer is initially dissolved in EtOH, (b) which is evaporated to induce a film formation. (c) The film is rehydrated and allowed to swell overnight without stirring, and (d) formed GUVs deposit on the bottom of the vial. 133
6.8 CLSM image of GUVs with encapsulated P(NIPMAm-*co*-MAAc) microgels (D_H= 150 nm), obtained *via* the film rehydration method at RT and neutral pH. The microgels are in pink, whilst the GUV membranes were not stained and therefore nto visible here. 134
6.9 Schematic representation of the double emulsion-templated microfluidic set up, showing the encapsulation of microgels. Microgel-loaded inner aqueous phase (IA, in green) is enveloped by the polymer-containing organic phase (PO, in purple), and the resulting jet is periodically broken by the external aqueous phase (OA, in blue). Evaporation of the organic phase leads to GUV formation. 136
6.10 CLSM images of a (a) fluorescence signal and (b) transmission of the bottom of a GUV filled with 1% wt/V PNIPMAm microgel and (c)fluorescence signal and (d) transmission of the middle section of the same GUV, showing its empty lumen. 137
6.11 CLSM images of a 5 wt% microgels dispersion in MilliQ water encapsulated in AB at RT. (a) bottom of the GUV imaged in fluorescence and (b) in transmission; (c) airy scan processing of a slice alog the focal plane and (d) z-stack slices along the focal plane. 138

6.12 CLSM images of a 5% wt microgels solution in 10% wt/V PEG 6000 encapsulated in 6 mg/ml PDMS-*b*-PMOxa GUVs at RT and neutral pH. The GUVs are made from microfluidic chips with (a) 50 μm and (b) 100 μm channels. 139
6.13 Reconstructed 3D image of GUVs filled with 5% wt/V PNIPMAm microgels at RT and neutral pH. 140
6.14 CLSM images of a (a) fluorescence signal and (b) transmission of the bottom of a GUV filled with 1% wt/V P(NIPMAm-*co*MAAc) microgel and (c)fluorescence signal and (d) transmission of the middle section of the same GUV, showing its empty lumen. 141
6.15 3D reconstruction of GUVs obtained by stacking all slices taken along the Z plane. 142
6.16 Middle Z slice of GUV filled with 1% wt/V NIPMAm microgels at 40 °C at (a) *t*=0 s, (b) *t*=1 s, (c) *t*=2 s, and (c) *t*=3 s. Circled in pink: microgel at the membrane; circled in purple: free microgel in the lumen. Lines are placed to help the reader. 143
6.17 Middle Z slice of GUV filled with 5% wt/V NIPMAm) microgels at 40 °C at (a) *t*=0 s, (b) *t*=1 s, (c) *t*=2 s, and (c) *t*=20 s. Circled in pink: microgel at the membrane; circled in purple: free microgel in the lumen. Lines are placed to help the reader. 143
6.18 Middle Z slice of GUV filled with 1% wt/V P(NIPMAm-*co*-MAAc) microgels at 40 °C at (a) *t*=0 s, (b) *t*=1 s, (c) *t*=2 s, and (c) *t*=20 s. Circled in pink: microgel at the membrane; circled in purple: free microgel in the lumen. Lines are placed to help the reader. 144
6.19 Middle Z slice of GUV filled with 5% wt/V P(NIPMAm-*co*-MAAc) microgels at 40 °C at (a) *t*=0 s, (b) *t*=1 s, (c) *t*=2 s, and (c) *t*=20 s. Circled in pink: free microgel in the lumen. Lines are placed to help the reader. 144

9.1 Turbidity of 0.1 wt% P(VCL-*co*-IA) (*M*15) microgel samples in (1) water, (2) after the addition of 1 mM Ca^{2+} to the solution and (3) after the addition of acid to equilibrate to pH 3. 185
9.2 Dogbone molds of (a) NIPAm-450, (b) NIPAm-400 and (c)NIPAm-350 crosslinked under UV light (60 mW/cm^2. 185
9.3 Dogbone mold of PNIPAm-400 against black background under diffused light, cured with low intensity UV light. 186
9.4 P(VCL-*co*-IA) microgels compressed by ultracentrifugation at RT. 186

9.5 P(VCL-*co*-GMA) microgels compressed by ultracentrifugation at RT in 10% AAm aqueous solution. The ink was printed in a 2 layer grid with a printing pressure of 70 kPa and 10 mm/s printing speed. 186
9.6 PVCL microgels compressed by ultracentrifugation at RT in 10% AAm aqueous solution and 1% of CMC 90 kDa. The ink was printed in a 2 layer grid with a printing pressure of 70 kPa and 10 mm/s printing speed. 187
9.7 Double network of PVCL-IA-15-400 crosslinked in 10 wt/V% of AAm in the presence of 50 mM of CaCl2. 187
9.8 Shear recovery plots of (a) PVCL-IA-15-500 and (c) PVCL-IA-15-550 containing 0.1 M $CaCl_2$ from dispersions centrifuged at 282k RCF at RT and neutral pH. G' (in black) and G" (in pink) are plotted against time, at 10% strain (filled dots) and 1% strain (hollow dots). 188
9.9 PNIPAm-400 extruded by hand at RT into a PDMS bath. 188
9.10 NIPAm-AA-300 DNGH under (a) diffused light, (b) and (c) direct light. . . 189
9.11 TEM images of $PMOXa_8$-$PDMS_{45}$-$PMOxa_8$ based vesicles and micelles, assembled in PBS at RT with the film rehydration method. 189
9.12 TEM image of $PMOXa_8$-$PDMS_{45}$-$PMOxa_8$ based vesicles, assembled in PBS at RT with the solvent switch method. 190

List of tables

1.1 List of applications involving microgels with one relevant microgel as example. 11

2.1 Amount of dimethylitaconate (IADME) incorporated and itaconic acid (IA) groups 28
2.2 R_g/R_H of P(VCL-*co*-IADME) (N*n*) microgels in pure water at pH 7 and P(VCL-*co*-IA) (M*m*) microgels in pure water at pH 7 and pH 3. R_g was determined *via* SLS and R_H *via* DLS. 33
2.3 Hydrodynamic diameters obtained by DLS of M8-M30 at 10^{-4} mM and 10 mM divalent metal salts ($CaCl_2$, $MgCl_2$, $SrCl_2$, $CuCl_2$ and $FeCl_3$) measured at RT and neutral pH in MilliQ water. 38
2.4 D_H (nm), as determined by DLS, of homopolymeric VCL microgel N0 in pure water and in the presence of 10 mM $M^{2+/3+}$ ions at 10 °C and neutral pH. 39

3.1 Concentration of COOH groups in solution, Ca^{2+}ions bonded at pH= 7 and the bonding ratio between the two. 45
3.2 Concentration of COOH groups in solution, M^{n+} ions bonded at pH= 7, and the bonding ratio between the two. 47
3.3 Percentages of Mg^{2+} and Fe^{3+} ions bonded at ambient conditions: in PBS at RT with a 0.1 wt% of M10 solution. The number of non bonded ions is determined by ion chromatography and the resulting difference is reported in the table. 47

4.1 Microgels size as measured by DLS for each P(NIPAm-*co*-MAAc) microgel, measured in MilliQ water at neutral pH, and in 10 wt/V% of AAm, both at 20 °C. 67

5.1 Homopolymeric PVCL microgels of varying size. Each sample is listed with the code that is used throughout this chapter. 91

5.2 P(VCL-*co*-IA) microgels obtained from direct copolymerization of VCL and IA, with varying size and constant monomer composition. 92
5.3 P(VCL-*co*-IA) microgels, with varying size and composition. Each sample is listed with the code that is used throughout this chapter. 92
5.4 D_H of P(VCL-*co*-GMA) microgels measured in water and AAm (10% wt/V in water) measured at RT and neutral pH. 93
5.5 Microgels size measured for each P(NIPAm-*co*-AlAm) microgel, measured in MilliQ water at neutral pH, and in 10% wt/V of AAm. 94
5.6 D_H, color, and extrusion behaviour of PVCL in H_2O containing AAm (10% wt/V) at RT, 21 gauge nozzle at RT and neutral pH. 95
5.7 P(VCL-*co*-IA) microgels soaked in 10% wt/V of AAm, and 0.1 mol% PI, at a pH=7, at RT. Table displays their color after centrifugation at 282k RCF at RT for 2 h, and their behaviour when extruded from the printing nozzle. . . 97

6.1 Name, D_H at RT and at 40 °C of the microgels used in this study, all of them containing BIS as crosslinker and MRB as fluorescent dye. D_H are measured in buffer (ringer solution), ad give only a qualitative estimation of their size for this chapter. 125
6.2 Summary of solvent sequences used to encapsulate 0.1% wt/V P(NIPAm-*co*-MAAc) microgels in ABA- based vesicles, and the result of self-assembly. 127

8.1 Synthetic amounts for VCL-*co*-IADME microgels for a reaction volume of 150 ml. 153
8.2 SDS concentrations used to obtain PNIPAm-based microgels used in Chapter 4. 154
8.3 SDS concentrations used to obtain PNIPAm-AA microgels used in Chapter 5. 154

9.1 Synthetic conditions for the polymerization of neutral microgels with various N-vinylcaprolactam (VCL) and dimethylitaconate (IADME) ratios. 183
9.2 Hydrolysis yield for each microgel sample determined by potentiometric titration. 183
9.3 R_g/R_H of P(VCL-*co*-IADME) (N*n*) microgels in pure water at pH 7 and P(VCL-*co*-IA) (M*n*) microgels in pure water at pH 7 and pH 3 184
9.4 Comparison of the D_H of P(VCL-*co*-IA) (M*n*) microgels in the presence of Ca^{2+} and at pH 3 at T = 20 °C 184
9.5 R_g/R_H ratio of M5, M10 and M19 taken at 20 °C, at pH 7, 1 mM Mg2+ and pH=2. 184
9.6 . ζ-potential of P(VCL-*co*-IA) (M*n*) microgels samples in pure water and loaded with Ca^{2+} ions. 184

9.7 Amount of Mg^{2+} ion bonded at ambient condition in PBS 185
9.8 Molar constituents of microgels used in Chapter 6. 187

Abbreviation	Full name
$3D$	Three-Dimensional
AAc	Acrylic Acid
AAm	Acrylamide
AB	Diblock copolymer
ABA	Triblock copolymer
AMPA	Aminopropiondiimidine
APMA	*N*-(3-aminopropyl)methacrylamide
ATR-FTIR	Attenuated Total Reflection - Fourier transformed Infra Red
CLSM	Confocal Light Scanning Microscopy
CMC	Critical Micelle Concentration
CMC 90k	Carboxymethylcellulose
-*co*-	Copolymer
COOH	Carboxyl group
CTAB	Cetrimonium Bromide
CytC	Cytochrome C
DEAm	Diethylacrylamide
D_H	Hydrodynamic Diameter
DLS	Dynamic Light Scattering
DMAm	Dimethylacrylamide
DMAPMA	*N*-[3-(Dimethylamino)-propyl]-methacrylamide
DNGH	Double network granular hydrogel
EDTA	Ethylenediaminetetraacetic acid
ϕ_{eff}	Effective volume fraction
FCS	Fluorescence correlation spectroscopy
GMA	Gylcidyl methacrylate
GPC	Gel permeation chromatography
GUV	Giant unilamellar vesicle
^{1}H NMR	Proton Nuclear Magnetic Resonance
HPC	Hydroxypropylcellulose
IA	Itaconic Acid
IADME	Dimethylitaconate
ITC	Isothermal Titration Calorimetry
kDa	Kilo Dalton
KPS	Potassium Persulfate
LCST	Lower Critical Solution Temperature

N_{agg}	Aggreagtion Number
NIPAm	*N*-Isopropylacrylamide
M	Molar
MAAc	Methaacrylic Acid
MAS	Magic angle spinning
MC	Merocyanine
M_w	Molecular Weight
MWCO	Molecular Weight Cut Off
PBS	Saline phosphate buffer
PDMS	Polydimethlsiloxane
PEG	POly ethyleneglycol
pH	Negative decimal logarithm of proton concentrations
pK_a	Negative decimal logarithm of acid constant
ppm	Part per Million
PTA	Phosphotungstic acid
PVA	Polyvinylalcohol
RC	Regenerated Cellulose
RCF	Relative centrifugal force
R_g	Radius of Gyration
R_H	Hydrondynamic Radius
rpm	Rounds per Minute
RT	Room Temperature
SAXS	Small angle x-ray scattering
SEM	Scanning electron microscope
SLS	Static Light Scattering
SDS	Sodium Dodecylsulfate
SP	Spiropyrane
TBAm	terbutylacrylamide
TEM	Transmission Electron Microscopy
THF	Tetrahydrofurane
TCL	Thin layer chromatography
UV	Ultraviolet
VCL	Vinylcaprolactam
VIm	Vinylimidazole
VIS	Visible
VP	Vinylpyrrolidone

VPTT	Volume Phase Transition Temperature
ζ	Vlume fraction

ace

Chapter 1

Introduction

1.1 Microgels

Microgels are gel networks ranging in size from hundreds of nanometers to tens of micrometers that swell in good solvents.[1] *Microgel* is a general term and is frequently used without regard to the actual size of the particles in discussion, since gels with a diameter in the *n*m range should be called *nano*gels. For the sake of clarity, this thesis will refer to all gels that have a size between 10 nm and 10 μm as microgels.

More specifically, microgels are micro- and nano- sized colloidal $3D$ cross-linked polymeric networks that are swollen to their full volume by the solvent in which they are dispersed, and are colloidally stable due to steric or electrostatic repulsion.[1][2][3] Microgels can be regarded as a class of hybrid materials, as they sit at the interface between hard colloids, surfactants and macromolecules (Figure 1.1).[1] They are, first and foremost, macromolecules, as they can be chemically tailored to have the same chemical functionality as linear and branched macromolecules.[4] Nonetheless, microgels are 3D cross-linked, and behave like colloids in solution, and thus are characterized by particle properties, such as size, surface charge, elasticity and porosity.[4] Microgels can also be considered surfactants: despite being neutral in most cases, residual charges in these microgels make them surface active.[5]

The most distinctive characteristic of microgels is their inherent softness. This softness is the reason why they can be compressed or deformed, whilst remaining highly elastic and resistant to mechanical strain.

In some cases, the compression can be done mechanically, by confiningmicrogelss within a very constrained environment. Another way to prompt microgel compression is to induce the deswelling of the network, where the microgel expels solvent and shrinks. This can be done, for example, by increasing the osmotic pressure outside of the gel, inducing the solvent to abandon the microgel network. The polymeric chains within the microgel rearrange,

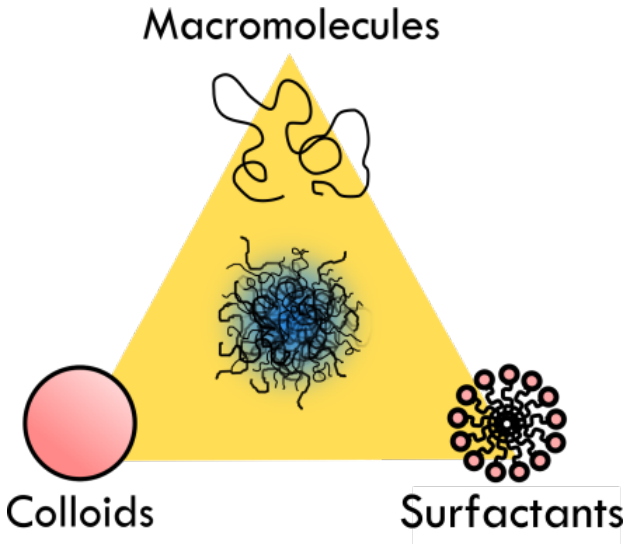

Fig. 1.1 Microgels position themselves in between three classes of materials: surfactants, hard colloids and polymers.[1]

inducing the collapse of the microgel's network whilst -generally- keeping the system colloidally stable.[6][7] Apart from osmotic pressure, shrinking can be triggered by physical changes of the external environment, such as temperature,[1] pH,[7] ionic strength,[8] electrochemical potential, [9] light,[10] hydrostatic pressure,[11] solvent composition[12] and ionic strength.[13]

The fabrication of stimuli-response microgels requires specific chemical tailoring, so that the chain solubility adapts according to the external conditions. This "*smart*" behaviour along with their high inrernal area due to porosity, has been exploited for the use of microgels as drug and gene delivery systems,[14] optical devices,[15] water purification systems,[16] emulsion breakers and stabilizers,[17] in food technology[18] and as sensors for biological and carcinogenic molecules in the biomedical field.[19] Microgels are also used as model systems to explore the transition from a soft colloid to a hard sphere, due to their ability to undergo this transition reversibly upon the application of an external trigger.[20]

1.2 Synthesis and purification

Microgel Synthesis

Microgels can be produced in batch, semi-batch, and in flow, depending on the targeted size, shape, and architecture. Generally, microgels that are smaller than 1 μm are produced in batches *via* dispersion polymerization, where a monomer, soluble in a solvent (generally

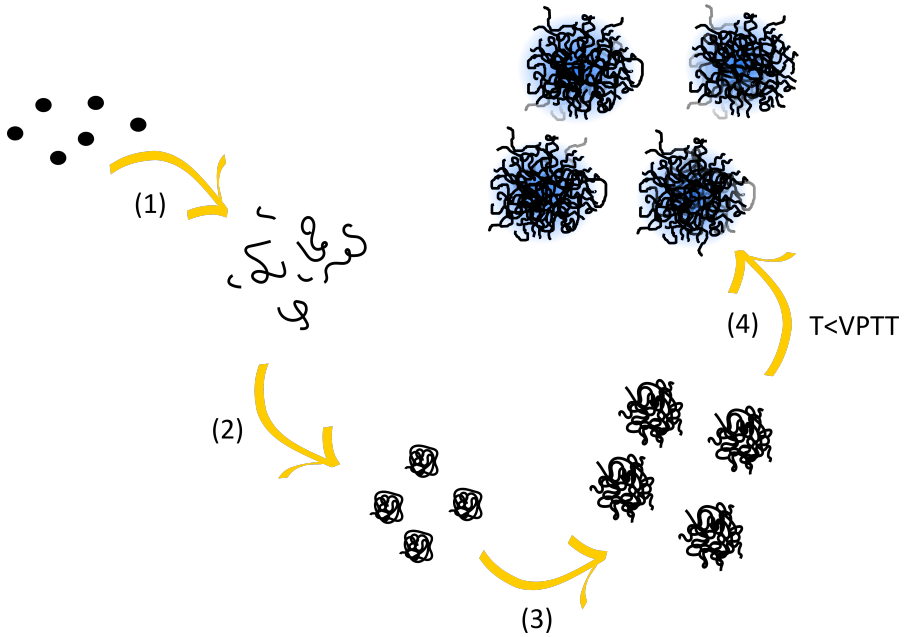

Fig. 1.2 Simplified schematic of dispersion precipitation polymerization: (1) oligoradicals start growing from monomers, then they reach a critical molecular weight (2) and form small unstable particles which keep growing (3) staying collapsed as the reaction temperature is higher than the volume phase transition temperature (VPTT). When the temperature is decreased to below the VPTT and the polymer chains become soluble again, the particles swell and swollen microgels are formed (4).

H_2O), is copolymerized with a crosslinker upon initiation by a radical initiator (KPS, AMPA) (figure 1.2).[21]

As the oligomeric chain grows, it reaches a critical molecular weight above which the polymer is not soluble anymore, and will crash out of solution, forming oil droplets. The small oil droplets (primary particles) will then grow by monomer addition on the surface and coalescence or Ostwald ripening, as they are not colloidally stable.[22] The growing radical chains and the charges from the initiator will be directed towards the surface of the particle. An increase in the volume, and thus the surface area, will lead to higher colloidal stability of the growing particle. The rapid, uniform seed formation, coupled to the steady growth of the chains (and thus networks) leads to monodisperse droplets and hence the formation of monodisperse microgels. However, to obtain monodisperse microgels, the primary particles need to be as small and narrowly distributed as possible, so that the growth is only dictated by chain addition and surface growth.[22] To this end, the primary particles are stabilized by a surfactant,commonly the charged surfactants SDS or CTAB. The higher the amount of surfactant, the slower the coalescence, and hence the smaller the resulting microgel particles. The surfactant should be below its critical micelle concentration (CMC), as the formation of

micelles would hamper the formation of monodisperse primary particles. Termination of the polymerization reaction is generally achieved by quenching the initiator and the radicals that are still propagating.

More complex architectures than simple spherical, homogenous microgels can also be obtained *e.g.* by seeded precipitation polymerization, where a certain number of gels or nanoparticles is injected into the polymerization solution, where the monomer will polymerize around them.[23] This enables the production of monodisperse core-shell or core-shell-shell microgels, and, if the core is sacrificial, hollow-shell microgels.[24] If the core is anisotropic, anisotropic core-shell and hollow microgels can also be obtained.[25]

Microgels between 1 and 5 μm can be produced in semi batch-fed approaches, which feature controlled temperature increases and monomer addition, leading to spherical, monodisperse isotropic microgels that range from 1 micrometer to 5 micrometers.[26]

Microgels with sizes greater than 5 μm are obtained with flow processes, such as oil/water single emulsion microfluidic set-ups, where monodisperse droplets already containing the monomers, crosslinker, and initiator, are produced and then polymerized.[27] By engineering when and how the droplets are polymerized, the microgels can be obtained in different shapes and architectures.[28] When monodispersity is not necessary, microgels of large dimensions are obtained with very simple batch approaches, such as emulsion polymerization and gel trituration. [29] The former technique enables the formation of spherical microgels with diameters that range from a few to a few hundred micrometers.[30] Mechanical smashing of the gels leads to similar sizes, but the shape of the gels is more irregular. Recently, spaghetti-like microgels have also been obtained, by squeezing a gel slab through a sieve, yielding elongated microgel structures hundreds of micrometers in length.[29]

Microgel Purification

Most of the applications that involve microgels rely on purified gels, where the residues of the polymerization are removed. When producing microgels, typical impurities include unreacted monomers, small uncrosslinked chains, or too-small particles that come from badly crosslinked microgels that could hamper the characterization or even lead to toxicity and interference with certain applications. There are two major methods to purify microgels, namely centrifugation and dialysis. Depending on the size, density, tendency to aggregate and solvent in which they are dispersed, either of the two can be suitable. Less frequently used is ultrafiltration, another suitable technique.

This thesis will consider only microgels that are smaller than 2 μm, and hence are obtained mostly *via* precipitation polymerization. Most microgels obtained with this technique present lower critical solution temperature (LCST) behaviour in water, meaning the polymer chain

will be soluble and have a random coil conformation below a certain temperature (the LCST) and is insoluble above that temperature, resulting in a globule conformation, therefore one has to regard the final solubility of the resulting polymer. If the resulting network is too hydrophilic, the growing chains will not phase-separate into monodisperse droplets, hampering the whole process.

1.3 Temperature responsive microgels

Microgels can change their degree of swelling, represented by the changes in their volumetric and mass between their dry and swollen states. For macroscopic gels, the degree of swelling is determined by weight, whilst, due to the reduced size of a microgel, the degree of swelling is addressed through volumetric changes. Microgels whose degree of swelling is dependent upon temperature are referred to as temperature responsive. The temperature at which a microgel changes its degree of swelling is called the volume phase transition temperature (VPTT).[31][32][33] The VPTT of a thermoresponsive microgel can correspond to the LCST of the linear polymer, however the precise value is also affected by factors such as crosslink density and network extension.[34][35] When the amount of crosslinker exceeds a certain threshold, the microgel will not be able to shrink or swell significantly. Interestingly, the preparation of microgels requires a much higher crosslinker concentration than that of their macroscopic counterparts. In fact, a macroscopic gel requires 0.25 mol% of crosslinker, compared to the 10-fold 2.5 mol% used in most microgels. The most studied temperature responsive building block in water is *N*-isopropyl acrylamide (NIPAm) which produces a polymer that has a LCST of 32 °C.[36] If the crosslinking density and monomer composition are correct, the microgel can have a comparable VPTT. Other well known LCST polymers are Poly(*N*-isopropylmethacrylamide) (PNIPMAm, LCST= 42 °C), Poly(diethylacrylamide) (PDEAm, LCST= 33-35 °C), and Poly(vinylcaprolactam) (PVCL, LCST= 32-34 °C),[36] and t-butylacrylamide (TBAm, LCST= 5 °C) (Figure 1.3).[36] The LCST of a polymer chain can be tuned to different values by co-polymerizing a monomer along with a polymer with different polarity. This can shift the overall solubility of the chain, modifying the LCST values to higher or lower values. Alternatively, one can also copolymerize two monomers with different LCST to obtain a polymer with a third LCST.[36] An example is the copolymerization of DEAm and TBAm, where the LCST can be tuned to fall between the limited LCST values of the homopolymers, depending linearly on the monomer ratio.[37] Not all dependencies are linear however, as is seen in the case of copolymerizations of DMAm with DEAm.[38] For most polymers, the LCST behavior is only partially explained, but the coil-to-globule transition upon temperature increase is typically thought to be accompanied

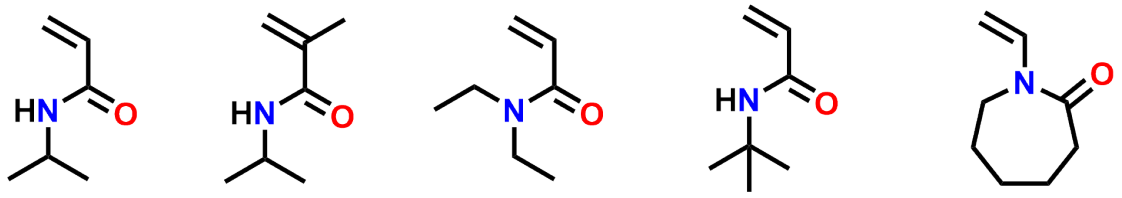

Fig. 1.3 Chemical structures of monomers that produce temperature responsive polymers. From left to right: NIPAm, NIPMAm, DEAm, TBAm and VCL.

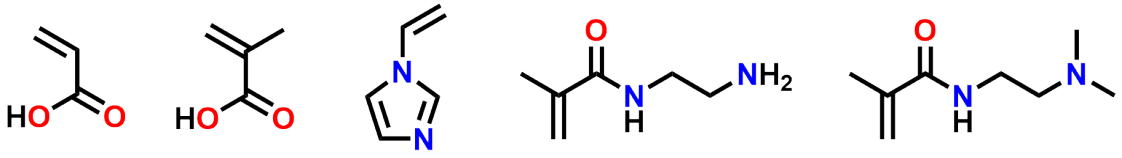

Fig. 1.4 Chemical structures of monomers that produce pH responsive polymers. From left to right: AAc, MAAc, VIm, APMA and DMAPMA .

by an endothermic enthalpy increase. For example, in the case of PNIPAm, an increase in temperature promotes more favoured polymer-polymer interactions between the hydrophobic isopropyl chains and the olefin backbone, causing an invagination of the structure and the expulsion of water pockets from the network pores.[39]

The most popular microgels are generally composed of PNIPAm and PVCL, due to their VPTT which is close to physiologic temperatures. Hence, they have been applied most often in drug delivery and gene delivery applications.[1] Although both polymers are biocompatible, VCL shows superior biocompatibility, as the lactam group does not undergo hydrolysis as easily as PNIPAm's amide groups, preventing the free circulation of toxic amines.[40][41][42]

1.4 pH-responsive microgels

pH-responsive moieties are those that can be protonated or deprotonated over a certain pH range, i.e. pH changes can influence the swelling of a microgel by changing the charge of its chains.[43] Such functionality can be incorporated into microgels through monomers that carry a pH responsive group: acrylic acid (AAc),[44][45] methacrylic acid (MAAc),[46] vinylimidazole (VIm),[47] *N*-(3-aminopropyl)methacrylamide (APMA),[45] and *N*-[3-(Dimethylamino)-propyl]-methacrylamide (DMAPMA) (Figure 1.4).[48]

These pH-responsive monomers are either homopolymerized or copolymerized with a neutral comonomer such a s NIPAM or VCL. When copolymerized, the pH responsive monomers are only used at concentrations up to 10 mol%. This is mainly due to two factors:

swelling and solubility. Even a small amount of pH-responsive monomer has an effect on the swelling of the microgel. When a critical monomer content is reached, it will overpower the responsive properties of the main monomer, such as NIPAm or VCL. Moreover, most microgels in the sub-μm range are obtained *via* precipitation polymerization. Adding too much of a hydrophilic comonomer will prevent precipitation, making this synthesis impossible. For these reasons, most highly charged pH-responsive microgels are obtained by inverse mini emulsion precipitation or post-polymerization modification approaches.[30][33] For instance, in order to obtain hollow charged microgels, a neutral shell composed of dimethylitaconate is polymerized around a sacrificial core, and the ester groups are cleaved to form carboxyl groups.[49] By copolymerizing monomers with different pK_a values, different degrees of swelling can be reached along the pH scale, as inthe case in a ternary system composed of VCL, itaconic acid and VIm.[50]

1.5 Behaviour of multi stimuli responsive microgels with metal cations

1.5.1 Temperature- and pH-responsive microgels in the presence of metal cations

Microgels can be made responsive to metal cations, especially divalent and trivalent ones, with functional groups that can act as ligands *i.e.* those who have high binding affinities to the cations and can thus form stable complexes.[51] The incorporation of such moieties into a cross-linked microgel causes change in the physical properties of the microgel to occur in response to metal complexation, altering the degree of swelling, color,[52] or colloidal stability.[46]

When it comes to alkaline earth and transition metal cations, which play a role in the homeostasis of biological systems, there is a range of functional groups that can coordinate metal cations. However, these functional groups are also subject to changes in protonation depending on the environmental pH.[53] The most common functional group used is COOH, as its pK_a when bound to various monomers and copolymerized with NIPAM is well understood.[53] The effect of metal cations on microgels can be investigated by means of dynamic light scattering (DLS), where the hydrodynamic radius (R_H) changes in response to ion concentration changes. The addition of an ion which can bind to COOH generally leads to two main effects: charge correlation and screening, and supramolecular crosslinking.[54][55][56] The majority of swelling studies have been performed on copolymer microgels containing PAAc or PMAAc and a thermoresponsive polymer, such as PVCL

or PNIPAm.[57][58] This is most likely due to the fact that highly-charged microgels lose colloidal stability even at low divalent cation concentrations, making their characterization highly challenging.

As a result, we need to differentiate between experiments below and above the VPTT of a microgel, where porosity, density, and accessibility of surface groups change dramatically. In particular, when inducing the collapse of a copolymer network, the repeating units will be dragged closer together, exposing more functional groups with the ability to interact with the metal on the microgel's surface.

For instance, in the addition of Ca^{2+} to PAAc microgels, which are not temperature responsive, the ion binding groups from different chains are close to each other. In this case, Dalmont *et al.* observed a decrease of the hydrodynamic radius (R_H) and -to a certain extent- the presence of aggregation as a result of Ca^{2+} addition.[46] When the microgels were highly concentrated they formed a liquidish paste, but oscillatory rheology measurements showed that no colloidal gel was formed, suggesting that the ion binding was not strong enough to induce gelation.[46] Hence, although some degree of intermicrogel crosslinking is present in highly charged microgels, the main cause for deswelling is charge correlation.[54]

By introducing thermoresponsive monomers, such as PNIPAm, into the system aggregation can be induced at a temperature above the VPTT. In fact, a P(NIPAM-*co*-AAc) microgel system has been shown to be colloidally stable at high Ca^{2+} concentrations below the VPTT, and then to aggregate above that temperature.[58] This was explained by the LCST-induced collapse exposing free, hydrophilic COOH groups on the surface, resulting in an increased propensity for inter-microgel aggregation. Possibly, this tendency towards increased aggregation might also derive from a reduced steric hindrance in the collapsed state above the VPTT when compared to the swollen state.[58]

Not all metal cations bind the with the same strength to COOH-decorated microgels. The binding affinities of ions such as Ca^{2+}, Mg^{2+}, Sr^{2+} and Ba^{2+} were estimated *via* isothermal titration calorimetry (ITC) measurements, showing the formation of complexes with high binding affinities within the network.[59] Eichenbaum *et al.* found that the binding affinity increases with the size of the ion topping out with Ba^{2+}. He also noted that there was only a small difference in the binding affinity bewteen Ca^{2+} and Mg^{2+}.[59]

1.5.2 Light responsive polymers and microgels

Light-responsive microgels are formed by the introduction of molecules that change their conformation and solubility under the influence of light. When it comes to microgels, 5 to 10 mol% light-responsive functionality is generally sufficient to induce dramatic responsivity in the network. The light responsive moieties that are most widely employed for microgels are

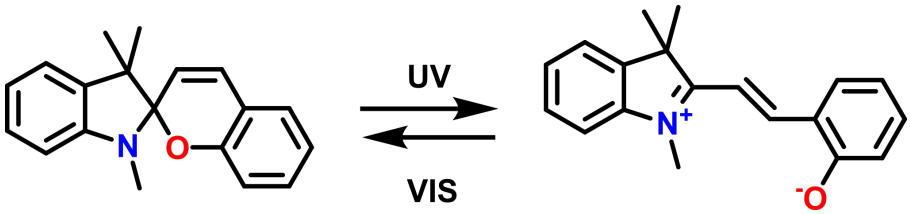

Fig. 1.5 Schematic representation of the spiropyran isomerization between its closed hydrophobic SP form and open zwitterionic MC form.

azobenzene[60] and spiropyranes (SPs).[61] Azobenzenes reversibly change their isomerization from cis to trans when subjected to a light stimulus, causing a change in polarity and hydrophilicity. Azobenzenes have been attached to microgels to induce light-mediated volume changes.[60] However, the functionalization generally es through EDC/NHS coupling, or direct copolymerization, yielding low functionalization percentages.[62] Recently, azobenzene surfactants have been used in combination with temperature-responsive P(NIPAM-*co*MAAc) microgels, to tune their VPTT upon a light stimulus.[62] This second approach is preferred due to the low solubility of azobenzene-based monomers in water, which makes them challenging to copolymerize or tether to the microgel network.[62] Azobenezenes do respond only to light inputs, providing only one possible stimulus to change the microgel's swelling.

In the case of SPs, the molecule undergoes isomerization between a closed, hydrophobic form (SP) and an open, zwitterionic, hydrophilic and highly absorbing merocyanine (MC) form, as a result of light, pH, ionic or mechanical changes (Figure 1.5).[63][64]

The isomerization is generally observed *via* UV-VIS absorbance spectroscopy, thanks to the dramatic shifts in absorbances between the open MC form and the closed SP form.

The main challenge that arises for spiropyran-based materials is the incorporation of the monomer within the microgels structure due to solubility issues.[65] Especially when attempting direct copolymerization in water, the solubility of the light-responsive monomer is often so low that it will both not react and promote the aggregation of the forming microgel particles, as the apolar spiropyran monomer droplets act as nucleation points for the primary microgel particles.[65] Therefore post-polymerization approaches are more common, where the spiropyran is attached to the microgel. This is the case for amino-functional microgels, to which carboxyl-functional SP moieties can be tethered *via* amide bond formation.[61] SP can also be attached to a linear polymer chain, and the SP-functional polymers are subsequently cross-linked to form microgel particles, for example *via* Micheal addition.[65] The latter approach not only provides much higher control over the comonomer content, but also enables the incorporation of higher amounts of spiropyran (»5 mol%). These systems have, however, not been explored further than their swelling behaviour under UV or temperature

changes.[61] The chemistry of the substituent of the aromatic rings of SP influences the position of its isomerization equilibrium and responsiveness to light.[66][67] In fact, SP needs an electron withdrawing group in meta or para position to the oxygen which provides the ring closing of the isomer, in order to be responsive to light. The most common substituent for this purpose is a nitro group in para position. As it follows, when SP is tethered to a polymer, the equilibrium position also depends on the main chain chemistry.[68]

The interactions between light-responsive polymers and metal cations has been widely investigated, focusing on the coordination changes induced by light.[69] Some light responsive molecules, such as carboxyfluorescein and different SPs, change their absorbance spectrum upon coordination with a metal cation.[70][71] This shift has been widely used to detect ions even at very low concentrations. This is achieved by embedding the molecules in films or gels, and observing changes in color with the naked eye. Mostly, microgels are employed as rapid sensors for $Cu^{(II)}$ detection, whilst other metals are generally sensed by free molecules not attached to a gel.[72][73] There are, however, barely any examples of light-responsive microgels that can interact with ions for means of controlled coordination and release.

1.6 Main applications

In this section the main applications and latest advances in the past few years is presented to provide an overview for the microgel field in terms of application.

Microgels are soft, deformable and elastic, and can adapt their shape and swelling to their external environment.[1] In recent years, thanks to such properties and their small size, microgels have attracted attention as candidates to model soft interactions, such as soft tissue interactions with proteins or protein-protein interactions.[74] Additionally, their high surface area, softness, and excellent colloidal stability make microgels suitable candidates for a wide range of other applications. Such properties have been exploited to expand the use of microgels as bio-catalyst supports,[75] biological sensors,[76] absorbers,[77] and cell scaffolds and delivery systems.[78] Their inherent softness and colloid-like behaviour at high volume fractions makes them interesting for formulation purposes at ultra high volume fraction.[79] Furthermore, the possibility to obtain monodisperse gels and their ability to assemble into ordered structures has been used for optical devices.[45] As mentioned in section 1.1, microgels are also surface-active, and have been employed as emulsions stabilizers and breakers.[80] Table 1.1 sums up the following subsections (1.6.1-1.6.3), in terms of listing the state of the art of core-only microgels employed in the various applications described in more detail in the following subsections.

Table 1.1 List of applications involving microgels with one relevant microgel as example.

Application	Microgel	Reference
Enzyme protection	PNIPAm	[81]
Protein delivery	Poly(carboxybetaine)	[82]
Antibacterial peptide carrier	P(EAc-*co*-MAAc	[83]
SiRNA delivery	P(NIPMAm-*co*-NIPAm-*co*-lysine)	[84]
Cargo uptake and release	P(NIPAm-*co*-tBAm)	[85]
Detoxification	P(NIPAm-*co*-tBAm-*co*-MAAc)	[86]
In vivo drug delivery	PVCL (degradable crosslinker)	[87]
Tumor Targeting	P(NIPAm-*co*-sulfobetaine)	[88]
Cell delamination	PNIPAm	[89]
Thermochromic film	PNIPAm	[90]
Temperature sensor	P(NIPAm-*co*-AAc)	[91]
pH sensor	P(NIPAm-*co*-AAc)	[92]
Light sensor	P(NIPAm-*co*-Azobenzeneacrylamide)	[60]
Electrochemical sensor	PNIPAm	[93]
Emulsion stabilizer	PNIPAm	[20]
Biocatalysis	PNIPAm	[3]

1.6.1 Biomedical and drug delivery systems

Microgels are able to entrap a variety of biologically-relevant molecules within their network. Combined with their proven biocompatibility, this makes them perfect candidates for *in vivo* toxin scavenging and drug delivery applications.[94] The chemical structure of a microgel's network is responsible for generating a more energetically favourable chemical environment than water for certain molecules. By tweaking the gel's chemistry, the gels are able to selectively entrap within their network a target molecule. This has been leveraged, for example, for toxin scavenging by designing a microgel network that a toxin will preferentially sequester into: when NIPAm is copolymerized with a hydrophobic monomer (tBAm) and an anionic one (AAc), the resulting microgels bind to Melittin, the toxic pore-forming peptide contained in bee venom. The microgels were effective *in vivo*, where mice were successfully detoxifed.[85]

Microgels are not only able to entrap and store molecules in their network, they can also release it in response to external stimuli. Typically, stimuli-responsive microgels change their polarity and swelling in response to environmental changes. Triggered deswelling can lead to the expulsion of molecular cargo, as a consequence of the change in solubility of the network's chains and the resulting reduction of pore and cavity size as the gel's network collapses. Toxin-scavenging microgels have therefore also been designed in a way where the microgel is able to release the toxin after entrapping, by changing the external pH, for recovery purposes.[86] Such *on demand* release has also been investigated for stimuli other than pH, like temperature and ionic strength.[94] As an example, Yoshimatsu *et al.* designed a thermo- and pH-responsive microgel composed of PNIPAm, PTBAm and PAAc, which would entrap lysozyme in its network and release it on demand.[86] However, despite this approach working well *in vitro*, when it comes to *in vivo* applications, there are some limitations to such functional microgels. The main challenges that arise from such systems are their accumulation in the body and the limited scope of therapeutics that can be effectively delivered.[95] To prevent accumulation, research has addressed the need for biodegradable microgels, which possess cleavable crosslinks that can be degraded chemically or enzymatically. For instance, by swapping out the commonly used methylene bisacrylamide (BIS) crosslinker for a disulfide-containing diacrylate, PVCL microgels could be easily degraded in the presence of a reducing agent.[87] Using an inverse approach to increase biocompatibility, microgels made of methacrylate-functional dextrane were crosslinked *via* the methacrylate groups, whilst the main chain could be enzymatically degraded.[96]

Along with biocompatibility and degradation, bioavailablity and half-time in the body can also be addressed by changing the chemistry of the microgels. Overall, thanks to their adaptable chemistry that can selectively target cells, softness, and porosity, microgels perform

well for the detection of tumors and delivery of therapeutics.[88] In the case of POEGMA-, PNIPAm- based microgels the addition of sulfobetaine to their network improved tumor localization by 10% compared to control nanoparticles, which targeted healthy cells more unspecifically.[88] Moreover, increasing the architectural complexity of a microgel, for example, by producing core-shell or core-shell-shell microgels, permits the controlled release of different drugs over time or under a certain stimulus.[97] Hence, a smart way to reduce drug resistance in tumors, is to build a microgel with parts that synergistically contribute to the localization, targeting, and delivery of a therapeutic agent to the tumor cells. An example of this technique is the work presented by Wang *et al.*, where a core-shell-shell microgel decorated with targeting RGD peptides, would encapsulate a chemotherapeutic drug and a drug-resistance inhibitor separately in the core and in one shell, in order to enhance the effectiveness of the system.[98]
The delivery of small drugs has been extensively studied in the last years, and recently an major focus has been placed on the delivery of macro-therapeutics. Microgels are particularly well-suited for protein delivery, since the highly porous and hydrated core of a microgel can simultaneously protect the protein from degradation.[82] Other macrotherapeutics that have been successfully delivered by microgels are antimicrobial peptides[83] and siRNA.[99] For the latter, PNIPAm-based microgels, carrying ionizable groups which can be protonated when moving from the cytoplasmatic to the lysosomal environment, enable cytoplasmatic DNA/RNA delivery.[20] Similarly, fully cationic microgels were effective in the delivery of RNA to tumors.[84] By increasing the microgel size, cells were delivered *in vivo*. When microgels become cell carriers, *i.e.* interfaces on which the cells can attach, applications like cell delivery,[100] cell delamination,[89] and cell growth on soft adaptable scaffolds are also possible.[101] The main challenge that arises from this approach is the potential cyto-toxicity and inflammatory response that synthetic polymers can provoke.[95] While alginate/Ca^{2+} microgels are cytocompatible and widely used, "smart" microgels that can change their behaviour to enable more refined applications, seem to produce inflammatory responses *in vivo*, reducing their applicability.[102]

1.6.2 Smart devices and sensors

Monodisperse microgels can assemble into ordered, packed structures, typically into face-centered-cubic (fcc) and body-centered-cubic (bcc) crystalline lattices.[103] The crystallinity of such densely packed assemblies depends on the volume fraction, size, degree of crosslinking and architecture of the microgels.[104] [105] The volume fraction influences the crystalline structure and thus, the macroscopic optical properties of the material.[106] Below a certain volume fraction, the gels will move in a disordered fashion with Brownian motion,

yielding milky solutions. When the volume fraction increases, the microgel can assemble into crystalline lattices, forming soft crystals which will reflect light due to Bragg diffraction. Above such a volume fraction, the microgels start to interpenetrate each other, and a disordered solid with gel-like properties will arise. When the size of the microgel is comparable to visible-light wavelengths, the ordered packing of surfaces with microgels produces vibrant structural colours, as the result of Bragg diffraction on the surface.[107] [108] Generally, in order to achieve changes in colour, there has to be an ordered mismatch in refractive index between the crystalline structure and the matrix.[108] By tuning the size of the microgels in a mismatching matrix, the color can be changed accordingly.[105] So far, the formation of crystals assembled from microgels has been of interest chiefly for physicists and material scientists to investigate the phase behaviour of microgels and deepen the understanding of this class of soft materials. Large scale application of microgel crystals for materials and sensors is hampered mainly by the poor processabiliy of these kinetically-stable yet mechanically-labile crystals. Such crystals do form overtime, but do not resist mechanical stress (like gentle shaking) and are characterized by very low viscosity, making them more susceptible to low-level mechanical stress which will disrupt the crystalline structure.[109][104] Instead, existing in macroscopic materials, rely on the ordered 2D assembly of microgels into hexagonally-packed films on surfaces.[110] Since the diffraction of light depends on the spacing between the ordered microstructures, the structural colour of a film can also be modified post-assembly by physically increasing the packing distance for instance by pulling the film apart.[108][111] With this, mechanochromic films have been developed as strain and pressure sensors. By introducing stimuli responsive microgels, thermo- and solvato-chromic materials were made.[90] Another way to generate a refractive index mismatch, and thus, structural coloration, is to produce core-shell microgels composed of a hard silica or polystyrene core and surrounded by a soft corona with a different refractive index.[112] By increasing the difference in refractive index, the resulting colors become brighter and more saturated, like in the case of a poly(trifluoroethyl acrylate) core and poly(benzyl acrylate) shell microgel array.[113] While the preparation of core-shell microgels is lengthy and challenging to scale up, another way to make optical materials is the constructions of etalons.[114] Etalons are layers of microgels sandwiched between gold thin films, which enhance the reflectance of the film. The reflectance enhancement leads to brighter and more vibrant colors, where small swelling changes can also be made visible.[91] Etalons have been studied extensively as sensors for temperature,[91] pH,[92] light[60], electrochemical stimulus[93] and small molecules.[115] By exposing the film to microgels that are stimuli-responsive, the shrinking or swelling of the microgels is triggered, inducing a reversible colour change. Similarly, if the microgel responds to a chemical, such as glucose, the microscopic effect will be a

modification of the crystalline structure and thus a color change will be visible.[116]
By using a trigger that induces a gradual and quantifiable swelling or collapse of the microgel's network, one can obtain sensors. For instance, humidity sensors have been constructed by simply painting a microgel film on a flexible sheet.[117] Since the PNIPAm microgels change their swelling according to the environmental humidity, changes in humidity lead to the compression or extension of the film, triggering the gradual curling of the sheet. The swelling and shrinking of a microgel film has also been exploited for actuation purposes. By depositing microgels on a flexible surface , Li *et al.* were able to describe the temperature-induced folding of microgel painted sheets.[118]

1.6.3 Interfacial applications

The synthesis of microgels generally involves the use of ionic initiators and surfactants.[22] Usually, the excess surfactant is removed from the gels during the purification process, though it is more challenging to remove all residues of the initiator. The remaining charges lend an amphiphilic character to microgels, which makes them surface-active.[1] Combined with a dramatic reduction in energy when they assemble on oil-water or air-water interfaces, this makes microgels excellent emulsifiers.[1] Emulsions that are stabilized by particles are called Pickering emulsions, and similarly, emulsions that are stabilized by microgels, are named Mickering emulsions.[119] Contrary to Pickering emulsions, the stability of which is dependent only on the reduction of interfacial tension, the properties of Mickering emulsions are dependent also on the softness, deformability, and swelling of the microgel.[20]

Mickering emulsions bear the advantage of frequently having an active material at the interface between two immiscible phases.[120] By inducing swelling and polarity changes in the gels, the stability of the emulsion can be enhanced or reduced without the need to add further components.[20] Moreover, since the gels are also extremely porous, they can be used as supports that facilitate catalysis at the interface. When a microgel exists at the oil/water interface, the majority of its volume is swollen in the water phase, whilst only a small fraction of its volume is swollen in oil.[20] The high porosity of the microgel plays a key role in allowing the two phases to communicate.[3] For instance, in a two-phase system, where a water-soluble enzyme, which otherwise should ber reconstituted in a membrane, was entrapped in PNIPAm microgel-stabilized droplets dispersed in a substrate-containing oil phase, catalytic turnover was achieved. Since PNIPAm microgels become hydrophobic enough to break the emulsion at T> VPTT (*ca.* 40 °C), by heating the solution above the VPTT, the oil phase containing the biocatalytic product could be easily separated from the enzyme-containing aqueous phase.[3]

1.7 Aims of this thesis

There is a wide variety of plastic materials which are biocompatible, highly tolerated by the body for *in vivo* applications, and of low environmental impact, including both synthetic and natural polymers.[121]

Not just for drug delivery *in vivo*, but also for sensing and additive manufacturing applications, fine control over functionality is key to achieving the desired changes in chemical or physical properties of the system in response to a stimulus.[122] Despite attempts to use biocompatible materials derived from renewable feed stock, research and development therefore frequently turns to synthetic materials. The chemical versatility of synthetic polymers allows the fine-tuning of the final material's mechanical and chemical properties.[123]

Examples of widely-used monomers are *N*-isopropylacrylamide and *N*-vinyl caprolactam, which are known to produce biocompatible, inert, and thermoresponsive polymers.[124] When polymerized *via* dispersion polymerization in the presence of a crosslinker, these monomers form microgels, that have excellent *in vivo* biocompatibilty and are thermoresponsive.

Microgels composed of these monomers can include, to a certain extent, comonomers, generally without influencing the microgel's inertness, antifouling, and thermoresponsive properties, whilst endowing the microgel with additional properties. Through copolymerization, microgels can therefore become multi-responsive, producing a wide toolbox to make very specific sensors and actuators.

Despite the extensive research done in the past years on microgels, and the tremendous advances achieved on the control over synthesis, architecture and assemblies, there are still limitations in the field that should be addressed. First, the main issue that microgels face is their scalability.[95] Most synthetic procedures are optimized for the lab scale and are highly batch dependent, especially in the case of core-shell microgels or hollow shell ones. Dilute conditions to prevent uncontrolled aggregation, coupled with the necessity to use harsh chemicals like HF to generate a hollow lumen, relegate these soft particles to small scale approaches. For this reason, this study chooses synthetic routes that involve one to two synthetic steps, minimize batch dependency, and are scalable on large reactors, opening the way to these specific gels to be used on a larger scale, both for biomedical and material applications.

Due to their size and inherent softness, microgels are extremely deformable and compressible, which permits one to spatially constrain microgels in crowded environments, well over the hard sphere limit of 0.74. When microgels are polydisperse, they can generate, at very high volume fractions, very viscous, self-healing viscoelastic solids, which in some cases can be used as inks suited for additive manufacturing.[30] By date, there are scattering

studies on the assemblies of jammed monodisperse microgels describing how they organize and interpenetrate each other, there are however no insights on how monodisperse microgels can affect the rheological properties of 3D granular gels.[79] The majority of monodisperse microgel assemblies are relegated to 1 layer at an interface, or thin films. When monodisperse microgels are added as a component to a macroscopic gel, their use is limited as a delivery system in dilute conditions, with however no interest on using them as building blocks for granular hydrogels. Furthermore, the structural coloration that arises from packed monodisperse microgels assemblies on surfaces has also been not been further investigated in 3D, and the change in color is limited to two directions. Ideally, the responsiveness of these gels, combined with their potential formulation are 3D printing inks, could produce 3D-printable stimulus responsive sensors. The confinement of microgels in constrained volumes like in the case of jammed granular hydrogels involves the interpenetration and facetting of microgels with one another.[95] The prediction and visualization of such behaviour is challenging, thus further computational studies should be conducted on the topic, to elucidate which factors affect the packing and macroscopic behaviour of granular gels. Not only computational studies, but also the structural analysis of such systems can be challenging, and relies on techniques such as small angle x ray scattering (SAXS) and time consuming ones like small angle neutron scattering (SANS). One way to more directly visualize microgels is by using fluorescence microscopy, which has been useful to determine the facetting of a fluorescently labelled microgel among non-labelled ones. However, there is so far almost no investigation on the behaviour of confined microgels at curved interfaces, nor insights on the behaviour of microgels constrained in spherical, small volumes, which could serve as synthetic mimics for cell compartments. Microgels have so far only studied in their interactions *outside* curved lipidic structures, serving as models for soft interactions, aiming to mimic protein-lipid interactions. Being PNIPAm microgels, their responsiveness to temperature was invesitgated un terms of surface interaction, but not bringing the study any further in terms of chnage in behaviour due to several stimuli. The stimulus, and the same time potential cargo, that is the most ignored, despite its relevance is in biological processes are divalent cations, like Ca^{2+} and Mg^{2+}, opening the way both to sensors but also to ion uptake and release systems in cell mimicry applications.

This thesis next demonstrates, in Chapter 2, how multiresponsive microgels are prepared, and how they behave in response to temperature changes and the exposure to ions. The binding, release, and selectivity, of biologically-relevant ions are investigated in detail in Chapter 3. By changing the functionalization and making them responsive to multiple stimuli, one can tune their capabilities both in terms of ion uptake/release and as sensing devices. Furthermore, microgels can be used as building blocks for granular hydrogels,

which can be further crosslinked in granular double networks. By combining this concept with the crystallinity of microgel lattices, Chapter 4 describes a simple and effective method to construct mechanochromic soft granular gels, based on nanometer sized monodispersed NIPAm-based microgels. Due to their facile synthesis and scalability, Chapter 5 investigates the possibility to expand the processability of such microgels to additive manufacturing, to produce mechanochromic complex objects. In particular, this chapter builds on a library of microgels, some already presented and some new ones, in order to investigate how the chemistry, size, and formulation method can affect the formation of inks suitable for 3D printing. Finally, in Chapter 6, it is shown how microgels can be constrained in micrometer-sized environments, and how they interact with soft polymeric membranes, further widening the scope and versatility of these materials.

Ultimately, this works aim to investigate how the versatility of the PVCL- and PNIPAm-based microgels can be leveraged to prepare macroscopic, responsive materials that are capable of ion sensing, uptake and delivery, and mechanochromic changes. These investigations were conducted with an eye towards ease-of-use, aiming for the "sweet spot" of ready availability, ease to functionalization, and high (bio)compatibility, to allow these microgels and the materials derived therefrom to be used in different fields of application.

Chapter 2

Swelling behavior of metal cation responsive microgels

This chapter describes the swelling behaviour of itaconic acid-functional microgels in the presence of divalent and trivalent metal cations. After starting with the synthesis and characterization of the gels, this chapter will proceed with their analysis of the size changes in the presence of Ca^{2+} and other metals.

Parts of this chapter have been adapted from the publications [125] and [13]. I have designed all the experiments, procedures and characterization methods. All experiments from [13] were performed in collaboration with Simona Conti. Csaba Fodor contributed ideas, suggestions and discussions. Csaba Fodor and Phally Kong participated the proof reading of the two publications.

2.1 Introduction

A multitude of biological processes are controlled and regulated by divalent cations like Ca^{2+} and Mg^{2+}. Examples include muscle contraction,[126] nerve impulses,[127] and signaling [128] which are activated and regulated by the concentration of said divalent cations in cells. Moreover, the presence of Ca^{2+} in lysosomes regulates their behavior within the cell environment.[129] Muscle contraction, for instance, is triggered by the 10-fold increase of the cytosolic concentration of 100 nM at the resting state to 2-4 mM. When released from the sarcoplasmatic reticulum of the cell this concentration change activates the neurotransmitters which will signal the muscles to contract.[130] One of the challenges in cell biology is to deliver with high specificity a stimulus within the cell without triggering other processes. A very popular approach is to use selective release systems based on

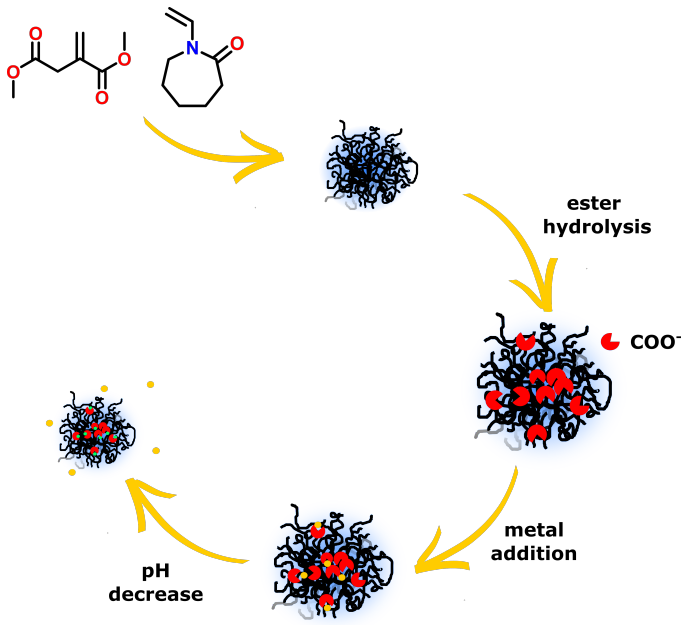

Fig. 2.1 Schematic representation of chapter content.

sub-compartments, where a reaction component is selectively released and interacts with a target. In order to achieve such compartmentalization, stimuli responsive liposomes or polymersomes are frequently chosen for the triggered release of water-soluble drugs,[131] or microgels.[132] Despite lipo-and polymersomes being the most commonly used materials, due to their high encapsulation efficiencies, facile purification and mechanical stability, in the last few years, microgels have also gained attention as cargo delivery systems.[1] Introducing pH-responsive moieties in a polymeric chain is the one of the most common approaches used to modulate the charged state of a responsive system.[133] Specifically, when it comes to the reversible binding of cargo, moieties that change their charge are a versatile tool for designing *on-demand* delivery. The possibility to fine-tune their size and responsiveness along with their proven biocompatibility makes them excellent candidates for cargo delivery, sensor, and catalytic applications.[134][1] Specifically, charged gels such as polyelectrolyte and polyampholyte gels have shown great uptake and release properties for drugs,[135] surfactants,[136] small molecules,[137] polyelectrolytes,[138] and small proteins such as Cytochrome C (CytC).[139] Whilst the uptake and release are generally diffusion driven in neutral gels, the introduction of charged moieties that can be modulated by pH changes provides a higher degree functionality for controlled release.[139][140] In the studies presented by Xu *et al.*, the introduction of charged moieties in the microgel's network permits the modulation of release kinetics. In fact, at neutral pH, the model drug CytC is released by diffusion, whilst the addition of acid, which protonates the carboxy

groups of the gels, induces a much faster "burst-like" release of the cargo.[139][140] Since fully charged microgels are rather unstable, gels containing charged moieties are more frequently copolymerized with a neutral comonomer, which provides steric stabilisation of ensure a higher colloidal stability of the system. Neutral comonomers such as NIPAm or VCL provide stabilisation, with the consequence of making the microgels additionally responsive to temperature. Hence, for drugs, surfactants, and small polyelecrolytes, there have been extensive studies performed on microgels exhibiting combined temperature and pH responsiveness.[95] Some of the most common gels are composed of either PNIPAm or PVCL as thermoresponsive components, and PAAc or poly(itaconic acid) (PIA) as the pH responsive component.[139][50] The combination of multiple stimuli allows the controlled release in different environments, which makes them strong candidates for *in vivo* applications.[141] Early studies performed on PAAc microgels showed how the addition of divalent ions, such as Ca^{2+}, triggered microgel collapse, yet the strength of the ion binding was not high enough to form a supramolecular colloidal gel.[46] This was attributed to the presence of the cationic initiator at the periphery of the microgel preventing significant intermicrogel bridging.

However, despite a number of studies investigating the swelling of charged microgels in the presence of earth alkali cations, little research has been done on the capability of gels to deliver an ionic stimulus. In contrast to that of alkali metal ions, and there is thus only limited data available on the uptake and release of earth alkaline and other biologically relevant, multivalent metal cations.[58][59] The binding affinity between the charged moieties in PAAc and Ca^{2+} was estimated via isothermal titration calorimetry (ITC) measurements, and discussed using the Eisenmann model which has been developed to explain the binding selectivity of crown ethers and ion channels.[142] The Eisenmann model describes the binding sites in more complex environments by taking into account the dehydrated radius of the ionic ligand site, r_i, the dehydrated radius of the metal cation , r_m, the interaction distance r as the sum of r_i and r_m and the water layer distance. Depending on how r varies, the environment is defined as a weak or strong field. In the weak-field scenario, r is large, due to either low charge density or the presence of water separating the ion from the ionic site. Weak-field environments favour large ions, such as Ba^{2+}. On the contrary, when the ion is small, with a high charge density, and dehydrated r is small, and the binding environment is a strong field. For strong-field interactions, the ion-site interaction dominates the exchange equilibrium, favouring small ions. On the contrary, in weak-field sites, the ion exchange equilibrium depends on the dehydration energy. Since small ions are more difficult to dehydrate, the equilibrium will be directed towards larger ions. Eichenbaum *et al.* demonstrated that, in the case of PMAAc microgels, the binding sites are weak-field, favouring and being selective to larger metal cations.[59] This was explained first by the

presence of water in the microgel network, regardless of its swelling, and by the fact that the enthalpy values measured for the binding indicated that the cations were not dehydrated. Due to steric constraints and the limited flexibility of the chain network, the distances between the anionic site and the metal cation increase, leading to a weak field site. [59] The introduction of a thermoresponsive comonomer such as VCL, can interfere with how the binding sites organize and restructure. In fact, in previous works by Eichenbaum *et al.*, the gels were composed of only anionic monomers, so each binding site was more constrained due to charge repulsion and the stiffness of the network. Introducing a monomer that does not account for the binding but can rearrange upon changes in temperature, alters the binding field's strength.[8] In this case, the PAAc microgels did not significantly aggregate or form a supramolecular gel in the presence of Ca^{2+}. On the other hand, P(VCL-*co*-AAc) microgels aggregate at temperatures above the PVCL VPTT (32 °C) and at neutral pH.[58] This is due to the increase in local density of complexing free groups on the microgel surface, which would lead to an increase in the available coordination sites for Ca^{2+} to bind, also between multiple microgels.[58][143]

Uncontrolled aggregation in *in vivo* applications can be fatal, especially if the nanoparticles or microgels are injected into the bloodstream. Since gels of this type are intended to eventually be used as ion carriers, as models in synthetic biology, and eventually for *in vivo* applications, preventing aggregation is crucial. In the aforementioned examples of PAAc and P(VCL-*co*-AAc) microgels, the microgels are stable below physiological temperature, but aggregate at 37 °C. By changing the microgel design, one could try to overcome the aggregation issue. For instance, physically distancing the COOH groups from each other could be achieved by producing a core-shell microgel, where the core contains the COOH groups and the outer shell is neutral. In this way, the coordination sites for the metal are physically distanced from microgel to microgel, and the microgel is sterically stabilized by the neutral chains. For this reason, we designed a thermo- and pH-responsive anionic microgel, composed of VCL and IA with a pseudo core-shell structure. This reduces the synthetic efforts and optimizations posed by seeded polymerization, as it is not highly batch dependent anymore, has reduced aggregation issues, and can be more easily scaled up. To simplify synthetic procedures, the gels in this work feature a pseudo core-shell structure, in which the microgel is still random but there is a gradual depletion of IA moieties along the microgel's radius.[47] Such gradient gels can be prepared in a one-pot procedure rather than in a two-step process necessary for sharply delineated core-shell structures, but they still feature the desired architecture to prevent ion-induced aggregation. In particular, this should prevent the gels from any temperature-triggered aggregation above the PVCL VPTT of 32 °C in the presence of ions and provide a stable system for eventual *in vivo* applications. Such

microgels are already known to be biocompatible and have been shown to have potential as carriers for small cationic molecules and proteins.[139] However, the behavior of such microgel towards Ca^{2+} or towards divalent ions in general has not been studied.[139]
After discussing synthesis and a thorough characterization of thermo- and pH- responsive P(VCL-*co*-IA) microgels, this chapter focuses on first investigating how different monomer compositions influence the microgel's swelling behaviour in response to Ca^{2+}. Once this is established, the chapter describes a second smaller set of microgels which interact with Mg^{2+}, Sr^{2+}, Cu^{2+} and Fe^{3+}, in order to see if the nature of a cation also influences the swelling of such microgels in H_2O.

2.2 Microgel synthesis and characterization

2.2.1 Neutral microgels synthesis and chemical characterization

Neutral microgels were prepared as precursor microgels which were then hydrolyzed in a second step to obtain anionic microgels. This two-step approach incorporates a larger amount of carboxyl groups in the core of the microgels, compared to a direct copolymerization of VCL and IA approach. In fact, when co-polymerizing VCL with IADME *via* dispersion polymerization, the IADME monomers accumulate within the core of the microgel, due to their higher reaction rates than VCL and hydrophobicity, which pushes the IADME monomers in the oil phase of the reaction. Using itaconic acid directly as a comonomer, despite saving one step in the synthesis process, will lead to poor yields, due to the failed precipitation of P(VCL-*co*-IA) growing chains. This is a result of the carboxyl groups of IA, which make the growing polymeric chain too hydrophylic even at low comonomer feeds, and will hinder the precipitation of the precursor particle, limiting this the formation of microgels. A low IA feed might lead to a random distribution of the charges in the network, which could trigger aggregation at higher metal concentrations.

The neutral microgels were obtained *via* precipitation polymerization in the presence of a quaternary ammonium surfactant (CTAB) by varying the molar ratio between VCL and IADME, whilst keeping the crosslinker and surfactant concentrations constant to stabilize the growing droplets. The molar amounts used are shown in Table 9.1, and the gels are named N*n*, with n corresponding to the IADME feed in mol% (N0 to N30).

The reaction crudes contain microgels, short, non crosslinked polymer chains, and unreacted monomers, which need to be removed prior to characterization, as they would interfere with the analysis. Hence, the resulting materials underwent 2 weeks of dialysis in milliQ water to remove unreacted IADME, VCL, BIS, CTAB and residual linear chains. ^{1}H NMR spectra were recorded (Figure 2.2) in $CDCl_3$ to determine the molar ratio between VCL and IADME moieties, and the results were compared with the relative intensity of the signals recorded in the ATR-FTIR spectra (Figure 2.3 in the appendix). Integration of the ^{1}H NMR spectra displayed final copolymer compositions consistent with the comonomer feed, and the integrals of the IADME methyl protons showed an almost quantitative incorporation of IADME within the PVCL chains. By integrating the signals at 3.64 ppm (PIADME methyl esters, 6H) and the signal at 4.42 ppm (CHN in aliphatic chain, 1H), we can assume that the incorporation of IADME in the VCL network is quantitative. These results were consistent with the results obtained by ATR-FTIR spectroscopy, which is used only for qualitative purposes, as it does not allow the quantitative analysis of single signals within the spectra (Table 2.1 in the appendix). The main characteristic absorption bands of PVCL are

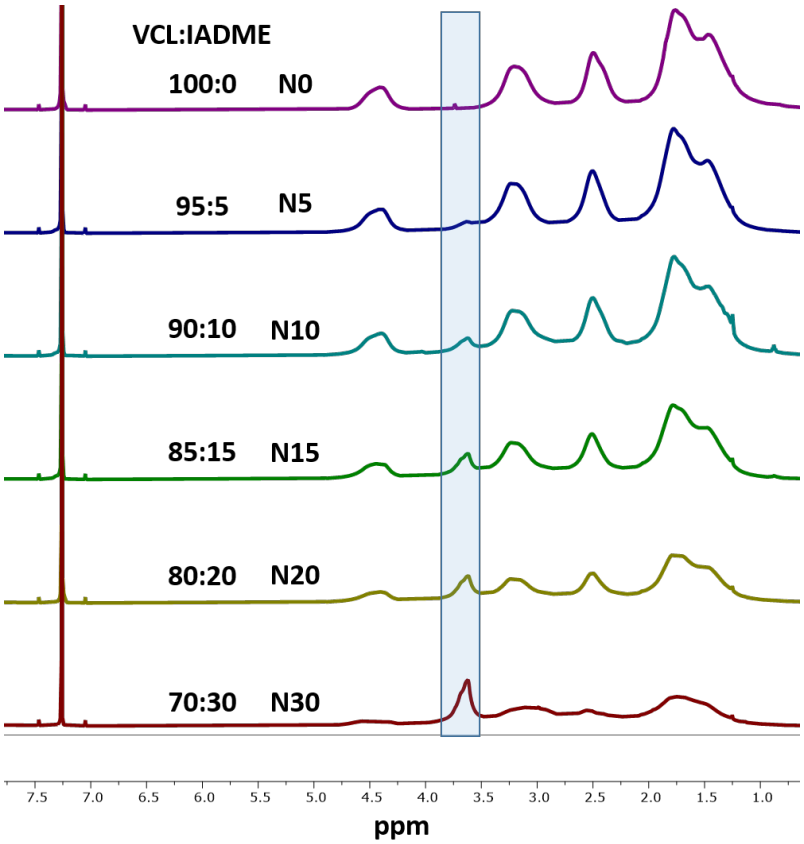

Fig. 2.2 ^{1}H NMR spectra ($CDCl_3$, 400 MHz, 256 scans) of PVCL (purple, 100:0) with no signal at 3.64 ppm, P(VCL-*co*-IADME) 5 mol% (blue, 95:5), 10 mol% (turquoise, 90:10), 15 mol% (green, 85:15), 20 mol% (lime, 80:20) and 30 mol% (red, 70:30). Methyl ester peaks are highlighted in blue.

assigned to the carbonyl (C=O, stretching) which appears at 1630 cm^{-1} and the aliphatic CH stretching peak at 2926 cm^{-1}. The characteristic band for IADME was assigned to the ester moieties which appear at 1730 cm^{-1} (C=O stretching). Since PVCL absorbs moisture, the broad signal found at 3507 cm^{-1} can be assigned to the O-H stretching of absorbed water.

The dry morphology of the N*n* gels was imaged *via* transmission electron microscopy (TEM). As is apparent from Figure 2.4, the neutral gels are uniformly stained by the uranyl acetate, meaning that there is no significant anionic charge accumulation within the microgel structure.

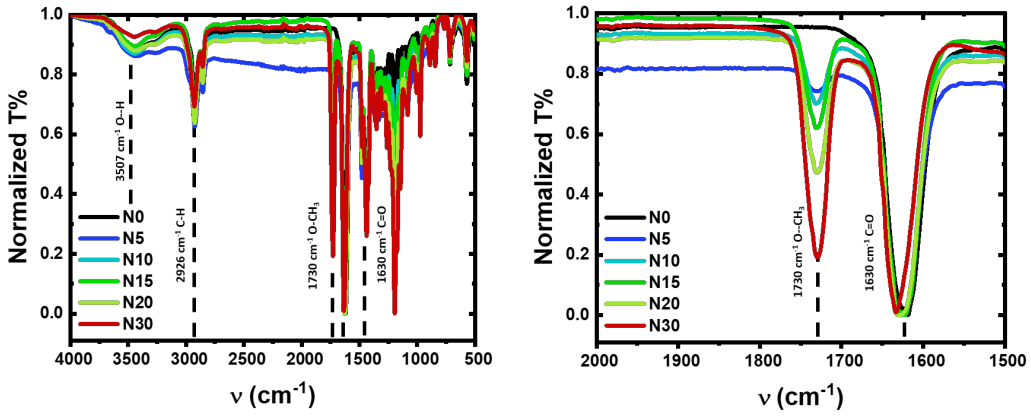

Fig. 2.3 ATR-FTIR normalized spectra of P(VCL-*co*-IADME) microgels; (a) full spectra and (b) the relevant characteristic peaks.

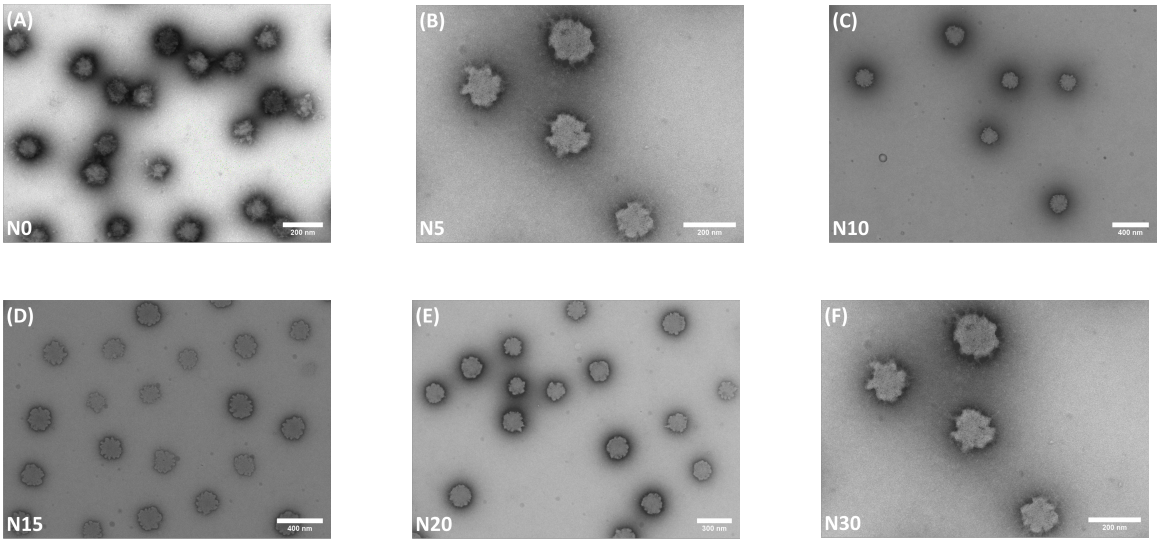

Fig. 2.4 TEM images acquired of (a) N0 homopolymeric PVCL microgels and (b) N5 (20 mol% IADME),(c) N10 (10 mol% IADME) (d) N15 (15 mol% IADME) (e) N20 (20 mol% IADME) and (f) N30 (30 mol% IADME) microgels, all stained with uranyl acetate.

2.2.2 Anionic microgels synthesis and chemical characterization

Subsequent hydrolysis of the IADME ester groups in NaOH was performed to obtain negatively charged P(VCL-*co*-IA) microgels bearing COOH moieties able to bond metal cations. Each meutral N*n* microgel was hydrolyzed into the corresponding M*m* microgel. In this nomenclature, the *m* indicates the mol% of COOH with respect to the total monomer content of the microgel. The molar content of COOH was determined *via* potentiometric

titration, and is shown further ahead in the chapter (Table 2.1). The hydrolysis was begun but not allowed to proceed to completion, as the partially hydrolyzed gels proved to be more stable than the fully hydrolyzed ones. When the gels are subjected to strongly-basic conditions for too long, the amide crosslinkers start to hydrolyze, too. This leads to smaller microgel fragments with irregular shapes, which can then aggregate due to their uneven charge distribution. The chemical structure of the partially hydrolyzed gels was also evaluated via ^{1}H NMR in order to monitor the disappearance of the methyl ester signals. In Figure 2.5, the spectrum for each partially-hydrolyzed microgel is depicted, with its former monomer content and new code according to COOH content, determined by potentiometric titration. The absence of the methyl ester groups suggests complete hydrolysis, however the low solubility of the methyl ester groups of unreacted IADME in D_2O decreased the overall "swellability" of the microgel in solution, dramatically lowering the signal intensity. As can be seen in the figure below, the signal for M30 is weak and almost overlaps with the baseline.As the other solvents display the same solubility issue, only qualitative information about the partial hydrolysis is obtained (Figure 2.5).

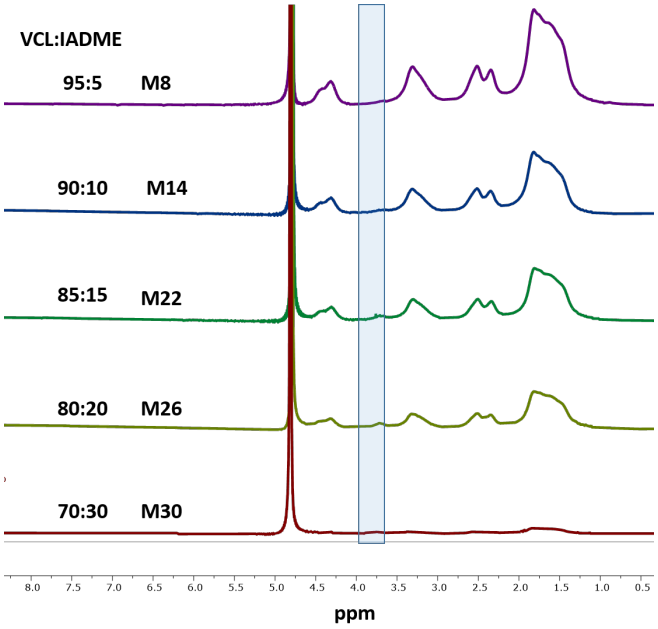

Fig. 2.5 ^{1}H NMR spectra of hydrolyzed microgels M8 to M30 in D_2O (400 MHz, 256 scan, room temperature (RT)). Highlighted in blue, the absence of the methyl ester protons (compare in Figure 2.2).

ATR-FTIR spectroscopy was further used for qualitative analysis focusing on the disappearance of the ester signals at 1730 cm^{-1} to track the formation of new carboxylic acid functional groups. The C=O stretching relative to the carboxylic acid band however overlaps

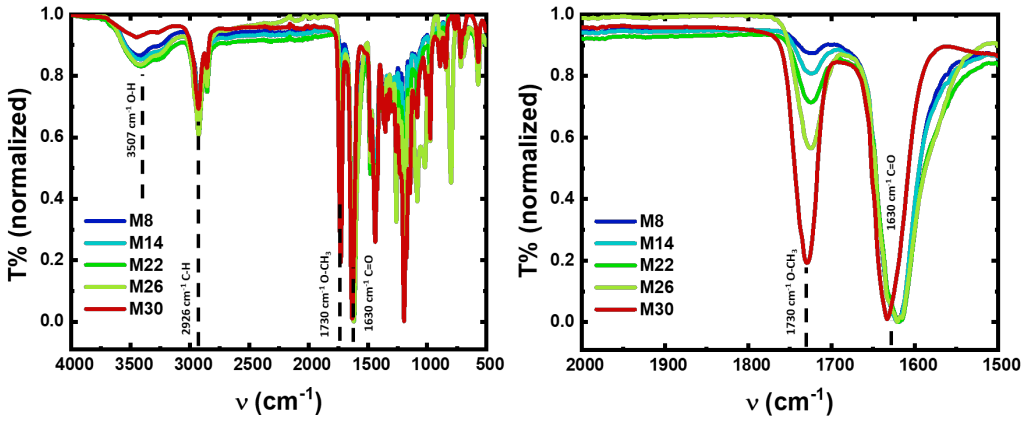

Fig. 2.6 Normalized IR spectra of P(VCL-*co*-IA) microgels; (a) full spectra and (b) the relevant characteristic peaks.

with the C=O amide stretching relative to the VCL comonomer at 1630 cm^{-1}. (Figure 2.6). Instead, the integration of the O-CH_3 stretching ester band belonging to PIADME against the peak corresponding to the amide C=O stretching of the PVCL was performed, permitting a qualitative estimate of the degree of hydrolysis and thus of the number of carboxy groups. Because of uncertainty in the final molar values due to the amide stretching, carbonyl band overlap, the unknown extinction coefficient of the structures, the number of COOH groups was determined by potentiometric titration, as shown in table 2.1, 9.4 and 9.2 in the appendix.

Table 2.1 Amount of dimethylitaconate (IADME) incorporated and itaconic acid (IA) groups

Sample	Theoretical IADME mol%	NMR value IADME mol%	ATR-FTIR value IADME mol%	Sample	IR value COOH mol%	Titration value COOH mol%
N0	0	0	0	NA	NA	NA
N5	5	5	5.775	**M6**	5.775	5.8
				M8	8.160	7.6
N10	10	10	9.395	**M10**	9.395	10
				M14	10.942	14
N15	15	15	16.013	**M22**	14.858	22
N20	20	20	22.950	**M19**	22.950	19
				M26	20.918	26
N30	30	30	31.068	**M30**	31.422	29

The results show a partial hydrolysis of the ester moieties from 35% to almost 60%, and the titration only displayed one plateau, indicating that of the two possible methyl esters, only one was hydrolyzed to a carboxy group (pK_{a1}= 3.84, pK_{a2} 5.55).

The dry morphology of all microgels was determined by TEM (Figure 2.7). The anionic gels were stained with phosphotungstic acid (PTA) instead of the more commonly used uranyl acetate (UAc). This is due to the presence of carboxyl groups, which would strongly bind U, leading to overstaining of the sample. The lower-affinity PTA e helps to better visualize the morphology of the gels. At higher comonomer content, the anionic microgels show a transition from a homogeneous structure to a core-shell one, consistent with previous reports.[47] This is evident when comparing Figure 2.7a and 2.7e, where the staining in the core of the microgels in (e) is clearly visible.

The resulting pseudo core-shell structure can be explained by the different reactivates of IADME as compared to VCL. In the case of low molar ratio between the two comonomers (up to 15 mol% of IADME), even though VCL reacts slower and IADME is localized in the core, it is diluted enough to not be visible by TEM. Thus, the microgels appear quite homogeneous in the TEM images (Figure 2.7, (a), (b), (c) and (d)). By increasing the relative concentration of highly reactive monomer, the hydrolysis product of IADME is present with a higher relative ratio within the core of the microgel structure, which becomes visible after hydrolysis in the TEM images (Figure 2.7e). The accumulation of IADME within the core was studied in very similar microgels (containing VCL, IADME and vinylimidazole) by Schachschal *et al.* via magic angle sample spinning (MAS) NMR. [47] Schachschal *et al.*, despite never measuring the reaction kinetics of a P(VCL-*co*-IADME) microgel, explain the accumulation of IADME in the microgel's core by comparing the system to a poly(*N*-vinylpyrrolidone-*co*-dimethylitaconate) polymer (PVP-*co*-IADME), where PVP is assumed to have a comparable reactivity to PVCL. In the case cited by Schachsal, the reactivity ratios found were r_1= 0.5 (PVP) and r_2= 1.3 (IADME), and assumed that in the case of precipitation polymerization, where the more hydrophobic monomer is dragged towards the growing polymer droplets, the reactivity ratio r should be even higher. These reactivity ratios, are consistent with the experimental findings, since they suggest the gradual depletion of the IADME along the microgel radius.

2.3 Light scattering characterization of neutral and charged microgels

The hydrodynamic diameter, D_H, of all microgels swollen in H_2O was measured via dynamic light scattering (DLS) (Figure 2.8). The swollen D_H of the gels was recorded in water at 20 °C, far below their VPTT, where the D_H decreased with an increase in the initial VCL:IADME ratio. The homopolymeric N0 is characterized by a D_H = (387 ± 39) nm,

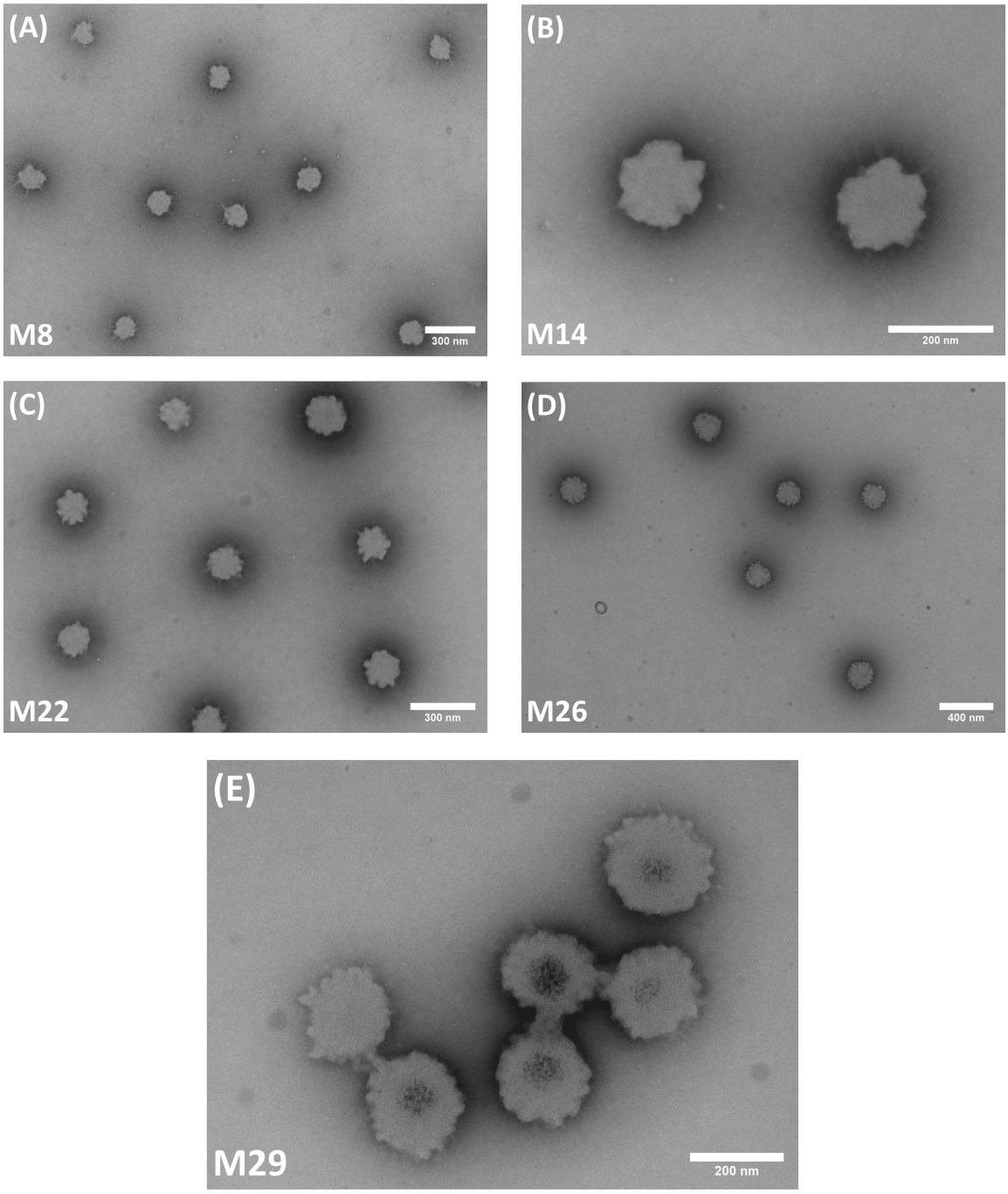

Fig. 2.7 TEM images recorded of P(VCL-*co*-IA) M8, M14, M22, M26 and M30 microgels by stained with PTA and imaged at an acceleration voltage of 80k mV.

which steadily decreased to D_H = (218 ± 3) nm for N25 (Figure 2.8). The size decrease is linked to the increase in hydrophobicity of the networks due to the methyl ester contributions. This hinders the gel's network to swell and reduces the overall swollen size of the microgel.

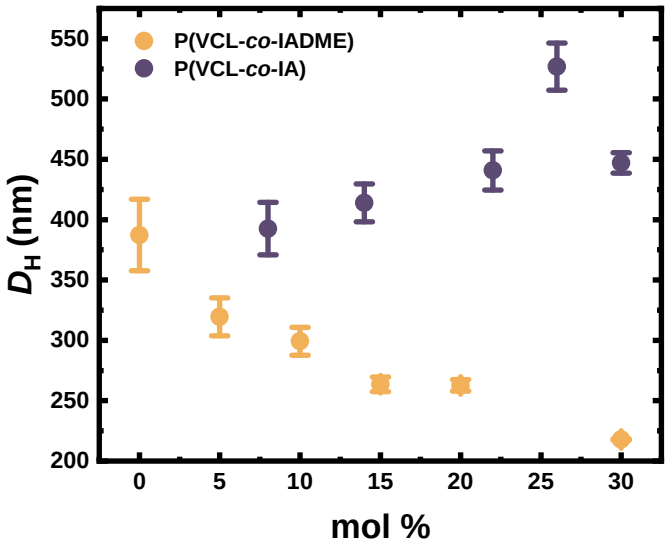

Fig. 2.8 D_H of P(VCL-*co*-IADME) (N*n*) and P(VCL-*co*-IA) (M*m*) microgels in water at T= 20 °C according to the IADME mol% (N micro-gels) and COOH moieties (M microgels) measured by DLS at pH=7.

After partial hydrolysis, the anionic microgels have larger volumes than the corresponding neutral microgels. The higher the amount of hydrolyzed comonomer, the larger the degree of swelling due to the repulsion between negative charges. In fact, M8 is characterized by a D_H = (392 ± 27) nm and the D_H increases along the series until M26 (D_H = (520 ± 26) nm). The D_H of M30 is (440 ± 9) nm, and thus lower than the D_H of M26. This is due to the large number of remaining ester groups, which render the polymer chains slightly more hydrophobic (Figure 2.8), even though the number of COOH moieties further increases.

To determine the temperature responsiveness of the neutral and ionic microgel systems, the D_H in pure water was determined as a function of temperature in the range of 10 to 50 °C (Figure 2.9 for temperature and Table 2.2 for pH).

Increasing the IADME molar ratio leads to decreased D_H values due to an increased hydrophobic character of the polymer chains that comprise the microgel. At 30 mol%, the size does not significantly decrease above the VPTT, meaning that the hydrophilic contribution of VCL starts to become negligible (Figure 2.9a). Moreover, above 30 mol% IADME, the gels not only lose their thermoresponsiveness, but gels lose the colloidal stability that M8-M26 have, thus no higher IA content is presented here.

The thermal response characteristic of VCL gels can be observed for all the microgels, though the ones containing 30 mol% of IADME (Figure 2.9b) do not show significant

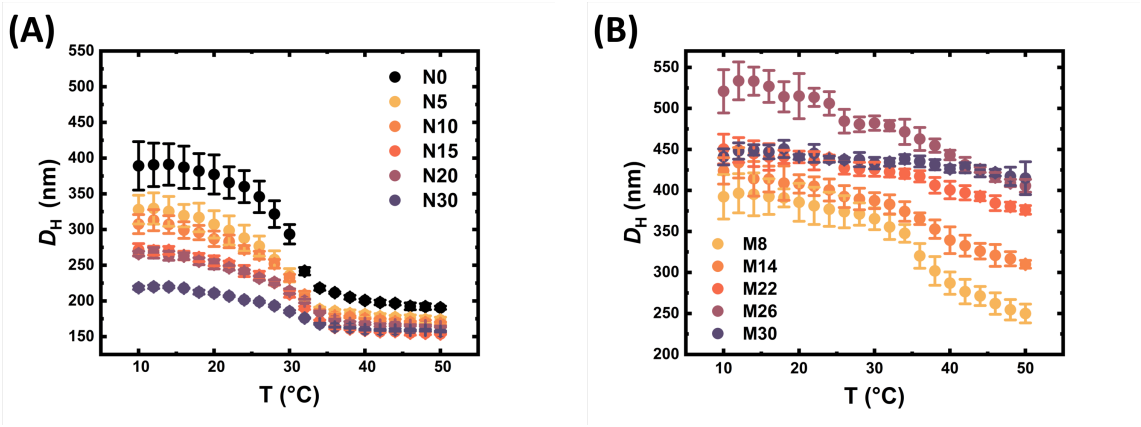

Fig. 2.9 D_H, as determined by DLS, of (a) P(VCL-*co*-IADME) (N*n* samples) and (b) D_H of P(VCL-*co*-IA) (M*m* samples) as functions of temperature, both measured by DLS in pure water at pH=7.

swelling anymore. The temperature responsiveness of the hydrolyzed microgel systems showed less pronounced deswelling than the precursors, consistent with the former's greater hydrophilicity. The temperature-dependent swelling diminishes with increasing IA content. The microgels almost completely lose their responsiveness towards temperature at an ionic content of 30 mol% (sample M30, Figure 2.10b). The amount of comonomer has an influence not only on the degree of swelling, but also on the temperature response, spreading the volume phase transition over a larger temperature interval. This expanded thermal response makes the determination of the VPTT somewhat ambiguous: the steepest point of the curves is considered to be the transition temperature, however, the VPTT is shifted slightly below 32 °C, in accordance with the more hydrophilic character of the network.

The swollen microgel structures were further examined by dynamic and static light scattering (SLS), which give the hydrodynamic radius (R_H) and the radius of gyration (R_g), respectively. The ratio between R_g and R_H provides information about the structure of a spherical object.[139]

As shown in Table 2.2, neutral gels show R_g/R_H values from 0.55 to 0.74 that increase along with the IADME molar content. The literature value typical for a hard sphere is 0.775, and in the case of microgels the value is generally considerably lower, due their gradient density structure.[139] Microgels composed of more hydrophilic chains are expected to have values around 0.55, due to their high degree of swelling. Increasing the hydrophobic content in the microgel triggers the partial collapse of the chains, which subsequently shifts the R_g/R_H ratio, closer to the hard sphere model value. After hydrolysis of the methyl groups, the microgels are composed of PVCL, PIA, PIADME and poly(itaconic acid monomethyl ester). The R_g/R_H drops to a value around 0.40 for every hydrolyzed gel, and shows the lowest

Table 2.2 R_g/R_H of P(VCL-*co*-IADME) (N*n*) microgels in pure water at pH 7 and P(VCL-*co*-IA) (M*m*) microgels in pure water at pH 7 and pH 3. R_g was determined *via* SLS and R_H *via* DLS.

Neutral microgels	R_g/R_H (pH=7)	Anionic microgels	R_g/R_H (pH=7)	R_g/R_H (pH=3)
N0	0.55			
N5	0.52	**M8**	0.37	0.63
N10	0.61	**M14**	0.38	0.60
N15	0.61	**M22**	0.42	0.63
N20	0.66	**M26**	0.52	0.63
N30	0.74	**M30**	0.37	-

values for the M8 and M14 samples. This value is typical for star polymers, suggesting that the hydrolysis of the methyl ester moieties leads to a more porous structure, where the corona chains are more distanced from each other. The R_g/R_H of the charged microgels were investigated at pH 3, in order to investigate the structural changes that the gels undergo when the protonation of the carboxylic acid groups takes place. This results in R_g/R_H values of 0.6, which is consistent with the collapse of the microgel structure due to the protonation of the carboxylic groups, eliminating the repulsion between negative charges at pH = 7. Only one sample (M30) could not be measured as this sample aggregates at pH 3, likely because the presence of surface-exposed carboxylic acid groups diminishes the colloidal stability of the microgel at pH=3.

Direct copolymerization of IA with VCL would lead to a more random microgel monomer distribution within the network, which however should be avoided in the present study to prevent aggregation. Hence, a pseudo core shell structure should prevent said aggregation, ensuring the colloidal stability of the system at higher temperatures. Since we could observe their stability at RT, we investigated the stability of such gels above their VPTT, like in previous reports.[58][143] To prove their stability, the D_H of the gels was measured over a period of 6.5 h at 40 °C, at a Ca^{2+} concentration of 10 mM, showing no change in the size or dispersity of the samples (Figure 2.10).

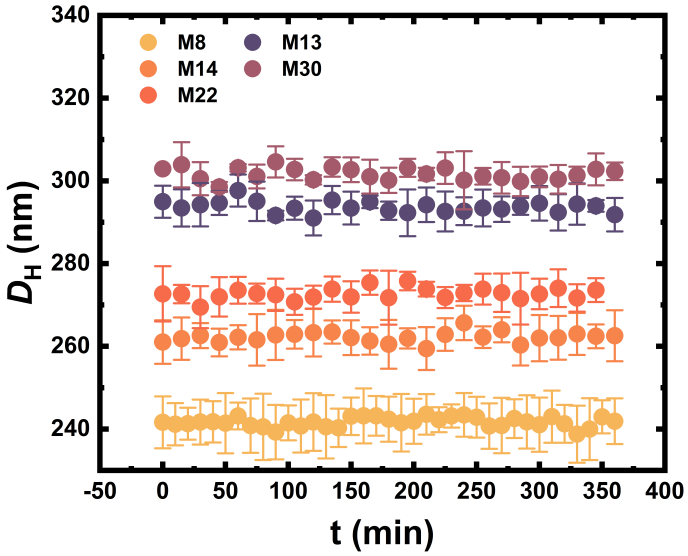

Fig. 2.10 D_H, as determined by DLS, of P(VCL-*co*-IA) (M*m*) microgel samples against time, at a Ca^{2+} concentration of 10 mM and T= 40 °C at neutral pH.

2.4 Microgel behavior in the presence of metal cations

2.4.1 Swelling behaviour towards Ca^{2+} ions

In order to show that the presence of COO^- groups is necessary to complex Ca^{2+} ions, the D_H of neutral and charged gels were first measured in a solution with a Ca^{2+} concentration of 10 mM (Figure 2.11).

Only M*m* microgels deswell in the presence of Ca^{2+} ions, whereas the D_H of N*n* microgels remains unchanged despite the high Ca^{2+} concentration. Therefore, the presence of the COO^- groups is necessary to induce the shrinkage of the network by binding the divalent ions. The bonding is energetically favourable, as shown by ITC measurements.[59] The release of monovalent ions when being replaced by divalent ones increases the entropy of the whole system, promoting the uptake of Ca^{2+} ions.[144] Moreover, Ca^{2+} acts as a cross-linker between the charged groups, as it can bond at least two COO^-, moieties, which monovalent ions like Na^+ are unable to do.[58] This additional cross-linking can force the COO^- groups to move closer to each other, changing the conformation of the polymer chains within the network and causing the observed shrinking of the anionic microgels. In addition, Ca^{2+} ions screen the negative charges, diminishing the electrostatic repulsion between the chains. The concentration range in which the microgels start to respond to the presence of Ca^{2+} ions by collapsing and shrinking in size was determined by performing DLS at different

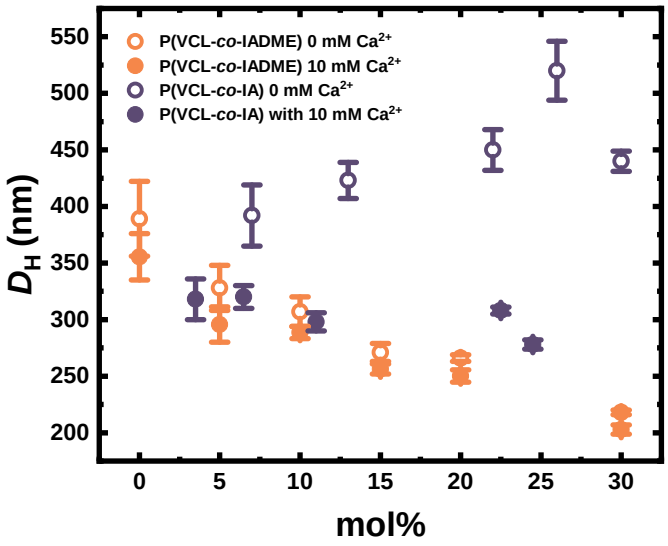

Fig. 2.11 D_H, as determined by DLS, of P(VCL-*co*-IADME) (N*n*) microgels (orange) and P(VCL-*co*-IA) (M*m*) microgels (purple) as determined by DLS, recorded in MilliQ water at pH=7 (hollow symbols) or in 10 mM $CaCl_2$ solution (filled symbols), all at T= 10 °C. For simplicity, the monomer % for the ionic gels is counted as each IADME that has been hydrolyzed has turned into a itaconic acid methyl ester.

Ca^{2+} concentrations, chosen to contain the cytosolic Ca^{2+} concentration (150 nM) and the physiological muscle resting/contraction range (0.0001-100 mM)(Figure 2.12) .[126] For all gels, regardless of composition, the microgel collapse starts at concentrations of 0.01 mM and is completed by 1 mM.

Remarkably, the gels do not shrink at the cytosolic concentration of a resting muscle cell, and undergo dramatic deswelling at the concentrations at which muscle contraction occurs. As is apparent from Figure 2.12, the microgels are fully collapsed at a final concentration of 1 mM, and stay colloidally stable up to 100 mM Ca^{2+}. The degree of deswelling is higher with increasing anionic content, as the concentration of possible crosslinks between the chains increases. As shown in Figure 2.12, the D_H of M8 microgels goes from 400 nm when swollen to 300 nm when collapsed, whilst M30 gels decreased their D_H by more than 50%, going from 500 nm to ca. 250 nm (Table 2.3).

However, the divalent cation concentration necessary to collapse a charged microgel does not really depend on the COOH concentration present in the gel. By comparing these results with the work on PAAc made by Byrne *et al.*, one can observe the same collapse range for fully homopolymeric PAAc gels and P(VCL-*co*-IA) microgels.[145] Byrne observed a collapse range of 0.1-0.05 μM for the cation, which would vary according to the amount

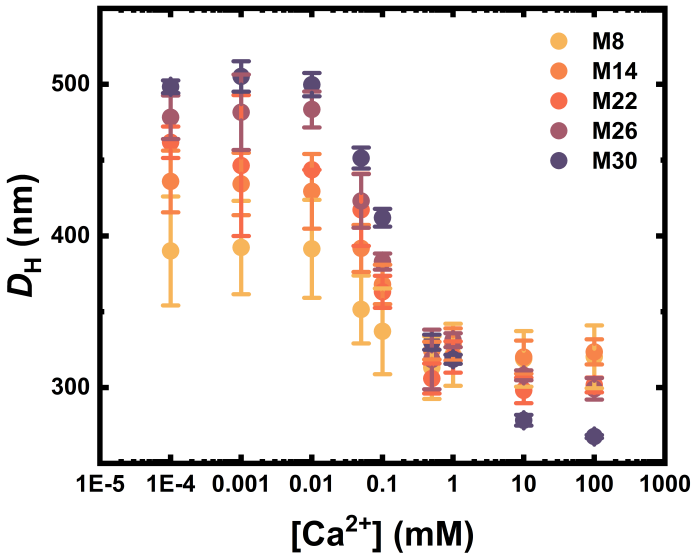

Fig. 2.12 D_H of P(VCL-*co*-IA) (M*m*) microgels determined by DLS at T = 10 °C in water at different $CaCl_2$ concentrations at neutral pH.

of NaCl added to the system. Recently, Ferrand *et al.* demonstrated how the pK_a of densely packed polymer brushes changes according to the ionic strength of the solvent.[146] Specifically, at the same pH, the higher ionic strength induces the ionization of the acid groups, which in the case of a gel, leads to the swelling of its network.[146] With a microgel diameter range of few hundreds of nm, the concentration interval in which the collapse happens remains unchanged, with the exception of M30 .[143] This might be explained by assuming that the core of a microgel behaves similarly to densely packed polymer brushes, by that theory, the degree of protonation in the microgel core should also depend on the ionic strength of the solution, influencing its swelling.

Comparing the fully-protonated gels to the ones in the presence of Ca^{2+} (Table 9.4), it is apparent that Ca^{2+} does not fully screen the negative charges, which are neutralized at low pH. The D_H of the microgels containing Ca^{2+} at pH = 7 is larger than the one measured for the microgels at pH = 3, the COOH groups being fully protonated under the latter conditions (table 9.4). This suggests that the swelling of the system also depends on the polyelectrolyte effect, rather than only on Ca^{2+} bridging between two or more COO^- groups and physically pulling the polymeric chains closer together.

2.4.2 Swelling behavior in the presence of other metal cations

The responsiveness of the microgels to metal cations other than Ca^{2+} has been investigated with DLS.

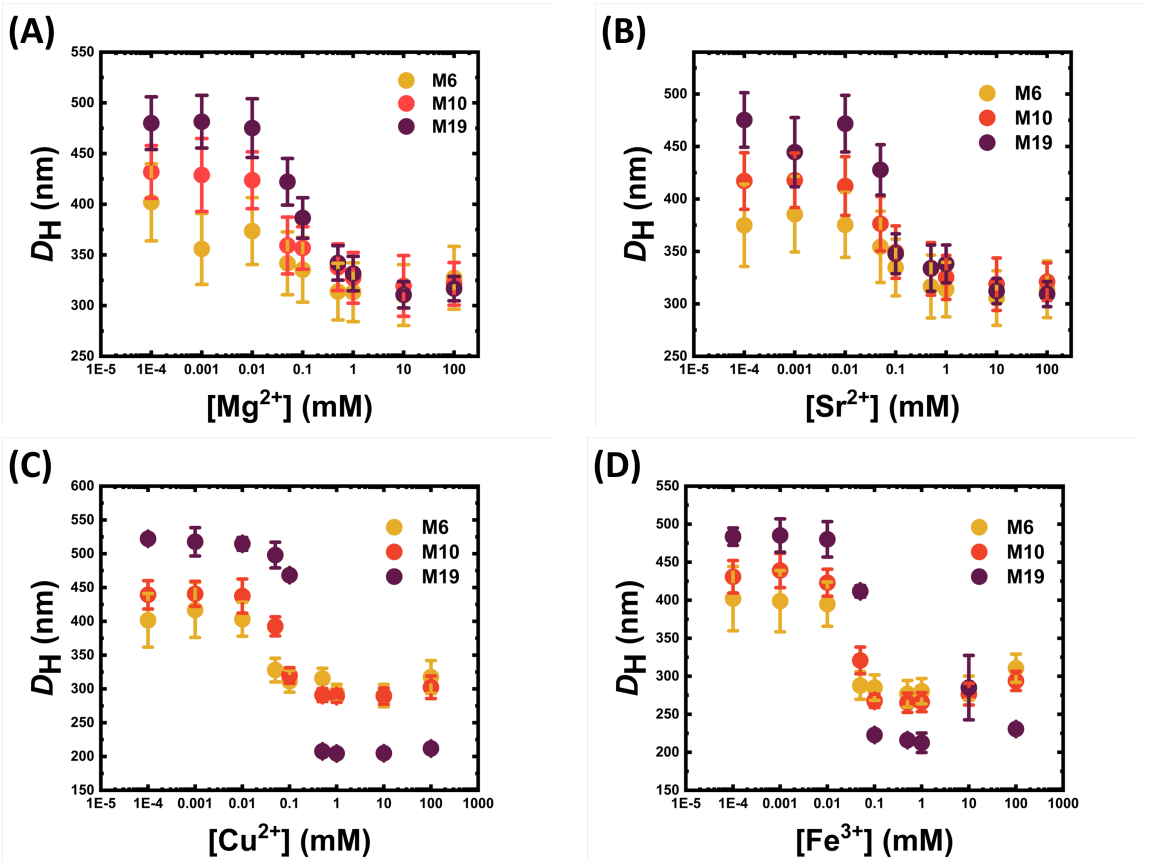

Fig. 2.13 D_H of M6 (6 mol% COOH), M10 (10 mol% COOH) and M19 (19 mol% COOH) at different concentrations of a) $MgCl_2$ b) $SrCl_2$ c) $CuCl_2$ d) $FeCl_3$ determined by DLS at T = 10 °C at neutral pH in MilliQ water.

As is apparent from Figure 2.13, the gels are swollen at low ion concentrations and start deswelling in a concentration range of 0.05-0.1 mM. The precise metal cation concentration at which the microgel structure shrinks by expelling water from its network is slightly dependent on the nature of the ion. The size dispersity also decreases accordingly, hinting at a more compact structure, which is confirmed by the R_g/R_H ratio increasing from 0.4 to 0.6, measured for each microgel at a metal concentration of 1 mM (see Table 9.5 in the appendix). The concentration range in which the microgels drastically decrease in size is narrower for the transition metal ions than for main-group metals, especially in the case of Fe^{3+}, where the collapse of the microgel is complete at Fe^{3+} concentrations of 0.1 mM. When multivalent cations are added to the systems, they can influence chain-chain interactions by screening

the COO^- charges and thus reducing the electrostatic repulsion as well as behaving as crosslinkers between the COO^- groups. D_H changes according to the metal ion used, as is evident from a comparison of swelling changes for the same microgel sample (*e.g.* M10) and ion concentration: when an alkaline earth metal ion is present, gels normally shrink to an average size of 450 nm to 300 nm, losing 20-40% of the D_H, whilst transition metal ions lead to a decrease in D_H up to 60% (for full data, see table 2.3 below).

Table 2.3 Hydrodynamic diameters obtained by DLS of M8-M30 at 10^{-4} mM and 10 mM divalent metal salts ($CaCl_2$, $MgCl_2$, $SrCl_2$, $CuCl_2$ and $FeCl_3$) measured at RT and neutral pH in MilliQ water.

Microgel	D_H 10^{-4} mM Ca^{2+} (nm)	D_H 10 mM Ca^{2+} (nm)	% D_H decrease
M8	390 ± 35	318 ± 20	18 %
M14	435 ± 20	320 ± 10	26 %
M22	461 ± 10	298 ± 9	35 %
M26	478 ± 14	308 ± 3	35 %
M30	498 ± 35	278 ± 3	44 %
Microgel	D_H 10^{-4} mM Mg^{2+} (nm)	D_H 10 mM Mg^{2+} (nm)	% D_H decrease
M6	401 ± 74	318 ± 6	20 %
M10	446 ± 48	303 ± 30	32 %
M19	479 ± 65	310 ± 26	35 %
Microgel	D_H 10^{-4} mM Sr^{2+} (nm)	D_H 10 mM Sr^{2+} (nm)	% D_H decrease
M6	380 ± 40	305 ± 26	20 %
M10	417 ± 25	318 ± 25	23 %
M19	475 ± 26	312 ± 12	34 %
Microgel	D_H 10^{-4} mM Cu^{2+} (nm)	D_H 10 mM Cu^{2+} (nm)	% D_H decrease
M6	401 ± 39	290 ± 16	27 %
M10	439 ± 21	289 ± 11	34 %
M19	522 ± 5	204 ± 2	60 %
Microgel	D_H 10^{-4} mM Fe^{2+} (nm)	D_H 10 mM Fe^{2+} (nm)	% D_H decrease
M6	402 ± 42	284 ± 15	29 %
M10	430 ± 21	276 ± 14	26 %
M19	483 ± 11	285 ± 9	42 %

Therefore, the presence of a transition metal cation might coordinate the carboxyl groups to form bridging between the polymer chains. The oxidation number does not seem to influence the degree of swelling in charged gels, as both Cu^{2+} and Fe^{3+} ions lead to a final D_H of M19 of 200 nm. However, homopolymeric VCL microgels (N0), seem to shrink in

the presence of a higher ionic strength (10 mM XCl_x), provided that the same counter ion is used (Cl^-), though not as strongly as in the case of the anionic systems (see tables 2.4s and 9.5 in the Appendix).

Table 2.4 D_H (nm), as determined by DLS, of homopolymeric VCL microgel N0 in pure water and in the presence of 10 mM $M^{2+/3+}$ ions at 10 °C and neutral pH.

Sample ID	D_H (nm) H_2O	D_H (nm) Ca^{2+}	D_H (nm) Mg^{2+}	D_H (nm) Sr^{2+}	D_H (nm) Cu^{2+}	D_H (nm) Fe^{3+}
N0	375 ± 19		355 ± 20	355 ± 22	360 ± 27	340 ± 35

The N0 microgels do not shrink at lower ion concentrations, as shown in Figure 2.8. Fe^{3+} leads to a decrease in D_H of N0, which suggests coordination of Fe^{3+} by the lactam groups of the PVCL present in the microgel periphery. However, upon Fe^{3+} addition, the sample displays an increase in size dispersity, likely due to aggregation, whilst the same microgel solution remains stable in the presence of any of the other ions. The gels are structured in a way that the coordination sites for divalent cations are located in the core of the microgel, whilst being shielded by a neutral, non-coordinating corona, which prevents the microgels from aggregating in the presence of a divalent metal cation. Hence, the eventual aggregation caused by Fe^{3+} ions suggests that there are further interactions in the corona of the gels, which is composed mainly of VCL units.

When measuring the swelling of the M10 microgels in the presence of monovalent ions such as K^+ or Na^+, the observed swelling behavior of each microgel is more gradual compared to the one observed in the presence of divalent ones. In fact, when at concentrations higher than 1 mM, both Mg^{2+} and Na^+ trigger the collapse of the gels (Figure 2.14).

However, as seen in Figure 2.14, a sharper change in swelling ratio between the collapsed state and the swollen state is observed with M^{2+}. At the same cation concentration, provided that the counterion is the same (Cl^-) the ionic strength of a M^{2+} or M^{3+} is 3 times or 6 times higher, respectively, than the one associated to an M^+ solution. This suggests that the influence of the ionic strength is negligible in that area, and the collapse of the network is mostly due to the screened repulsion between the COO^- charges by the doubly charged ion. Moreover, Mg^{2+} as another divalent metal cation can act as a supramolecular cross-linker between the COO^- groups if they are in close proximity. In Figure 2.8, the collapse of the same microgel is much more abrupt in the presence of Mg^{2+} in the range of 0.01 M and 100 mM.

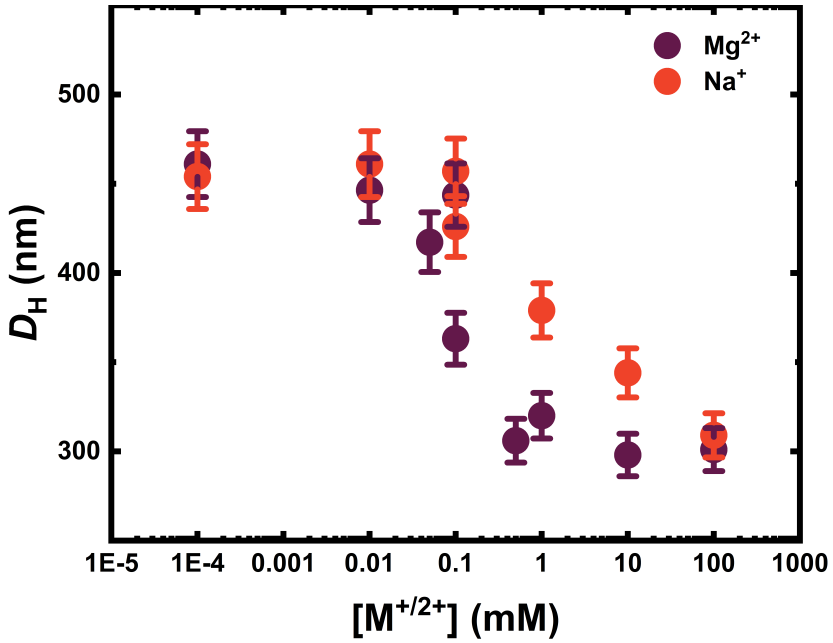

Fig. 2.14 . Hydrodynamic diameter D_H of M10 (10 mol% COOH) measured via DLS in the presence of Mg^{2+} (purple) and Na^{+} (red) in MilliQ water, at neutral pH and RT.

2.5 Summary

In summary, we introduce the concept of divalent metal ions being used as a trigger to change the size and conformation of a gel. Neutral gels were first synthesized and fully characterized for their chemical and physical structure and used as reference system for the ionic gels. The series of neutral microgel was subsequently hydrolyzed to obtain a library of anionic gels with different degrees of anionic content whilst retaining some hydrophobic moieties to ensure stability against spontaneous aggregation. Each anionic microgel was also fully characterized for its composition, structure and responsiveness towards temperature, pH and divalent ion concentration. The swelling and collapse of the microgels in the presence of divalent ions, such as Ca^{2+}, was investigated to optimize the conditions at which uptake and release studies were performed. The same method proposed within this work can be further widened to more divalent cations with biologically relevant activity, such as Mg^{2+} and Cu^{2+}, and trivalent ions such as Fe^{3+}, which opens the way for use of those gels in sensing applications, desalination membranes, and synthetic biological systems.

Chapter 3

Anionic microgels' uptake, storage and release of metal cations

Parts of this chapter are adapted from the publications [125] and [13]. I designed all the experiments, procedures and characterization methods. All experiments regarding the data taken from [13] were performed in collaboration with Simona Conti. Csaba Fodor contributed ideas, suggestions and discussions. Csaba Fodor, and Phally Kong contributed to the proofreading of the two publications.

3.1 Introduction

Divalent and trivalent metal cations are of crucial importance in biochemical reactions within the body, yet can also act as toxins when they exceed physiological concentrations.[147] For instance, some metals such as Pb^{2+} are commonly known as pollutants due to their toxicity even at minimal concentrations, whilst other metals like Fe^{3+}, typically not harmful, can lead to long-term damage at high concentrations when in combination with pre-existing conditions, such as β-thalassemia or diabetes.[148][149][150] The uncontrolled accumulation of metal ions in the body can lead to oxidative stress and cell damage, and their removal requires invasive and lengthy therapies, such as injections of chelating agents and dialyses.[150][151] The most common and effective chelating agent used in these therapies is ethylenediaminetetraacetic acid (EDTA), however it has the major drawback of bonding Ca^{2+}, and a multitude of other ions necessary to the body. The use of EDTA is thus linked to hypocalcemia, which can lead to bone resorption.[152] Normally a severe drawback, this has been positively exploited by Karamched *et al.*, who presented anti-elastin antibody decorated

albumin nanoparticles loaded with EDTA which can bond Ca^{2+} and reduce calcification and the formation of kidney stones in patients with chronic kidney disease.[153]

An alternative way to remove toxic ions is to bind them before they enter the bloodstream. To prevent such ions from entering the blood stream when ingested, larger particles or polymers can be employed. In this way, the sequestering agent for the targeted metal ion can be expelled from the digestive tract whilst carrying the toxic ion, avoiding the need for more invasive interventions such as intravenous injections. Commercial polymers for this application are already available, and one prominent example is Kayexalate®, which is widely employed to fight hyperpotassemia. Kayexalate® is composed of polystyrene sulphonate, and works as an ion exchange resin. Its initial counterion is Na^{+}, which is exchanged with K^{+} when ingested. However, when consumed in combination with sorbitol, this polymer leads to strong side effects such as internal bleeding and intestinal necrosis.[154][155] Hence, there is a need to reduce the interaction of the active moieties with larger molecules or soft tissue, suggesting the use of other polymer architectures, which can physically screen such interactions whilst still adsorbing ions: gels and microgels. Positively-charged metal ions bind strongly to electron-donating ligands such as amines, carboxyl groups, thiols and hydroxyl groups.[156] These can be incorporated into materials *e.g.* by designing cross-linked polymer networks decorated with functional groups that can specifically bond certain ions, playing with the affinity of the targeted ions towards the ligands.[157][158][159] The simplicity of these systems allows one to elegantly produce materials that selectively entrap a specific ion, generally a pollutant, such as Pb^{2+} or Hg^{2+}.[160] There are plenty of examples in which negatively charged hydrogels or polymeric membranes have been used as water purification systems.[161][162] However, due to their large dimensions and the poor shape-adaptability of crosslinked gels, they are less useful for *in vivo* applications in terms of ion removal. The only gels which find wider medical application in the biomedical context are injectable supramolecular gels, thanks to being both shear-thinning and self-healing.[163][164] These gels have so far been proven to be excellent candidates for tissue scaffolding or drug delivery but their potential for ion uptake/release has been largely overlooked.[165]

Designing these gels to be responsive to external stimuli such as temperature or pH, introduces the possibility to uptake or release a cargo "on demand", whether it be small molecules, polyelectrolytes or metal cations.[139] Chapter 2 demonstrated that by using microgels composed of vinylcaprolactam (VCL) and itaconic acid (IA) we could design a system that is stable at physiological temperatures (36-38 °C), is biocompatible and responds to divalent metal cations. In this chapter is presented the quantification of a set of divalent cations that can be coordinated by an anionic microgel, from which the release of the ions can be stimulated by a pH trigger (Figure 3.1). We investigate the effect of chemical

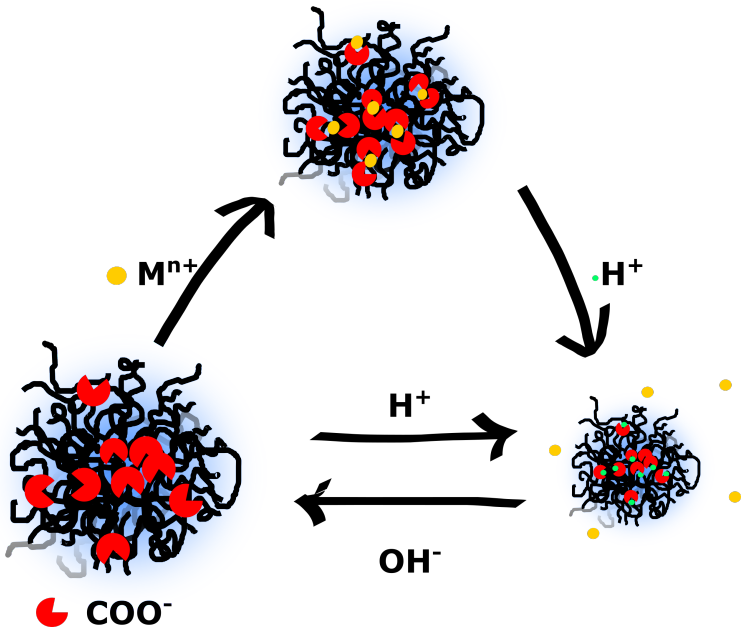

Fig. 3.1 Schematic representation of the metal uptake and release of the microgel system.

composition on the uptake and release capability of the microgels, progressively increasing the gels' anionic content. Furthermore, tests were made for a series of biologically relevant, potentially toxic ions, and it is shown how these microgel systems can capture metal cations, store them, and eventually release them. The possibility to remove ions from an aqueous environment is investigated for cations that can play a role in biochemical reactions (such as Fe^{3+}), trigger the polymerization of biomolecules such as G-actin into F-actin (Mg^{2+} and Ca^{2+}), play a role in muscle contraction (Ca^{2+} or Sr^{2+}),[166] or be hazardous at high concentrations (Cu^{2+}or Sr^{2+}).[166][167]

3.2 Cation uptake quantification

As discussed in sections 2.4.1 and 2.4.2 of Chapter 2, anionic P(VCL-*co*-IA) microgels undergo changes in degree of swelling with an increase in Ca^{2+} and other metal cations. The swelling change depends on the ion concentration, and on the overall ionic strength of the solution (section 2.4.2). It is the presence of COOH groups in the network that leads to dramatic swelling upon the addition of a divalent or trivalent metal cation, due to charge screening and metal-ligand coordination. Generally, when a microgel incorporates a cargo, it then releases it either *via* diffusion, or it pushes it out as a response to an external stimulus. In the latter case, the storage and release of the cargo is not diffusion-controlled, and can be activated by regulating the external environment. In this case, the cargo needs to physically

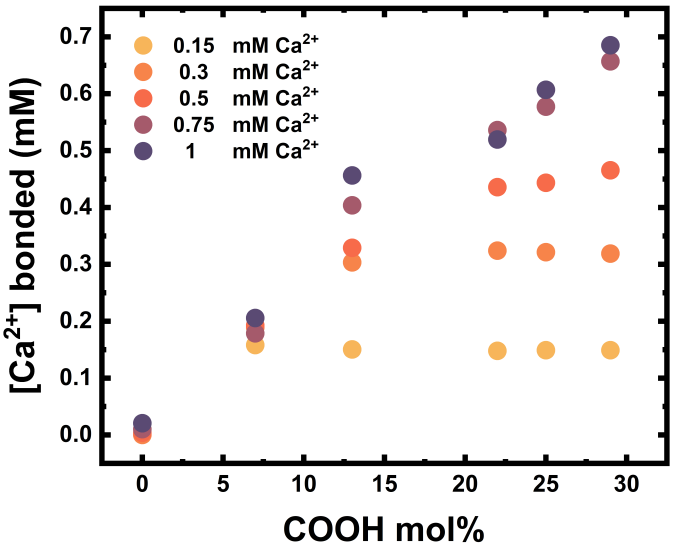

Fig. 3.2 The number of Ca^{2+} ions retained by a solution of 0.1 wt% P(VCL-*co*-IA) according to the COOH concentration of each microgel, performed at different initial Ca^{2+} concentrations (mM). Samples were soaked at a given concentration of $CaCl_2$ at room temperature and neutral pH, and then spin filtrated. The retained number of ions was determined by ion chromatography of the filtrate.

be entrapped within the network. When the microgel is responsive to a certain stimulus, changing it will trigger changes in the chemical or physical environment of the microgels' network, inducing conformational changes. For instance, the shrinking of the network due to an increase of hydrophobicity, will lead to the fast expulsion of a hydrophilic cargo entrapped within the network. In order to have a system that traps and releases the cargo "on demand", guest molecules or ions need to be retained in the network, and not passively diffuse out due to osmotic differences or mechanical stress.

To determine whether the metal-ligand coordination within the microgel is strong enough to retain the ions within the network, the P(VCL-*co*IA) microgels (Mm) were soaked in a solution containing a metal cation at a certain concentration, and then filtered. The filtrate contains the number of ions not bonded by the gel, and using that figure, the number bonded by the gels was calculated.

The amount of Ca^{2+} (or other ions) in the filtrate was determined by ion chromatography. In order to determine which concentration is ideal for the loading of any divalent cation in the gels, a series of Ca^{2+} dilutions within the microgel collapse region (Figure 2.12) were made with a 0.1% wt/V microgels concentration (Figure 3.2).

Table 3.1 Concentration of COOH groups in solution, Ca^{2+}ions bonded at pH= 7 and the bonding ratio between the two.

Sample ID	[COOH] (mM)	[Ca^{2+}] (mM)	[COOH]/[Ca^{2+}]
N0	0.00	0.00	-
M8	0.43	0.21	2.04
M14	0.87	0.45	1.93
M22	1.3	0.54	2.4
M26	1.6	0.62	2.03
M30	2.1	0.78	2.6

The measurements were performed for microgels with increasing COOH content, containing up to 15 mol% -COOH groups including a homopolymeric VCL microgel as a reference (N0) (Figure 3.2). The reference microgel showed no bonding at all, as the measured cation concentration was equal to the one added to the gel. By contrast, if we assume that the ion can bind between one and two COO groups, according to the flexibility of the chains bearing the groups and their freedom to optimize the coordination geometry, the microgels containing IA retained Ca^{2+} ions, proportionally with respect to the total amount of IA present, [168][169]

The microgels, regardless of their comonomer composition, quantitatively take up all the Ca^{2+} ions present in solution, when the Ca^{2+} amount is lower than the amount of COOH tethered to the gels. Above that amount, the gels are saturated by the ions and are unable to bind all the Ca^{2+} ions present in solution. In general, the amount of Ca^{2+} bonded increases linearly with the IA content. As stated in previous works, Ca^{2+} can coordinate with one or two COO^{-} moieties through simple bridging between polyelectrolyte chains.[170]

Since all studies presented here use acrylic acid as the COOH-ligand source in gels or microgels, it is difficult to discern if there is a contribution to the coordination shell by other local groups or not, which would be the case for homopolymeric PVCL microgels. In this case, the ratio between COO^{-} moieties and Ca^{2+} ions is around 1:1 (Table 3.1), showing an expected apparent coordination numbers of two COOH per every one Ca^{2+} ion. Only for M22 and M30, the apparent coordination number is higher than two but still lower than three. This might be explained by the relative stiffness in the core of the microgels that are unable to provide the spatial presence for enough COOH moieties to bond Ca^{2+}. When recalling the synthetic method of the studied microgels (in section 2.2.1), the microgels have a more crosslinked core and a more fuzzy corona, suggesting that weak binding occurs when the ions are sterically constrained in a highly cross-linked microgel. As in the case described here, the strength with which the gels are able to bond Ca^{2+} ions decreases, and the bridging might not take place. However, due to the extremely high coordination affinity of Ca^{2+} to COO^{-} groups, the microgels are still capable of taking up the metal ions, yet with a coordination

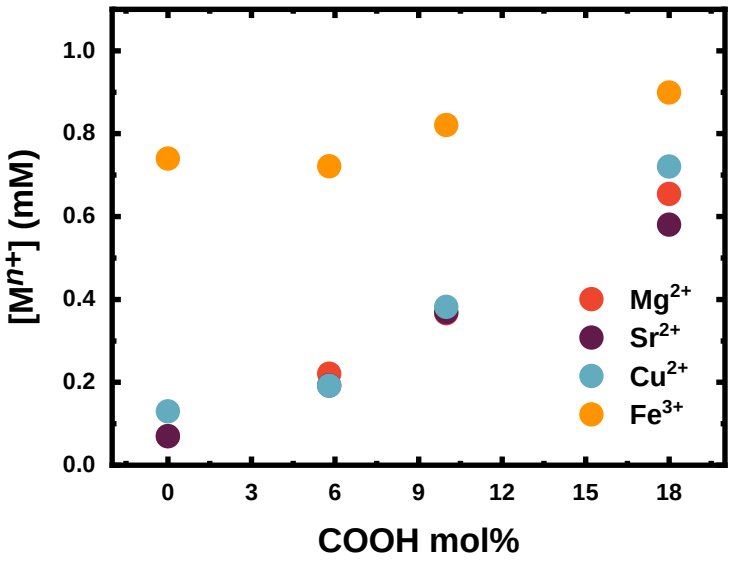

Fig. 3.3 Concentration of Mg^{2+}, Sr^{2+}, Cu^{2+} and Fe^{3+} bonded by a 0.1 wt% microgel solution with different COOH concentrations per gel: N0 (0 mol% COOH), M6 (6 mol% COOH), M10 (10 mol% COOH) and M19 (19 mol% COOH) at RT and neutral pH. The samples were soaked at an initial MCl_x concentration, filtered, and the concentration of the filtered ions was determined by ion chromatography.

number of up to two.[168] Moreover, the incomplete, moderately regioselective hydrolysis of the initial ester groups is likely to produce pendant groups carrying both an ester and carboxy group, as was apparent from the ATR FT-IR spectra in Chapter 2 (Figure 2.6). The proximate ester is likely able to participate in the coordination of Ca^{2+}, with only one COO necessary to form a relatively stable complex.

Varying the affinity and valency of the ions interacting with the microgels leads to different results than those for Ca^{2+}. The concentration of ions coordinated by a 0.1 wt% solution of microgels at different COOH concentration is shown in Figure 3.3. The uptake was calculated as the difference between the initial concentration of the aqueous metal-cation solution and the concentration of the filtrate obtained after ion uptake by the gels. An initial concentration of 1 mM was chosen.

Clearly, the number of ions coordinated by the P(VCL-*co*-IA) microgel network is dependent upon the amount of COOH present. The presence of COOH groups is required for coordinating alkaline earth ions and Cu^{2+}, as the neutral N0 microgel does not uptake significant numbers of these ions. Both homopolymeric neutral N0 and anionic Mm microgels are able to retain iron at a neutral pH. The amount of Mg^{2+}, Sr^{2+} and Cu^{2+} coordinated by the microgels is dependent on the number of COOH groups, and the COOH/M^{n+} ratio is

Table 3.2 Concentration of COOH groups in solution, M^{n+} ions bonded at pH= 7, and the bonding ratio between the two.

Sample ID	[COOH] (mM)	$[Mg^{2+}]$ (mM)	$[COOH]/[Mg^{2+}]$
N0	0	0.07	-
M6	0.415	0.22	1.88
M10	0.714	0.36	1.9
M19	1.35	0.65	1.95
Sample ID	[COOH] (mM)	$[Sr^{2+}]$ (mM)	$[COOH]/[Sr^{2+}]$
N0	0	0.07	-
M6	0.415	0.19	2.18
M10	0.714	0.37	1.92
M19	1.35	0.58	2.08
Sample ID	[COOH] (mM)	$[Cu^{2+}]$ (mM)	$[COOH]/[Cu^{2+}]$
N0	0	0.13	-
M6	0.415	0.19	2.18
M10	0.714	0.38	1.87
M19	1.35	0.72	1.87
Sample ID	[COOH] (mM)	$[Fe^{3+}]$ (mM)	$[COOH]/[Fe^{3+}]$
N0	0.10	0.74	-
M6	0.415	0.73	0.56
M10	0.714	0.82	0.87
M19	1.35	0.89	1.52

about two (Table 3.2), which makes it straightforward to predict the number of these metal ions bonded for each sample.

By contrast, the binding and retention of Fe^{3+} is more complex. In fact, the $[COOH]/[Fe^{3+}]$ binding ratio is significantly lower, implying a higher amount of Fe^{3+} in the network. Hence, the M*m* gels retain additional Fe^{3+}, at a much higher concentration than for the alkaline earth ions and Cu^{2+}.

Moreover, in PBS buffer, Fe^{3+}, despite its phosphate salt being insoluble in water, is still coordinated within the network at neutral pH, whilst Mg^{2+} in the same medium is not bonded at all, due to the formation of insoluble $(Mg)_3(PO_4)_2$ (see Table 3.3).

Table 3.3 Percentages of Mg^{2+} and Fe^{3+} ions bonded at ambient conditions: in PBS at RT with a 0.1 wt% of M10 solution. The number of non bonded ions is determined by ion chromatography and the resulting difference is reported in the table.

Microgel	% Mg^{2+}	Fe^{3+}
M6	0	100
M19	0	100

The amount of Mg^{2+}, Sr^{2+} and Cu^{2+} coordinated by the microgels is dependent on the number of COOH groups, and the COOH/M^{n+} ratio is about two, which makes it straightforward to predict the amount of metal bonded for each sample. On the contrary, Fe^{3+} might also interact with the lactam groups of the microgel, however, preferring the lactam group as the bonding cannot be described as easily anymore.

3.3 Leaching experiments

Leaching experiments were performed to test the stability of the metal ion-microgel systems. If the bonding affinity is too low, the microgel will lose metal ions overtime. The affinity between the COOH group and the metal ion also has an impact on how well the system can retain the given ion when the microgel is subjected to mechanical stress and changes in the external environment. Initially, we measured the leaching of the ions as a function of the gel's COOH mol%in the presence of Ca^{2+} by subjecting them to several cycles of washing with pure water at pH 7 (Figure 3.4). In Figure 3.5, the amount of Mg^{2+}, Sr^{2+}, Cu^{2+} and Fe^{3+} is analogously plotted against the number of centrifugation and dispersion cycles. All microgels showed excellent retention of the Ca^{2+} ions over several cycles of washing, only declining in retention after > 5 washing cycles.

Ca^{2+} is fully retained within the network (Figure 3.4), due to its high binding affinity to COOH. On the other hand, The alkaline earth metal ions Mg^{2+} and Sr^{2+} (Figure 3.5a and 3.5b) tended to leach from freshly-loaded gels to a higher degree than Ca^{2+} (Figure 3.4), until a plateau is reached. Gels with lower acid content (M6) seem to lose more ions than the highly charged ones (M19). This could be attributed to the COOH distribution within the network: although both gels have a pseudo core shell structure, the latter have a higher concentration of charged groups in the network. This might provide a more favourable binding environment for the ions, which will be retained better by the microgel network. The microgels seem to retain the transition metal ions much better (Figure 3.5c and 3.5d, as no leaching is observed at all. This is especially true for Fe^{3+}, which is bonded in much higher quantities (Figure 3.3) and forms very stable complexes with the network. The microgel might be entrapping Fe^{3+} much better than the other ions, as it can contribute with tertiary N and the lactam O to the coordination shell of the cation, stabilizing its bonding.

3.4 Triggered cation release

The metal ions typically bind to carboxyl groups. Hence, full or partial protonation of the carboxyl groups should disrupt the metal-ligand interactions, causing the metal to be released

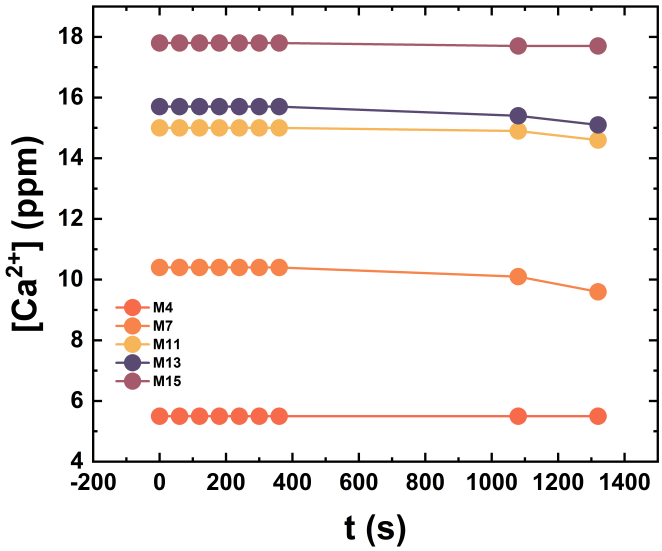

Fig. 3.4 Concentration of Ca^{2+} retained overtime at pH 7 and T= 20 °C of a 0.1 wt% solution of P(VCL-*co*-IA) microgel (Mm microgels). Each datapoint represents a washing cycle, where the gels are diluted in MilliQ water, centrifuged and filtered, and the ions present in the filtrate are determined by ion chromatography.

from the microgel. pH-dependent DLS (Table 2.2) showed how the D_H of the microgels at pH = 3 is smaller than the D_H of the Ca^{2+}-containing gels. This suggests that the dehydration due to proton bonding is much more significant than that due to ion bonding. As discussed in section 2.1, the formation of complexes within the microgels' networks should be dominated by weak-field bonding sites, which involve the presence of water in the site, stabilizing the complex. The presence of protons can lead to the formation of energetically-favourable hydrogen bonds between water and the COOH moieties, causing the expulsion of both water molecules and the previously coordinated ions. In order to determine the number of Ca^{2+} ions released as a function of pH, ion chromatography was used (Figure 3.6). At pH $<$ 3, the gels release the uptaken ions quantitatively, whereas the amount released decreases at pH = 4, and they retain almost all Ca^{2+} at pH $>$ 5 (Figure 3.6).

For all the remaining ions, as depicted in Figure 3.7, the pH required to release the metal ions in solution is below 4, with a release of 90-100% at pH = 2. The datapoints that indicate the percentage of Mg^{2+} and Sr^{2+} released at pH4 are almost consistent with the leaching contribution, observed in figure (3.5) (a) and (b). Although it is less than for pH $<$ 4, the sun of the alkaline earth metal leached and that lost to the partial protonation of the COO^{-}

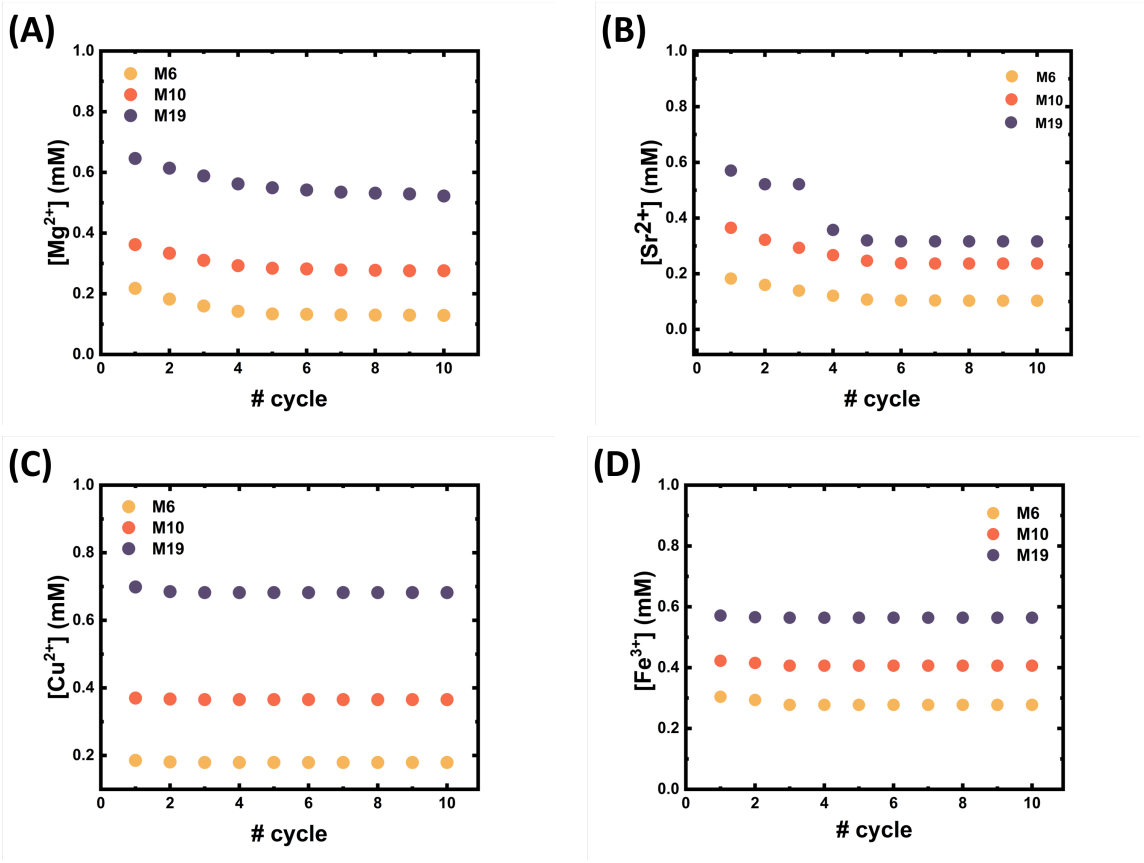

Fig. 3.5 The concentration of (a) Mg^{2+} , (b) Sr^{2+} ,(c) Cu^{2+} and (d) Fe^{3} retained for a 0.1 wt% microgel solution at neutral pH and RT when subjected to consecutive cycles of centrifugation and dispersion in MilliQ water. The sampels were initially soaked in 1 mM of (a) $MgCl_2$, (b) $SrCl_2$, (c) $CuCl_2$ and (d) $FeCl_3$, washed by centrifugation and redispersion in MilliQ water 2 times, and then subjected to the cycled. The concentration of leached ions is determined from the filtrate by ion chromatography.

groups, reveals that the gels lose 30% of the ions even at pH = 4. In order however, to achieve a more significant release, the gels require a pH<3.

When ions are better retained within the network, as for Cu^{2+} where leaching is negligible (Figure 3.3c), the number of ions that they release as a function of pH is not gradual, but much more abrupt. Especially at pH = 3, the percentage of ions released reaches an average of 75%, much higher than the 20% released at pH = 4 (Figure 3.5c). There is no real difference observed between the different cations in the analogous experiment below pH 3, except for Fe^{3+} (Figure 3.7d), which leach at pH 2, though only partially (about 40 %).

These results further confirm the ability for the microgel to capture Fe^{3+}, which binds the network non-selectively. The Fe^{3+} bonded to the COOH are released, whilst the remaining ions are maintained within the polymer chains. As is also apparent from Figure 3.3, Fe^{3+}

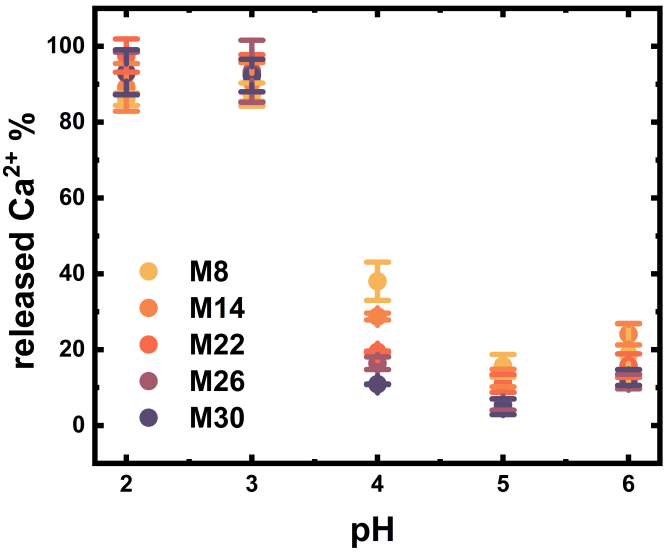

Fig. 3.6 Concentrations of Ca^{2+} ions released by a 0.1 wt% P(VCL-*co*-IA) (Mm) microgel samples solution at different pH in pure water at room temperature. Concentrations were determined from the filtrate of the centrifuged-filtered microgel samples *via* ion chromatography.

ions not only interact with the charged moieties of the polymer network but also bond to the lactam groups, where even the neutral microgel N0 is able to retain Fe^{3+} within its network (Figure 3.3).[171][172]

3.5 System reversibility: cyclic loading and unloading

To confirm the reversibility of ion uptake and release, the gels were subjected to cycles of loading and unloading a model ion. The ion chosen was Mg^{2+} due to its potential biological application, chiefly the triggering of the polymerization of G−actin into F−actin, and thus the formation of the cytoskeleton.[173] The gels were subjected to 3 successive cycles of ion addition at a high pH, followed by release at low pH. Figure 3.8 displays the concentrations of Mg^{2+} that a 0.1 wt% microgel solution can load at ambient conditions and no added salts.

After equilibration at pH = 7, the pH is reduced to 2 by adding HCl (data point 2 in Figure 3.8) to ensure the complete protonation of the COOH groups in the system and to trigger the release of Mg^{2+} ions. Once the pH is 2, the quantity of cations remaining in the polymer matrix is close to zero. To ensure that changes in ionic strength do not affect the uptake of Mg^{2+} by the gels, each sample is subjected to centrifugation and filtration to

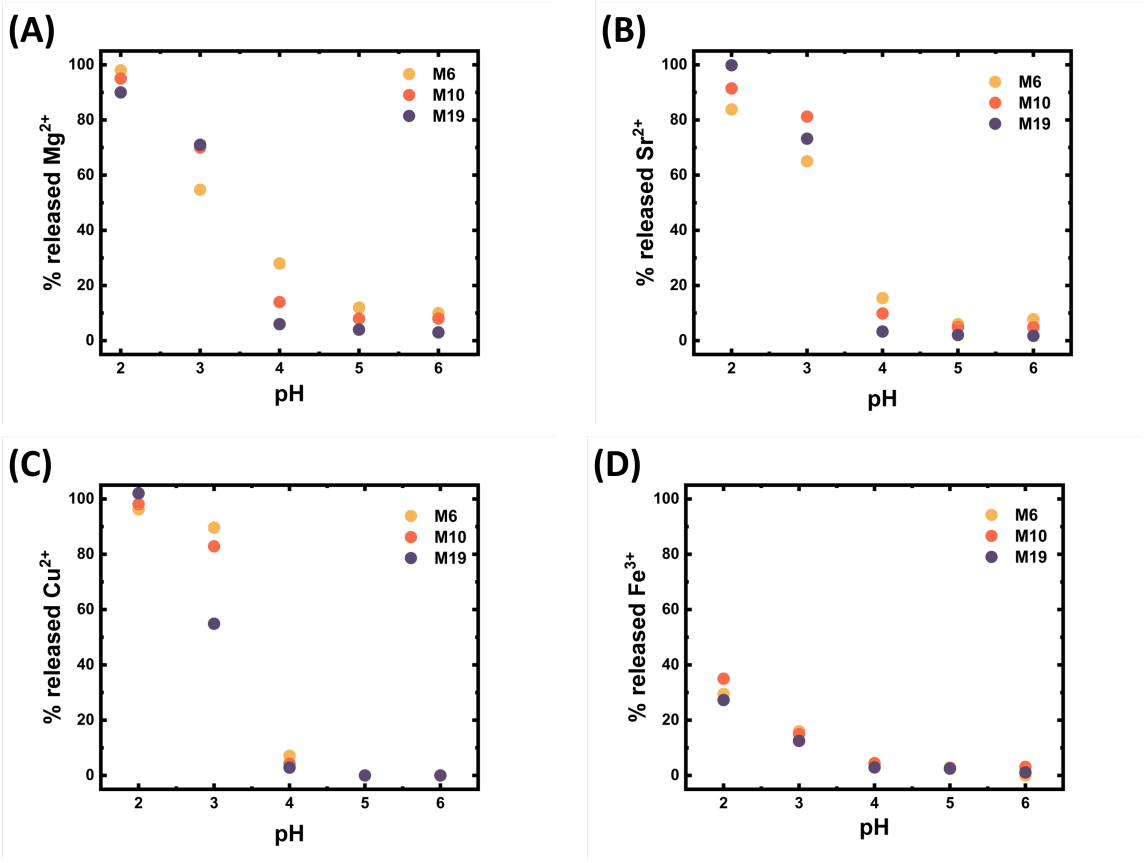

Fig. 3.7 Percentage of released (a) Mg^{2+} (b) Sr^{2+} (c) Cu^{2+} and (d) Fe^{3+} for a 0.1 wt% solution of M6 (6 mol% COOH), M10 (10 mol% COOH) and M19 (19 mol% COOH) at different pH values, RT, values measured after an equilibration time of 2 h after pH switch from pH 7.

separate the gels from the ion rich solvent, which is replaced by MilliQ water. The addition of a base, such as NaOH, can disrupt the stability of the gel. Full reversal of the system is performed by increasing the pH back to neutral whilst keeping the ionic strength low, which involves the use of pure MilliQ water and no base addition. Thus, a truly reversible loading can be ensured only by lowering the pH down to 2, and then increasing it *via* successive cycles of dilution and spin filtration, and not counter titration with a strong base.

3.6 Swelling and deswelling dynamics during cation uptake and release

Studies of molecular uptake and release in microgels are generally performed using polyelectrolytes or small proteins such as Cytochrome C (CytC).[139] The release times, regardless of

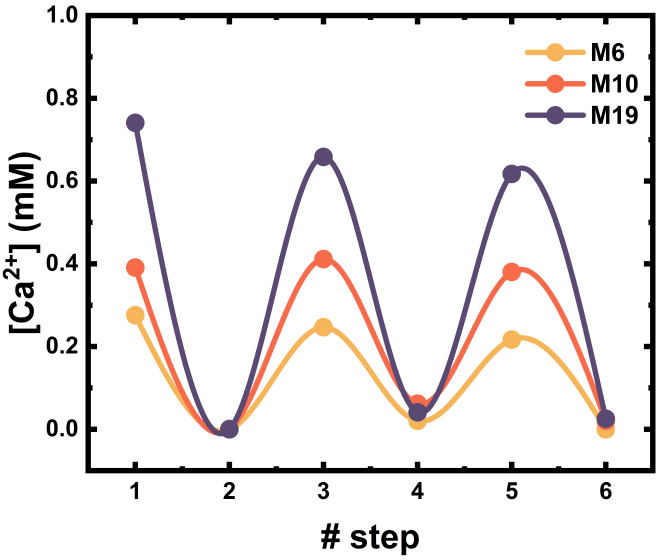

Fig. 3.8 Mg^{2+} concentration of M6 (6 mol% COOH), M10 (10 mol% COOH) and M19 (19 mol% COOH) 0.1 wt% microgel solutions at room temperature. Odd data points on the x-axis represent the loaded concentrations of Mg^{2+} within the total amount of microgels (1,3,5) and the even data points refer to the Mg^{2+} concentration left within the microgel sample after pH trigger (2, 4, 6).

the trigger used (*e.g.* pH or temperature) typically range in the hours, and quantitative release is normally achieved between 6 and 48 h.[138][139] In stark contrast, quantitative release of Ca^{2+} ions from M8-30 microgels studied in this work occurs in the range of seconds.

To study the uptake-release dynamics, changes in turbidity of the sample were monitored. When the gels bind ions, their size shrinks, increasing their density. When brought to pH 3, they shrink even further, expelling the ions, as seen in section 3.4. The microgel shrinks further, increasing its optical density, and thus the two collapse transitions can be monitored by following the turbidity changes of the solution, an effect which is not only visible to the naked eye (Figure 9.1) but is confirmed by an increase in the R_g/R_H ratio (Table 9.4). Turbidimetry experiments were performed with the help of an automatized injector coupled to a SpectraMax® device to track the changes in absorbance of the solution.

The series of gels with increasing anionic content (M8, M14, M22, M26 and M30) were measured at three different M^{2+} concentrations (0.1, 1, and 10 mM Ca^{2+}) in the microgel collapse region.

The collapse of the network upon the addition of Ca^{2+} is observed within 5 seconds of the rapid injection of the ion, after which presumably all carboxyl groups have been coordinated by the Ca^{2+}. This assumption is based on the fact that the added Ca^{2+} ions are in slight

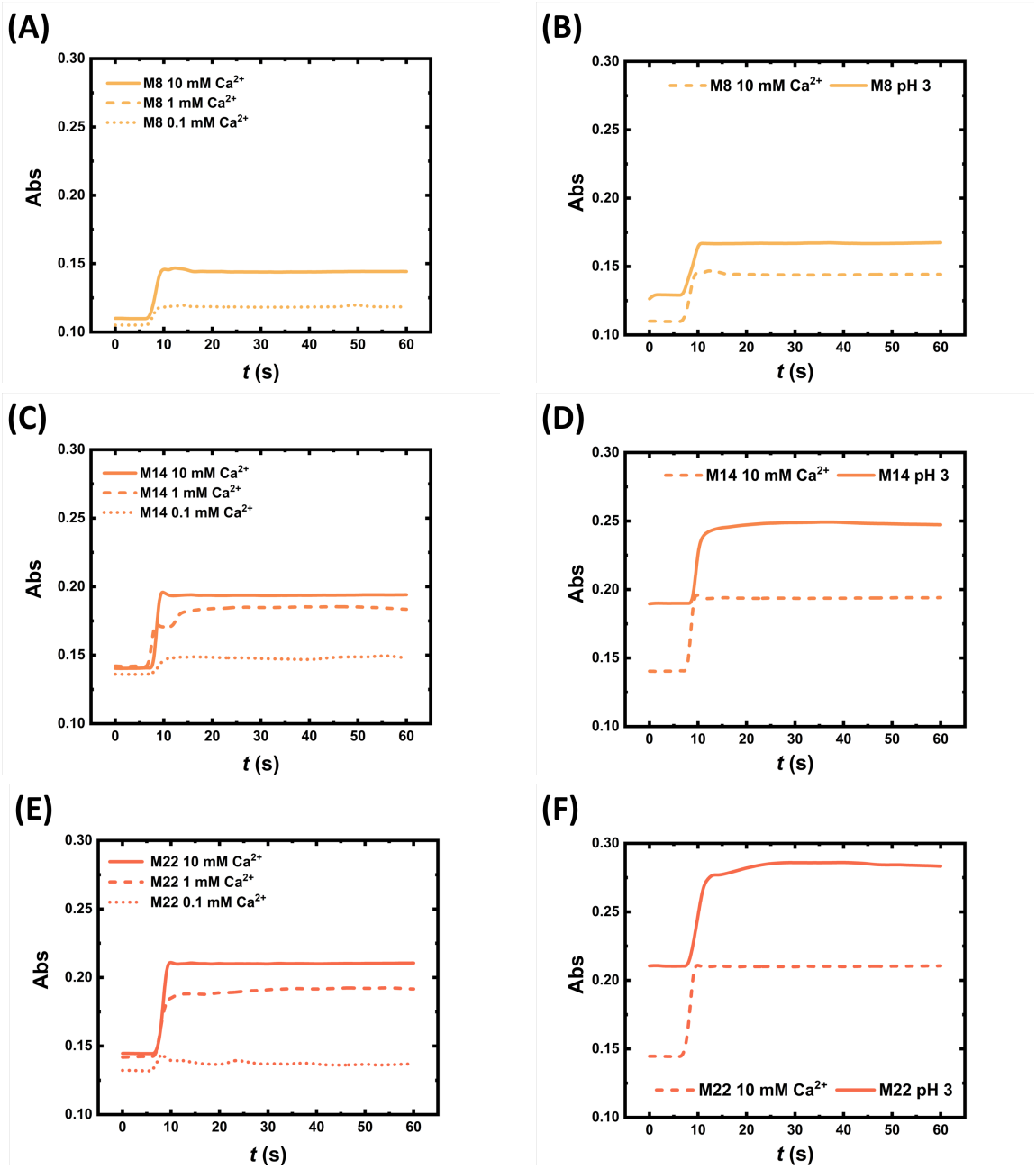

excess compared to the COOH groups, as calculated from the data obtained from Figure 3.3, hence the plateau in the absorbance curve should correspond to the full coordination of Ca^{2+} within the gels (Figure 3.9).

The change in absorbance observed in each experiment is abrupt for microgels with lower COOH content (M8, M14 and M22) (Figure 3.9a, 3.9c and 3.9e), while it smoothly reaches a plateau for M26 and M30 (Figure 3.9g and 3.9i), qualitatively showing how the network collapses whilst the ions are diffusing within (Figure 3.9).

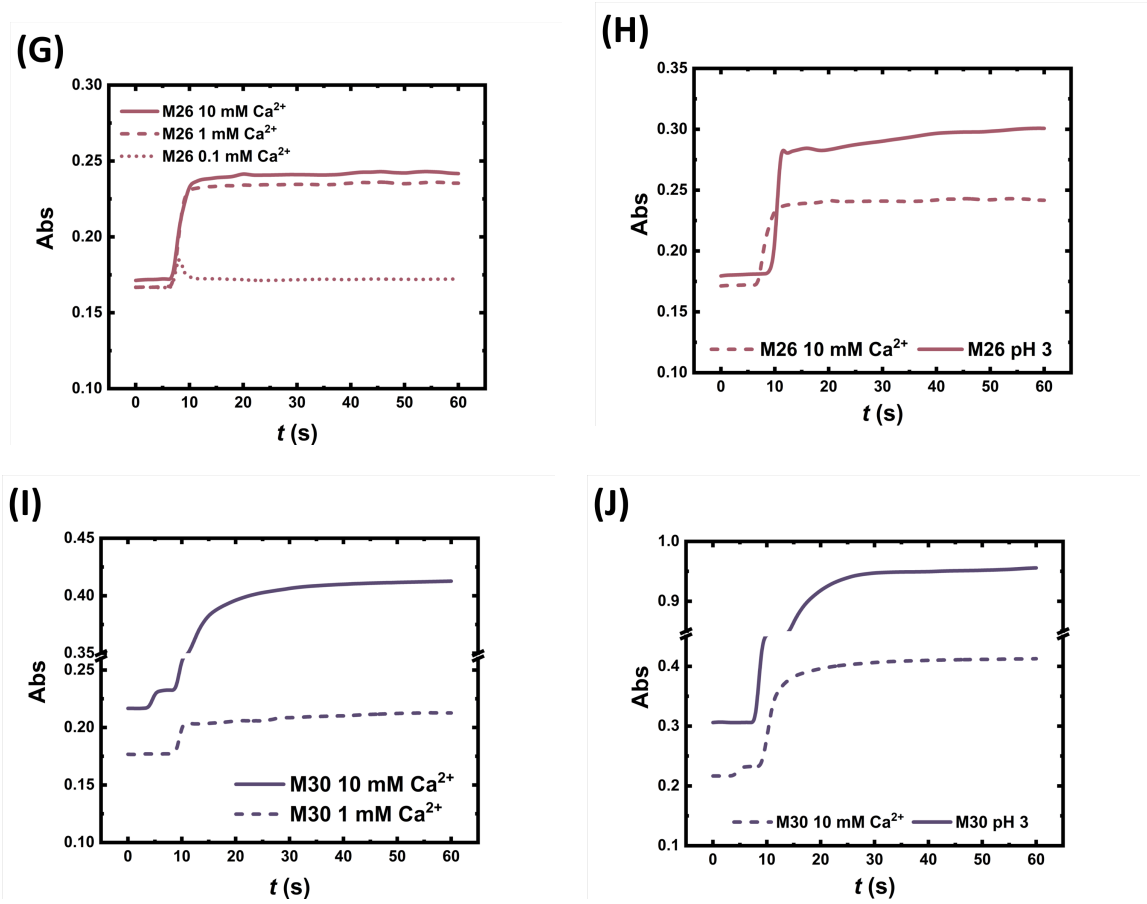

Fig. 3.9 Absorbance intensity (700 nm wavelength) measured of a 0.1% wt/V microgel dispersion as a function of time, measured with a scanning rate of 1 measurement per second; (a),(c),(e),(g),(i): measurements were made at T= 20 °C and pH= 7, (b),(d),(f) and (j): measurements were performed in the same cuvette at T= 20 °C, with a starting pH= 7.

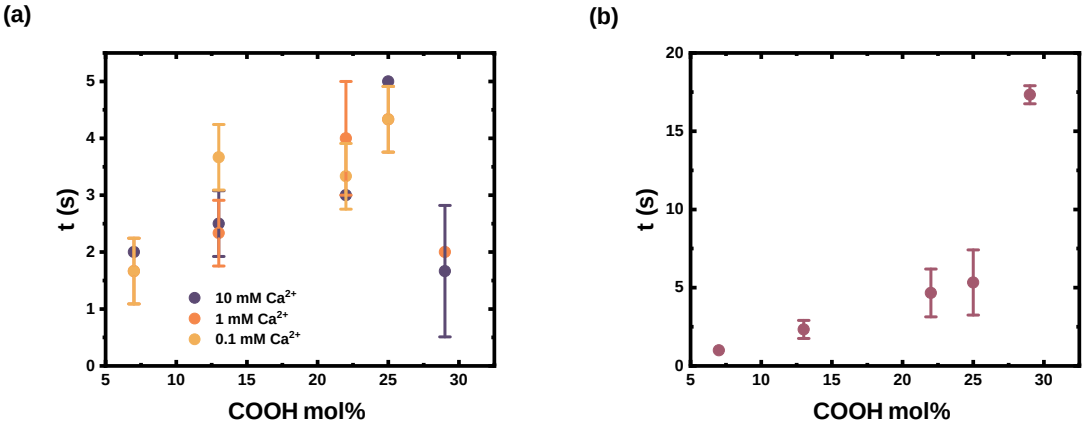

(a) Ca^{2+} addition (b) pH change to 3

Fig. 3.10 Uptake and release times: (a) bonding and (b) release time of Ca^{2+} of a 0.1 wt% P(VCL-*co*-IA) (Mn) microgel samples at RT. Concentrations are final calcium concentrations.

Figure 3.10 shows that with a concentration less than 26% COOH, the time necessary to collapse the network increases with the COOH mol%, as expected, and that all three tested Ca^{2+} concentrations are sufficient to induce the network collapse (Figure 3.10a). In this range, higher mol% of charged groups require more time to be saturated with Ca^{2+} ions, as the divalent ion has to diffuse within the gels and coordinate them. The concentration of Ca^{2+} has no significant impact on the bonding times in this regime, even though the amount of available Ca^{2+} for bonding is higher. This suggest that the kinetics are largely diffusion driven. However, for the sample with the highest acid content (M30), only high concentrations of Ca^{2+} (10 and 1 mM) are sufficient to trigger the microgel collapse, and no change in absorbance is observed for a concentration of 0.1 mM (Figure 3.9j). This can be explained by a difference in functional group distribution, where the COOH groups are strongly concentrated within the core of the microgel, as indicated by TEM images (Figure 2.7), and thus the deswelling of the network triggered by ion bonding is much faster compared to the rest of the microgels.

The debonding pH was chosen to be 3, as at higher pH, the release was not found to be quantitative, which would have led to smaller transmittivity change. Figure 3.10b shows that all microgel have a fast release, where within 1 to 5 s absorption changes can no longer be observed. The release time increases steadily with the COOH molar content, jumping to almost 20 s for M30. Microgels M8-M26 deswell at a comparable rate as with the addition of Ca^{2+}, the much larger discrepancy observed for M30 is a further evidence that microgel M30 possess an internal structure that is different from the rest of the gels.

3.7 System selectivity

The selectivity of the microgel for a target cation depends on the chemistry of the polymeric chain, which affects bonding sites, binding affinity, and accessibility of the sites themselves, in terms of network density and structure. In this study, microgels have a porous, accessible network, where the retention and binding of the ions should only be determined by the ligands belonging to the network. The greater the affinity that the microgel matrix has to the cation, the greater the probability that the microgel network will retain the cation. This might depend not only on the number of charged COO^- groups in the network, but also on the neutral monomers present, which can contribute lone pairs in the coordination of the metal cation, especially in the case of the transition metals. Hence, to study the selectivity of the microgels, two metal ions at the same starting molar concentration were mixed in the presence of microgels. Figure 3.2 and 3.3 show each sample, regardless of their COOH fraction, can bind to a maximum cation concentration of 0.8 mM. For this reason, the concentration of ions was chosen to ensure the eventual saturation of the system by each of the competing ions. Hence, each ion present in the sample has a starting concentration of 1 mM. In this case, a microgel sample is placed in an equimolar solution of two ions (Mg^{2+} and Sr^{2+} for example), and then spin filtrated. The filtrate contains the ions that are not retained by the network, and their concentration can be determined with ion chromatography. By calculating the difference in concentration of the initial cation concentration and the non bonded one, it is possible to calculate the amount of each ion species bonded by the microgels. The different percentages of metal retained in the gel's network whilst in the presence of another cation is depicted in 3.11 and 3.12.

Figure 3.11 focuses on the competition between Mg^{2+}, Sr^{2+} and Cu^{2+}, for 3 microgels with different COOH concentrations.

The system is not especially selective in mixtures of Mg^{2+} (green in Figures 3.11 and 3.12) and Sr^{2+} (red), since they bond in almost equal amounts. However, the bonding ratio of two is consistent with the observations of Eichenbaum *et al.*, where the authors saw a higher binding constant of larger alkaline earth alkali ions to the PAAc network.[59] In their observations, Mg^{2+} displayed a binding constant of (2.4 ± 0.1) x 10^3 K (M^{-1}), which is slightly lower than the constant found for Sr^{2+} (3.9 ± 0.2) x 10^3 K (M^{-1}).

Finally, When Ca^{2+} is mixed either with Mg^{2+} (red) or Sr^{2+} (green), the ions distribute equally among the binding sites, leaving 50 % of the ions in solution. In the presence of transition metals, Ca^{2+} is displaced by Cu^{2+} and Fe^{3+}, which will bind 95% and 100% of the binding sites respectively (Figure 3.13).

From observations outlined in section 3.2, the microgels bind significantly more Fe^{3+} in comparison with the rest of the ions investigated.

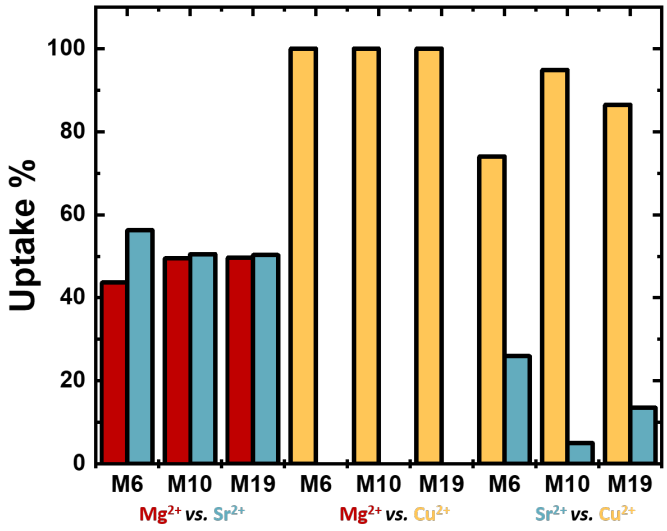

Fig. 3.11 . Percentage of coordinated ions with respect to its competitor for each microgel, M6, M10 and M19 at pH 7 and room temperature. Colour coding: yellow represents Cu^{2+}, red represents Sr^{2+} and green represents Mg^{2+}. The microgels used are M6 (6 mol% COOH), M10 (10 mol% COOH) and M19 (19 mol% COOH).

The capacity of the microgels to bind Fe^{3+} is overall higher and the binding modes are different: Fe^{3+} is coordinated by both the COO^- groups but also to the lactam moieties. Hence, for the sake of clarity, the competition experiments involving such ions were done separately. Figure 3.12 shows the competition between the above-mentioned ions and Fe^{3+}, where each 0.1 wt% solution of microgel (M6, M10 and M19), was mixed with 1 mM of two different ions. From Figure 3.12 it is clear that, apart from minimal amounts of Cu^{2+} and Sr^{2+}, the microgels predominantly retain Fe^{3+} in their network. Since the percentage of ions bonded is related to the amount that is present in the filtrate as determined by ion chromatography, a 0% retention (as in the case of Mg^{2+}), means that the same concentration of Mg^{2+} cations was measured in the starting solution and in the final solution. The figure thus does not graphically describe the accumulation of Fe^{3+} in the network. As seen in Figure 3.3, the concentration of Fe^{3+} retained by the microgels is significantly higher than those of other ions. The percentage of retained metal cations is calculated based on the total concentration of starting cations added to the solution. As a matter of fact, when measuring the amount of Fe^{3+} bonded when in the presence of another ion, there is a complete selective uptake of the metal, in that the same amount is observed as if the Fe^{3+} was alone (Figure 3.12). In this way, the system can target one ion in particular, which is Fe^{3+} for the microgels M6,

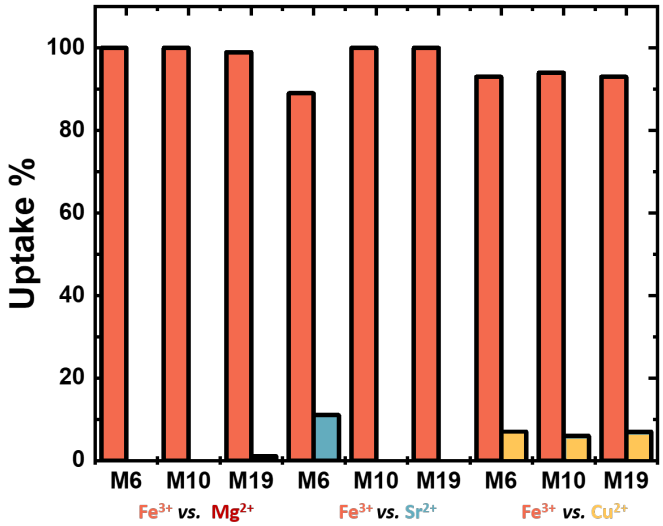

Fig. 3.12 Percentage of Fe^{3+} (in orange) bonded by a 0.1 wt% microgel solution at pH 7 and room temperature in the presence of Mg^{2+} (not visible, first 3 data sets for M6, M10 and M30), Cu^{2+} in green and Sr^{2+} in red. The microgels used are M6 (6 mol% COOH), M10 (10 mol% COOH) and M19 (19 mol% COOH).

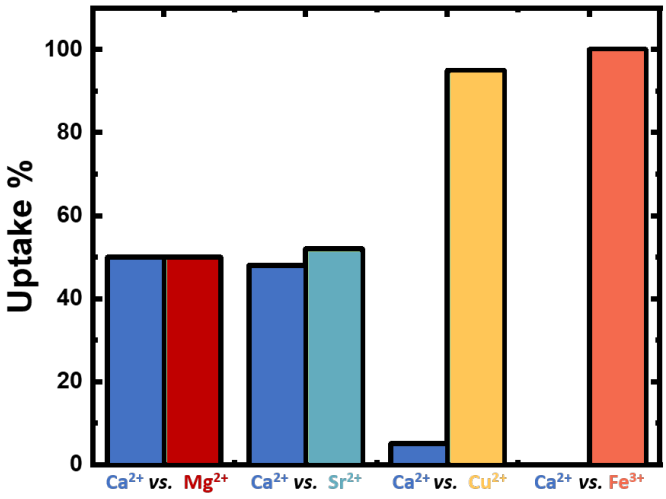

Fig. 3.13 Percentage of Ca^{2+} (in blue) bonded by a 0.1 wt% M10 microgel solution at pH 7 and room temperature in the presence of Mg^{2+} in red, Sr^{2+} in green, Cu^{2+} in yellow and Fe^{3+} in orange.

M10, and M19 when in aqueous ambient conditions. As seen in Figure 3.3, homopolymeric PVCL microgels bind a significant number of Fe^{3+} ions, despite the absence of COOH groups. Nonetheless, for P(VCL-*co*-IA) microgels, the COOH also prefer to bind Fe^{3+} instead of the rest of the studied ions, showing how Fe^{3+} ions displace the other ions from both neutral and charged ligands. Hence, in a complex mixture, Fe^{3+}, would out compete the rest of the ions, making this system selective towards Fe^{3+}.

As just seen, the gels do discriminate between competing ions, but no observations were made on how strong the system can bind one ion when there are competing ligands present. When placing the microgels in a solution such as PBS, where the formation of insoluble Mg and Fe salts is favoured, the system is still capable of retaining Fe^{3+} (see Table 3.3), showing further how these gels are an excellent tool to capture and retain Fe^{3+}.

3.8 Summary

In this chapter, the uptake and release of several alkaline earth and transition metal cations by P(VCL-*co*-IA) microgels was studied in terms of loading capacity, loading rate and reversibility, and ion selectivity .

The behaviour of each microgel with a COOH molar content up to 30% has been studied in the presence of 5 multivalent cations: Ca^{2+}, Mg^{2+}, Sr^{2+}, Cu^{2+} and Fe^{3+}. The possibility for the cations to function as cargo where they can be uptaken at neutral pH and released at acidic pH has been studied. All divalent cations are released at low pH, and only partial or no release of the cations is observed at pH > 5. The results differfor Fe^{3+}, where only a 40% release could be achieved even at pH = 2. Additionally, the binding of ions is prevented, when PBS is used instead of pure water, suggesting that the release of alkaline earth ions can also be triggered by competing salt formations, like in the case of phosphate magnesium and calcium salts. As an exception, the microgels also retain Fe^{3+} ions in PBS, which indicates that Fe^{3+} can be taken up by the microgel matrix with the same efficiency as in pure water. The microgels have also proven to be capable of undergoing multiple cycles of loading and release of their cargo, given that the external conditions like ionic strength are highly controlled. After investigating the binding and release capabilities of such gels, their time dynamics of these processes were investigated. The microgels show a significantly shorter response time when compared to their macroscopic counterparts, but have time scales that suggest that there is hindered diffusion of the ions throughout the network. To determine whether there is a preference of the network for a certain ion, competition experiments were performed. The gels have a specific selectivity towards Fe^{3+}, which is due to the sum of

two contributions. The first contribution is the favoured formation of Fe^{3+} complexes with COO^{-}, and the second derives from the presence of lactam groups.

For further investigations, these gels could also be tested for highly poisonous transition metal ions, such as Hg^{2+} or Pb^{2+}, which could be prevented from entering the bloodstream by simple ingestion of the gels and subsequent expulsion through the digestive tract.

Chapter 4

Mechanochromic microgel double networks

This chapter describes a method to produce smart mechanochromic and thermochromic double-network granular hydrogels (DNGHs). Starting with the choice of microgels, brief descriptions of their syntheses and characterization, this chapter will then focus on the formation of the double networks and the characterization of their strain- and temperature-dependent behaviour.

This chapter consists of unpublished (at the time of submission), recently obtained results and some experiments are still ongoing. The project has been performed in collaboration with Matteo Hirsch from the SMaL Lab (EPFL, Esther Amstad Group). Matteo contributed ideas on the application of the microgels and took part in the mechanical characterizations. Alba Sicher (ETH, Eric Dufresne Group) performed the reflectometry measurements, and Nicholas Bain (ETH, Eric Dufresne Group) also took part in the mechanical characterization. Daniel Messmer contributed ideas, suggestions, and discussions.

4.1 Introduction

Many colorful materials in nature do not owe their colors to pigments, but to ordered microstructural mismatch.[108] The most striking and saturated colors come from ordered periodic microstructures combined with an ordered refractive index mismatch along an axis, a surface, or a volume. Two eye-catching examples are the Morpho butterfly wings,[174] where a combination of differently-refractive layers and surface micropatterning generate their famous blue color and the chameleon skin, in which guanine nanocrystals immersed in a transparent matrix change the chameleon's bright skin colors according to their orientation.[175] Such colors are a result of Bragg diffraction, in which a light beam is diffracted by periodically spaced reflecting grooves, which are comparable in size to visible light wavelengths.[107] Such diffraction is described in three dimensions by a combination of the Bragg law and the Snell equation 4.1:

$$m\lambda = D\sqrt{\frac{8}{3}(n_{avg}^2 - sin^2\theta_0)} \tag{4.1}$$

where m represents the order of diffraction, λ is the wavelength of incident light, D is the spacing between closely-packed planes, n_{avg} is the weighted average of the refractive indices of the two materials and θ is the angle between the incident light and the crystal planes. Essentially, the spacing between the planes determines the angle at which monochromatic light is diffracted, *i. e.* at which angle the light waves will constructively interfere, generating strong colors.[107]

When the light is composed of different wavelengths, the scattering angle will change depending on the wavelength and the perceived color is therefore angle dependent. 2D reflecting surfaces rely on the periodicity of a surface, where the refractive index mismatch varies in two directions. An example of synthetic structural color is the self-assembly of silica nanoparticles in hexagonally packed surfaces, which generate iridescent nacre-mimetic structures.[176] When the silica nanoparticles are stacked in 3 dimensions, opalescent structures arise, where the materials reflect bright color throughout their entire volume.[177] Changing the size or spacing of the nanoparticles will alter the reflective point distance altering the color of the material. Similarly, when the particles are stacked in 3D, changes in color can arise along one or more of the three axes, depending on where the material is stressed. This peculiarity, which is unique to structural color, is particularly exploited in high-precision strain sensors.[178] Strain-dependent color in 3D crystalline materials is achieved in three directions, giving even more insight into the strain distribution throughout the material. Especially in the formation of 3D stress-responsive materials, having a transparent material that shows the intensity and location of the resulting strain by changing color can be

of importance in self-reporting strain sensors, which directly produce a visible signal due to changes in the strain within them. By contrast, in materials that contain mechanochromic molecules, where the change in color derives from the activation of a mechanophore, the color change does not necessarily provide precise information on the anisotropy of the stress that the material is subjected to, but rather signals the number of activated sites, where the mechanophores are activated.[108]
Since the color in structurally-colored material arises from a refractive index mismatch, materials that are such a color are composed of two materials with different refractive indices n, as in the case of monodisperse silica nanospheres embedded in a soft polymer matrix.[179] Similarly, core-shell nanoparticles composed of a polystyrene core and a soft polymer shell produced iridescent and colorful surfaces.[180] When using all-organic materials instead of inorganic or a combination of the two, *e. g.* using core-only microgels, the addition of a contrast surface and a support is required, like in the case of etalons.[92] Ordered microgels on surfaces have been used as temperature, pH, mechanical stress, light, and small molecule sensors, where the respective stimulus is able to induce a change in the swelling of the microgels, leading to a modification in the diffraction grid and consequently to a color change.[181] Most examples of ordered patterns that are made with nanoparticles are applied on thin films or monolayers.[111] In this way, the refractive index mismatch is enhanced, giving rise to stronger color, and the assembled films, which generally lack mechanical resistance, are structurally reinforced by a solid support.[179] There are a very few examples of free-standing microgel films, which are brittle and lack mechanical resistance.[182] Especially in 3D objects, the mechanical stability of such particle assemblies is labile and relies on double networks, which generally disrupt the ordered packing. Mechanically-stable 3D assemblies composed of microgels generally consist of granular double networks, where polydisperse microgels are soaked in a monomer, which is then polymerized in the presence of a crosslinker, forming double network granular hydrogels (DNGHs).[30] These DNGHs are exceptionally strong and form tough networks when microgels are jammed together in closely-packed structures, and further polymerized into a percolated network. When the microgels are monodisperse, they can form structural colors, the shade of which depends on the microgel size and the distance between them.

By forming structural colors with DNGHs, this chapter provides an extremely simple yet effective method to obtain cost-effective mechanochromic material, the gradual color changes of which is reversible. The choice of using PNIPAm-based microgels further enhances the functionality of the proposed material to be responsive to temperature. The results presented in this chapter have been in large part obtained shortly before the submission date of this

thesis, and therefore the in-depth characterization of all of the presented materials in most cases has yet to be completed due to time constraints.

4.2 Microgel synthesis and Characterization

4.2.1 P(NIPAM-*co*-MAAc) Microgels

PNIPAm-based microgels have been studied extensively in the few past years due to their well-understood chemistry, responsiveness, and ease of production and handling. Compared to the PVCL-based microgels described in Chapter 2 and 3, PNIPAm-based microgels are easier to synthesize in narrower size distributions and can be purified not only by dialysis, but also with ultrafiltration and ultracentrifugation. Moreover, PNIPAm-based microgels can be freeze-dried and easily redispersed in water, permitting a higher degree of freedom in choosing the operational concentration. The thermoresponsive PNIPAm microgels were formulated to include methacrylic acid (MAAc), which makes the microgels responsive to pH changes and metal cations, with an eye to the eventual use of such materials as multiresponsive sensors. Contrary to the PVCL-based microgels described in Chapters 2 and 3, charges are evenly distributed throughout the microgel, and not dominantly present in the core, as is the case in P(VCL-*co*-IA) microgels. P(NIPAM-*co*-MAAc) microgels were obtained by precipitation polymerization, using a procedure adapted from the literature (Figure 4.1).[46] The resulting microgels were purified *via* cycles of ultracentrifugation and redispersion in MilliQ water, and lyophilized for storage (see section 8.2 the experimental procedure in detail). The amount of of MAAc in the microgel network was kept constant at 6.5 mol%, and only the size of the microgels was varied, in order to investigate the effect of size on the resulting color, packing density, and ink rheology (see Chapter 5).

Different sizes were obtained by varying the amount of anionic surfactant sodium dodecylsulphate (SDS). Higher SDS concentration in the reaction crude lead to smaller gels

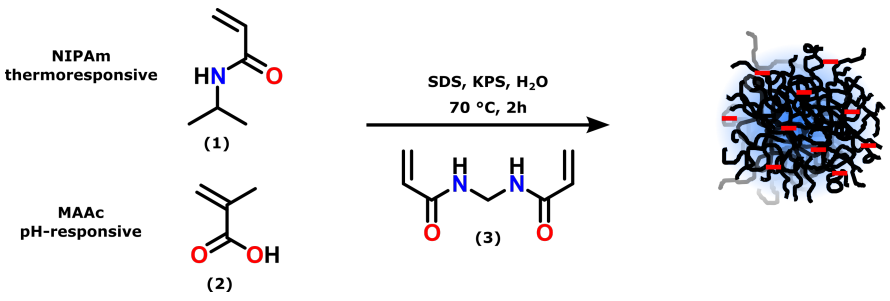

Fig. 4.1 Schematic representation of P(NIPAm-co-MAAc) microgel synthesis, where SDS concentration was varied to obtain anionic microgels in a range of sizes.

Table 4.1 Microgels size as measured by DLS for each P(NIPAm-*co*-MAAc) microgel, measured in MilliQ water at neutral pH, and in 10 wt/V% of AAm, both at 20 °C.

Microgel	D_H (nm) RT in H_2O	D_H (nm) 50 °C in H_2O	D_H (nm) RT in AAm	D_H (nm) 50 °C in AAm
PNIPAm-350	267 ± 3	124 ± 1	343 ± 9	166 ± 2
PNIPAm-400	275 ± 4	128 ± 1	386 ± 17	182 ± 1
PNIPAm-450	328 ± 7	163 ± 1	453 ± 17	221 ± 2

since the surfactant stabilizes the primary particles during the polymerization process.[183] Microgels varying in size from 267 nm to 328 nm were obtained (measured in MilliQ water, see Table 4.1) (see Section 8.2 for detailed synthesis). Table 4.1 also displays the radius of the gels in 10% wt/V AAm solution, which was chosen as the monomer that will produce the double network and thus should be considered in the characterization of the gels before curing to properly determine the microgel assemblies' color. However, the reported absolute D_H values in AAm solution should be taken with some caution, since DLS evaluation depends on the viscosity and the refractive index, which will be both influenced by the presence of AAm. The microgels listed in Table 4.1 are named for the main monomer and their D_H in 10% wt/V AAm solution, and will be referred to such throughout this chapter.

As is apparent from Table 4.1, the microgels swell considerably when soaked in the AAM solution.[184]

Their swelling profiles in response to temperature were measured, both in pure MlliQ water and in 10% wt/V AAm. The microgels in water display the characteristic sharp swelling transition from swollen to collapsed at $\approx$ 32 °C (Figure 4.2a, 4.2c and 4.2d). When looking at the transition of the same gels in AAm (Figure 4.2b, 4.2d and 4.2e), the volume transition is spread out over a larger temperature range, but remains centered around 32 °C. The collapsed radius in AAm solution is larger than that observed in MilliQ water. The dry morphology of the gels was imaged with electron microscopy in order to visualize the single microgel architecture (by TEM), and their packing at high concentrations (with SEM).

In Figure 4.3, the TEM images of the microgels stained with PTA show that the P(NIPAm-*co*-MAAc) microgels feature a dense core (in white) and a fuzzy corona (in grey). When deposited and dried on the TEM grid, they assemble hexagonally. It is not possible to image concentrated solutions by TEM hence, SEM was used to image how the gels assemble when tightly packed together. Figure 4.4 shows how the microgels pack hexagonally and start faceting, due to their high concentration.

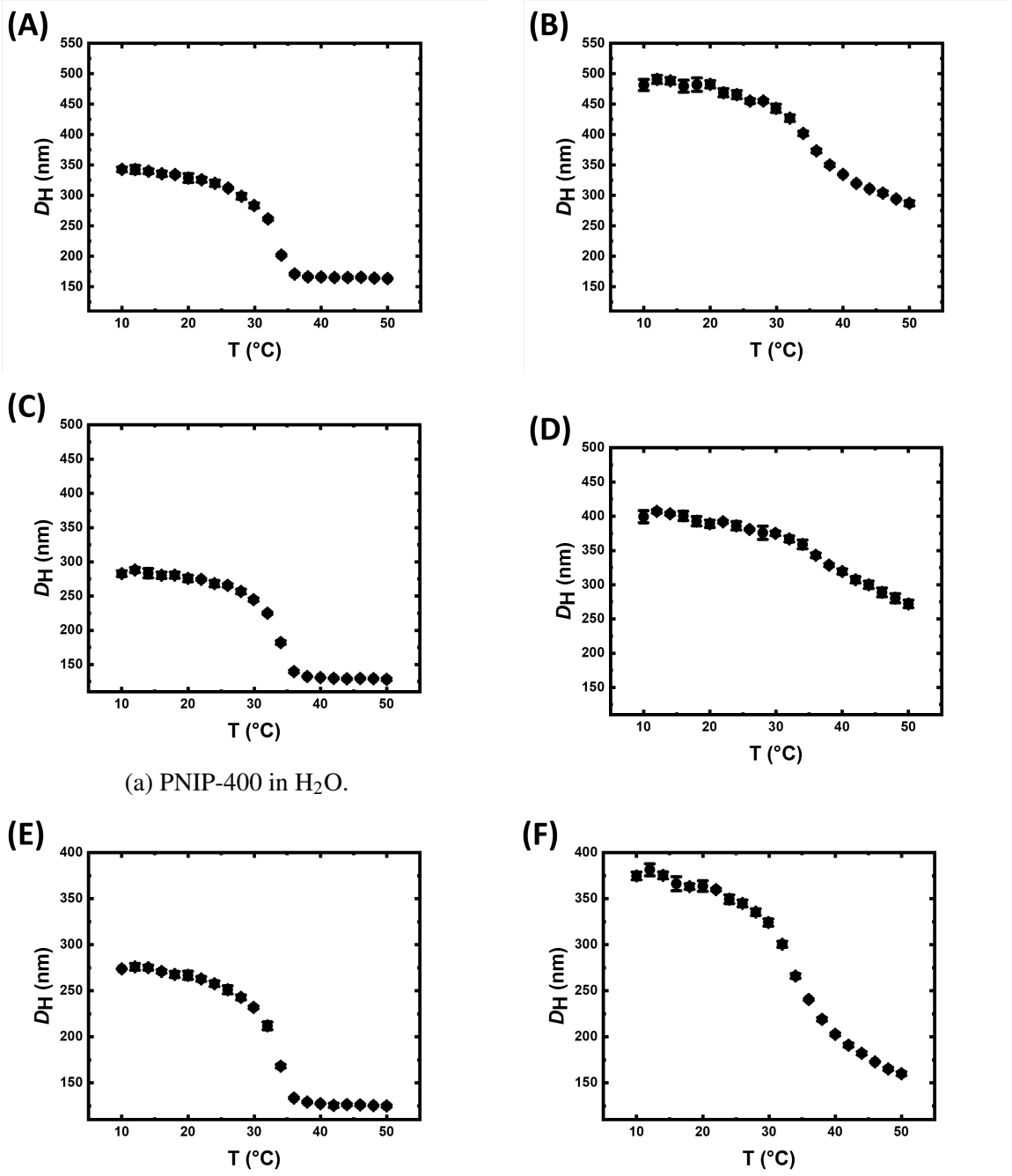

(a) PNIP-400 in H_2O.

Fig. 4.2 D_H values at neutral pH measured by DLS; PNIPAm-350, PNIPAm-400, and PNIPAm-450 (a), (c), (e) in water and (b), (d), (f) in 10% wt/V AAm from 10 °C to 50 °C.

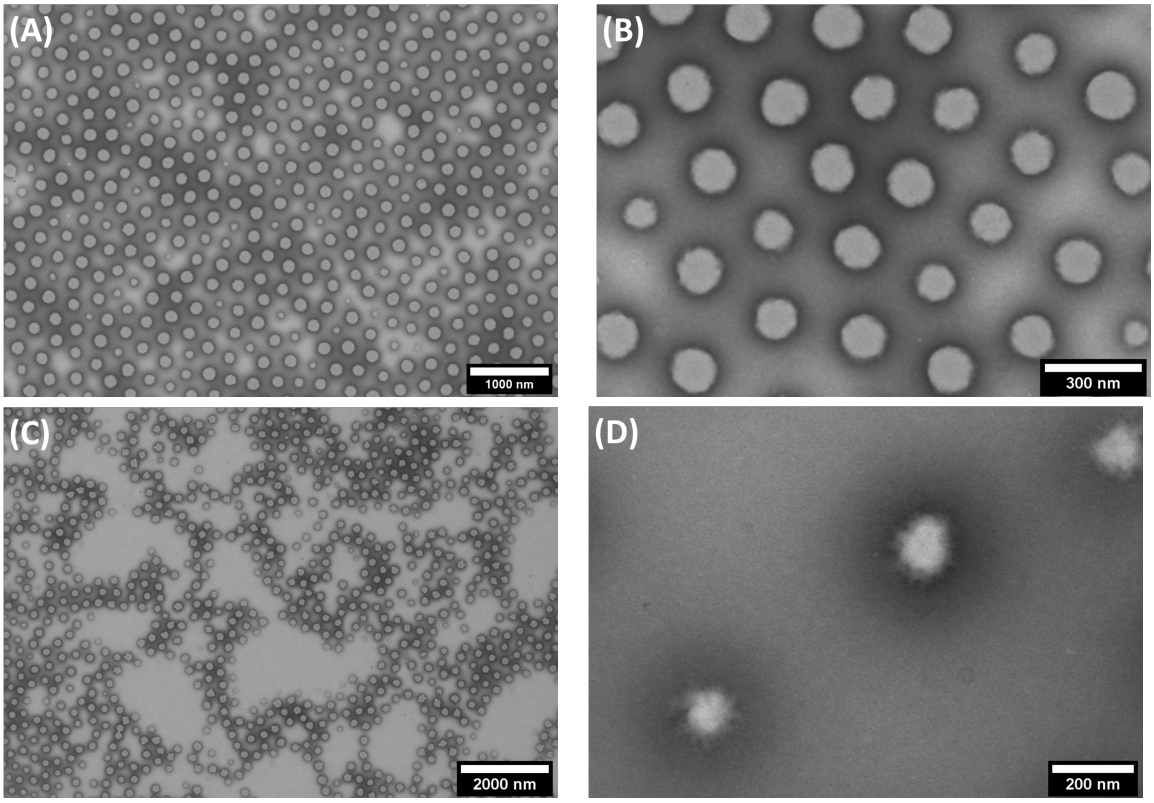

Fig. 4.3 TEM images of P(NIPAm-*co*-MAAc microgels stained with PTA at neutral pH. The microgels here represent an overview of PNIPAM-400 at (a) 0.1% wt/V concentration, (b) 0.1% wt/V, close up, (c) at 0.01% wt/V and (d) a close-up of PNIPAm-400 microgels. The darker shadow behind the microgels belongs to the grid, and is a staining effect fromthe PTA stain.

4.3 Double network formation and characterization

4.3.1 Structural color formation

Colored pellet formation

Monodisperse microgels pack in bcc and fcc lattices when in constrained environments.[103] In most cases, crystalline structures are obtained from redispersion in water, which generates labile crystals or, if the concentration is too high, transparent gels over time (as will be shown in section 5.4.6).

One way to force the microgels into ordered dense packing is to centrifuge them at high speed and immediately remove the supernatant. In this way, semi-crystalline domains can be obtained, vastly accelerating the crystal formation compared to the alternative redispersion method, which typically takes several days and involves the rehydration of the gels with

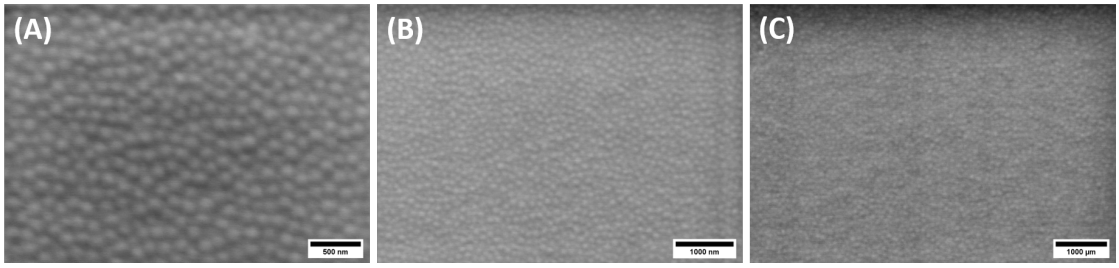

Fig. 4.4 SEM images of (a) NIPAm-450, (b) NIPAm-400, and (c) NIPAm-350, aquired with an accelertion of 5 kV.

very precise amounts of solvent to obtain the desired volume fraction.[185] For this reason, ultracentrifugation is an effective method to pack microgels in the submicrometer range. Importantly, it overcomes the formation of mechanically-labile structures that disperse upon handling.

In this case, when P(NIPAm-*co*-MAAc) microgels were centrifuged, they yielded soft, iridescent pellets with a distinct color, depending on the size of the swollen microgel (Figure 4.5). Each sample was prepared from a 1 wt% P(NIPAm-*co*-MAAc) solution in 10% wt/V AAm, which was centrifuged for 2 h at 282k RCF. The AAm-containing supernatant was discarded, and the colorful pellet was transferred in a Luer-lock syringe for processing. Each 30 mL sample yielded 4 ml of pellet volume.

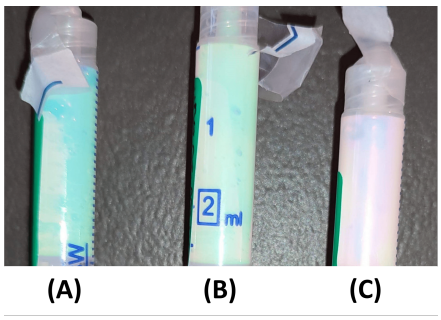

Fig. 4.5 P(NIPAM-*co*-MAAc) microgels compressed by ultracentrifugation at 282k RCF for 2 h at RT. (a) NIPAm-350 in blue (b) NIPAm-400 in green (c) NIPAm-450 in pink. Images are taken under diffused natural light.

Photocuring method

The gels were then cured under two different UV sources in order to investigate whether the curing rate has an effect on the packing of the microgel. Under a strong UV source (365 nm, 60 mW/cm^2, VP CL-1000), the compressed microgel dispersions turned from colorful to

(a) PNIPAm-450 Before curing.

(b) PNIPAm-450 After curing.

(c) PNIPAm-400 Before curing.

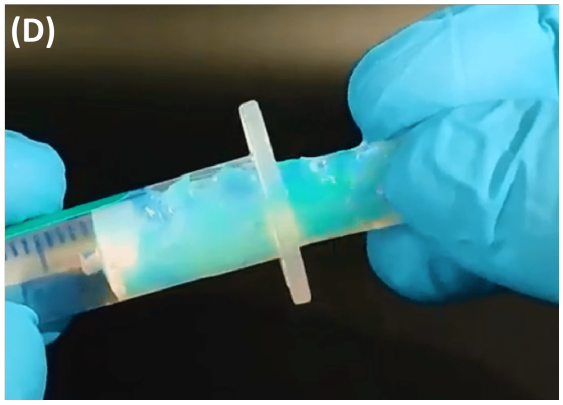

(d) PNIPAm-400 After curing.

(e) PNIPAm-350 Before curing.

(f) PNIPAm-350 After curing.

Fig. 4.6 (a) PNIPam-450, (c) PNIPAm-400, and (e) PNIPAm-350 compressed by ultracentrifugation at 282k RCF for 2 h, before photocuring. (b) PNIPam-450, (d) PNIPAm-400, and (f) PNIPAm-350 after being exposed to 15 min UV light (2 mW/cm^2).

white, and remained so after curing (Figure 9.2 in the Appendix). The irreversible whitening might be linked to of too-fast AAm polymerization that displaces the microgels the heat

generated by the intense 60 mW/cm^2 in the curing vessel, which is sealed, or a combination of the two. The gels are thermoresponsive, and will shrink at T $>$ 40 °C, decreasing their volume fraction, leaving voids that can be occupied by the AAm network, disrupting the ordered pattern. This disruption might be the cause of all wavelengths being scattered incoherently, and as a result, the solid appears white to the observer. Using a weaker curing lamp (2 mW/cm^2, fluorescent tube for TLC), and curing for 15 min whilst ensuring proper ventilation to keep the temperature at RT, yielded in some cases colorful DNGH, depending on the size of the microgels (Figure 4.5). PNIPAm-450, which was initially white with pink reflections (Figure 4.5a) became white under these conditions as well (Figure 4.5b) and did not show any responsiveness after curing. PNIPAm-450 was therefore not characterized in its responsiveness any further. Meanwhile, PNIPAm-400 partially retained its green color, though turning somewhat less vibrant (Figure 4.5d). PNIPAm-350 retained its blue color, as seen in Figure 4.5f.

4.3.2 DNGH characterization

DNGH microstructure

SEM measurements were performed to investigate the uncollapsed structure of the double network. PNIPAm-400-based DNGH was freeze dried and then analyzed by SEM. Figure 4.7 shows how the microgels maintain their packing throughout the whole volume even after crosslinking.

The sample was ripped for imaging, as visible in Figure 4.7b and 4.7c. The ripping of the already dried specimen led to the rupture of the DN, resulting in the formation of holes (where the microgels were displaced) and protruding structures on the surface, which seem to be elongated and deformed microgels (Figure 4.7b). Microgels *per se* are soft and deformable, and deform under stress, *e. g.* at interfaces. Similarly, the double network confines the gels within a rather close packed environment, inducing them to deform when under stress. The images taken by SEM are of freeze-dried samples, meaning that a significant amount of the PAAm network has lost its elasticity, forcing the gels to remain compressed during the break formation.

Thickness dependent color

Due to time constraints, it was only possible to qualitatively assess the thickness-dependent color. PNIPAm-450 and PNIPAm-400 DNGHs were poured into dog bone molds with a thickness of 1 mm, and then cured under UV light (2 mW/cm^2). The resulting double networks changed color after curing, as observed before with PNIPAm-450 DMGH becoming

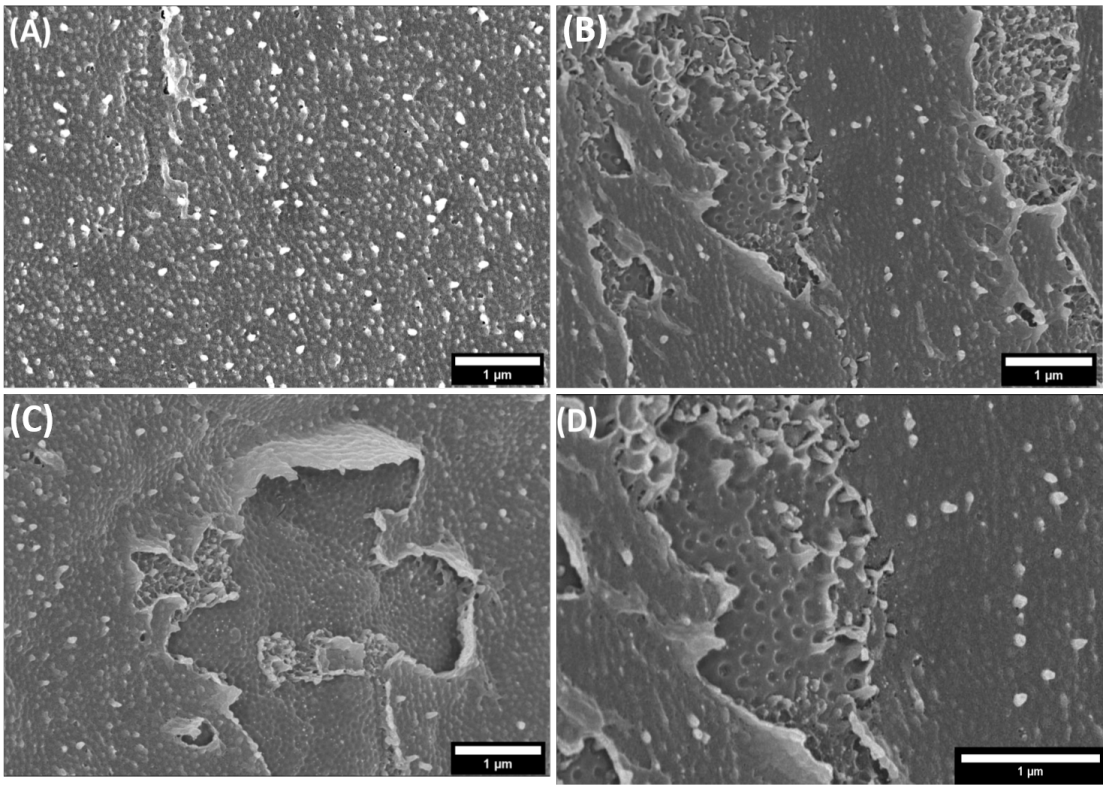

Fig. 4.7 PNIPAm-400 in 10wt/V% Aam double networks, imaged *via* SEM, as (a) close up of smooth surface, (b) and (c) overview of ripped surface and (d) close-up of ripped surface. Smooth surface was imaged on a non-ripped specimen, while the ruptured surface image was taken at the interface of a torn specimen.

white and PNIPAm-400 DNGH not showing the same vibrant green as before crosslinking. The PNIPAM-400 DNGHs dogbone only showed a blueish color in reflection against a black background (Fig 9.3 in the Appendix). Thus, the gels require a certain thickness in order to show structural color, since specimen with a diameter of 5 mm or 1 cm were colorful not only in reflection, but in transmission (Figure 4.5).

4.4 Responsiveness

4.4.1 Mechanochromic responsiveness of PNIPAm-350 DNGH

PNIPAm-350 pellet was molded into a cylindrical shape with a diameter of 5 mm. As is apparent from Figure 4.12, the obtained double network is green-ish (Figure 4.12a) in its resting state. When extending the DNGH cylinder, the material displays a blue shift (Figure 4.12b), becoming purple-transparent while under compression, its color becomes more vibrant and shifts towards green with yellow tones (Figure 4.12c). This process is fully reversible and can be performed over multiple extension/compression cycles.

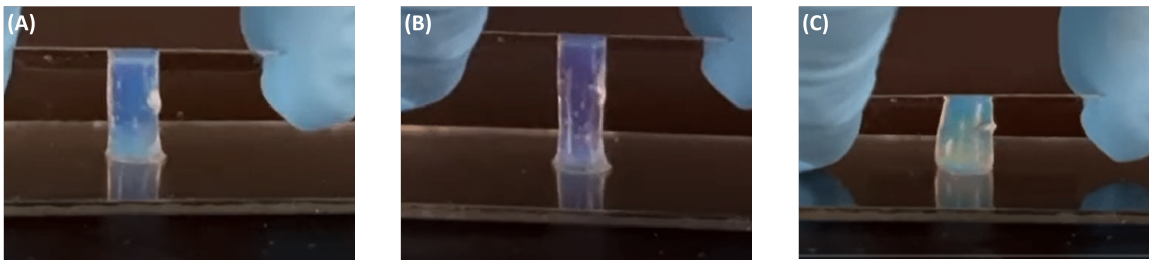

(a) Neutral position. (b) In extension. (c) In compression.

Fig. 4.8 DNGH of PNIPAm-350 in 10% wt/V of AAm in its (a) neutral position, (b) extended and (c) compressed, at RT.

In 3D photonic materials, the color depends on the interplane spacing between closely-packed crystal planes, which scatter more efficiently that the crystal spacing in the same plane. Hence, changes in color depend on the changes in interplane distances, Figure 4.9. These changes can be done through sample extension (where the plane are dragged closer) or compression (where they are distanced). The planes that are dragged closer are parallel to the axis of deformation, hence, despite the scattering points (nanoparticles or microgels) increasing their relative distance in the same plane, their distancing will not affect the color as much as their position relative to the scattering points in the adjacent, parallel, plane does. The observed color changes are consistent with this model, and can be described by equation 4.1.

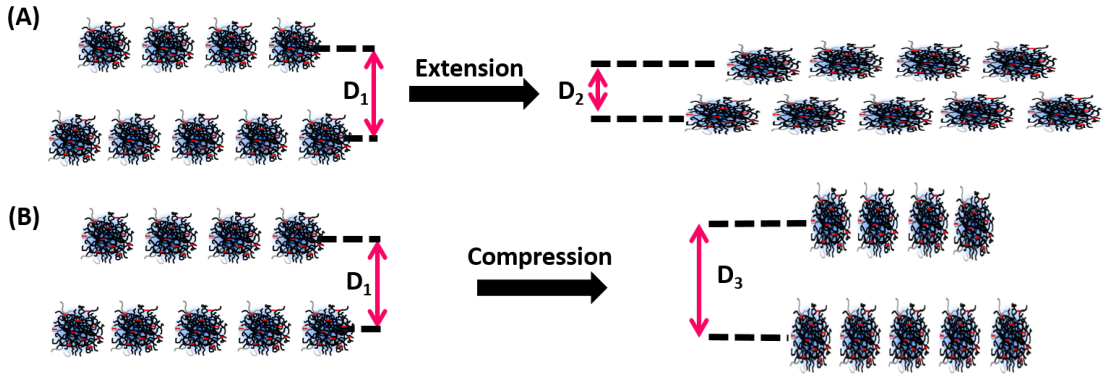

Fig. 4.9 Schematic representation of crystalline plane modification in a microgel-based photonic crystal. (a) represents the effect on the interplane spacing upon uniaxial extension and (b) upon compression. D_1 is the distance between the planes at rest, D_2 is the interplane distance during extension and D_3 during compression.The scheme is not to scale.

Upon uniaxial extension, a blue shift is observed, as the interplane distance between the microgels shrinks, and a red shift is observed, upon compression, as expected for composite materials containing hard nanoparticles.[186]. However, the positioning of the color change in the material defies expectations: there is not a homogeneous color change in the material, like in macroporous inverse opals or in hard-nanoparticle-based composites.[187][186][179] These materials are all reported as thin films, and the strain triggers a more homogeneous color change. Instead, in the sample pictured in Figures 4.12 and Figure 4.11, the color change is more evident where the material is subjected to highest strain: the middle part. This result is similar to that observed in elastomeric materials containing mechanochromic molecules, which provide information on where the strain is generated, due to the activation of the mechanochromic molecular center.[188] Hence, this material seems to have a behaviour in between a complete homogeneous color change and a more localized strain-induced color change. A possible explanation lies in the elasticity of the microgels, which are able to deform and thus reduce the effect of strain on at the periphery of the material.

Crosslinked PNIPAm-350 DNGH displays color-dependent color in reflection, depending on the angle between the incident light and the observation point. The resulting color thus depends not only on the strain in the material, but on the incident angle, and the resulting color can be determined by reflectance measurements.

The specimen analysed is composed of NIPAm-350 microgels, jammed by ultracentrifugation with 10% AAm and then polymerized into a 5 mm diameter cylinder shaped specimen, which can be measured vertically and, when tilted by 90 °, horizontally. It is worth noting that the sample measured was soaked in water overnight; this resulted in swelling and a

reduction in the intensity of the specimen's color, possibly indicating increased disorder in the sample.

The preliminary reflectance spectra displayed in Figure 4.10, were measured, with the incident light perpendicular to the sample surface, at intervals of 10 °rotation around the cylinder axis.

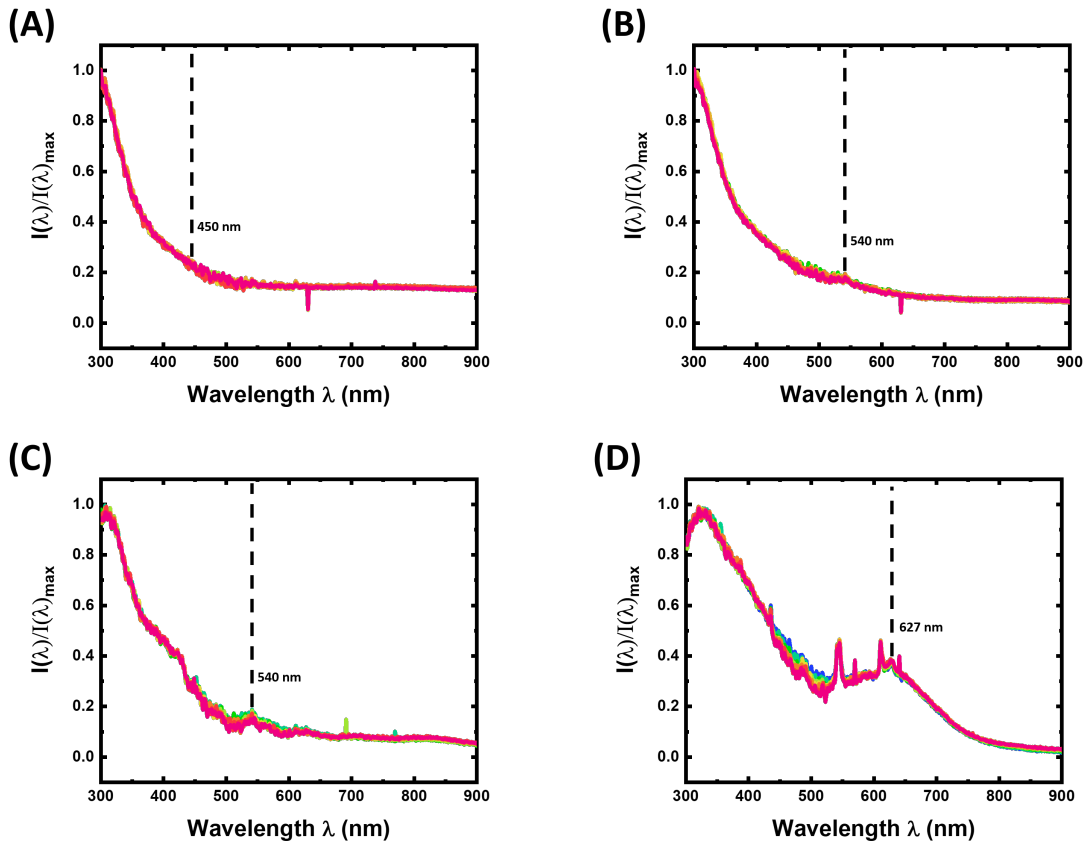

Fig. 4.10 Strain-dependent reflectance spectra of PNIPAm-350 DNGH (10% AAm), after being soaked overnight, taken at RT from a cylindrical specimen and measured with a light incidence perpendicular to the sample. Spectra (which overlap) are taken at angles (20-90 °in 10 °intervals. The size of the illuminated spot varied from ≈3 mm to ≈2 mm to increase the resolution of the spectrum. Spectra of the vertically-mounted specimen are recorded (a) at rest with an aperture of ≈3 mm,(b) with 35% compression an aperture of ≈3 mm, (c) with 43% compression and an aperture of ≈2 mm. Spectra of the horizontally measured specimen (d) was recorded.

Figure 4.10a shows the spectra of the specimen at rest , which appears blue-ish to the naked eye and provides a spectrum with a small shoulder at 460 nm, corresponding to the blue-ish perceived color. However, the signal is weak could just as well be attributed to disordered Mie scattering rather than Bragg scattering. Under compression (35% strain,

shown in Figure 4.10b), the spectrum shows a more pronounced, though still small, shoulder at 540 nm, which corresponds to green in the visible spectrum. By increasing the strain to 45% and reducing the aperture to have a smaller sample surface illuminated (and thus measured), a more distinct peak can be observed at the same wavelength (Figure 4.10c), suggesting that the strain-dependent color change is localized. The spectrometer measured the signals over the entire surface and, if multiple different wavelength are destructively reflected in different points of the sample, the spectrometer will average and cancel them out. However, faint, a green shift is detectable with compression; Figure 4.10a, b, and c are measured on a sample mounted vertically, and its surface is curved. The curvature interferes with angle- dependent measurements, as the perceived angle remains constant. By changing the positioning of the sample, from horizontal to vertical, the curvature is eliminated, as the detector now rotates around the horizontal axis, and a more distinct signal, with a peak at 627 nm (which corresponds to red) is detected. The same horizontal sample positioning was not measured in a natural state, due to a lack of time.

4.4.2 Mechanochromic responsiveness of PNIPAm-400 DNGH

PNIPAm-400 was molded in a 3 ml syringe, affording a cylindrical sample with a 1 cm diameter. Upon curing, the material changed form a vibrant green to a less intense green color (Figure 4.5d), possibly due to a diminished refractive index mismatch upon polymerization. The result of crosslinking with 10% AAm is a colored, elastic material that changes color upon compression and extension, as is apparent in Figure 4.11.

(a) Neutral position. (b) In extension. (c) In compression.

Fig. 4.11 PNIPAm-400 double network, crosslinked in 10 wt/V% of AAm and molded into 1 cm *d* cylinder, in its (a) neutral position, (b) extended and (c) compressed, at RT.

The green color observed in the resting state corresponds is the color expected based on the microgels' diameter and the colors arising from compression and extension match the trends observed for PNIPAm-350-based DNGH (Figure 4.12).

More clearly than with the previously discussed PNIPAm-350-based DNHG, the present material exhibits localized strain-induced color changes: when the cylinder is compressed, the stress accumulates in the centre of it, where the gels are compressed more easily. Compression

of the material elongates the contained microgels and increases the interlayer lattice spacing, producing a red shift. Similarly, upon elongation, a shift towards blue is seen, in the center, where the material is subjected to the highest tensile stress. Since microgels are elastic, the microgels and plane positions deform most strongly in the center of the samples and remain unchanged (as detectable by naked eye), where the strain is minor, *i. e.* near the peripheral attachment points of the specimen.

4.4.3 PNIPAm-350 DNGHs embedded in PDMS slab

PNIPAm-350 DNGH was also embedded in a PDMS matrix, in order to elucidate if the material can sense multiple-axis stress variations (*i.e* bending and twisting). Figure 4.12a depicts the DNGH slab at rest, embedded in the PDMS elastomer, showing a "resting state" blue-ish color, in accordance with the constituent microgels' diameter of 350 nm.

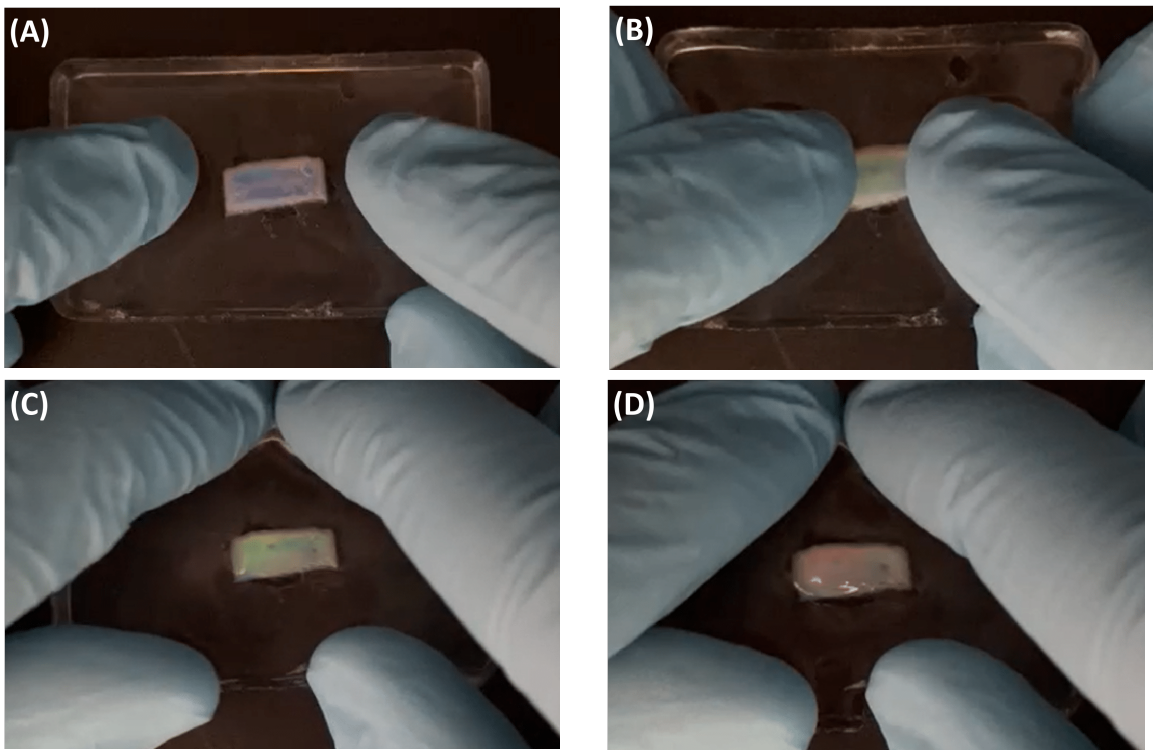

Fig. 4.12 The PNIPAm-350 double network, crosslinked in 10 wt/V% of AAm and embedded in a PDMS slab. The object is (a) in its neutral position, (b) compressed form above, (c) compressed from the sides with medium force and (d) compressed from the sides with high force, at RT.

Figure 4.13 depicts the changes in color of PNIPAm-350 DNGH as a rectangular specimen, embedded in the PDMS elastomer when the PDMS is compressed from above on

the sides, inducing and oblique strain. Depending on the compression strength, the DNGH changes color.

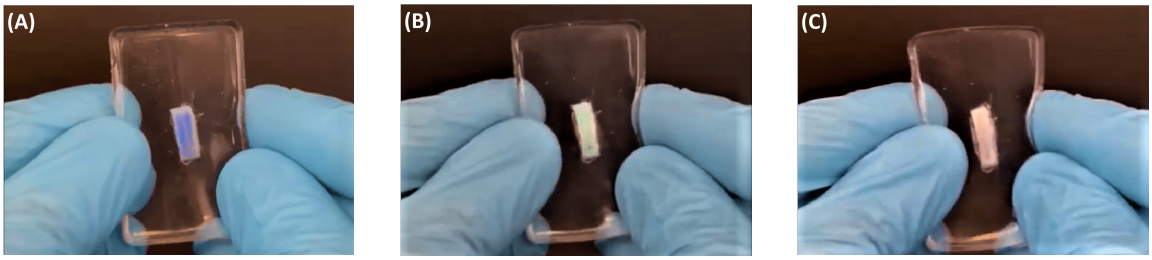

Fig. 4.13 The PNIPAm-350 DNGH, crosslinked in 10 wt/V% of AAm and molded into a PDMS slab, compressed into an oblique form from the sides by hand. (a) The DNGH in neutral position, (b) under medium compression and (c) under stronger compression.

The color is detectable and clearly visible in reflection, where the color is dependent on the angle between incidence and observation. This angle-dependent color is generally an indication of long-range crystalline order, suggesting that the microgel assemblies are tightly packed in fcc or bcc lattices; however, this should be confirmed analytically by small angle x-ray scattering (SAXS). The angle dependent color change can be exploited for anisotropic stress detection, as bending the DNGH in one direction will yield color change, whilst the exact same bending in the other direction will have a different response. The rectangular PNIPAm-3500 DNGH specimen is located on the upper side of the PDMS. Figure 4.14 shows how the DNGH is bent along with the PDMS and turns red along its horizontal axis. The bathochromic shift of the DNGH depends on the spatial constraint to which the upper microgel layer is subjected. This might induce a radial deformation of the microgel into a pancake, increasing its D_H along the x-axis, increasing the reflection pitch that the incident white light encounters at that angle,consequently resulting in the reflection of red instead of blue light.

The response is immediate and highly dependent on the compression/light incidence angle.

Mechanosensors generally switch between two states, or need additional stimuli to undergo finer changes in color. By contrast, P(NIPAm-*co*-MAAc) PAAm DNGHs gradually shift from blue to red, reversibly and over multiple cycles. For other 3D strain sensitive materials, the expansion of the material and consequent color change is generally irreversible or requires several cycles of swelling and shrinking to recover the resting state. Moreover, these materials are not compression sensitive, limiting their applications to stretch related stresses. Instead, PNIPAm microgel-based DNGH can be used as a sensor that can detect the real-time direction of bend depending on which face of the slab one is looking at,

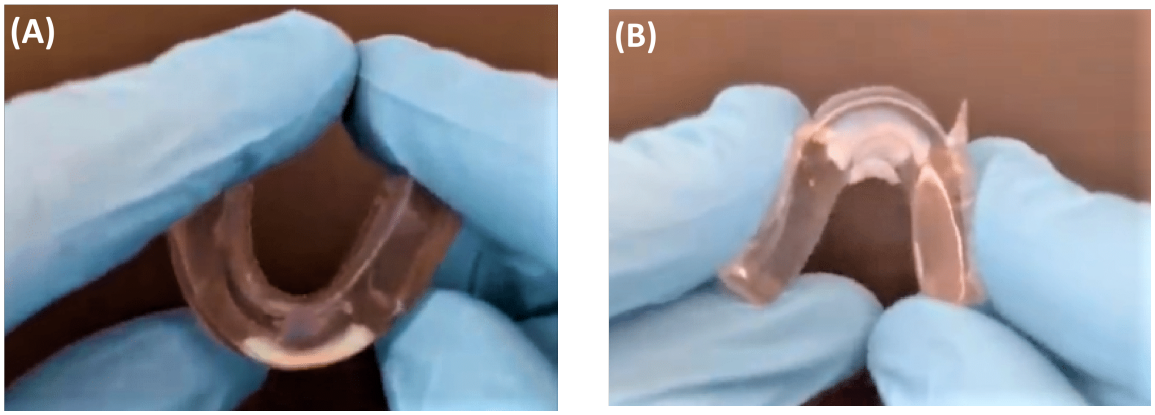

Fig. 4.14 The PNIPAm-350 double network, crosslinked in 10 wt/V% of AAm and embedded in a PDMS slab. The object is (a) bent up, (b) bent down at RT. Pictures are taken under diffused light from a 90 °angle.

thanks to the extra-fast responsiveness and reversibility. Similarly, although again, only in extension, reversible fast color changes are only observed in rotaxane-containing polymers, however, the production of which requires significant synthetic effort. Less synthetically demanding are silica-containing polymer sheets however, they are generally only available as films.[188][179]

Temperature responsiveness of P(NIPAM-*co*-MAAc) DNGH

As previously stressed, PNIPAm is a thermoresponsive polymer, and the microgels used in this study also respond to temperature changes. Small angle neutron scattering (SANS) measurements by other groups have demonstrated that double networks of PNIPAM embedded in a non-responsive polymer matrix can still shrink with temperature increase.[189] When placing the PNIPAm-350 DNGH in hot water (T> 40 °C), there is an immediate color change. As seen in Figure 4.15, the DNGH submerged in hot water turns milky, with a bathochromic shift from blue towards green tones.

Similar to the strain-induced changes described in Section 1.4, this material changes color when placed in water at T > VPTT (32 °C). The color transition is fully reversible and can be repeated over several cycles. The color shift and turbidity increase could be attributed to the shrinkage in volume of the microgel, which induces a shift in refractive index and decrease in size of the microgel. The latter widens the interplane distance between the microgels, inducing a shift of reflected color, as observed previously upon compression of the DNGH composed of the same PNIPAm-350 microgels (Figure 4.10b). The size decrease also induces the microgel to expel water from it network and change its average refractive index (PNIPAm network + water), which will increase the refractive index mismatch with

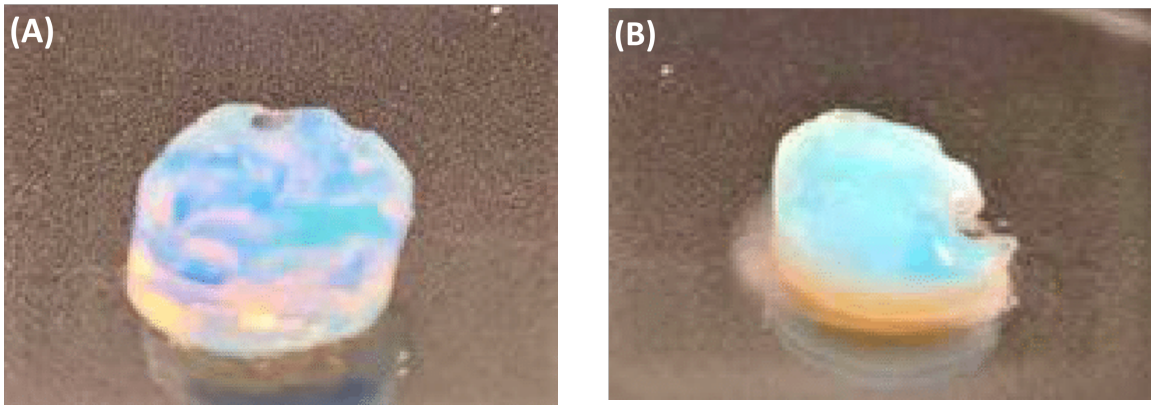

(a) PNIPAm-400 at RT

(b) PNIPAm-400 at T=60 °C

Fig. 4.15 PNIPAm-350 double network, crosslinked in 10% wt/V of AAm. The object is (a) kept at RT, (b) submerged in a t= 60 °C water bath. Pictures are taken under diffused light from a 90 °angle.

the hydrated PAAm network. This thermochromic effect seems to be limited to a dual color change, from blue to green-ish (Figure 4.15), as the volume transition is also limited to two states: swollen and collapsed.

4.5 Conclusions and outlook

In this chapter, a simple, yet effective method to form a 3D anisotropic strain- and temperature-responsive material is presented. The material presented is composed of thermo- and pH-responsive P(NIPAm-*co*-MAAc) microgels, jammed by ultracentrifugation into a crystalline-packed assembly and then covalently cross-linked by an interpenetrating double network composed of PAAm to form PNIPAm-based DNGHs.

First, the synthesis and full characterization of P(NIPAm-*co*-MAAc) microgels was described, alongside their behavior in acrylamide (AAm). The synthesis of these gels is scalable, high yielding and easily reproducible, preventing issues with batch variance. Second, the formation of the granular double networks was described, consisting simply of soaking the gels in AAm solution, centrifuging and subsequently crosslinking under a low intensity UV light. Third, the responsiveness of the resulting DNGHs was investigated. The DNGHs undergo changes in color dependent on the magnitude and direction of the applied mechanical strain. The same material also changes reflected color depending on the environmental temperature.

Due to time constraints, a complete characterization of these materials and their properties has not been possible. The following outlines possible future studies that will enable a more quantitative and analytical understanding of the mechanoresponsive DNHGs:

- **Curing conditions:** Section 4.3.1 described the use of two UV lamps with different intensities, yielding, in one case, colorful material (2 mW/cm^2), and, in the other case white samples (60 mW/cm^2). A systematic study of the curing times, irradiation intensities (under constant temperature), and the resulting color should be performed, to further improve color retention and gain insights into and standardize the curing process.

- **Crystalline packing:** Small Angle X-ray scattering would be suitable to determine which kind of order and packing is present within the DNGH. Detailed analysis of peak shapes would provide additional information about the degree of crystallinity and the size of ordered domains within the bulk material, supporting the qualitative information that can be inferred from optical observations with data.

- **Mechanical properties:** The mechanical properties of the DNGHs should be investigated by tensile strength and compression testings, to determine the toughness and elasticity of the DNGHs.

- **Reflectance spectroscopy:** Although color changes are visible by eye, it is necessary to determine precisely which wavelengths are reflected by the DNGH. Reflectance spectroscopy studies should be performed on both uncrosslinked and crosslinked samples, to observe whether there is a shift in the reflected light upon crosslinking. Moreover, more in-depth strain-dependent reflectance measurements should be performed, to quantitatively relate the strain-induced color changes. Similarly, the thermoresponsiveness of the DNGHs should be studied.

- **Stimuli responsiveness:** The microgels presented in this chapter are also pH- and metal cation-responsive, and thus the characterization of their behaviour towards such stimuli should be investigated.

Mechanochromic materials that are used as strain sensors are typically limited to colloidal films, which rely on a solid support and report strain mainly in two dimensions. This chapter presents a straightforward method of producing 3D objects that are mechano- and thermochromic and could be used as strain sensors due to their capacity to sense compression, strain directionality, and strain in three dimensions. In this chapter, these materials are produced in molds, which has its limitations in terms of resolution and shape choice. To overcome this

issue, the material could be 3D printed to produce anisotropic strain and temperature sensors. The following chapter (Chapter 5) will discuss just that possibility, attempting to 3D print DNGHs related to the ones presented in this chapter.

Chapter 5

3D printing of smart microgels

This chapter describes the formulation of inks based on sub-micrometer microgels for additive manufacturing to obtain smart mechanochromic and thermochromic objects. Starting with the choice of microgels, brief descriptions of their syntheses and characterization, this chapter will then focus on the formulation methods applied to obtain useful inks for the 3D printing of microgel-based double network granular hydrogels (DNGHs) that display strain-dependent structural color. For each formulation method, this chapter presents the outcomes of the ink printing and its subsequent crosslinking. Finally, the responsivity of a set of 3D printed and molded DNGHs is presented. This chapter consists of unpublished (at the date of submission), recently obtained results and some experiments are still pending. The project has been performed in collaboration with Matteo Hirsch from the SMaL Lab (EPFL, Esther Amstad Group). Matteo contributed ideas on the formulation and application of the microgels and performed the 3D printing and part of the mechanical characterizations. Daniel Messmer contributed ideas, suggestions and discussions.

This chapter consists of unpublished, recently obtained results (as of the date of publication), and some experiments are still pending. The project has been performed in collaboration with Matteo Hirsch, from the SMaL Lab (EPFL, Esther Amstad Group). Matteo Hirsch contributed ideas on the formulation and application of the microgels, performed the 3D printing and part of the mechanical characterizations. Daniel Messmer contributed ideas, suggestions and discussions.

5.1 Introduction

One elegant way to produce 3D objects with high resolution for rapid prototyping is additive manufacturing (also known as 3D printing).[190] There are several ways to 3D print an object and the technique varies depending on the material used and the desired resolution. In the case of polymers used for sensors and soft robotics, the target resolution typically lies between 1 mm and 1 μm. The main techniques that can achieve such resolution levels are:

- **Direct ink writing:** The ink is directly extruded from a nozzle onto a substrate at controlled flow rates, and cured after deposition. Curing can occur by solvent evaporation, cooling, or polymerization.[191]
- **Inkjet printing:** Picoliter droplets of liquid ink are sprayed onto a substrate, generally directed by a piezoelectric transducer. After curing, objects with μm resolution are obtained.[192]
- **Two-photon polymerization:** A photocurable resin is targeted with a light source that will trigger photocrosslinking. The material polymerizes with high accuracy and resolution, as it requires a high-intensity, focused laser at wavelengths where the absorption of two photons is required to initiate the polymerization.[193]

There are many more 3D printing techniques, all of which are described in detail elsewhere.[194] *Direct ink writing* and *inkjet printing* are the most important techniques for this chapter, with an eye on two-photon polymerization for future applications. Arguably, the most commonly used and efficient way of constructing 3D hydrogels is direct ink writing as it only requires an ink and a target and the printed object is ready to use after curing with no additional clean-up steps required.[194] Despite the accessibility of direct ink writing and the wide range of materials that it can process, is heavily dependent on the mechanical properties of the ink used.[195]

Inks suited for 3D printing, regardless of the precise technique, should be viscous enough to not flow significantly while at rest, and they should have almost instant shear recovery, going from liquid during extrusion to solid in the moment they reach the target.[195] Recently, Hirsch *et al.* developed a formulation of granular double networks, comprising jammed, μm-sized polydisperse poly(acrylamido-2-methylpropane sulfonic acid) (PAMPS) microgels. These microgels were soaked in acrlyamide (AAm) and formed tough double network granular hydrogels (DNGHs) after photocuring.[30] However, the size and dispersity of the microgel particles led to opacity and the DNGHs appeared white.[30] To expand the functionality of such DNGHs in the direction of mechanochromic and thermochromic sensors, the microgels constituting the DN need to be modified. For instance, to generate structural

color, the microgels need to be monodisperse and in sizes ranging from 200 to 500 nm, as explained in Chapter 4. Sizing down the microgels to the nm range to match visible light wavelengths and reducing the dispersity to obtain crystalline structures causes viscosity problems. The volume fraction ϕ of a colloid is the volume occupied by the particles relative to the total available volume, and for a hard sphere, it can reach a maximum value of 0.74 (Equation 5.1).[185]

$$\phi = \frac{N_p V_p}{V} \tag{5.1}$$

Where N_p is the number of particles, V_p the volume occupied by one particle and V the total available volume. Microgels, which are soft and compressible, can pack at ϕ>0.74, and are thus described by an effective volume fraction (ζ) (Equation 5.2).[104][105]

$$\zeta = N_p \cdot V_p \tag{5.2}$$

where V_p is the volume of the non-deformed particle. Microgels, whose volume fraction depends on their chemistry and crosslinking density,[20] crystallize in body-centered-cubic (bcc) and face-centered-cubic (fcc) lattices at ζ>0.54, producing vibrantly opalescent structures.[103] Below the volume fraction at which crystallization occurs (ϕ<0.64,ζ<0.54) the system exists as a mixed crystalline and fluid phase, and at ζ<0.49 the microgels are too diluted and Brownian motion leads to milky dispersions which scatter light incoherently. At volume fractions above the range suited for crystallization, which varies depending on the crosslinking and chemistry of the microgels, they start interpenetrating and faceting, leading to the formation of a homogeneous solid, which is optically transparent as the refractive index variations are minimized.[196] At an intermediate range above the fluid phase and the homogeneous solid phase, which varies with the chemistry of the microgels, there is the formation of structural color.[185][105]

The main challenge in capturing the soft opals lies in their fragility. Crystalline order tends to disperse upon gentle shaking, and trying to embed the microgels in a double network also often leads to the disruption of the crystalline packing. One way to seal microgels in a crystalline packing is to decorate them with boronic acid (BAc) moieties and hold them together by a self-healing supramolecular network that interpenetrates the microgels, using a polyol polymer as a dynamic crosslinker.[197] Ma *et al.* showed that P(NIPAm-*co*-BAc) microgels could be soaked in a polyol-functional acrylate, allowed to crystallize and then exposed to UV, triggering the polymerization of a double network in which the boronic acid-polyol bonds reversibly form and break providing the material with self-healing behaviour. However, although printable, these systems can not be cured, severely limiting

their applicability. Hence, there is a need to produce easy-to-make, readily functionalizable microgels that are suitable for the 3D printing of structural colors. Moreover, since microgels can also be designed to be stimuli responsive, they could be leveraged to construct sensors responsive to a range of stimuli, changing color depending on the input that is given. Based on the results shown in Chapter 4 where P(NIPAm-*co*-MAAc) microgels were used to construct mechano- and thermochromic objects, this chapter expands on the concepts introduced there, applying them to crystalline double networks in additive manufacturing, to produce colorful, responsive DNGHs that can be shaped directly by 3D printing, affording the desired geometries without further processing. This approach could be used to build anisotropic sensors for mechanical strain that selectively change color depending on the deformation axis. To that end, a library of stimuli-responsive microgels in sizes ranging from 200 to 600 nm was prepared with varying chemical properties and responsiveness, to find ink formulations that retain their structural coloration. Different jamming and printing methods are presented, as well as the results of molding and embedding the microgel inks. In the end, a simple yet effective method to produce 3D-printed, microgel- based, mechanochromic sensors is presented.

5.2 Microgel library choice

Microgels with different chemical functionalities and sizes were chosen to present a library of microgels to be used in the ink formulation.

The first microgels chosen were **PVCL** and **P(VCL-*co*-IA)** microgels, which have been described extensively in chapters 2 and 3. These microgels were a natural first choice for ink bases, due to their i) responsivity to temperature change provided by the VCL moieties, ii) responsivity to pH and metal cations provided by the COOH groups from the partially hydrolyzed dimethylitaconate, and iii) softness, which could facilitate jamming. When compared to polydisperse PAMPS microgels produced by emulsion polymerization by Hirsch *et al.*, these microgels are smaller and more monodisperse, which should affect both the optical and mechanical properties of the 3D printed objects. The microgels were purified via dialysis, and stored as dispersions in water.

To expand the functionality of neutral PVCL-based microgels, this chapter describes the synthesis of **P(VCL-*co*-GMA)** microgels, which can offer opportunities for post-printing functionalization.

P(NIPAm-*co*-MAAc) microgels are also thermoresponsive due to the PNIPAm component and pH- and ion-responsive thanks to the COOH groups present in their network. Unlike PVCL-based microgels, they can be stored as solids, and redispersed easily even at high concentrations. P(NIPAm-*co*-MAAc) microgels were purified by consecutive cycles of centrifugation and redispersion in MilliQ water, since they are able to redisperse without significant aggregation. More so than dialysis, centrifugation also ensures the removal of smaller microgels, further lowering the polydispersity index (PDI) of the samples. The synthesis and characterization of these microgels has been already described in Chapter 4.

Lastly, a set of poly(*N*-isopropylacrylamide-*co*-allylamine) **P(NIPAm-*co*-AlAm)** microgels were chosen for two main reasons: The first was to provide a thermo- and pH- responsive microgel to compare with P(NIPAm-*co*-MAAc) microgels. Second, they were chosen to form supramolecular microgels by means of dynamic covalent bonds, in an attempt to include a dynamic biocompatible network as a secondary network to increase the microgels' printability and applicability in regenerative medicine.[198] The primary amine groups of these microgels were envisaged to bond with an oxidized alginate, producing aldehyde groups and, forming dynamic bonds by the reversible formation of imine bonds.

In general, the chemical composition of each microgel was chosen to promote non-covalent interactions, that might play a favourable role in the formation of stronger colloidal gels at high volume fractions. The neutral PVCL microgels were chosen as a control against the charged COOH-containing microgels. The presence of carboxyl groups, first more in the core (P(VCL-*co*-IA)) and then homogeneously distributed throughout the microgel's

entire volume (P(NIPAm-*co*-MAAc)) promotes intermicrogel repulsion. However, adding a supramolecular crosslinking agent, such as a divalent cation, could lead to the formation of a supramolecular colloidal gel. Microgels decorated with NH_2 moieties should instead promote hydrogen bonding, and form labile covalent bonds with a second network. Supramolecular and dynamically crosslinked gels are shear thinning, and can thus be extruded through a syringe, which is a step in additive manufacturing. This chapter aims at investigating if the colloidal gels composed of microgels are not only shear thinning and self-healing, but also if their viscosity is high enough for them to retain shape after extrusion.

Each microgel type was prepared in different sizes for two main reason: first, the size could have an effect on the jamming and as a result, the rheological properties of the ink. This is based on the observation made by Hirsch *et al.* on monodisperse micrometer-sized microgels, which did not assemble, possibly due to a missing void filling given by the homogeneous size distribution. In polydisperse microgel samples, small microgels fill the interstices between the larger ones, increasing achievable volume fractions. Using nanometer-sized microgels, where the density of the corona is lower than the density of the core (as described in chapter 2, section 2.1), could promote jamming. Second, the microgel size influences the pitch of the soft photonic crystal formed, affecting both the color and the change in color when the system is subjected to external strain.

The synthesis, characterization, and morphology of each microgel sample will be described here.

Microgel nomenclature

To help the reader, the following list outlines the microgel nomenclature employed in this chapter. Naming is based on the microgels' monomer composition first and on their size second.

- **PVCL microgels** VCL-D_H (nm) (*e.g* VCL-300)
- **P(VCL-*co*-IA) microgels** VCL-IA-mol%IA-D_H (nm) (*e.g* VCL-IA-15-500)
- **P(VCL-*co*-GMA) microgels** VCL-GMA-D_H (nm) (*e.g* VCL-GMA-300)
- **P(NIPAm-*co*-MAAc) microgels** NIPAm-D_H (nm) (*e.g* NIPAm-400)
- **P(NIPAm-*co*-AlAm) microgels** NIPAm-AlAm-D_H (nm) (*e.g* NIPAm-AlAm-400)

5.3 Microgel synthesis and size characterization

5.3.1 PVCL Microgels

PVCL microgels were obtained *via* precipitation polymerization, where the monomer and crosslinker content was kept constant, and only the amount of CTAB was varied, to obtain microgels in different sizes. Purification by dialysis then resulted in homogeneous samples of microgels in sizes from 333 to 600 nm (see table 5.1 in section 1.3), as measured by DLS in MilliQ water. The microgels were stored as dispersions in water. Although lyophilization is generally preferred as a storage method for microgels such as PNIPAm as it prevents the hydrolysis of the ester or amide bonds present in the network, this is not the case for PVCL microgels. In fact, once freeze dried, PVCL microgels redisperse in aqueous solvents only in very dilute conditions, under constant stirring and over extended periods of time. This might be acceptable for analytical purposes, but prevents the direct redispersion at high concentrations, which is of great interest in the context of bulk materials preparation.

Table 5.1 Homopolymeric PVCL microgels of varying size. Each sample is listed with the code that is used throughout this chapter.

VCL mol%	D_H (nm) RT in H_2O	D_H (nm) 50 °C in H_2O	D_H (nm) RT in AAm	D_H (nm) 50 °C in AAm
VCL-333	333 ± 10	420 ± 28	500 ± 25	200 ± 14
VCL-450	450 ± 17	580 ± 40	578 ± 50	250 ± 19
VCL-600	588 ± 30	650 ± 50	642 ± 66	301 ± 3

The D_H of the microgels was also measured in a 10% wt/V AAm aqueous solution, to determine the swollen D_H in the DN precursor solution. As the microgels will be compressed in a pellet and will thus shrink due to physical constraints (ζ>1), the microgel D_H is likely smaller than the one in AAm, which is set as the upper limit.

5.3.2 P(VCL-*co*-IA) Microgels

P(VCL-*co*-IA) microgels from direct copolymerization

P(VCL-*co*-IA) microgels were obtained *via* the direct copolymerization of VCL with itaconic acid to observe if the change in approach to the previous P(VCL-*co*-IA) microgels would have an effect on their packing and responsivity. These microgels were purified by centrifugation, upon which they assembled into white pellets, with and iridescent layer, only visible at the interface between the bulk of the pellet and the centrifuge tube's wall. The microgels obtained

by this route are relatively large ($D_H \approx 800$ nm, Table 5.2), which is possibly the reason why these microgels turn opaque when compressed even though they are monodisperse. Similarly, VCL-600 (D_H= 588 ± 30 nm in H_2O at RT, see Table 5.1), yielded white pellets when centrifuged. The pellets' absence of visible colour made them less desirable for the present target applications, since opaque pellets, have been previously studied. Consequently, P(VCL-co-IA) microgels were not investigated beyond the characterization reported in table 5.2.

Table 5.2 P(VCL-*co*-IA) microgels obtained from direct copolymerization of VCL and IA, with varying size and constant monomer composition.

Sample code	IA mol%	D_H in H_2O (nm)
VCL-IA-680	10 mol%	680 ± 30
VCL-IA-730	10 mol%	730 ± 62
VCL-IA-800	10 mol%	800 ± 53

P(VCL-*co*-IA) microgels from P(VCL-*co*-IADME) hydrolysis

P(VCL-*co*-IA) microgels were obtained from the hydrolysis of previously synthesized P(VCL-*co*-IADME) microgels. Their synthesis and characterization are described extensively in section 2.2.2 in Chapter 2. These microgels were varied in monomer composition and size, to determine if either could have an effect on the printability and colour of ink formulations. pH titration provided an estimate of the COOH mol% of the network. In table 5.3, the compositions and sizes of all microgels are listed:

Table 5.3 P(VCL-*co*-IA) microgels, with varying size and composition. Each sample is listed with the code that is used throughout this chapter.

Sample code	IA mol%	D_H (nm) RT, in H_2O	D_H (nm) 50 °C, in H_2O	D_H (nm) RT, in AAm	D_H (nm) 50 °C, in AAm
IA-5%-450	5 mol%	450 ± 35	280 ± 23	508 ± 51	345 ± 40
IA-5%-560		560 ± 24	430 ± 32	665 ± 10	536 ± 25
IA-10%-460	10 mol%	466 ± 10	290 ± 17 550 ± 37	427 ± 20	
VCL-IA-15-460	15 mol%	460 ±			
VCL-IA-15-490		490 ±	399 ± 50	557 ± 32	399 ± 52
VCL-IA-15-500		488 ± 21	253 ± 13	507 ± 14	350 ± 24
VCL-IA-15-550		527 ± 67	270 ± 24	556 ±38	426 ± 20
VCL-IA-15-650		600 ± 20	312 ± 23	637 ± 56	195 ± 20

To estimate the size before curing, they were also measured in AAm (10% wt/V). The microgels swell to higher D_H at RT in AAm than they do in water. Above the VPTT (T ≈32 °C) at 50 °C, they also shrink less than in water.

5.3.3 P(VCL-*co*-GMA) Microgels

In this case, VCL and gylcidyl methacrylate (GMA, 6.5 mol%) were copolymerized into microgels by dispersion polymerization. These microgels contain pendant glycidyl groups, which can be used as functionalization sites by reacting with a nucleophile. Only one batch of these microgels was produced and purified by dialysis, and its D_H values in MilliQ water and in 10% wt/V AAm at RT and 50 °C are listed in table 5.4. When the microgels were centrifuged, a blue-colored pellet formed, indicating that they could be good candidates for 3D printing (Figure 5.5).

Table 5.4 D_H of P(VCL-*co*-GMA) microgels measured in water and AAm (10% wt/V in water) measured at RT and neutral pH.

Sample code	GMA mol%	D_H (nm) RT in H_2O	D_H (nm) 50 °C in H_2O	D_H (nm) RT in AAm	D_H (nm) 50 °C in AAm
GMA-350	6.5 mol%	350 ± 12	200 ± 4	398 ± 18	230 ± 8

5.3.4 P(NIPAm-*co*-AlAm) Microgels

P(NIPAm-*co*-AlAm) microgels were synthesized to provide microgels decorated with amine groups that can be further functionalized after polymerization. Previous studies demonstrated that allylamine (AlAm) can be easily incorporated into a PNIPAm network.[61] Thus, microgels were obtained by precipitation polymerization, by copolymerizing NIPAm with 10 mol% AlAm. The microgels were purified *via* dialysis against MilliQ water, and lyophlized for storage and redispersion. Allylamine gives the microgel dispersion an off-white/ pinkish color, that is not dependent on scattering but the chemical composition of the microgels. Once dried, the microgels turn white. In table 5.5, the sizes of the microgels measured by DLS in water at neutral pH and AAm are listed both at RT and at 50 °C.

Their chemical composition was assessed qualitatively by IR spectroscopy, and their responsiveness towards temperature in water and AAm was measured (Table 5.5). The microgels swell in AAm, yet retain their thermoresponsiveness, shrinking significantly at T > VPTT. As already observed in section 4.2.1, the microgels in AAm display a less dramatic temperature-induced collapse, due to the presence of AAm.

Table 5.5 Microgels size measured for each P(NIPAm-*co*-AlAm) microgel, measured in MilliQ water at neutral pH, and in 10% wt/V of AAm.

Microgel code	D_H in H_2O (nm)		D_H in 10% wt/V AAm (nm)	
	T= 20 °C	T= 50 °C	T= 20 °C	T= 50 °C
NIPAm-AlAm-300	297 ± 38	100 ± 12	387 ± 25	167 ± 8
NIPAm-AlAm-400	390 ± 50	146 ± 23	495 ± 76	206 ± 30
NIPAm-AlAm-600	580 ± 100	321 ± 11	651 ± 80	428 ± 30

5.4 Microgel jamming and 3D-printing

5.4.1 Centrifuging pure microgels

Networks composed of jammed microgels are typically composed of polydisperse, micrometer-sized microgels.[30] Their larger mass and higher density facilitates their centrifugation, and their size dispersity promotes filling the voids between larger microgels by the smaller ones. For this reason, polydisperse micrometer-sized microgels make excellent inks for direct ink writing, as they do not flow once extruded from the printing nozzle. In the case of smaller microgels, one key issue is their density, which is comparable to water and prevents them from sedimenting by "normal" centrifugation ($\approx$ 15k RCF). When the microgels are hydrophilic and are of submicrometer size, their density is reduced to a point where only ultracentrifugation at high RCF and for long times (>1 h) is sufficient to sediment the microgels. Hence, ultracentrifugation was used, to force the microgels into a solid pellet possibly suitable for use as an ink. All microgels were soaked overnight in an aqueous solution containing 10% wt/V AAm, 0.25 mol% crosslinker and 1 mol% photo-initiator (PI), and subsequently ultracentrifuged at 232k RCF for 2 h at RT. Once the pellet was formed, the supernatant was discarded and the walls of the tubes were tapped dry, to prevent any liquid from re-swelling and diluting the pellet. Ultracentrifugation was first attempted with the microgels swelled in the second network precursor (AAm).

PVCL and P(VCL-*co*-IA) microgels

Centrifugation of homopolymeric **PVCL microgels** was performed at 13k, 27k and 232k RCF, and only the samples centrifuged at 232k RCF formed a pellet that could be scooped out with a spatula and transferred into a Luer-lock syringe for processing. To investigate whether the size of the microgels has an impact on the rheology of the inks formed, a set of microgels of varying sizes was chosen. VCL-333 and VCL-450 were compressed into blue-ish, iridescent pellets, while VCL-600 formed a white, amorphous pellet, that was

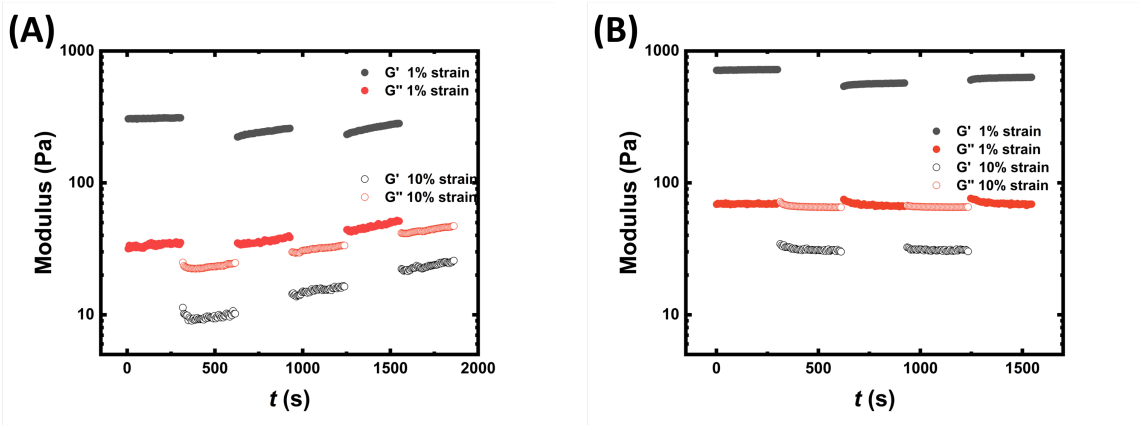

Fig. 5.1 Stress recovery tests of compressed PVCL microgels with a D_H of (a) 333 nm and (b) 450 nm soaked in 10% wt/V of AAm. G' (black) and G" (red) of the pellet at 1% oscillation strain (filled circles) and at 10% oscillation strain (hollow circles).

not characterized any further. When extruded from the printing needle (21 gauge, 15 kPa pressure), different regimes were observed, as summarized in table 5.6. VCL-333 was too liquid and displayed dripping behaviour, while VCL-450 was viscous enough to be controllably-extruded from the syringe.

Table 5.6 D_H, color, and extrusion behaviour of PVCL in H_2O containing AAm (10% wt/V) at RT, 21 gauge nozzle at RT and neutral pH.

D_H (nm)	Colour	Extrusion flow
333 ± 10	iridescent/blue	dripping
450 ± 10	iridescent/transparent	jetting
600 ± 36	white	-

To better understand this behaviour, the viscoelastic properties of these formulations were analyzed. The compressed pellets have a gel-like behaviour at low strains, with a storage modulus (G') of about 300 Pa for VCL-333 and 800 Pa for VCL-450. At high shear rates, the loss modulus (G") becomes dominant.

Shear recovery tests are self-healing tests, which consist of subjecting the pellet to consecutive changes of high (10 % strain) and low shear (1% strain), while measuring G' and G" overtime. As the change from high to low shear is immediate, it is possible to observe in which timescales the viscoelastic solid regains its "solid-like" behaviour. Despite these pellets reacting quickly to the change in shear (less than 10 s, as seen in Figure 5.1), the storage modulus and viscosity are low and for the VCL-333-based pellet, only dripping upon extrusion was observed. This might be due to the fact that the microgels do not interpenetrate

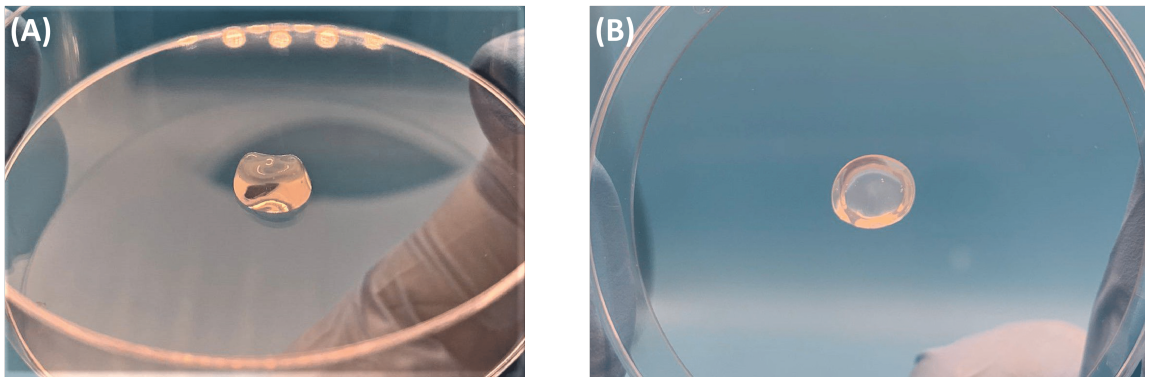

Fig. 5.2 VCL-450 double networks composed of PVCL-450 in 10% wt/V AAm, extruded with a pressure of 70 kPa and 10 mm/s printing speed. (a) view from the side and (b) from the top.

properly and dispersion forces are not sufficient to provide the jammed microgels with a more "solid-like" behaviour at rest, which is necessary in this application. Slight differences in the rheology of the microgels can be noticed when changing their size, where G' of VCL-450 rises to almost 1 kPa, compared to the 300 Pa of VCL-333, suggesting that the VCL-450 microgels jam better when compressed in a pellet, probably due to their larger size.

As the sole specimen with the desired transparency and favourable rheological properties, only VCL-450 could be printed (Figure 5.2) However, the extruded filament was not viscous enough, losing its shape on the support. This can be related to the low G' of the pellet even at low shear. Comparisons to established inks, *e.g.* PAMPS-based inks, show that there is an order of magnitude difference in G' values (*ca.* 1000 Pa *vs.* 10000 Pa).[30] Upon extrusion, the VCL-450-based ink turned into a shapeless pellet, which remained colourless upon crosslinking (Figure 5.3b).

P(VCL-*co*-IA) microgels obtained from the hydrolysis of P(VCL-*co*-IADME) microgels contain COOH groups that contribute to their hydrophilic character, and ester groups which give the network a partially hydrophobic character. These microgels were chosen in different sizes and COOH contents to understand if a certain balance between hydrophobic and hydrophilic character is beneficial for promoting better packing and higher viscosity. When compressed at RT and neutral pH, the pellets formed are optically transparent, with a blueish tinge and iridescent highlight, suggesting the formation of soft photonic crystallites (Figure 9.4 in the Appendix).

In table 5.7, the results of jamming and printing attempts are summarized.

Although some ink formulations (particularly VCL-IA-5-560, VCL-IA-15-490, and VCL-IA-15-500), seemed promising at least in terms of extrusion, none of them were 3D printable: independent of the printing speed and pressure, they would consistently flow if

Table 5.7 P(VCL-*co*-IA) microgels soaked in 10% wt/V of AAm, and 0.1 mol% PI, at a pH=7, at RT. Table displays their color after centrifugation at 282k RCF at RT for 2 h, and their behaviour when extruded from the printing nozzle.

Sample Code	D_H (nm)	Colour	Extrusion flow
VCL-IA-5%-450	450 ± 10	iridescent/transparent	dripping
VCL-IA-5%-560	560 ± 10	iridescent/transparent	jetting
VCL-IA-10%-460	466 ± 10	iridescent/transparent	dripping
VCL-IA-15%-460	460 ± 10	iridescent/transparent	jetting
VCL-IA-15%-490	490 ± 17	iridescent/transparent	jetting

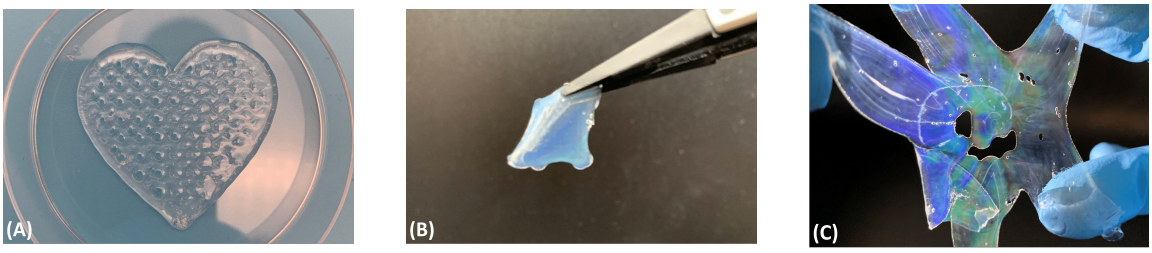

(a) VCL-IA-5-560 (b) VCL-IA-15-490 (c) VCL-IA-15-500

Fig. 5.3 single-layer printed and crosslinked (a) VCL-IA-5-560, (b) VCL-IA-15-490 and (c) VCL-IA-15-500, P(VCL*co*-IA) microgels, obtained from P(VCL-*co*-IADME) hydrolysis. The inks were obtained from 2h ultracentrifugation at 232k RCF at RT and neutral pH in 10% wt/V of AAm, extruded with a pressure of 70 kPa and a speed of 10 mm/s.

more than one layer was extruded. Evidently, the ink is of insufficient viscosity to prevent flow at the low shear applied in the printing of a second layer. P(VCL-*co*-IA) containing 5 mol% of IA could be printed as a single layer (Figure 5.3a), however, the pellet, which was iridescent in the syringe, turned into a transparent ink and remained transparent upon crosslinking (figure 5.3b). By increasing the amount of IA (and hence the contribution of charges and hydrophobic moieties), better results were obtained in terms of color, probably due to a lower ζ, which falls within the intermediate range that form structural colors. It might be that the less charged microgels are compressed significantly during curing, landing in ζ regions where the pellet has an homogeneous refractive index, while the presence of more negative charges prevents the microgels from coming too close to each other due to electrostatic repulsion. Additionally, the hydrophobic IADME moieties might contribute to an increased refractive index mismatch. VCL-IA-490 and VCL-IA-500 displayed the most promising properties when it comes to transparency and iridescence retention (Figure 5.3c and 5.3d), despite only being printable in 2D.

In Figure 5.4, shear recovery plots of the inks are shown where the pellets obtained from ultracentrifugation were subjected to consecutive cycles of low strain (1%) and high strain (10 %). In terms of the magnitude of G', forinks that could be extruded as a jet (Figure 5.4b, 5.4d, and 5.4e), it was 500 Pa and those that merely dripped from the nozzle (5.4a and 5.4c) had a G' around 200 Pa. Otherwise, all samples have a gel-like behaviour at low shear, where G'>G" in all cases. At higher strain (10%), all the pellets exhibit liquid-like behaviour (G">G').

P(VCL-*co*-GMA) microgels

P(VCL-*co*-GMA) microgels were centrifuged at 232k RCF, after being soaked in 10% wt/V of AAm overnight. The microgels formed iridescent pellets that could be scooped out from the tube and transferred into a Luer-lock syringe. In parallel, the same microgels were stained with a 0.1 wt% nigrosine solution (Figure 5.5). Nigrosine is a black dye that readily diffuses into the microgel network, thus enhancing the contrast with the medium and increasing the opacity of the system, yielding much more vibrant colors.

The pellets were extruded and printed at a printing speed of 10 mm/s over 2 layers (Figure 9.5 in the Appendix). When crosslinking the obtained slabs under UV, phase separation occurred, yielding white gels. For the nigrosine-containing microgels, patches of black appeared on the white gel. This process has not been further investigated and was set aside.

P(NIPAm-*co*-MAAc) microgels

P(NIPAm-*co*-MAAc) microgels used here have already been described in Chapter 4. These microgels were not printable by direct ink writing. Regardless of the extrusion pressure, only dripping was observed, due to the low G' and viscosity of the ink, as apparent from the rheological measurements in Figure 5.6.

A different approach was thus tried, to circumvent the dripping and poor shape retention after extrusion. One way to print low viscosity inks is to extrude them in a high viscosity matrix, which can make space for he injected ink without affecting the resulting printing pattern. Once the ink is photocured, the matrix can be washed away.

Immiscible support High viscosity PDMS was used as a printing bath, since PDMS is immiscible with water and will not take up any of the components of the microgel-containing aqueous phase. NIPAm-400 was used as test-ink. When the ink was extruded by hand into a PDMS bath, the printing pattern retained its shape and color overtime (Figure 9.9). Upon mechanical printing, with printing speeds that varied from 1 to 10 mm/s, the ink did not retain the printing pattern, phase separating into a sphere due to surface tension contributions.

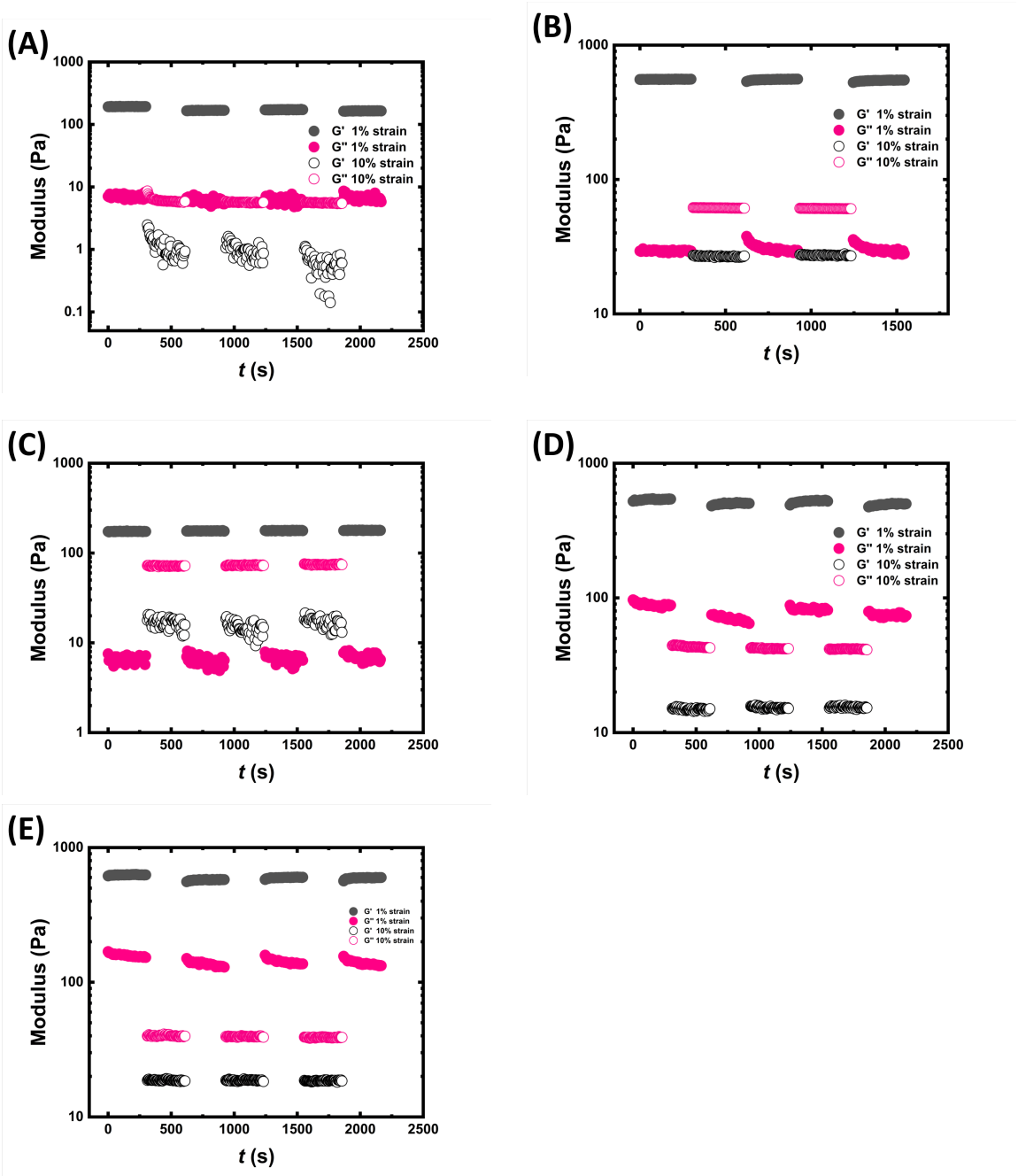

Fig. 5.4 Shear recovery tests of (a) VCL-IA-5-450 and (b) VCL-IA-5-560, (c) PVCL-IA-10-466, (d) VCL-IA-15-460, and (e) PVCL-IA-15-490 pellets taken at RT, centrifuged at 282k RCF at RT and neutral pH. G' (in black) and G" (pink) are plotted against time, at 10% strain (filled dots) and 1% strain (hollow dots).

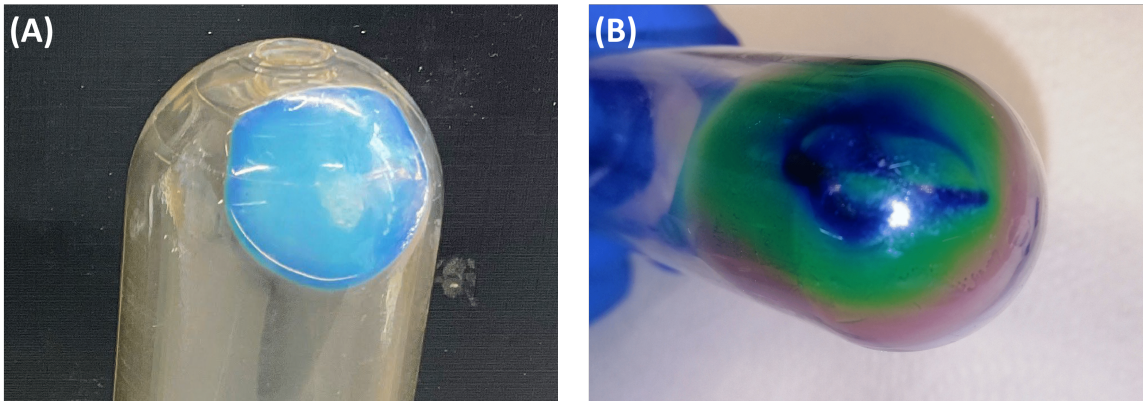

Fig. 5.5 GMA Microgels compressed by ultracentrifugation for 2 h at 232k RCF in 10% wt/V AAm. (a) VCL-GMA-350 against a black background, (b) VCL-GMA-350 stained with 0.1% nigrosine solution.

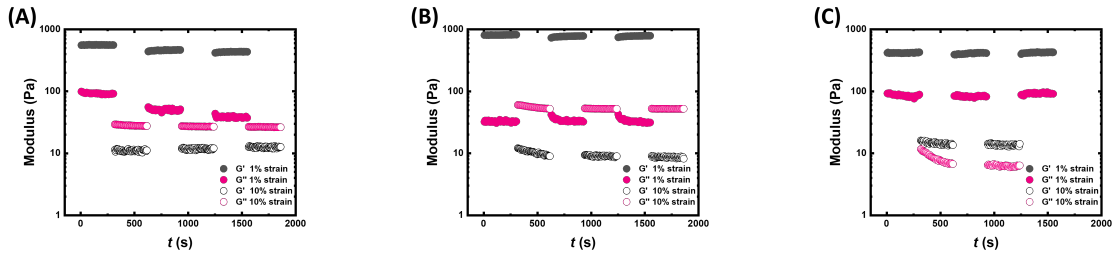

Fig. 5.6 Shear recovery tests of (a) NIPAm-350, (b) NIPAm-400, and (c) NIPAm-450, redispersed in 10% wt/V AAm solution, and centrifuged at 82k RCF for 2 h. G' (in black) and G" (pink) are plotted against time, at 10% strain (filled dots) and 1% strain (hollow dots).

This suggest that the conditions, like PDMS viscosity, operational temperature and printing speed need to be optimized.

Granular hydrogel support A cryo-milled 2 wt% PAAc granular hydrogel was rehydrated in water, and allowed to swell until reaching optical transparency. PNIPAm-400 was printed in the granular hydrogel, with a printing speed of 7 mm/s and a printing pressure of 70 kPa. The printed sample retained shape over multiple layers, indicating that the viscosity of the support gel was high enough (Figure 5.7). However, upon photocuring, the outer layer of the printed grid turned white, suggesting a change in surface ordering of the microgels. This can be attributed to the miscibility of the two phases. PAAc is swollen in water, and due to osmotic difference, will take up first AAm, leading to an osmotic change in the outer layer of the ink. This might lead to a change in swelling and a slight loosening of the compressed pellet, which in turn would lead to a disruption of the crystalline packing on the surface. One alternative might consist in swelling the support in AAm as well, to minimize the loss of AAm in the microgel phase.

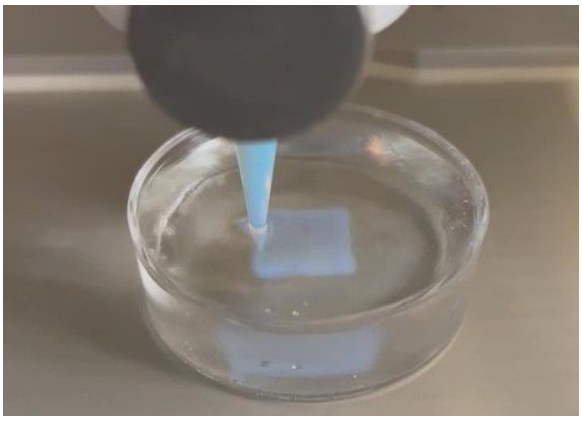

Fig. 5.7 PNIPAm-400 printed into a 2 wt% PAAc granular hydrogel, obtained from cryo-milling a macroscopic PAAc hydrogel. The grid has been printed at RT, with a printing pressure of 70 KPa and a printing speed of 7 mm/s. The PAAc granular hydrogel only contained water.

P(NIPAm-*co*-AlAm) microgels

P(NIPAm-*co*-AlAm) microgels were centrifuged for 2 h at 232k RCF after being soaked in 10% wt/V AAm. The pellets formed where grey with a pink tinge, independent of the size of the microgels used. It is possible that these microgels, despite their monodispersity, reach volume fractions that are too high to form crystalline domains. Ultracentrifugation as a method for ink preparation was thus discarded for this microgel composition.

Summary on ultracentrifugation

Jamming microgels to form gel-like pellets is possible at high RCF (282k) and prolonged centrifuging times (2h). Depending on the chemistry and size of the microgels, the pellets were characterized by significantly different mechanical properties. Of the various compositions and sizes investigated only two instances were modestly successful: inks containing P(VCL-*co*-IA) microgels with 15 mol% COOH and D_H= 500 nm were viscous enough to be printed, however only as single layer structures. Similar results were obtained for P(VCL-*co*-IA) microgels with 5 mol% COOH and D_H = 560 nm. The remaining inks studied were generally too liquid and only displayed dripping upon extrusion, and thus could not be printed. Depending on the size and chemistry of the microgels, the color of the inks varied from transparent (VCL-IA-5-560), to strongly colorful (VCL-GMA-350), to iridescent (VCL-500 or VCL-IA-15-500). Encouragingly, most microgels retained their color after crosslinking and DN formation with the exception of VCL-GMA-350, which turned white.

5.4.2 Ca^{2+} as an intermicrogel crosslinker for P(VCL-*co*-IA) microgels

P(VCL-*co*-IA) microgels can reversibly bind ions, as described in Chapters 2 and 3. One way to confine the microgels in a constrained environment whilst enhancing their interactions could be to add Ca^{2+} as a supramolecular crosslinker. This could lead to a weakly crosslinked supramolecular hydrogel, viscous enough to retain shape and sufficiently dynamic to be self-healing, so that it can be extruded from a nozzle. The microgels discussed extensively in Chapters 2 and 3 were specifically designed to not aggregate in the presence of Ca^{2+} ions, so it was necessary to include an additional spatial constraint which would drive the COOH from separated microgels to induce crosslinking. This force can be provided by centrifugation at high speed, which has already been a useful tool to jam the microgels, outlined in Section 5.4.1. The influence of Ca^{2+} on the viscosity of the pellet was investigated by varying the $CaCl_2$ concentration and centrifugation method whilst keeping the microgel type and AAm concentration constant. The microgels used are listed in table 5.7, and contained 15 mol% IA. The microgels chosen are VCL-IA-15-500 (D_H = 488 $\pm$ 21 nm), VCL-IA-15-550 (D_H = 527 $\pm$ 67 nm) and VCL-IA-15-650 (D_H= 600 $\pm$ 56 nm). The samples were prepared by soaking 1% wt/V microgels solution in 10% wt/V AAm solution, 0.25 mol% crosslinker, and 1 mol% PI. Different solutions were prepared varying the amount of free $CaCl_2$ in solution: (1, 0.05, and 0.01 M $CaCl_2$). Adding 1 M of $CaCl_2$ led to immediate, uncontrolled aggregation and thus these samples were discarded. The remaining samples (0.05 and 0.01 M $CaCl_2$) were split into two batches each, to observe how the same solution behaves in different centrifugation methods. It must be pointed out that that the ultracentrifuge allows for full temperature control, even at very high speeds. By contrast, a simple Minispin centrifuge, with which one can centrifuge up to 12k RCF, heats up during the process as it runs in air.

Low speed centrifugation: Minispin

Centrifuging the solutions containing 0.05 and 0.01 M Ca^{2+} in a minispin centrifuge led to pellet formation (60 min spinning), however, the pellets were too liquid to be processed. Increasing the Ca^{2+} concentration to 0.05 M led to the formation of an optically-transparent pellet that could be extruded from a 1 mL syringe (Figure 9.7 in the appendix). After crosslinking, the material remained transparent. The absence of color indicates the presence of a disordered solid with no refractive index mismatch between the network and the solvent. This, in turn, indicates that the microgels are jammed at a volume fraction above their crystallinity volume fraction (ζ>1). This overcrowding can be explained by the minispin centrifuge heating up during the centrifugation run. The thermoresponsive microgels shrink and deposit as a pellet (which is an opaque white right after centrifugation) at the elevated

process temperature. When the samples return to RT, the microgels swell again to their RT radius and interpenetrate due to the crowded environment, leading to the observed thick, transparent pastes (Figure 9.7 in the appendix). The scaling of this technique is challenging, as the volume yield was extremely low: 2 ml of sample (1 wt/V% microgel) would yield around a 20-50 μl pellet. For these reasons, centrifuging with a Minispin was abandoned.

High speed centrifugation: ultracentrifuge

Increasing the centrifugation speed to 232k RCF and the time to 2 h on a thermostatted ultracentrifuge yielded colorful pellets, which could be scooped out and transferred into a syringe. The addition of Ca^{2+} (5 mM $CaCl_2$) leads to a decrease in D_H of the microgels, reducing the volume of the obtained pellet.

Hence, the volume yield of this technique is suboptimal, as 30 ml of initial dispersion yield merely 200μl of pellet. With this method, each batch (150 ml) would yield ca 3 ml of sample. This is sufficient to print small test objects, but would require the combination of many batches to print cm-sized objects. Figure 5.8 shows the shear recovery test of the pellets obtained from the microgels in the presence of $CaCl_2$ (0.01 M or 0.05 M). The inks show similar values of G' and G" at the same $[Ca^{2+}]$ = 0.01 M, with G' decreasing slightly with the D_H increase, as apparent from comparing Figure 5.8a (G'= 486 Pa, VCL-IA-15-500), 5.8c (G'= 497 Pa, VCL-IA-15-550), and 5.8e (G'= 295 Pa, VCL-IA-15-650). These values are comparable to the G' measured for VCL-IA-15-460 and VCL-IA-15-500, which were ultracentrifuged without the addition of $CaCl_2$ salts, and displayed G'= 555 Pa and G'= 618 Pa respectively. An increase of $CaCl_2$ concentration to 0.05 M leads to an increase of G' for all inks, to values above 1000 Pa. Similarly, the value of G" increases, especially at high shear (10% strain), where G" increases from 40 Pa at low shear for $[Ca^{2+}] < 0.01$ M to $\approx$ 200 Pa for the inks formulated with 0.05 M $CaCl_2$. This suggests the existence for the desired interactions between the COOH groups from different microgels, promoting the bridging between microgels, and leading to an increased "solid-like" behaviour of the ink. Increasing the concentration to 0.1 M leads to a sharp decrease in both moduli (G' $\approx$ 350 Pa for VCL-IA-500 and $\approx$ 250 Pa for VCL-IA-550, Figure 9.8 in Appendix), probably due to charge screening.[199]

The pellets obtained are colorful yet transparent and look “solid like”. After transferring them into a 1 ml syringe, they could be easily extruded by hand, and retained their shape, as seen in figure 5.9.

The resulting objects are free-standing, retain their shape, and their angle-dependent structural color is retained after crosslinking.

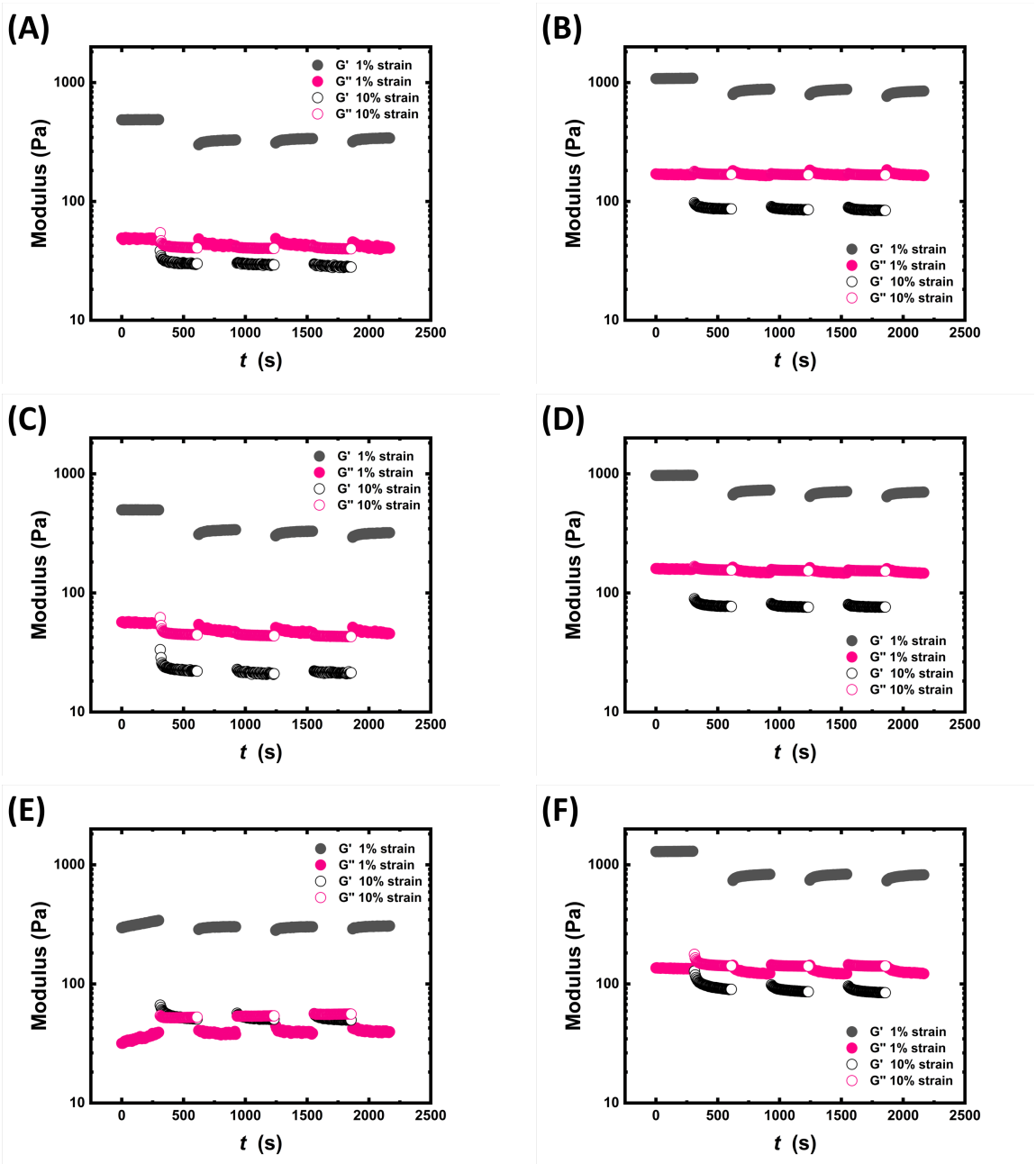

Fig. 5.8 Shear recovery plots of (a) PVCL-IA-15-500 and (c) PVCL-IA-15-550, (e) PVCL-IA-15-600 containing 0.01 M $CaCl_2$ and (b), (d), and (f) 0.05 M $CaCl_2$, from dispersions centrifuged at 282k RCF at RT and neutral pH. G' (in black) and G" (in pink) are plotted against time, at 10% strain (filled dots) and 1% strain (hollow dots).

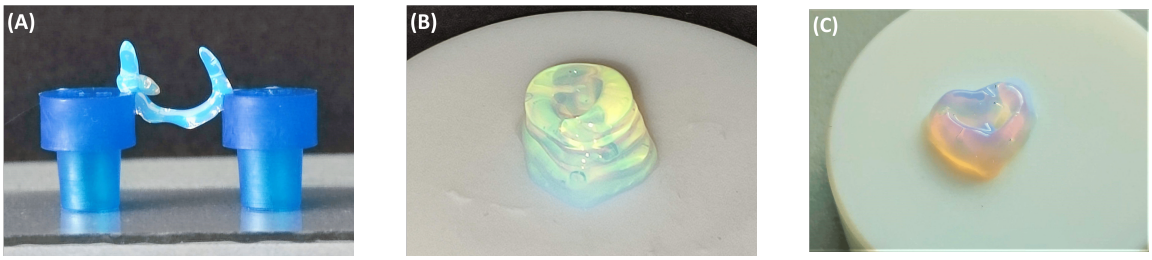

Fig. 5.9 Microgels compressed by ultracentrifugation for 2 h at 232k RCF in 10 wt/C% AAm and 0.05 M $CaCl_2$ concentration, then extruded by hand and crosslinked uner UV light. Figure (a) VCL-IA-15-500, (b) VCL-IA-15-550 and (c) VCL-IA-15-650.

Despite the rheology of these ink formulations being very promising, when the pellets were transferred into a Luer-lock syringe and processed by a 3D printer, the pellets could not be extruded, even at the highest pressure possible with that printer (140 kPa). The shear recovery tests show that G' is higher in the first run at low strain (ink at rest) than in the second run at 1 % strain. This indicates that the inks should be preruptured before printing, to disrupt the Ca^{2+} bridges between the microgels. Prerupturing the networks and trying to extrude them again at the highest pressure also did not lead to successful extrusion, as the samples was still too viscous under shear. Since a printer with a higher ultimate pressure was not available, these ink formulations were temporarily put aside, In addition to rheological issues, the necessary balance between microgel COOH and $CaCl_2$ crosslinker concentration requires further, relatively time-intensive optimization.

5.4.3 Temperature-induced aggregation

Ultracentrifuged P(NIPAm-*co*-MAAc) microgels (282k RCF for 2h at RT) form a pellet that is too liquid to be processed using direct ink writing. However, these pellets display the strongest color of the tested microgel samples (Figure 5.10) and yield the highest amount of concentrated material. Hence, an alternative way to form a processable ink was explored, exploiting these microgels' thermally-induced aggregation in the presence of Ca^{2+} ions. A publication by Zhou *et al.* elegantly demonstrated how to obtain structurally-colored PNIPAm-based microgel films exploiting their volume change at high temperature.[200] Specifically, a solution of microgels was heated up in an oven, triggering microgel aggregation. By removing the supernatant and allowing the microgels to swell at RT, the authors obtained self-assembled films with vibrant colors. Inspired by this work, P(NIPAm-*co*-MAAc) microgels, which aggregate upon temperature increase in the presence of Ca^{2+}, were dispersed in solutions with $CaCl_2$ concentrations that varied from 0.01 M to 0.5 M and

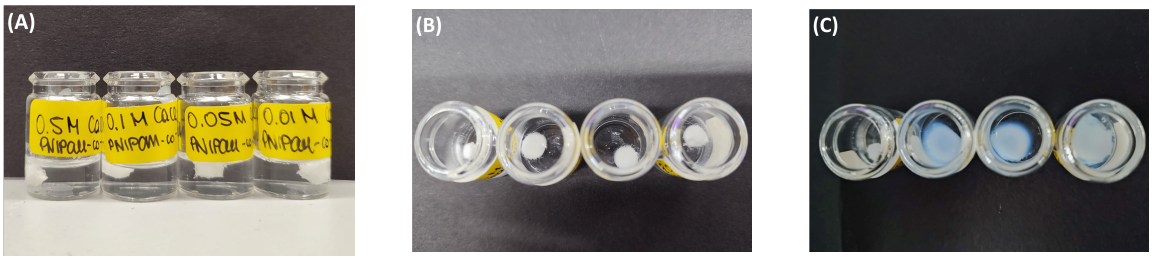

Fig. 5.10 Temperature-induced aggregation of 1% wt/V NIPAM-*co*-MAAc, with [Ca^{2+}] decreasing from left to right (0.5 M - 0.01 M);(a) side view of microgels kept at 80 °C for 1 h in the oven, (b) top view of microgels kept at 80 °C for 1 h and (c) top view of microgels 5 min after removal from the oven, when allowed to cool down to RT.

heated. The microgels assembled into white pellets in all cases, and behaved differently upon cooling down, depending on the concentration of Ca^{2+} in solution.

At the highest Ca^{2+} concentration, 0.5 M, the assembly was irreversible and the microgels remained aggregated as a white pellet. At intermediate Ca^{2+} concentrations, the pellets swelled into blue, very soft pellets which could not be collected as they disintegrated when touched with a spatula. The lowest concentration attempt (0.01 M $CaCl_2$) redispersed briefly after having reached RT. None of these approaches yielded a useful formulation, as the two intermediate samples (0.1 and 0.05 M $CaCl_2$) were too soft to be processed. Since this approach is applicable only to microgels that aggregate at high temperatures and in the presence of a metal cation which can act as crosslinker, this approach was not pursued for any other microgels and ultimately abandoned.

5.4.4 Thickener addition

Rheomodifiers are constituents of a mixture that affect the overall viscosity of the starting mixture. When using thickeners, as the word implies, the viscosity of the system increases. Important thickeners in aqueous dispersions are poly(vinyl alcohol), PEG, and carbohydrates like alginate, cellulose, and starch. Since most of the formulations described in section 1.4.1 were too liquid, this section covers attempts to increase the ink viscosity by adding thickeners to PVCL microgels (listed in section 1.4.1, table 5.6). The thickeners chosen based on their frequent use were poly(vinylalchol) (PVA), sodium alginate, high viscosity hydroxypropylcellulose (HW HPC), low viscosity hydroxypropylcellulose (HW HPC), and carboxymethyl cellulose (CMC, of M_W= 90kDa and M_W=250 kDa).

PVCL and P(VCL-*co*-IA) microgels were soaked overnight in solutions containing 1 or 2% wt/V thickener, 10% wt/V AAm, 0.25 mol% BIS to be used as a crosslinker, and 1 mol% PI. In this way, the thickener would contribute to the mechanical properties of the pellet and

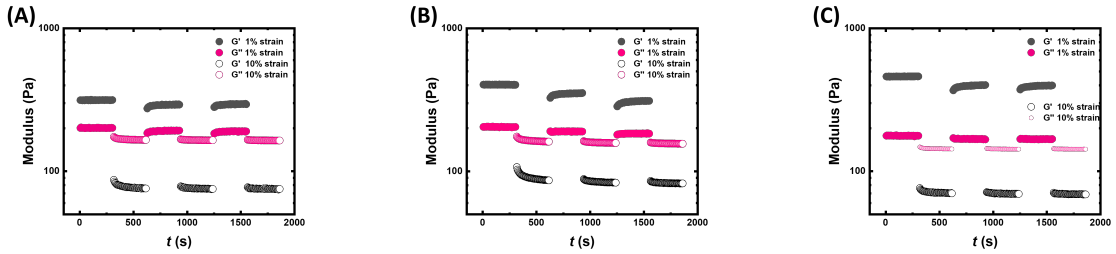

Fig. 5.11 Shear recovery tests of PVCL-based microgels redispersed in 1% wt/V CMC (M_W = 90 kDa) in MilliQ water. Microgels used for the inks are (a) VCL-333, (b) VCL-450, and (c) VCL-600. G' (in black) and G" (pink) are plotted against time, at 10% strain (filled dots) and 1% strain (hollow dots).

the AAm would covalently crosslink the pellet in a double network. The microgels were then centrifuged at 13k RCF with a mini-spin centrifuge for 20 minutes and the supernatant was discarded. Centrifugation at higher speed (232k RCF) did not yield significantly different results.

Only CMC 90K, LV HPC, and alginate at 1 wt% allowed for the successful jamming of the microgels, generating thick pastes while retaining color (VCL-450) or turning white (VCL-600). However, regardless of microgel size or thickener, the inks still appeared fairly liquid. This impression was confirmed by rheology measurements, which were measured as representative for CMC 90k. As seen in Figure 9.6, it is apparent that the determined G' value was comparable to non-formulated microgels (400 Pa), whilst G" did increase.

Although the viscosity of the system increased slightly and though extrusion led to the desired jetting rather than dripping, printed shapes did not fully retain their shape (Figure 9.6 in the Appendix). Moreover, after photocrosslinking, the obtained slabs turned from iridescent to white, indicating phase separation, as described in section 1.4.1 for GMA-containing microgels. This could be linked to the formation of a double network, due to the presence of the high molecular weight thickeners, which disrupt the packing of the microgels. Since this approach only yielded non-printable, white slabs, it was set aside.

5.4.5 Supramolecular granular networks

The major issue encountered in the previous sections is related to the viscosity of the ink formulations. In the majority of cases, the sample would flow under its own weight and not retain its shape, limiting the printing to a single layer and preventing the construction of 3D objects. To overcome this issue, as described in Section 1.4.2 the use of Ca^{2+} as intermolecular crosslinker was proposed. However, this approach yielded formulations too viscous to be extruded with the available printer. An alternative way to form supramolecular

networks is to exploit dynamic covalent bonds which can form and break swiftly, providing the microgels with shape retention and self-healing properties. One major advantage of using covalent dynamic bonds over metal-ligand interactions is increased biocompatibility and reduction of shrinking due to ion addition. This is especially true when the functional groups that participate in the dynamic bond are part of the network's main chains as they act simultaneously the crosslinkers and the main scaffold, reducing erosion by crosslinker leaching[201]. The ink should be formulated in a way that the reactive sites can bind to the microgel without hampering the microgel's assembly into a crystalline structure. Among the available dynamic bonds,[202] such as imines, thioesters, and oximes, this project relied on imine formation, where an aldehyde reacts with an amine to form an imine and water. Since the microgels are soaked in water, the equilibrium will be shifted for the starting materials, providing enough exchange of bonds for the self-healing of the network. Partially-oxidized alginate was chosen as an aldehyde-bearing cross-linker, whereas P(NIPAm-*co*-AlAm) contained the amine groups.

Oxidized alginate was prepared following a procedure optimized by Morgan *et al.* by using KIO_4.[198] The oxidation was qualitatively assessed by adding adipic dihydrazide as a crosslinker. Gelation was observed after 20 minutes in PBS (without Ca^{2+} or Mg^{2+}), but not in MilliQ water, indicating that the gel formation is closely bound to the ionic strength of the solution.

The microgels were synthesized with 10 mol% AlAm, to maximize the number of reactive groups while retaining thermoresponsivity. Three microgels were chosen (described in section 1.3.4, in table 5.5): NIPAm-AlAm-300, NIPAm-AlAm-400, and NIPAm-AlAm-600.

The double networks were formed by first redispersing microgels at 5% wt/V in a 1% wt/V alginate solution and the system was equilibrated overnight, resulting in an opaque jelly. The sample was then ultracentrifuged at 232k RCF for 20 minutes, turning to a transparent solid that could be extruded by hand with a syringe. The extruded solid, independent of the size of the microgels, could be printed with a pressure of 140 kPa and a printing speed of 10 mm/s. The resulting objects were transparent and retained their shape. The objects were then crosslinked by the addition of Ca^{2+} ions. $CaCl_2$ (0.1 M) was added to the printed object, and allowed to equilibrate for 5 min before being washed away. Depending on the microgel used, variations in the resulting transparency and turbidity of the sample were observed (Figure 5.12).

Although these dynamically alginate-crosslinked inks possess the best rheological properties for additive manufacturing among all the formulations described thus far, the constituent microgels do not seem to assemble into crystalline lattices and merely turn white/less trans-

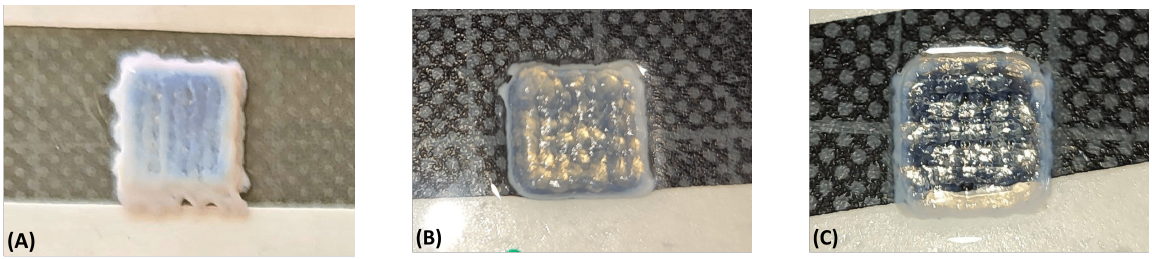

Fig. 5.12 3D-printed and crosslinked alginate networks containing P(NIPAm-*co*-AlAm) microgels. (a) PNIPAm-AlAm-350 microgels printed as a 2-layer grid with a pressure of 140 kPa and 10 mm/s printing speed, (b) PNIPAm-AlAm-250 microgels and (c) PNIPAm-AlAm-200 microgels printed as a 2-layer grid with a pressure of 70 kPa and 5 mm/s printing speed. The microgel pellets were printed at RT and neutral pH, and then crosslinked with 0.1 M $CaCl_2$.

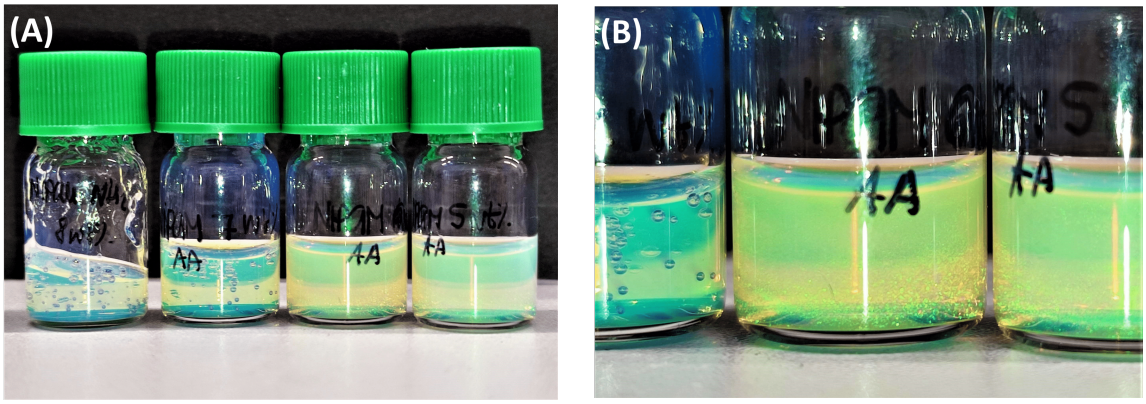

Fig. 5.13 NIPAm-AlAm-400 microgels resuspended in 10% wt/V AAm at RT, at (a) (from left to right) 10, 8, 6, and 5% wt/V microgel solutions. (b) Close-up of the 6% suspension, where the opalescent crystal can be seen, as sparkles at the bottom of the vial.

parent upon the addition of $CaCl_2$. Moreover, supramolecular, rather than covalent fixation by Ca^{2+}, makes the resulting double network more prone to erosion, when subjected to mechanical stress and washings. Hence, due to a combined lack of color and possible erosion, this approach was discarded too.

5.4.6 Microgel rehydration

The formation of bcc or fcc lattices in microgel dispersions occurs spontaneously at certain volume fractions. Microgels such as P(NIPAm-*co*-AlAm) containing 10 mol% AlAm with respect to NIPAm can be rehydrated after lyophilization and their resuspension at crystal-inducing volume fractions may lead to the formation of structural colors.

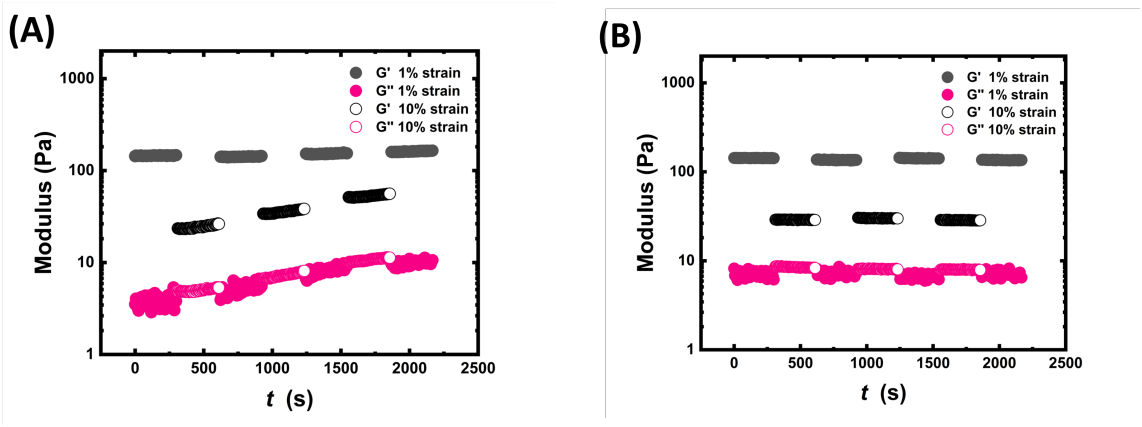

Fig. 5.14 Shear recovery tests of NIPAm-AlAm-400 microgels redispersed in 10% wt/V AAm at RT, at (a) 10% wt/V and (b) 11% wt/V in 10% wt/V AAm, at RT and neutral pH. G' (in black) and G" (pink) are plotted against time, at 10% strain (filled dots) and 1% strain (hollow dots).

The NIPAm-AlAm-400 microgels used for this study at 10% wt/V concentrations (5, 6, 7, 8, 10 and 11% wt/V in 10% of AAm, 0.25 mol% crosslinker, and 1 mol% PI), to determine which formulation would simultaneously provide color and adequate mechanical properties. The NIPAm-AlAm microgels used for this study in 10% AAm have a D_H of 495 $\pm$ 76 nm, higher than in H_2O (390 $\pm$ 50 nm) (Table 5.5). This is due to the fact that AAm penetrates the microgels' network, increasing their degree of swelling.

As shown in Figure 5.14, the microgels produce bright green suspensions at RT. At concentrations < %5 wt/V, the microgels are disorderdly dispersed in the medium, and the suspension appears milky. By increasing the solid content to between 5 and 6 wt/V%, the microgels assemble into bright green samples, and at 6 wt/V%, opalescent structures are formed, which disappear immediately after gentle shaking. The base green color, however, remains unchanged. At a microgel content > 6% wt/V, the intensity of the color decreases, while the viscosity of the sample increases, signaling the possible formation of a colloidal gel composed of interpenetrated microgels. Interpenetration leads to a higher degree of disorder and no refractive index mismatch, yielding an optically transparent solid. Shear recovery tests were performed to observe the behaviour of the more viscous gel-like dispersions, which could be extruded by hand with a syringe. Only the suspensions with a 10% and 11 % wt/V microgel concentration were extruded, as lower microgel contents yielded dispersions with viscosities similar to water.

The microgels were then crosslinked under UV light. The samples at >8% wt/V microgel content lost their green tint but retained their opalescence when light was shined through. More diluted samples became turbid and white, presumably due to the disruption of the

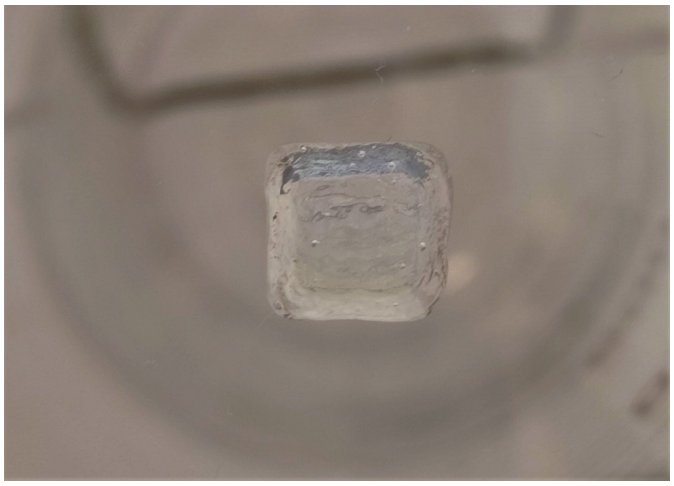

Fig. 5.15 NIPAm-AlAm-400 in 10% AAm, 3D printed into a three-layer grid. The specimen was cured under UV light and kept at RT.

lattice by the newly-formed PAAm network, which has significantly more space to expand and crosslink, in the dilute samples as compared to those at higher (>8% w/V microgel) content. The most promising samples contained 10% wt/V microgels, where the opalescence was retained and the rheology of the initial dispersion was promising for 3D printing. Thus, is was decided to proceed with such formulation.

PNIPAm-AlAm-400 was 3D printed into a three-layer grid with a 21 gauge needle, and crosslinked under UV light (Figure 5.15). Due to its softness, indicated by the low G'= 145 Pa, the ink flows a little under its own weight, producing a specimen which maintains its approximate, original shape but which is smeared on the sides. Depending on the light incidence, the sample shows an iridescent tint, which is only visible under direct light (Figure 9.10 in the Appendix).

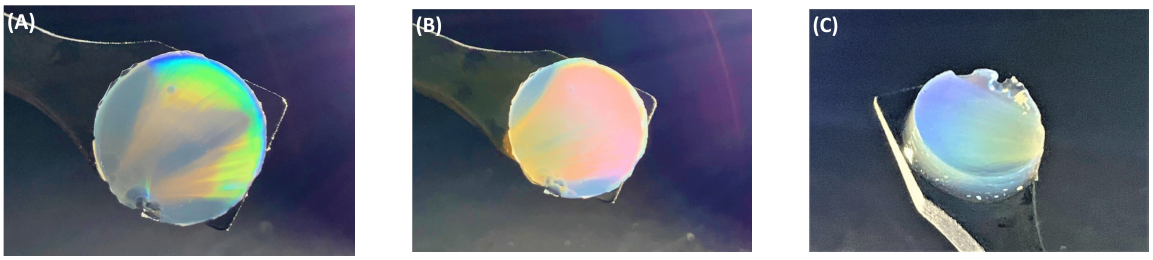

Fig. 5.16 VCL-IA-15-460 microgels crosslinked in 10 wt/V% AAm under UV light, at RT and neutral pH. The sample was prepared by ultracentrifugation and molding into a cylindrical specimen. Images are taken when the angle between incident light and observation is at approximately (a) 30 °, (b) 90 °and (c) 120 °.

5.5 Thermoresponsiveness of smart granular double networks

5.5.1 P(VCL-*co*-IA) Microgels in AAm

P(VCL-*co*-IA) microgel-based inks obtained by ultracentrifugation (in particular, VCL-IA-15-460, see Table 5.3 and Sections 1.3.2 and 1.4.1) were molded into 1 cm diameter cylindrical specimen, and crosslinked under weak UV light. This was the only iridescent specimen obtained, and the remaining samples, shown in Figure 1.3 were not investigated further. The crosslinked cylinder shown in Figure 5.16, displays colors depending on the angle between incident light and the observation point. Such angle-dependent coloration is generally due to long-range crystalline order.

The specimen was then placed in water at 60 °C, to observe if there is temperature-dependent color change, as already observed in Section 1.4 in Chapter 4. Figure 5.17a and 5.17b show the cylinder at RT with from two slightly different angles between the light source and the observer. The cylinder appears blue/green, and once placed in water, no noticeable difference in turbidity is observed, yet a slight color change is detectable by eye. However, in the absence of rigorous characterization by measuring angle- and temperature-dependent reflectometry, it is difficult to say whether the material possesses a significant thermal response.

By contrast, printing the same ink into a two-layer, 1 cm x 1 cm grid yields more noticeable results: the printed object, containing 10% wt/V AAm, was again crosslinked under weak UV light. Figure 5.18 clearly shows that there is a turbidity change in the material, turning from blue/transparent to milky with blue tones. This change in turbidity is fully reversible.

Fig. 5.17 VCL-IA-15-460 microgels crosslinked in 10% wt/V AAm under UV light, at RT and neutral pH. The sample was prepared by ultracentrifugation and molding into a cylindrical specimem. Images are taken when the incident light is at approximately (a) 30 °, (b) 90 °, where and the sample is at RT, and (c) 30 °incidence after having been placed in a 60 °C water bath.

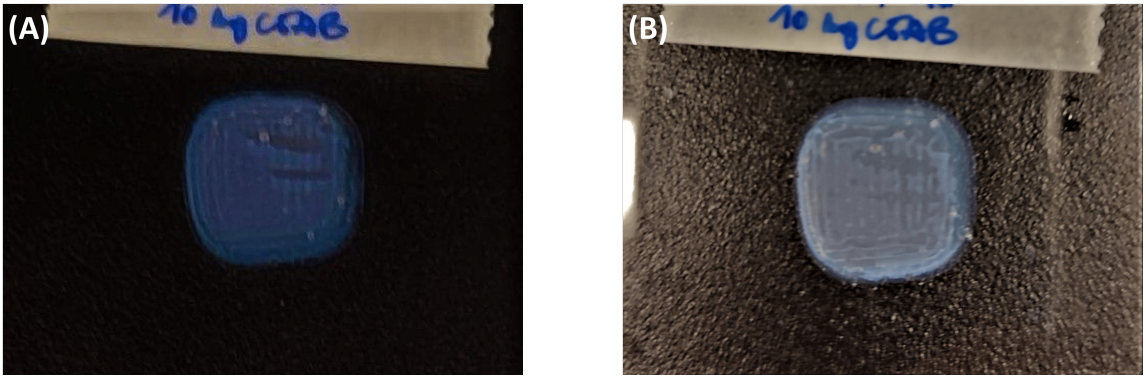

Fig. 5.18 VCL-IA-15-460 microgels crosslinked in 10% wt/V AAm under UV light, at RT and neutral pH. The specimen was printed in a 2-layer grid with a printing pressure of 70 kPa and 10 mm/s printing speed. The sample is (a) at RT and (b) right having been submerged in a 60 °C water bath.

Since only a change in transparency rather than in color is noticeable, this suggests that the shrinking of the microgels in the network disrupts the ordered packing state and that the sample might be composed of small, but randomly-oriented crystalline domains. However, when the microgels shrink in size, the disorder increases, as the microgels do not interpenetrate, leading to a more turbid sample.

5.5.2 P(NIPAm-*co*-AlAm) microgels in AAm

P(NIPAm-*co*-AlAm) microgel-based inks were printable when obtained by the "microgel rehydration" method (Section 1.4.6) from dispersions of 10% wt/V - 11 %. Since none of the inks displayed show evidence of structural colors, no investigations of mechanochromic properties were performed. However, the response towards temperature changes of the 3D-printed grid shown in Figure 5.15, composed of 10% wt/V NIPAm-AlAm-400 in 10% wt/V AAm, was investigated.

When the specimen, kept at RT, was placed under a hot water flow (T= 60 °C), the microgels showed an immediate temperature response, turning from transparent to opaque white (Figure 5.19). Similar to the examples mentioned in section 1.5.1, there is a change in transparency, though it is significantly stronger in this case (5.19). The microgels interpenetrate and form a homogeneous refractive index throughout the sample, which makes it appear transparent. When T>VPTT, the microgels shrink, but remain in their disordered positions in the network, reducing interpenetration and yielding a colloidal network with refractive index differences which will scatter white light. The thermal response is fully reversible, and can be observed over multiple cycles, without any obvious deterioration of the material or its responsiveness.

5.6 Summary and future work

In this chapter, several methods to formulate colorful microgel-based inks for additive manufacturing have been explored. With the aim of producing 3D-printed objects that display stimulus-dependent structural coloration, a set of thermo- and pH-responsive microgels were synthesized and then characterized by DLS. The microgels studied were based on PVCL, P(VCL-*co*-IA) - either from the direct copolymerization of VCL and IA or from the hydrolysis of P(VCL-*co*-IADME) - P(VCL-*co*-GMA), P(NIPAm-*co*-MAAc), and P(NIPAm-*co*-AlAm) microgels. A summary of each formulation method is listed below with its limitations and suggestions for future improvements.

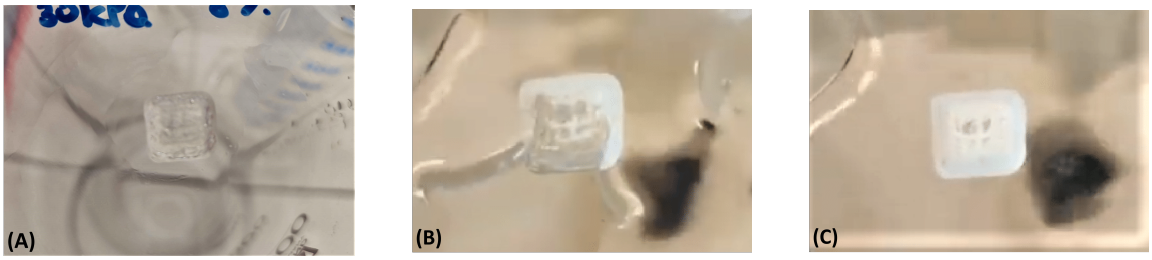

Fig. 5.19 NIPAm-AlAm-400 microgels in 10% wt/V of AAm, cured under UV light, at RT and neutral pH. The sample was prepared from redispersion of the microgels, centrifugation and 3D printing into a two-layer grid. Images are taken under diffused natural light. (a) A sample at RT, (b) a sample as it is being placed under a 60 °C water jet, which causes the sample to immediately turn white, and (c) when hot water is spread over the rest of the sample.

- **Ultracentrifugation** *Results and challenges:* Microgels were soaked in AAm and centrifuged at 282k RCF for 2h to form pellets that would be used as crosslinkable inks. All PVCL-based microgels formed colorful pellets when centrifuged. Aside from the ones composed of P(VCL-*co*-IA) (from direct copolymerization) and P(VCL-*co*-GMA), all inks retained their color after crosslinking. P(NIPAm-*co*-AlAm) did not show any structural color upon centrifugation. Almost all inks formulated by ultracentrifugation were too liquid to be used for direct ink writing. Only P(VCL-*co*-IA) microgels with 15 mol% COOH with diameters $\approx$ 500 nm could be printed as a single layer and successfully crosslinked into colorful 2D objects.

  Future work: Ultracentrifugation resulted in inks that display strong color in reflection, due to the structural color arising from the ordered packing of the microgels. To circumvent the low viscosity problem, the inks could be printed into a scaffold into for support, and then crosslinked to retain the shape. One example would be to use polydisperse, micrometer-sized, optically transparent microgels, derived from the cryo-milling of a frozen PAAc gel. These microgels form a gel at 1-2% wt/V, and can adapt to make space for another injected ink. Alternatively, an "immiscible scaffold", composed of a hydrophobic polymer, such as PDMS, could be used to prevent the diffusion of the microgels. In this way, the colored ink would be printed directly into an elastomer.

- **Ca^{2+} as crosslinker:** *Results and challenges:* microgels composed of P(VCL-*co*-IA) (15 mol% of COOH) were chosen in three different sizes, and jammed together by ultracentrifugation in the presence of varying $CaCl_2$ concentrations. Each microgel

could be compressed and formed inks with distinct color that was retained upon UV crosslinking. The major issue was related to the printability of these inks: Low Ca^{2+} concentrations (0.01 M of $CaCl_2$) possess the same mechanical properties as the metal-free inks containing microgels. A higher $CaCl_2$ concentration (0.05 M) led to an increase in the moduli, while even higher concentrations (0.1 M and 0.5 M) led to a drastic fall in viscosity and aggregation of the microgels, respectively. While promising in manual extrusion experiments, the ink containing 0.05 M $CaCl_2$ proved too viscous to be printable by the available printer.

Future work: These results are promising both in terms of the color and mechanical properties of the ink. First, a printer providing higher ultimate pressures could be employed. In combination with pre-rupturing of the ink to produce a workable viscosity, this approach could conceivably lead to successful 3D printing. Moreover, since the viscosity of the system depends on the micrgels' size and COOH content as well as $CaCl_2$ concentration, the formulation could be further optimized to find one that would meet suitable color and mechanical properties.

- **Temperature-induced aggregation:** *Results and challenges:* P(NIPAm-*co*-MAAc) microgels were dispersed in water in the presence of $CaCl_2$ at various concentrations. Once heated up to T>VPTT, the microgels aggregated and formed soft white pellets, which redispersed upon return to RT ([$CaCl_2$] = 0.01 M) or formed very soft blue-ish pellets, which could not be printed. High $CaCl_2$ concentrations (1 M) led to irreversible aggregation and the formation of a hard, brittle, non-self-healing solid. Since these results showed that no color besides the blue originating from Mie scattering could be achieved and the mechanical properties were unsuited for printing, this approach is unlikely to yield promising results.

- **Thickener addition:** *Results and challenges:* PVCL microgels were redispersed and centrifuged in the presence of a series of common thickeners. CMC (M_W = 90 kDa) and low viscosity HPC allowed for the retention of the iridescence of the jammed microgel pellets obtained from centrifugation. Upon crosslinking, phase separation occurred and only white materials were formed. The phase separation might occur due to the disruption of ordered packing during the AAm network formation, which interacts with both the microgels and the thickener. Moreover, since the printability of the resulting ink was not improved by the thickener addition, it is not recommended to continue investigating this approach.

- **Supramolecular granular hydrogel:** *Results and challenges:* P(NIPAm-*co*-AlAm) microgels with 10 mol% AlAm and sizes ranging from 390 to 600 nm were redispersed

in a solution of oxidized alginate, bearing aldehyde groups. Such dispersions were centrifuged and they formed transparent inks that were printable. Upon crosslinking in $CaCl_2$, depending on the size of the microgel, the printed specimen remained transparent or turned white.

Future work: Despite not yielding colors, this approach afforded biocompatible inks that can be printed by direct ink writing. These systems could be used as drug or ion delivery systems, as the microgels could carry the cargo, and the alginate would provide the scaffolding. Upon temperature or pH change, the microgels could expel the cargo for a controlled drug delivery application.

- **Microgel rehydration:** *Results and challenges:* P(NIPAm-*co*-AlAm) microgels in several concentrations were rehydrated in 10% wt/V of AAm to test for the formation of structurally colored dispersions. In general, the color formation comes in tandem with low viscosity, while higher viscosity and better printability characterized more concentrated microgel suspensions (> 8% wt/V) which were faintly colored or optically transparent (>11%). Microgels at 10 and 11% were printed and crosslinked, and they retained their opalescence, indicating that long-range order in the double network structure was retained.

  Future work: This approach is promising, as it has shown that rehydrating microgels at a certain wt/V% leads to suitable mechanical properties. This suggests that, by changing the size or crosslinker content, structural color could be achieved. Changing the crosslinker content would have an effect on the stiffness of the microgels, which might play a role in the jamming and interpenetration of the microgels, which in turn could affect color and rheological properties.

With complete success in 3D printing yet to be realized, inks composed of P(VCL-*co*-IA) microgels obtained by ultracentrifugation were molded and then cross-linked to form an iridescent disk to investigate bulk properties. These solids showed angle-dependent structural coloration and changed color upon temperature change, shifting from blue to green (observed from the same angle). It is necessary to characterize this system further, in particular by performing angle- and temperature-dependent reflectivity measurements, which could give accurate information about the reflected light. Moreover, small angle X-ray scattering (SAXS) could be a useful tool to determine the packing geometry and the degree of crystallinity of the microgels in these specimen.

P(NIPAm-*co*-AlAm) microgels were rehydrated at 10% wt/V, printed, and crosslinked, and they displayed a reversible transition from transparent to turbid (white) upon temperature increase. The fast dynamics and perfect reversibility of such a material would make them

good temperature sensors or smart temperature-responsive actuators. In order to characterize this thoroughly, the material's turbidity should be studied, along with the swelling of the microgels in the network in response to temperature changes.

Although direct ink writing is the most accessible 3D printing technique for hydrogels, lithographic methods are frequently a good alternative. Since the microgels described in this chapter are all nanometer-sized, two-photon polymerization printing could be an elegant approach to polymerize these inks at high resolution. This would lead to DNGHs with very sharp edges and could, given rapid enough photocuring, overcome the viscosity and flow problems encountered throughout this chapter.

In summary, this chapter presents a set of methods to jam temperature-responsive microgels into inks. With some optimization, these formulations could be used for additive manufacturing, to produce DNGHs suitable for temperature sensors, actuation, and drug delivery.

Chapter 6

Microgel encapsulation in polymer vesicles

This chapter is the result of a collaboration with Dr. Sarah Wypysek (RWTH Aachen), under the joint supervision of Prof. C. Palivan, Prof. W. Meier, and Prof W. Richtering (RWTH Aachen).

The microgels described in this chapter were synthesized and characterized by Sarah Wypysek. Polymers were produced and characterized by Sven Kasper (SK19) and Riccardo Wehr (RW32). Microfluidic set up and encapsulation optimization was done in collaboration with Elena Dos Santos. CLSM imaging was done in collaboration with Andrea Belluati and Elena Dos Santos. Andrea Belluati contributed significantly with ideas and support.

6.1 Introduction

In nature, physical separation between reactive species is fundamental for the correct functioning of communication pathways, responses, and biosynthesis.[203] Within a cell, the requisite organization is ensured by the presence of lipid membranes, which form the basis of organelles, vesicles, and other compartments.[203] The various compartments communicate with each other through the selective uptake and release of molecular cues, which are moved from one compartment to the other by selective pores and membrane proteins.[204][205] In synthetic cell models, compartmentalization is achieved by means of vesicles made of lipids (liposomes) or polymers (polymersomes).[206][207] Liposomes are used more frequently than polymersomes, as they are made of the same material as biological membranes (lipids), are readily assembled, and have thin membrane, which facilitates membrane protein insertion. However, they lack responsivity, functionizability, and mechanical resistance,all of which

properties of polymersomes. For more complex architectures and assemblies, polymersomes are the go-to option.[208] A vesicle's structure allows for both the encapsulation of hydrophilic molecules in the lumen and the incorporation of hydrophobic ones within the hydrophobic domain of the membrane. By inserting chemoselective pores in the vesicle's membrane, the cargo in the vesicles lumen can come in contact with a selected reactant from the environment, mimicking the cell environment. In contrast to cells, polymer vesicles are decorated with a limited number of specific pores, to ensure the selectivity of the system.[208] The nature of the pores is largely dependent on the kind of molecules for which one wants to permeabilize the membrane.[209] For mono- or divalent ions, pore-forming antibiotic molecules like ionomycin,[210] gramicidin,[211] and mellitin[212] have been successfully inserted. For larger cargo, membrane proteins can be used as transport mediators.[209] Several membrane proteins have been successfully reconstituted into polymersome membranes, including outer membrane protein F (OmpF),[213] proteorhodopsin (PR),[214] and AquaporinZ (AqpZ)[215] via detergent-mediated reconstitution, electroformation, and microfluidic jetting.[216][209]

The ability to combine cargo encapsulation and selective pores in a synthetic membrane has led to the design and production of nanoreactors.[217] Thanks to the pores reconstituted into the membrane, a reactant can enter in the vesicle's lumen, react with the encapsulated enzyme to be transformed into a product and then leave the vesicle, due to the osmotic gradient generated by the transformation. Based on this principle, the *in situ* enzymatic production of antibiotics was achieved, simultaneously screening the enzymes from external oxidative species and thereby leading to higher turnover and enzyme lifetimes than in the case of non-encapsulated enzyme.[218] Further separation between different cargo within the same polymersome is required to increase the complexity of the system. Recently, Belluati *et al.* have shown how co-compartmentalization can be achieved by using Giant Unilamellar Vesicles (GUVs), which are vesicles with a size that exceeds 10 μm.[219] Thanks to their size, larger than the average 50-200 nm diameter of small unilamellar vesicles (SUV), they are able to encapsulate smaller compartments, giving space to cascade reactions and higher complexity reaction pathways.[173] These reactions require communication channels, especially when it comes to triggered cascade reactions.[219] The most controlled way to ensure communication between compartments is to permeabilize the membranes with selective pores, which allow the passage of only certain kinds of molecules, functioning in a manner akin to logical gates in computing.[216]

Polymer-based GUVs can be prepared by a range of techniques, such as film rehydration,[219] electroformation,[220] and microfluidic techniques.[216] The latter ensures excellent control over the size and dispersity of the GUVs, and maximizes the encapsulation efficiency of

cargo.[216] The main problem that arises from these systems is that, frequently, the insertion of pores (pore-forming peptides or transmembrane proteins) is difficult, inefficient, and costly. The pores need to be added in higher concentrations in one of the phases in order to migrate and be embedded in the resulting membrane. This leads to significant losses of material and, more importantly, great challenges in the reconstitution of membrane pores and their quantification.

Microgels, on the other hand, are cost-effective and easy to chemically and physically tailor in terms of porosity and affinity to molecules.[1] Smart microgels, which can respond to external stimuli, can change their degree of swelling in response to changes temperature, pH, and ionic strength, and their behaviour is presented in detail in chapters 1 and 2.[1] This means that they can also perform "catch and release" of a cargo *on demand*, providing selective and tunable spatial confinement.[86] In this way, they could provide a new tool for spatial separation and compartmentalization, reducing the need for membrane pores.

So far, the interaction between microgels and lipids has been investigated, but the interaction between microgels and polymersomes has not yet been investigated. The microgel-lipid tandem has been explored from two angles, both cases as proof-of-concept.[221][222] In the first case, one large (10 μm) PNIPAm-based microgel was encapsulated in a lipid membrane, to mimic a secretory granule.[221] This shows that a 3D network can retain and preserve a certain molecule when enveloped by an impermeable lipid bilayer that can be made porous and becomes leaky under ultrasound . The resulting porous-bilayer-encapsulated a microgel was used as a starting model for drug delivery systems. A second investigation diverged from biophysics into colloidal physics, as microgels provide great models for soft interactions, mimicking the mechanical properties of proteins and soft tissues while being easy to study theoretically. When spatially constrained on surfaces or in volumes, microgels can assemble into crystalline layers or lattices. For instance, Crassous *et al.* showed how microgels can spontaneously self-assemble into hexagonally packed structures on lipid membranes, especially curved ones. They generated lipid GUVs, allowed PNIPAm microgels to diffuse on the external surface of the microgel, and further investigated their behaviour in response to temperature.[222] So far, however, the behaviour of microgels within the GUV lumen has not been investigated. It is important to note that microgels, due to their soft and fuzzy nature, can be compressed when in constrained environments, which can affect their stimulus responsiveness, and this requires further investigation.[185] Hence, from a colloidal physics point of view, encapsulating microgels within a polymersome or GUV provides a tool to study the behaviour of such gels in crowded environments bounded by soft layers. This is in contrast to the hard glass vessels in which crowded microgel dispersions are generally studied. The latter are generally investigated by SAXS and SANS, and the encapsulation of

microgels into GUVs might enable further tools to study and image soft crystalline structures on a microscope. Furthermore, developing a method for the effective encapsulation of microgels in GUVs will allow for the design and production of more complex systems to be used as models for artificial cells. As microgels-in-vesicles have been investigated only cursorily, this chapter aims to elucidate where the possibilities to do so lie and what the best conditions are to recreate spatial confinements with or without the use of pores (Figure **??**). To this end, the behaviour of stimuli responsive microgels in response to temperature is explored.

6.2 Microgel and block-copolymer polymer choice

6.2.1 Membrane forming block-copolymer choice

When building a synthetic cell mimic, the choice of polymer plays an important role, as the chemical structure and architecture of the polymer influence the mechanical stability, flexibility, permeability, potential for pore insertion, and responsiveness of the self-assembled structure.[223][209] The use of polymers composed of poly(dimethylsiloxane) (PDMS) and poly(2-methyl-2-oxazoline) (PMOxa) is well-established for biomimetic approaches, as a result of the many benefits their membranes, such as mechanical stability, flexibility, and biocompatibility.[208] Remarkably, membranes assembled from PDMS-*b*-PMOxa diblock copolymers allow the insertion of membrane proteins which can act as selective channels.[210] Additionally, suitably modified PDMS-PMOXa block copolymers provide a platform for further functionalization, membrane poration, and possible *in vivo* applications.[224]

In this chapter, two polymers were chosen, both composed of a hydrophilic A block of PMOxa and a hydrophobic B block of PDMS: an AB diblock copolymer ($PDMS_{26}$-*b*-$PMOxa_9$) (which will be named AB from here), and an ABA triblock copolymer ($PMOxa_8$-*b*-$PDMS_{104}$-*b*-$PMOxa_8$) (which will be named ABA from here). The choice to use two different polymers derives from the different approaches to encapsulation that are presented in this chapter. ABA can self-assemble into SUVs with extremely thin membranes, comparable to lipid membranes.[210] This, combined with excellent mechanical stability, makes them perfect candidates to form smaller, more stable versions of secretory granules. The self-assembly of ABA triblocks is however limited to SUVs, and is achieved by the solvent switch method, as presented in section 6.3. On the other hand, the diblock AB was chosen, because it can be used, among other techniques, in microfluidic-assisted GUV formation, a technique presented in section 6.5.

The choice of this class of polymer was also made with an eye to microgel properties: PDMS-PMOxa copolymers are not responsive to temperature or pH, and are therefore stable under conditions that can effect changes in swelling and assembly of the encapsulated, responsive microgels.

The **$PMOxa_8$-*b*-$PDMS_{104}$-*b*-$PMOxa_8$** triblockcopolymer ABA (M_n = 9450 Da, PDI = 1.45 as determined by GPC) was prepared following an established protocol developed by Nardin *et al.*,[225] and the **$PDMS_{26}$-*b*-$PMOxa_9$** diblock copolymer AB (M_n (NMR) = 2000 g/mol and PDI = 1.17 as detemrined by GPC) was synthesized following an optimized protocol developed by Wehr *et al.*[226].

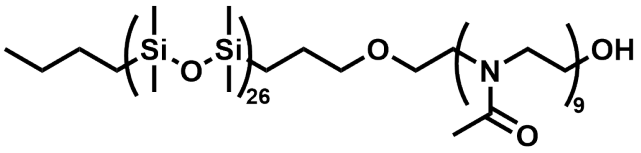

AB

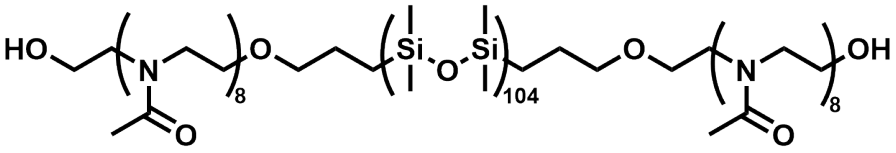

ABA

Fig. 6.1 Chemical structures of the A_9B_{26} and $A_8B_{104}A_8$ block copolymers used in this study.

6.2.2 Microgel choice

PNIPAm- and PNIPMAm-based microgels are among the most widely-studied thermoresponsive microgels due to their favourable combination of biocompatibility, mechanical resistance to strain and deformation, colloidal stability, and responsiveness to several external stimuli.[1][20] Their swelling can be modulated not only by temperature changes, but also by osmotic and hydrostatic pressure.[**?**] The VPTT values are 32 °C for PNIPAM and 40 °C for PNIPMAm. The microgels were designed to be composed either of P(NIPAm-*co*-MAAc) as pH- and temperature-responsive nanometer-sized networks, or alternatively as micrometer-sized PNIPMAm homopolymer networks or P(NIPMAm-*co*-MAAc) copolymer networks endowed with pH- and temperature-responsiveness. Every microgel contains methylene bisacrylamide (BIS) as the crosslinker and of methacryloxyethylthiocarboamoylrhodamine B (MRB), a fluorescent label which will permit confocal laser scanning microscopy (CLSM) and fluorescence correlation spectroscopy (FCS) analysis. The exact molar ratios are listed in Table 9.8 in the Appendix. To investigate the formation of nano- and micro-sized assemblies, microgels with a diameter of either 150 nm size (PNIPAm microgels) or 1 μm (PNIPMAm and P(NIPMAm-*co*-MAAc) microgels) were chosen. In order to encapsulate microgels within SUVs, which had an average size of 200 nm, only 150 nm microgels were used. For larger GUV assemblies, both small and large microgels were used. Micrometer-sized microgels were the preferred option when forming GUVs, since they can be visualized individually by CLSM.

Table 6.1 Name, D_H at RT and at 40 °C of the microgels used in this study, all of them containing BIS as crosslinker and MRB as fluorescent dye. D_H are measured in buffer (ringer solution), ad give only a qualitative estimation of their size for this chapter.

Sample	MAAc mol%	D_H (nm) T= 20 °C	D_H (nm) T= 40 °C
P(NIPAm-*co*-MAAc)	5.7	150	80
PNIPMAM	0	$1 \cdot 10^3$	800
P(NIPMAM-*co*-MAAc)	4.8	$1 \cdot 10^3$	800

PNIPMAm-based microgels were synthesized *via* dispersion polymerization, together with a Rhodamine methacrylate. The synthesis and characterization is described elsewhere.[227] A full characterization of the gels is still pending, as their radius has been measured in water and buffer, but not in the experimental conditions of this chapter (see appendix).

6.3 Spatial confinement of PNIPAM-based microgels in SUVs

In general, small vesicles that are obtained via "traditional" self-assembly, are in the nanometer range, with an average size from 50 to 500 nm.[208] Their size dispersity is generally above 15%, generating a significant variation in radius throughout the sample.

The ABA triblock ($PMOxa_8$-$PDMS_{104}$-$PMOxa_8$) was chosen for the preparation of the SUVs as it forms vesicles in PBS at RT with the "solvent switch" method (Scheme 6.2). In this method, the polymer is solubilized in a water-miscible, non-aqueous solvent (in this case, THF) and under continuous stirring, an aqueous rehydration buffer is added at a controlled rate. The gradual change in polarity of the solvent causes the polymer blocks to phase separate, leading to the formation of self-assembled vesicles, which encapsulate some of the buffer and its contents. In the presence of microgels of suitable size, these could be entrapped in the vesicle's lumen as well.

To first evaluate the self-assembly conditions, ABA was subjected to solvent switch without the presence of microgels. Using water as the rehydration medium for ABA at RT resulted into a mixture of vesicles and micelles (Figure 9.11 in appendix), while the use of buffers (PBS or boric acid(pH=9)) led to the formation of pure vesicles (Figure 9.12 in appendix). The size of the buffer-formed vesicles in their dried state, measured by TEM, was 161 ± 71 nm, indicating a highly disperse sample. The DLS value is not reported in this case, as the PDI of the sample was above 30%, making the resulting D_H obtained by DLS unreliable. Since the vesicles ranged from 50 to 200 nm in size, it was thought that the

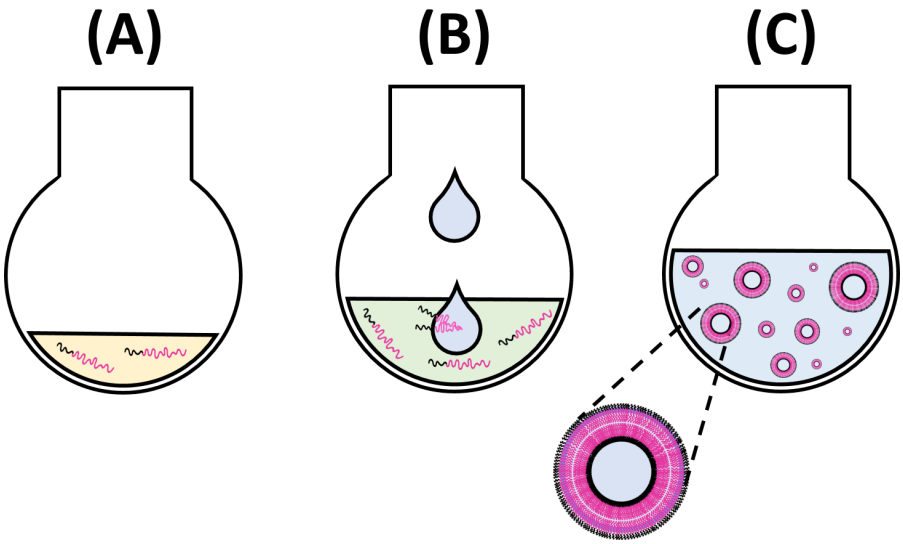

Fig. 6.2 Schematic representation of the "solvent switch" method. (a) PDMS-*b*-PMOxa is initially dissolved in a water-miscible organic solvent, (b) rehydration buffer is added to the mixture until (c) polarity of the solvent induces the self-assembly into polymersomes.

best microgels to use were 50 nm microgels (P(NIPAm-*co*-MAAc), with a D_H = 50 nm in buffer). It was theorized that the use of such small gels might permit a vesicle to entrap one or several microgels in its lumen. The microgels available in this size are anionic.

The results of a self-assembly process are dependent on a series of factors, including polymer concentration, temperature, solvent used, buffer, and self-assembly speed. With the goal of encapsulating microgels, the buffer composition was varied, while the temperature would have to stay constant, due to the microgels' responsiveness to both stimuli. Depending on the pH of the buffer, the microgels would be charged and swollen (basic pH), protonated and collapsed (acid pH), or partially deprotonated (physiological pH). In the following subsections, the attempts to encapsulate 150 nm P(NIPMAm-*co*-MAAc) microgels in vesicles by using the self-assembly of PMOxa-*b*-PDMS-*b*-PMOxa through "solvent switch" is described. In general, the polymer is solubilized in THF, and the rehydration buffer, containing 1% wt/V microgels is added to the organic solution. The resulting mixture is finally dialyzed to remove THF. The analysis of such results could only be performed by TEM, which is a practical tool for imaging polydisperse, inhomogeneous samples. For these samples, DLS is not a suitable analytical method, as it only provides reliable results for homogeneous, monodisperse samples. However, TEM can only prove the dried morphology, and thus information on the swollen state of these samples is not available. A summary of results is shown in table 6.2.

Table 6.2 Summary of solvent sequences used to encapsulate 0.1% wt/V P(NIPAm-*co*-MAAc) microgels in ABA- based vesicles, and the result of self-assembly.

Microgel	Initial buffer	Buffer pH	Dialysis	Nanostructures
P(NIPMAM-*co*-MAAc)	H_2O	6.8	MilliQ water	aggregates
D_H= 150 nm	PBS	7.4	MilliQ water	vesicles
	Boric acid	9.0	MilliQ water	vesicles
	Na_2CO_3	9.0	MilliQ water	aggregates
	Citric acid	3.0	MilliQ water	aggregates
	PBS	7.4	PBS	vesicles / micelles
	Boric acid	9.0	Boric Acid	vesicles / micelles

6.3.1 Self-assembly followed by dialyisis with MilliQ water.

Self-assembly in MilliQ water

During the addition of MilliQ water, the mixture became turbid and the dispersed components aggregated into macroscopic assemblies after being placed in dialysis in MilliQ water. This suggested that stabilizing components like ions are necessary for successful self-assembly.

Self-assembly in PBS

Since ionic strength could play a role in the self-assembly and stability of the products, the dialysis buffer was changed from MilliQ water to PBS. Following the addition of the microgels dispersed in PBS, the sample was dialysed in MIlliQ water. In this sample (Figure 6.3), the main nanostructures are vesicles, and almost no micelles were detected. Interestingly, when moving from MilliQ to PBS as the dialysis buffer, the vesicles formed remained intact, suggesting that the aqueous solution in which the polymers phase separate and in which the self-assembly process takes place is key to the final structure.

Figure 6.3 displays the result of self-assembly in PBS after dialysis against MilliQ water. The polymer structures formed resemble deflated hollow spheres in TEM images (Figure **??**), suggesting the formation of vesicles. These vesicles which have a size range from 100 to 200 nm and have equally-distanced microgels on their surface. There is an apparent ordered assembly of the gels on the vesicle (Figure 6.3b), which suggests that there is a rather strong interaction between the microgels and the polymer membrane. Also, the deflated appearance of the structures indicated that microgels are not present in the lumen of the vesicle, but are only arrayed on the outer layer of the polymeric membrane. The microgels observed in the TEM have a diameter around 20 nm in their dried state, indicating that they shrink

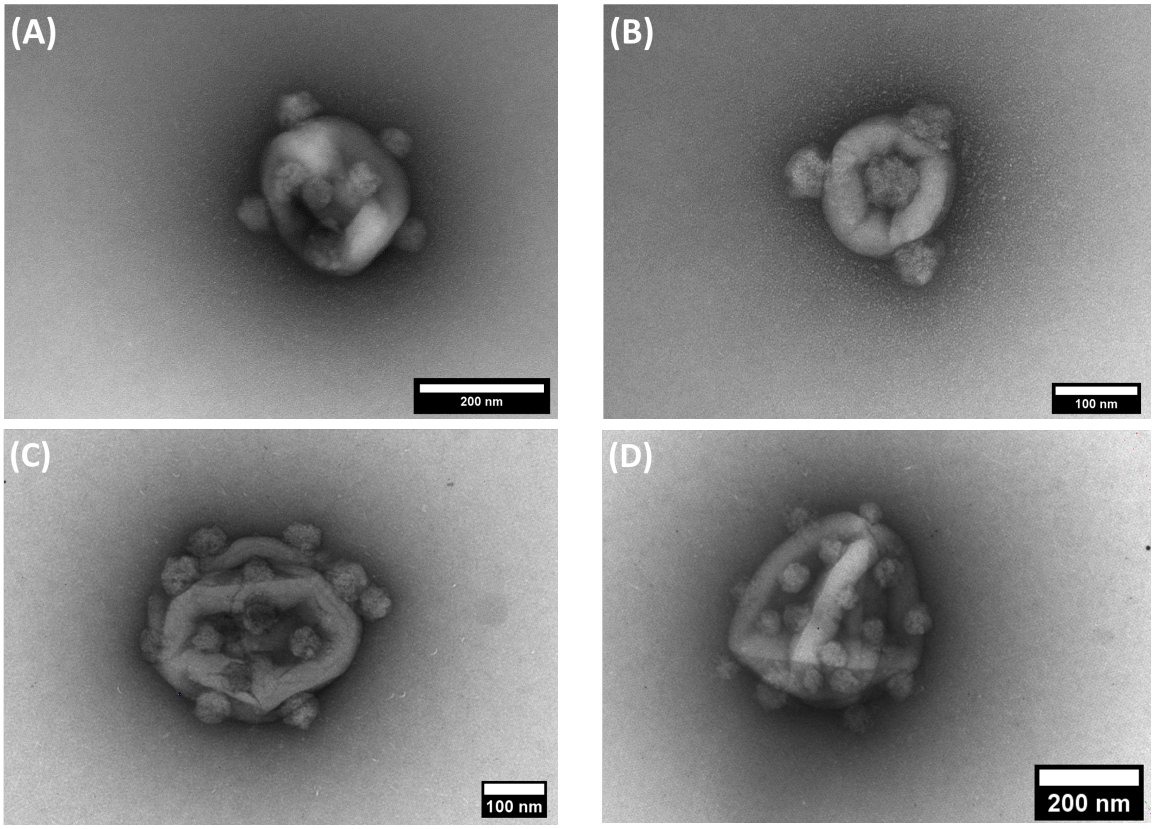

Fig. 6.3 TEM images of self-assembly between ABA and P(NIPAm-*co*-MAAc) microgels performed in PBS buffer and dialyzed against MilliQ water, stained with PTA at neutral pH. (a), (b), (c), and (d) are taken from the same sample.

considerably when the solvent is removed. Hence, they likely occupy a much larger area of the PDMS-PMOxa membrane when in solution.

Self-assembly in bicarbonate buffer and dialysis in MilliQ water

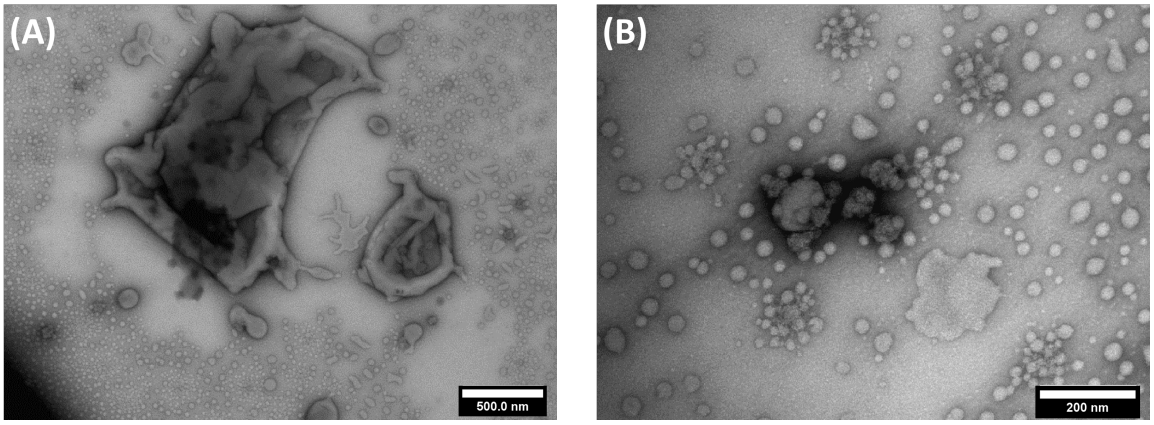

Fig. 6.4 TEM images of self-assembly between ABA and P(NIPAm-*co*-MAAc) microgels performed in bicarbonate buffer and dialysed against MilliQ water, stained with PTA at neutral pH.

The rehydration solvent used was buffered water (bicarbonate, pH=9.0), and the bicarbornate water/THF mixture was dialyzed against MilliQ water. TEM imaging (Figure 6.4) showed that almost no vesicles were formed. The lightly shaded, homogenous dots in Figure 6.4 are likely micelles, whilst the more "porous"-looking features are microgels. Unlike in the case of the vesicles shown in Figure 6.3, there is no significant interaction between the micelles and the microgels. Instead, most micelles are spread out on the TEM grid and do not interact with the microgels (Figure 6.4a). There are, however, some micelle/microgel spherical assemblies (Figure 6.4b), indicating there is the ability for these components to form raspberry-like structures.

Self-assembly in boric acid

P(NIPMAm-*co*-MAAc) microgels were dispersed in boric acid buffer (pH=9.2) and added to the THF solution within which ABA was dissolved. The mixture became turbid and remained so after dialysis against MilliQ water, and no signs of macroscopic aggregation could be observed. As observed with TEM, vesicles of different sizes were formed, and microgels are either adsorbed on the vesicles' surface or dispersed on the grid. Remarkably, vesicles are the only self-assembled nanostructure obtained, in contrast to the mixed-phase assemblies obtained in bicarbonate buffer (Figure 6.4), and there are no micelles present in the sample. Furthermore, the vesicles formed are significantly larger, measuring up to 1 μm (Figure 6.5d). Similar to the sample assembled in PBS (Figure 6.3), these microgels adsorb on the surface of the vesicle with an apparent ordered and equal spacing. Since the gels are

dried during the TEM sample preparation, the spacing between the microgels suggests that the microgels might be tightly packed on the surface in the hydrated state and separate upon drying to leave gaps visible in TEM samples.

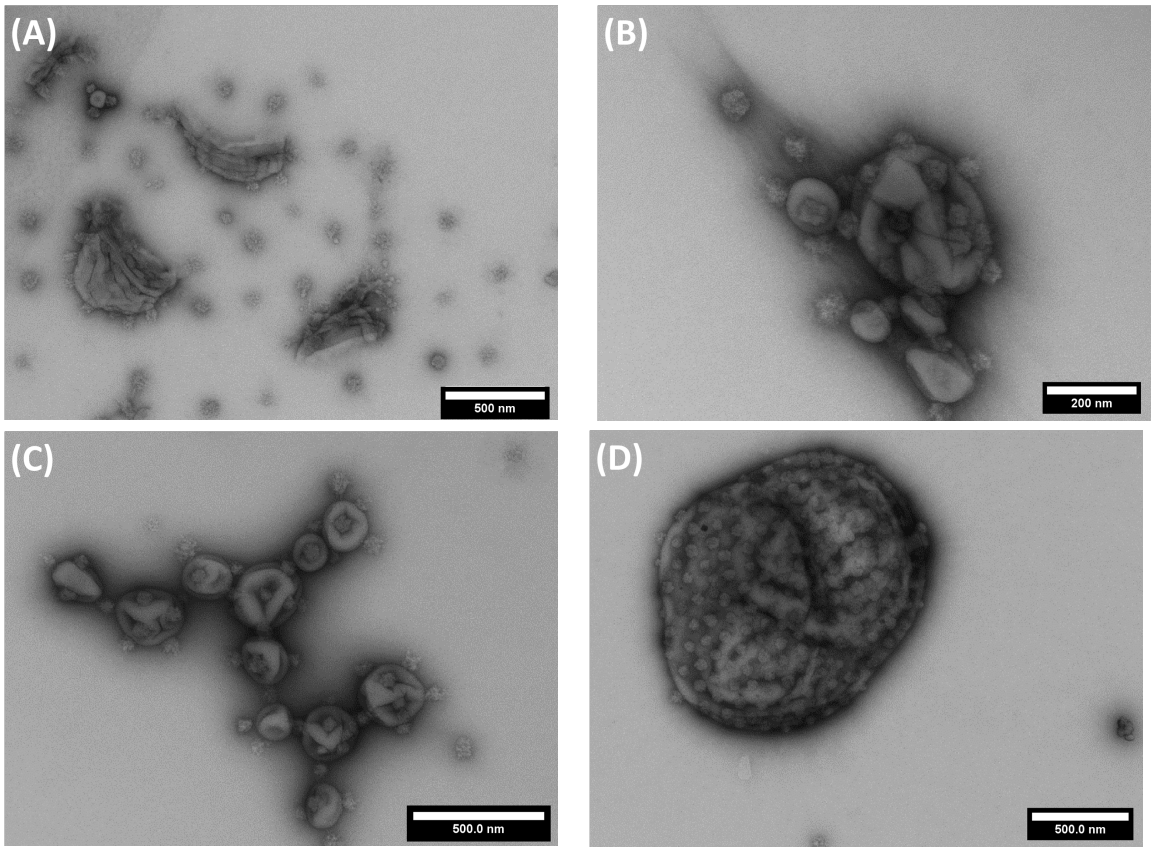

Fig. 6.5 TEM images taken of the self-assembly of ABA with P(NIPMAm-*co*-MAAc) microgels in boric acid buffer, and then dialysed against MilliQ water. Samples have been stained with PTA at neutral pH, and images are taken from several locations in the same TEM grid.

On larger surfaces, hexagonal arrays become evident, as can be seen in Figure 6.5d. They also appear to act as connectors between the vesicles in TEM images (Figure 6.5c and 6.5d), which confirms the results of DLS measurements, which indicated very high dispersities (PDI= 0.9). Moreover, upon gentle centrifugation, further aggregation was observed, reinforcing the notion that the microgels may act as vesicle connectors, likely a consequence of their apparent affinity with the polymer membranes. Figure 6.5b and 6.5c suggest that the microgels are on the outside of the vesicles, with the same reasoning as in the case of PBS as rehydration buffer: that the deflation might is a sign of an empty lumen and thus a failed encapsulation. Such deflation is present also on the large assembly in Figure 6.5d, but to a much lower extent.

6.3.2 Self-assembly followed by dialysis against buffer

Section 6.3.1 suggests that removing salt and altering pH by dialyzing the sample obtained from solvent switch against MilliQ water, produces only aggregated or bridged structures.

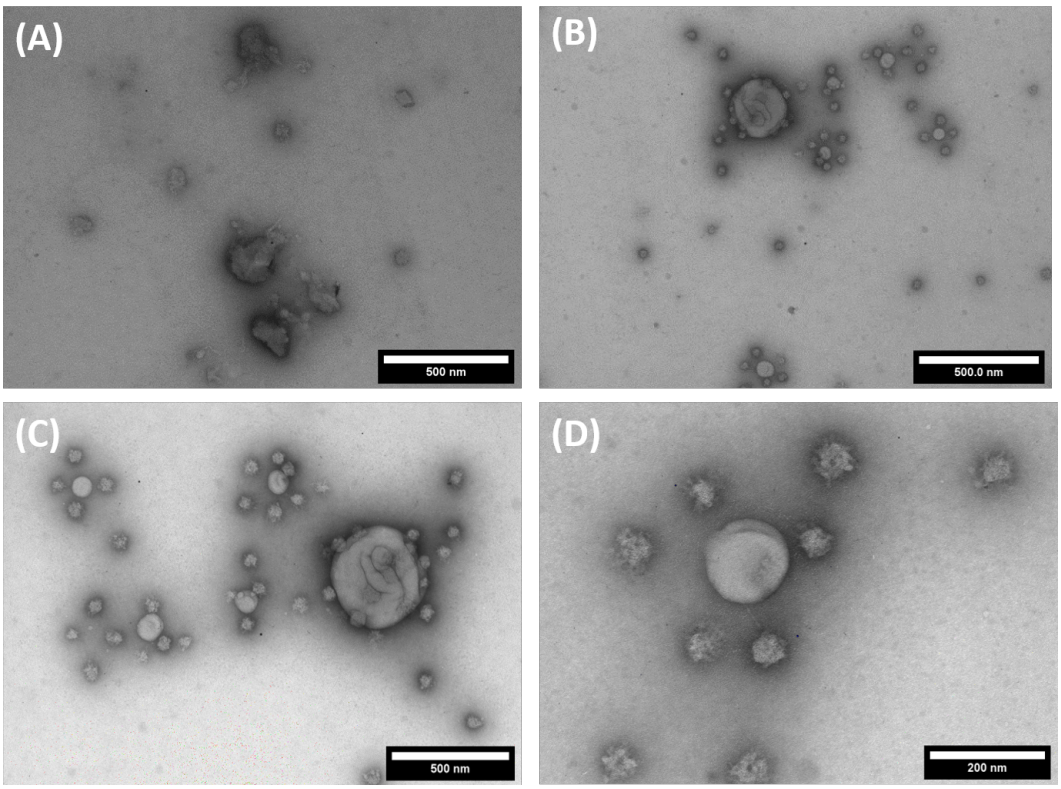

Fig. 6.6 TEM images of self assembly between ABA and P(NIPAm-*co*-MAAc) microgels performed at RT with the "solvent switch" method in (a) and (b) PBS buffer and dialyzed against PBS buffer and in (c) and (d) boric acid buffer and dialyzed against boric acid buffer.

From these results, the question arose whether stability and uniformity could be improved by keeping the ionic strength similar to the one at which the self-assembly takes place. To explore this, self-assembly with the "solvent switch" method using a buffer was performed (PBS, boric acid), followed by dialysis against the same buffer. As seen in Figure 6.6, the microgels seem to deposit around the vesicles present. It is possible that the ionic strength of the solution screens the interactions between the microgels and the polymer membrane, generating two almost independent populations in the suspension.

Conclusions on encapsulation by solvent switch

When “solvent switch” self-assembly was performed and followed by dialysis against MilliQ water, TEM images showed an interaction between the polymeric membrane and the mi-

crogels, regardless of the initial buffer used. The buffer had an influence on the formation and stability of the nanostructures: Boric acid (followed by MilliQ) promoted the formation of only vesicles, and bicarbonate (followed by MilliQ) afforded a mixture of vesicles and micelles. By changing the dialysis medium to match the respective rehydration buffer, only a small number of vesicles and almost no interaction between the microgels and the vesicles were observed. Hence, the removal of THF at high starting ionic strength is key to complete the vesicle formation, and the subsequent buffer exchange with MilliQ water reduces the ionic screening between the membrane and the gel, producing the assemblies noticed in section 6.3.1 which are absent in section 6.3.2.

This approach to confine microgels in small vesicles poses three main challenges. First, from the observations on self-assembly and dialysis, it is apparent that during self-assembly, there are no specific interactions between the microgels and the polymer membranes. Second, both the microgels and the vesicles formed are highly diluted, making the encapsulation of microgels reliant on stochastics. Third, once the self-assembly is complete, the purification of the assemblies by removing non-bonded microgels is non-trivial: centrifugation only leads to further aggregation and the microgels have roughly the same size as the vesicles, so size exclusion filtration or chromatography is not possible. Lastly, even if encapsulation and purification were successful, proving that the gels are inside the lumen of these vesicles is also quite challenging. One technique that might provide insights in the structure of a non-deflated structure is Cryo-TEM, where the assembly is cryogenically frozen in its solvent and then imaged. In addition to providing a view into the lumen of the vesicle, this would provide measures for the native microgel diameters and arrangements. Another way to demonstrate encapsulation would be to load the microgels with a dye that can be quenched by changing the pH. The non-encapsulated microgels attached to the vesicles are exposed to a change in pH, which would quench fluorescence, whereas microgels encapsulated within the ABA vesicles could still be observed *e.g.* by CLSM and studied by FCS.

One further observation is regarding the relative size of the microgels and vesicles, which are on the same order of magnitude. This suggests that, even in the case of a successful encapsulation, there would be only of a few gels per vesicle lumen. As the imaging of these systems is done by TEM, no information about the inner structure of the systems can be provided within this chapter.

To summarize, the microgel-vesicle assemblies generated in this section pose a series of challenges in terms of characterization. However, they are intriguing and novel raspberry-like colloids composed of porous and responsive compartments (the microgels), and vesicles, which can separate their cargo from the external environment. This system, could be of interest as a compartmentalized system in synthetic biology and biocomputing, but this is

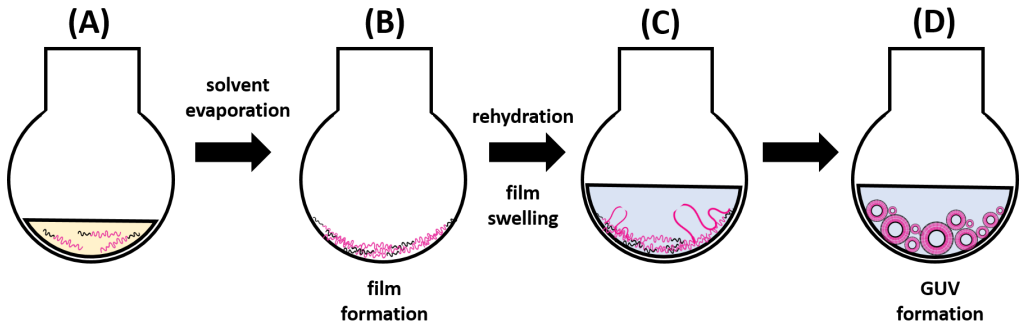

Fig. 6.7 Schematic representation of the "film rehydration" method. (a) polymer is initially dissolved in EtOH, (b) which is evaporated to induce a film formation. (c) The film is rehydrated and allowed to swell overnight without stirring, and (d) formed GUVs deposit on the bottom of the vial.

outside of the scope of this investigation. For this reason, this pathway was not taken any further and set aside.

6.4 Encapsulation of P(NIPMAm-*co*-MAAc) microgels in GUVs *via* film rehydration

Hoping to overcome the challenges encountered with the solvent switch method in section 6.4, the size of the microgels was kept at 150 nm but that of the vesicles was increased to the μm range. Giant unilamellar vesicles (GUVs) can be easily observed on an optical microscope, and their lumen can be imaged by just moving the focal plane along the z-axis by CLSM. One simple method to obtain GUVs is through "film rehydration".[219]

This method consists of drying a polymer solution, resulting in a thin film on the bottom of a vial, which is then rehydrated with a buffer. The buffer swells the polymer film, generating vesicles which start detaching from the vial. These vesicles are filled with the rehydration buffer, and thus are also able to encapsulate cargo that is solubilized or dispersed in the buffer.

In this case, the polymer used was ABA, which was rehydrated in P(NIPMAm-*co*-MAAc) microgels (D_H= 150 nm) dispersed in PBS, The resulting GUVs were then diluted in PBS buffer to remove some of the non-encapsulated microgels, and imaged by CLSM. In Figure 6.8, the GUVs are visible and appear to be evenly filled by the microgels. The microgels are too small to be optically resolved by the microscope, and only the fluorescence of the Rhodamine in their network is visible. Hence, the purple patches are attributed to the dye

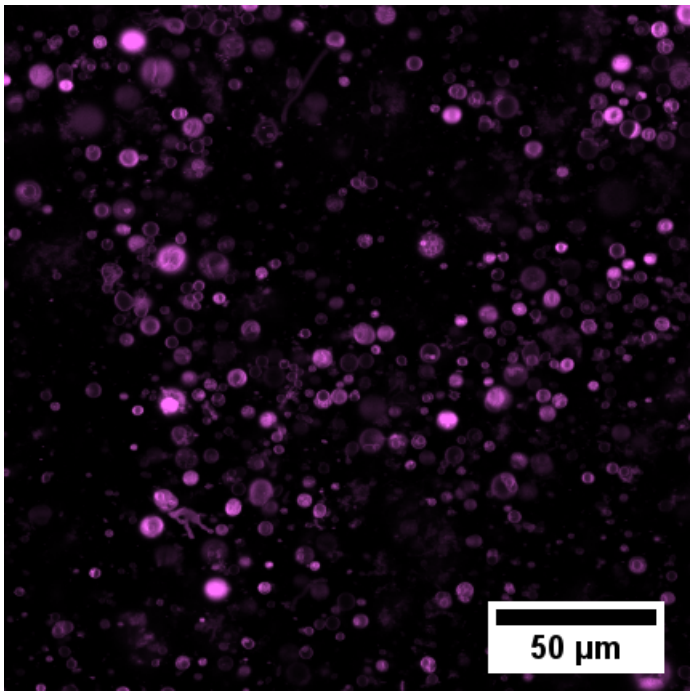

Fig. 6.8 CLSM image of GUVs with encapsulated P(NIPMAm-*co*-MAAc) microgels (D_H= 150 nm), obtained *via* the film rehydration method at RT and neutral pH. The microgels are in pink, whilst the GUV membranes were not stained and therefore nto visible here.

inside the microgels, indicating a higher microgel concentration where the pink is more intense.

Figure 6.8 shows GUVs at their cross-section, imaged by CLSM, where the pink signal is due to the rhodamine bound to the microgels. It is clear that the microgels were successfully encapsulated, in polydisperse GUVs, with sizes that range from 1 to 50 μm.

Unfortunately, the above results proved to be poorly reproducible: frequently, no GUVs were formed, and those that did form were filled unevenly. Moreover, little control over the microgel concentration inside the GUVs was possible, regardless of the initial microgel concentration. These results might be explained by two factors. First, the polymer used (ABA) is short enough to penetrate and swell the microgel network, so it is possible that during vesicle formation, the polymers diffuse into the microgels instead of assembling into a membrane. Second, it might be that the process through which the vesicles self-assemble does not permit the even filling of the GUVs. From Figure 6.8, it is apparent that the microgels that did not get encapsulated are still in the outer phase, due to the pink signal also present outside the GUVs. Attempts at centrifugation to separate the GUVs from the free microgels were not successful, as the GUVs tended to aggregate when gels are present in the outer phase, similar to observations made in section 6.3.1 (Figure 6.5c). Other separation

techniques such as extrusion and dialysis are also not suitable for this system, due to the sizes of the GUVs and the microgels. Extrusion would break the GUVs apart, whilst dialysis would retain both the GUVs and the non-encapsulated microgels. Furthermore, the GUVs produced are polydisperse, making their application in model studies more difficult, as curvature and filling number varies from GUV to GUV. For all these mentioned reasons, the film rehydration method to produce GUVs was abandoned in favour of the microfluidic approach presented in section 6.5.

6.5 Spatial confinement of PNIPMAm-based microgels in GUVs *via* double emulsion-templated microfluidics

An efficient and reproducible method to obtain polymer-based GUVs is double emulsion-templated microfluidics.[216] In this technique, a water/oil/water double emulsion is generated at the junction of three sets of channels, feeding an aqueous internal phase, an polymer-containing organic phase and, an external aqueous phase to a common 6-way junction. When the fluids (shown in schematic 6.9) encounter each other at the junction, they generate a jet of inner aqueous phase surrounded by the organic phase, which will be pinched off periodically by the flow of the outer aqueous phase, generating monodisperse double emulsions. GUVs are formed at the end of a process called dewetting, in which the organic phase evaporates and initiates the phase separation and consequent self-assembly of the polymer into a membrane.[216][228] By carefully setting the flow rates, monodisperse double emulsions and subsequently, GUVs, are obtained, the size of which depends mainly on the channels' size and on the flow rates.

For the encapsulation of microgels, the water/oil/water emulsion is composed of an inner aqueous layer containing a microgel suspension, which is enveloped in an organic phase containing PDMS-*b*-PMOxa (AB), which can form GUVs with this method. They are surrounded by an external PVA-based aqueous phase that osmotically matches the inner aqueous phase.[216]

6.5.1 Homopolymeric PNIPMAm microgels in PDMS-*b*-PMOxa GUVs

Homopolymeric PNIPMAm microgels (D_H= 1 μm as determined by DLS) were encapsulated in a PDMS-*b*-PMOxa GUV shell, in order to observe how the microgels' concentration influences the GUVs'stability and how the microgels distribute and assemble within the GUVs. The size of the microgels is suitable to be imaged and well-resolved by an optical microscope, making the characterization of these assemblies relatively straightforward.

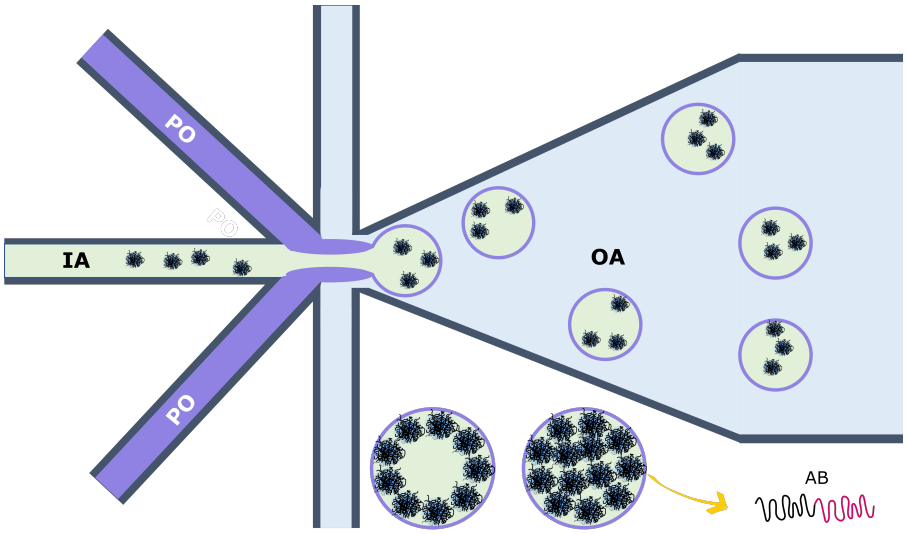

Fig. 6.9 Schematic representation of the double emulsion-templated microfluidic set up, showing the encapsulation of microgels. Microgel-loaded inner aqueous phase (IA, in green) is enveloped by the polymer-containing organic phase (PO, in purple), and the resulting jet is periodically broken by the external aqueous phase (OA, in blue). Evaporation of the organic phase leads to GUV formation.

Microgels were dispersed in solutions of 10% wt/V PEG (M_W=6000) in MilliQ water, the length of which should be large enough to not penetrate the microgel's network and swell them. PEG is generally added in the inner phase to increase its viscosity and to stabilize the GUV, as a counterbalance against the PVA contained in the outer phase. Nonetheless, as PEG could interact with the gels and exert an external osmotic pressure that might cause the gels to collapse, experiments were also conducted without PEG to observe a potential change in phase behaviour and assembly. The GUVs were formed in microfluidic chips with channel widths of 50 and 100 μm. The formed double emulsions were allowed to dewet and the resulting GUVs were diluted in the aqueous phase and analysed by CLSM.

1% wt/V PNIPMAm microgels

PNIPMAm microgels were suspended at a 1% wt/V concentration in 10% wt/V PEG (M_W= 6000), and encapsulated at RT. Figure 6.10a shows that the microgels present in the GUV's lumen assemble hexagonally (Figure 6.10a) along the GUV's membrane (Figure 6.10b), and there seem to be no free microgels floating in the lumen but only attached to the membrane (Figure 6.10c and 6.10d).To observe how the microgels pack on the membrane, a series of CLSM images was taken along the z axis of the GUV (Figure 6.10b). Since the membrane has not been stained, it is not possible to fully confirm that the microgels are inside the

GUV. However, by considering how the GUVS are formed, the gels would need to cross the membrane in order to assemble outside of the GUV.

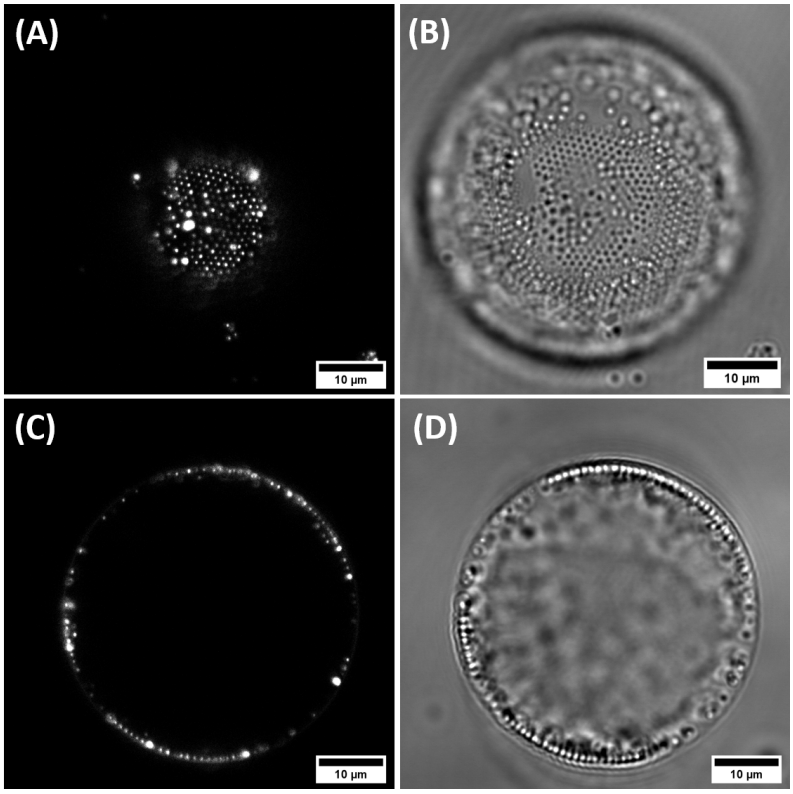

Fig. 6.10 CLSM images of a (a) fluorescence signal and (b) transmission of the bottom of a GUV filled with 1% wt/V PNIPMAm microgel and (c)fluorescence signal and (d) transmission of the middle section of the same GUV, showing its empty lumen.

5% wt/V PNIPMAm microgels

The upper limit for the concentration where PNIPMAm microgels were encapsulated was set to 5% wt/V. Above this, the viscosity of the inner phase became too high for the microfluidic devices. Microgels suspended at a concentration of 5% wt/V were encapsulated as a dispersion in 10% wt/V PEG concentration or in MilliQ water.

Figure 6.11a shows the cross-section of a GUV filled with 5% wt/V of PNIPMAm microgels in MilliQ water. The microgels are assembled into hexagonally ordered structures, with short-range order appearing in domains across the imaged surface (Figure 6.11a) and continuing along the membrane (Figure 6.11b) . To prove that the GUVs were evenly filled, a series of images along the z-axis was taken, as shown in Figure 6.11d. The GUV is filled with gels in its entire volume. Remarkably, the packing at the membrane is hexagonal, very similar to the assembly observed in Figure 6.10a and 6.10b. This long-range order on the

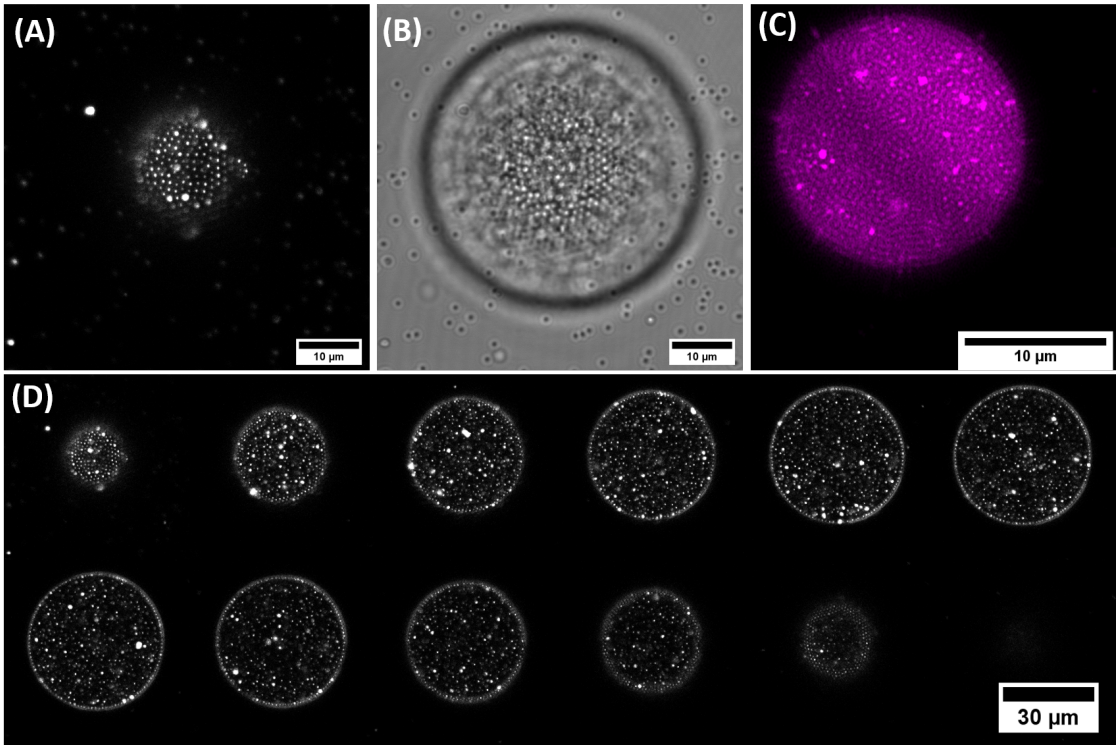

Fig. 6.11 CLSM images of a 5 wt% microgels dispersion in MilliQ water encapsulated in AB at RT. (a) bottom of the GUV imaged in fluorescence and (b) in transmission; (c) airy scan processing of a slice alog the focal plane and (d) z-stack slices along the focal plane.

vesicle surface is not present in the bulk, where small ordered domains are observable (Figure 6.11c. The images in Figure 6.11 were recorded 4 h after the microfluidic assembly. Since the crystallization of such gels typically occurs over an extended period,[20][185] the images could have captured a transient state on the way to more ordered structures. However, images were not taken after more time , as these microgel-packed GUVs lacked long-term stability and deflated, releasing the gels into solution after 12 h.

Aiming to increase the stability of the GUVs, 10% wt/V of PEG was added to the internal phase, yielding improved stability up to 24 h. Moreover, no differences in microgel packing were observed when the size of the channels in the microfluidic chip were varied. The size of the channel influences the size of the resulting GUVs and, in this case, 32 μm and 50 μm GUVs were produced in 50 and 100 μm channel chips, respectively. In the 32 μm GUVs and in 50 μm GUVs, the packing of the microgels was comparable (Figure 6.12), suggesting that the assembly could be adapted to even larger vesicles. Figure 6.12 shows how the the microgels distribute evenly and assemble in an ordered fashion within GUVs of different sizes.

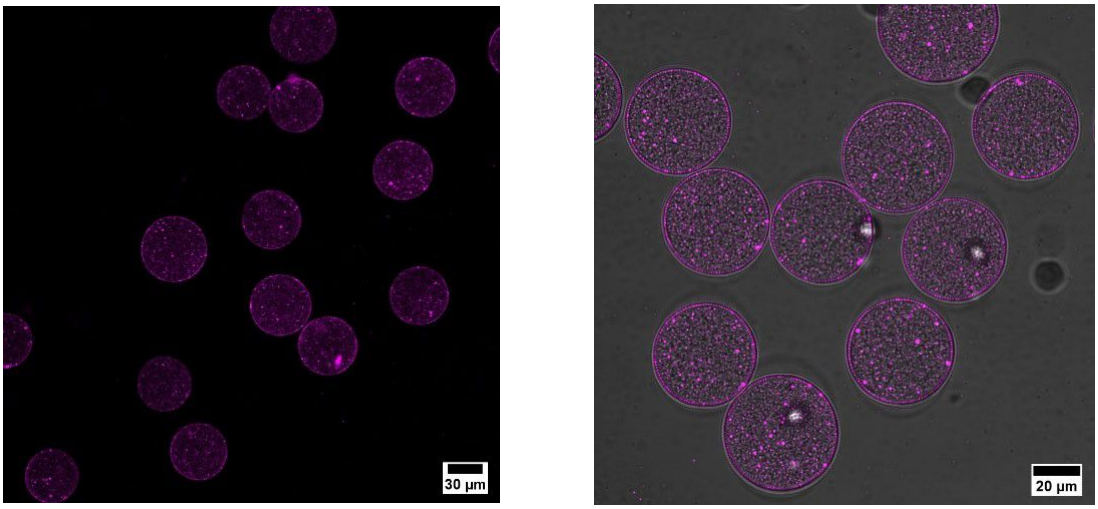

(a) 50 μm Channel,

(b) 100 μm Channel,

Fig. 6.12 CLSM images of a 5% wt microgels solution in 10% wt/V PEG 6000 encapsulated in 6 mg/ml PDMS-*b*-PMOxa GUVs at RT and neutral pH. The GUVs are made from microfluidic chips with (a) 50 μm and (b) 100 μm channels.

Hexagonally-arrayed double emulsions with incomplete dewetting, were scanned along their z-axis. The partial dewetting facilitates imaging in this case because it increases the thickness of the layer that separates each internal phase. This can be exploited to image multiple GUVs in the same frame, without having their signals overlap while performing a 3D reconstruction. The results of the 3D reconstruction of partially dewetted double emulsions results are shown in Figure 6.13, where it is clear that the microgels already assemble into ordered structures at the water-oil interface.

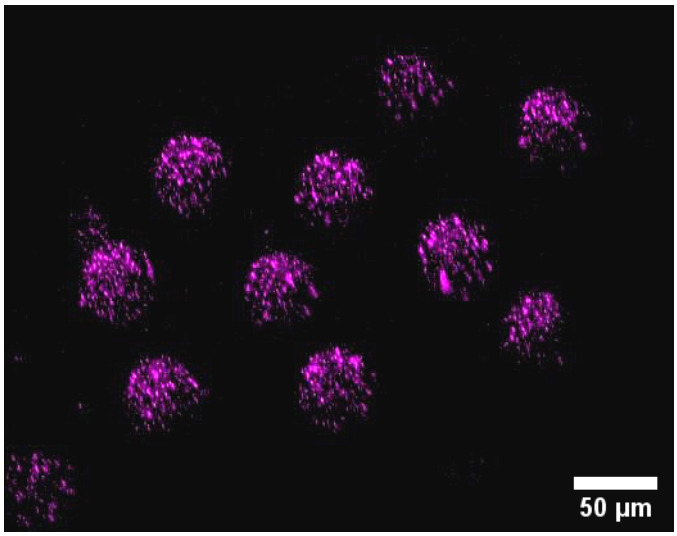

Fig. 6.13 Reconstructed 3D image of GUVs filled with 5% wt/V PNIPMAm microgels at RT and neutral pH.

6.5.2 Encapsulation of P(NIPMAm-*co*-MAAc) microgels in PDMS-*b*-PMOxa GUVs

P(NIPMAm-*co*-MAAc) (D_H= 1 μm, as determined by DLS in buffer) microgels were encapsulated within PDMS-*b*-PMOXa GUVs at RT and neutral pH. Two concentrations were chosen (1% wt/V and 5% wt/V) combined with 10% wt/V PEG (M_W= 6000 g/mol) in MilliQ water. In both cases, microgel-filled stable GUVs were obtained and imaged with CLSM at RT. At 1% wt/V microgel concentration, CLSM imaging shows how the microgels attach to the inner surface of the PDMS-*b*-PMOxa membrane, assembling hexagonally on the surface. The microgels saturate the membrane surface, and the ones not attached float in the lumen of the GUV (Figure 6.14a). This result is similar to the one obtained for 1% wt/V PNIPMAm GUVs (section 6.5.1, Figure 6.10), where the microgels migrate to and assemble at the interface. Electrostatic repulsion provided by the MAAc groups does not seem to influence the packing of the gels at the interface. At 5% wt/V P(NIPMAM-*co*-MAAc), however, the microgels do not seem to assemble into nicely ordered superstructures (Figure 6.14b), unlike their homopolymeric counterparts (Figure 6.12b). Still, they remain stable within the GUV.

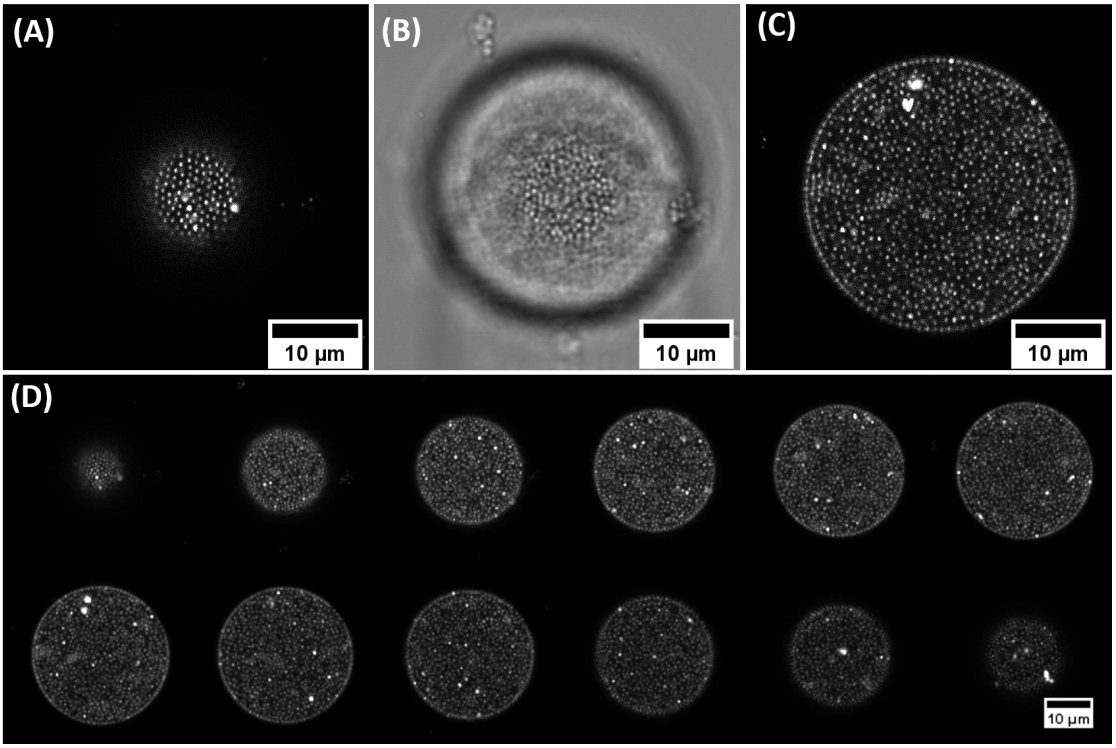

Fig. 6.14 CLSM images of a (a) fluorescence signal and (b) transmission of the bottom of a GUV filled with 1% wt/V P(NIPMAm-*co*MAAc) microgel and (c)fluorescence signal and (d) transmission of the middle section of the same GUV, showing its empty lumen.

6.5.3 Temperature responsiveness of microgels in PDMS-*b*-PMOxa GUVs

Both PNIPMAm and P(NIPMAm-*co*-MAAc) microgels are responsive to temperature in water, yet only mildly change their degree of swelling when the temperature increases above their VPTT (VPTT= 40 °C). In this section the changes in packing and behaviour of the gels in response to a temperature increase to 40 °C are described. 40 °C is the highest temperature accessible with the CLSM setup used for these studies, and thus the experiments could not be conducted significantly above the VPTT. The microgel-containing double emulsions (1% wt/V and 5% wt/V in 10% wt/V PEG) were formed at RT and neutral pH, and were allowed to dewet to form GUVs at RT. The GUVs were then imaged by CLSM at RT and incubated at 40 °C for 1 h prior to high-temperature imaging.

Thermoresponsive behaviour of PNIPAm microgels

GUVs containing PNIPMAm remained stable over 12 h at RT. As described in section 6.5.1, the microgels adsorb onto the membrane and pack hexagonally at RT, regardless of their concentration. Previous work by Wang *et al.*, showed how PNIPAm microgels that adsorb at the interface of lipid-based GUVs shrink and lose their packing above their VPTT of 37 °C. In the PDMS-*b*-PMOxa / NIPMAm microgel system, the results obtained are significantly different. This can be seen in Figure 6.15, where a reconstruction of a GUV containing 1% wt/V of microgels after 1 h at 40 °C is shown.

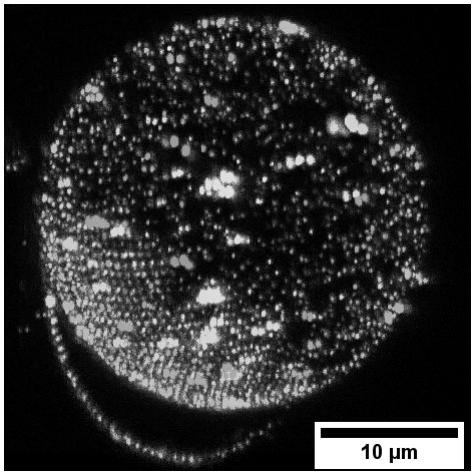

Fig. 6.15 3D reconstruction of GUVs obtained by stacking all slices taken along the Z plane.

The 3D reconstruction in Figure 6.15b shows the inside of the GUV membrane, covered unevenly by the PNIPMAm microgels, possibly due to a concentration that is not enough to cover the whole internal surface of the GUV. Nonetheless, the microgels tend to interact with each other on the membrane, giving rise to ordered patches, significantly different from what was observed by Wang *et al.* for a lipid interface. Imaging the same GUV over time gives insights on how the microgels at the interface behave at T= 40 °C. Figure 6.18 shows how the microgels remain in their positions over time, with no significant variations in the observed bright spots, likely stemming from particularly bright individual microgels. This suggests a very strong interaction between the neutral PNIPMAm microgels and the PDMS-*b*-PMOxa membrane.

When the microgel concentration is increased to 5% wt/V and the GUVs are incubated at 40 °C for 1 h, the microgel behaviour differs depending on its position in the GUV. The same GUV was imaged over time, to determine whether the microgels would migrate around the membrane or if any movement could be detected in the close packing. Figure 6.17 shows how

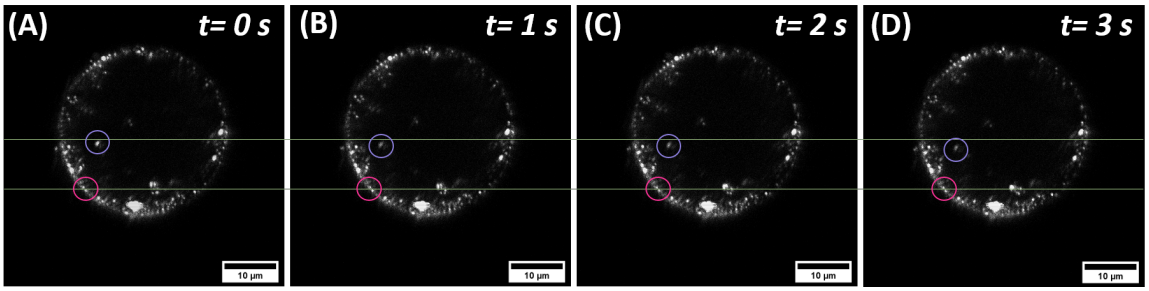

Fig. 6.16 Middle Z slice of GUV filled with 1% wt/V NIPMAm microgels at 40 °C at (a) *t*=0 s, (b) *t*=1 s, (c) *t*=2 s, and (c) *t*=3 s. Circled in pink: microgel at the membrane; circled in purple: free microgel in the lumen. Lines are placed to help the reader.

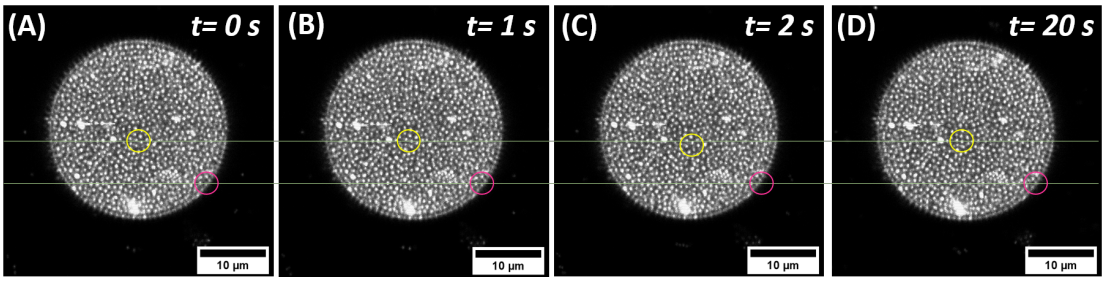

Fig. 6.17 Middle Z slice of GUV filled with 5% wt/V NIPMAm) microgels at 40 °C at (a) *t*=0 s, (b) *t*=1 s, (c) *t*=2 s, and (c) *t*=20 s. Circled in pink: microgel at the membrane; circled in purple: free microgel in the lumen. Lines are placed to help the reader.

the microgels located at the polymer/liquid interface interact strongly with the membrane and remain stable in their positions overtime.

In contrast, the microgels in the GUV's lumen can move more freely, and lose their ordered packing. Figure 6.17 shows (a) the GUV's cross-section at RT, and then (b) *t*= 0 s,(c) t= 5 s and (d) t= 10 s the same cross-section imaged by CLSM at 40 °C. As apparent from Figure 6.17 the microgels move within the lumen. This can be explained by a lower viscosity of the system provided by an increase in temperature, due to an increased temperature and some likely shrinking of the gels, which is however not detectable with this technique. A full characterization of these assemblies to affirm these hypotheses is yet to completed.

Thermoresponsive behaviour of P(NIPMAm-*co*-MAAc) microgels

Similar to the neutral PNIPMAm microgels, the behaviour of charged P(NIPMAm-*co*-MAAc) microgels was monitored at T= 40 °C. In this case, there is the additional interaction and intermicrogel repulsion between negative charges, which might affect the relatove motility of the microgels, although no significant differences in the stability of the microgel-membrane

interaction between these microgels and their homopolymeric congeneres could be observed at RT.

With a microgel concentration of 1% wt/V, the microgels pack hexagonally on the membrane (Figure 6.18a). The other 3 images (Figure 6.18b, 6.18c, and 6.18d) show how the hexagonal packing remains unaltered overtime, despite the temperature increase.

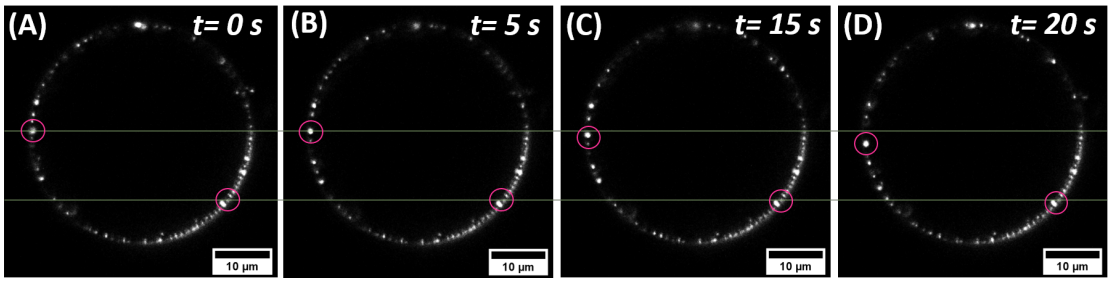

Fig. 6.18 Middle Z slice of GUV filled with 1% wt/V P(NIPMAm-*co*-MAAc) microgels at 40 °C at (a) t=0 s, (b) t=1 s, (c) t=2 s, and (c) t=20 s. Circled in pink: microgel at the membrane; circled in purple: free microgel in the lumen. Lines are placed to help the reader.

By increasing the microgel concentration to 5% wt/V, the result is comparable to that observed in Figure 6.18 for PNIPMAm microgels.

Again, the microgels seem to have a strong interaction with the membrane, whilst they seem to move freely in the lumen , as can be seen in Figure 6.19.

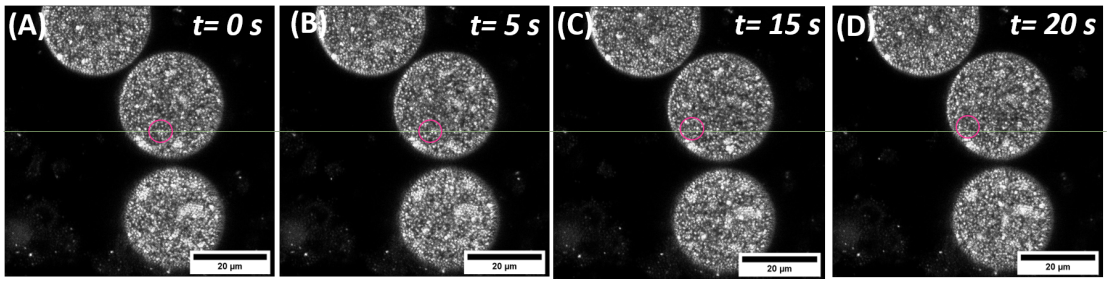

Fig. 6.19 Middle Z slice of GUV filled with 5% wt/V P(NIPMAm-*co*-MAAc) microgels at 40 °C at (a) t=0 s, (b) t=1 s, (c) t=2 s, and (c) t=20 s. Circled in pink: free microgel in the lumen. Lines are placed to help the reader.

6.6 Summary

This chapter described the confinement of thermo- and pH- responsive microgels into PDMS-*b*-PMOxa-based GUV membranes. Three microgel types were used: P(NIPAm-*co*-MAAc) (D_H= 150 nm), PNIPMAm (D_H= 1 μm), and P(NIPMAm-*co*-MAAc) (D_H= 1 μm). Due

to their size most closely resembling that of a typical self-assembled vesicle, P(NIPAm-*co*-MAAc) microgels were present during the co-assembly of the triblock copolymer ABA polymer to form SUVs. ABA was assembled into SUVs *via* solvent switch method in the presence of P(NIPAm-*co*-MAAc) microgels, and the results suggest that to form vesicles with ABA, high ionic strength is required: The assembly in MilliQ water led to aggregation, in contrast to buffered solutions, in which dispersed assemblies were observed. Slow removal of the salts contained in the buffer, through dialysis of the assemblies against MilliQ water induced the formation of bridged and raspberry-like structures, where the microgels assemble and pack on the outer layer of the membrane. While the present data strongly suggest that microgels are mainly attached to the outside surface of the polymersome membrane in these cases, encapsulation can not be fully excluded. Further investigations of the self-assembled structures *e.g.* by Cryo-TEM could shed light on this question.

The same 150 nm P(NIPAm-*co*-MAAc) microgels were encapsulated in ABA GUVs by film rehydration. While some attempts were successful, the reproducibility of this approach was poor.

Vastly more reproducible, micrometer sized PNIPMAm and P(NIPMAm-*co*-MAAc) microgels were encapsulated into GUVs based on the diblock copolymer AB by using double emulsion-templated microfluidics. The gels were encapsulated at 1% and 5% wt/V in the GUV and their assembly was characterized. By using microfluidic-templated self assembly, the formation of monodisperse GUVs that are evenly filled with microgels was achieved. The microfluidic approach therefore avoids the drawbacks of uneven filling and size distribution stemming from the film rehydration method described in section 6.4. Moreover, since the microgels are fed *via* the inner phase which is immediately encapsulated by the organic phase, in the ideal case of no jetting or tearing, the only microgels present in the external phase derive from the rupture of a GUV. In this case case, the removal of non-encapsulated microgels is easily overcome.

The gels pack hexagonally on the internal surface of the polymer membrane, where they appear to preferentially accumulate, floating in the lumen only when the membrane's surface is saturated. At concentrations of 5% wt/V in the inner aqueous phase, the microgels not only distribute on the surface, but they also form hexagonally-packed domains in the GUV's lumen. The behaviour of the microgels at 40 °C, which is close to their VPTT (44 °C) has also been investigated, and no significant variation in the behaviour of the gels interacting with the GUV membrane could be observed. The microgels in the bulk however appear to have a higher degree of freedom and break from their regular packing upon heating.

In summary, this chapter presents various attempts to confine microgels in polymeric vesicles. Particularly, the encapsulation of micrometer-sized microgels in microfluidic-

templated GUVs was successful. This highly efficient and reproducible approach could be used to further improve the understanding and gain insights on the behaviour of microgels in crowded environments. Moreover, thanks to the great control over the encapsulation concentration and efficiency, microgels-in-GUVs obtained with this method can be used not only as model systems for soft interactions, but also for compartmentalized reactions and memmbraneless organelles in synthetic biology.

Chapter 7

Conclusions and Outlook

7.1 Conclusions

The aim of this thesis consisted in exploring the use of thermo- and pH- responsive microgels in three different directions: biomedical use, material science and synthetic biology, in order to demonstrate the immense versatility of microgels in different fields.

First, a set of P(VCL-*co*-IA) microgels was synthesized, and their swelling behavior and stability was investigated (**Chapter 2**). The gels displayed cation concentration-dependent degree of swelling, and remained colloidally stable at high temperatures and high ionic strengths, unlike the commonly used P(VCL-*co*-AAc) or P(NIPAm-*co*-MAAc) microgels. The capacity of P(VCL-*co*-IA) microgels to remain stable at high salt concentrations and physiological temperatures makes them good candidates for biomedical applications involving biologically relevant metal cations. Hence, the "catch and release" of metal cations such as Ca^{2+}, Mg^{2+}, Sr^{2+}, Cu^{2+} and Fe^{3+} was quantified (**Chapter 3**). The number of ions coordinated and retained increased proportionally with the amount of COOH present, with the exemption of Fe^{3+}, which overaccumulated in the network. The pH dependent cation release started at pH<4, reaching completion at pH=2. The microgels proved capable of uptaking and releasing ions within seconds, making microgels much faster ion release systems compared to macroscopic gels. With the exception of Fe^{3+}, ion uptake and release were highly reversible. Moreover, the system was found to exhibit some selectivity towards transition metal cations over earth alkaline metal cations, with particularly strong preference for Fe^{3+}.

Another set of gels, namely P(NIPAm-*co*-MAAc) with varying radii was used to prepare mechano- and thermochromic 3D microgel granular hydrogel double networks (GHDN) (**Chapter 4**). A simple method was developed were PNIPAm-based microgels in sizes between in 200 and 500 nm were soaked in acrylamide together with a crosslinker and a

photoinitiator, and compressed into a pellet which displayed strcutural colors. Molding and UV curing generated elastic GHDN, which display angle-dependent color changes. The material changes color under mechanical stress (compression and elongation) and upon temperature changes.

By taking the findings from Chapter 2 and 3 on the swelling and uptake and release of ions, and combining them with the method developed in Chapter 4, **Chapter 5** tried to expand the use of P(NIPAm-*co*-MAAc) microgels to 3D printing. Hence, a library of microgels, including P(VCL-*co*-IA) and P(NIPAm-*co*-MAAc) microgels was produced to find formulations for printing 3D objects by direct ink writing. The library was first screened for color retention after crosslinking, which was dependent on the microgel's chemistry. Afterwards, different jamming methods and formulations were investigated, in order to find a formulation with rheological properties suitable for direct ink 3D printing. From all the formulations and methods tested, unfortunately none yielded an ink viscous enough to not flow under its own weight. However, a P(VCL-*co*-IA) microgel-based ink was molded and showed temperature-dependent coloration, similarly to the P(NIPAm-*co*-MAAc) microgel-based double network. A third kind of microgel, P(NIPAM-*co*-AlAm), was successfully printed in multiple layers, partially retaining their shape. Once cured, the MDN was transparent at RT, and reversibly changed color from transparent to white and back when switching back and forth between temperatures below and above the microgel's VPTT.

Finally, in **Chapter 6**, temperature responsive PNIPMAm microgels and temperature- and pH- resposponsive P(NIPAm-*co*-MAAc) and P(NIPMAm-co-MAAc) microgels were encapsulated into PDMS-*b*-PMOxa-based GUVs, and their concentration-dependent behavior in the GUVs' lumen was characterized as a function of temperature. The microgels display an extraordinary high affinity towards the polymer membrane, and preferentially assemble at the polymer-water interface. Moreover, their hexagonal packing is not affected by temperature increases to the proximity of the VPTT of both microgels. Highly concentrated microgels in the GUVs' lumen assemble into localized ordered structures. Comparison between the systems showed that, despite the charged P(NIPMAm-*co*-MAAc) microgels forming less ordered structures at high concentrations, no principal differences were spotted. Both set of microgels would interact strongly with the membrane at both low and high microgel concentration, and at temperatures well below and near the VPTT.

In summary, this thesis represents a varied study on the application of anionic microgels, that can be employed different fields, from drug release, to colloidal physics, to sensing applications. This thesis presents easy-to-make, cost-effective materials that can be used as accessible building blocks for systems in higher complexity. Thus, the investigated applications went from "catch and release" of metal cations, to mechano- and thermochromic materials

and their use as inks for additive manufacturing, to the generation of systems suited to investigating microgel-membrane interactions in crowded environments for compartmentalized systems.

7.2 Challenges and Outlook

Though a diverse set of potential applications for the presented microgels was investigated, a plethora of further applications and more in-depth investigations can be envisaged, which have not been directly addressed in this thesis, either because they were out of scope, or due to time constraints. For readability, each set of chapters that focuses on a specific application, will be addressed in their challenges and how to solve them, providing an outlook for future work, based on the outcomes and conclusions of this thesis.

Chapters 2 and 3: Metal cation uptake and relase

The microgels were aimed to be used in biomedical applications or in synthetic biology (*e.g* as granule mimic). Despite their excellent colloidal stability and selectivity towards certain ions like Fe^{3+}, these gels do not release the ions at a biologically-relevant pH values, such as pH=5 or pH=6. Hence, although these microgels are suitable candidates for metal removal and eventual recovery at low pH, and could be used in conditions that mimic the lysosomial environment where the pH is close to 4, they lack the versatility to be used *in vivo*. Hence, these systems should be optimized with new functional groups, that have a higher pKa, such as thiols, and that can bind and release metal cations at close-to-neutral pH. Alternatively, the uptake and release could be driven by the reversible ring opening and closure of photoacids, like in the case of spiropyranes.

Chapters 4 and 5: 3D thermo- and mechanochromic microgel double networks

Despite having shown an effective method to produce 3D microgel-based materials that display structural color, their printing with additive manufacturing has so far not been entirely successful. The main challenge in the formulation of these inks for direct ink writing lies in the fine balance between color formation and the ink's mechanical properties, both of which are dependent onmicrogel size and concentration. Chapter 5 has exhaustively shown how the formulations used were either too liquid when colourful, or on the opposite transparent when the rheology of the inks was appropriate for printing. Other approaches that could render the printing of liquid inks include:

- **Printing into sacrificial networks:** High viscosity, optically transparent cryo-milled PAAc microgels, which are obtained from frozen and mechanically smashed PAAc hydrogels, form optically transparent gels upon rehydration at low wt/V %. These

can be used as scaffolds for 3D printing: They physically support the ink and prevent it from flowing and can then be washed away after curing. Alternatively, the PAAc microgels can be soaked in the same prepolymer, crosslinker and PI as the microgel ink, and crosslinked with the microgels after printing.

- **Printing into a viscous elastomer:** To prevent microgel diffusion and solvent exchange that might impact the crystalline packing of the microgels and interfere with the structural coloration, a hydrophobic scaffold can be used. PDMS, which is hydrophobic, optically transparent and can be cured at RT, can be used as the matrix into which the ink is injected, and then cured at RT, leaving the printed sample inside unaltered in its crystalline packing and coloration.

Chapter 6: Microgel encapsulation in GUVs First, a thorough characterization of the swelling and phase behaviour of the microgels in PEG should be done. Moreover, a more detailed and in depth analysis of the assembled at the interface and at the bulk should be done. After having shown that microgels can be encapsulated into GUVS, their potential as compartments should be proven. This can be done by employing reactions that can be triggered or inhibited by the presence of 2 or more reactants, spatially separated in the GUV's lumen by the microgels. Environmental change, would trigger the shrinking of the microgels, and the expel the reactants from the network and would be helpful to study compartmentalized systems. Moreover, it would be interesting to make microgels/planar polymeric membranes, and study their interaction in function of temperature, and see if they produce structural, responsive coloration.

Chapter 8

Experimental

8.1 Chemicals

N-Vinylcaprolactam (VCL, 98%) was purchased from Sigma-Aldrich and purified via reduced pressure distillation. *N*-isoprylacrylamide (NIPAM, 97%) was recrystallized from hexane. Dimethylitaconate (IADME, 99%), N,N0 -methylene(bis)acrylamide (BIS, 99%), Glycydylmethacrylate (GMA, 98 %), methacrylic acid (MAAc, 99%) hexadecyltrimethylammonium bromide (CTAB, 99%), sodium dodecylsulphate (SDS, 97 %), High viscosity hydroxypropylcellulose (HV HPC) carboxymethylcellulose (90k and 120k g/mol, CMC, 97%), sodium alginate (99%), polyvinylacohol (hydrolized, PVA, 99%),low viscosity hydroxypropylcellulose (LV HPC, 97%), 2-hydroxy-2-methylpropiophenone (PI, 99%), calcium chloridie hexahydrate ($CaCl_2$, 98 %), magnesium chloride ($MgCl_2$ $6H_2O$), strontium chloride ($SrCl_2$ $4H_2O$, 99%), copper chloride ($CuCl_2 6H_2O$, 99%), iron chloride ($FeCl_3$ anhydrous, 99%), uranyl acetate (2% in H_2O, pH= 4.7) and sodium phosphotungstic acid (PTA 1% in H_2O, Ph=7) were purchased from Sigma Aldrich and used as received. 2-Azobis(2-methylproprionamide)dihydrochloride (AMPA, granular, 97%) was purchased from Acros Organic. Acrylamide (40% solution in H_2O), hydrochloric acid stock solution (HCl, 1 M), sodium hydroxide stock solution (NaOH 1 M and 0.01 M) and nitric acid (HNO_3, 12 M) were purchased from Merck. Phosphate buffer saline solution (PBS, without Ca^{2+} and Mg^{2+}) was acquired from Dulbecco. Bifuntional polydimethylsolixane (HO-PDMS-OH) was acquired from ABCR and dried prior to use. Deuterated chloroform ($CDCl_3$) and deuterated water (D_2O) were obtained from Cambridge Isotope Laboratories, Inc. All experiments were performed using Millipore water filtered over a 0.450 mm regenerated cellulose filter with a resistivity of 18 MO $cm^{-}1$ at neutral pH and in the absence of buffer. Each metal ion solution used was made by dissolving the hydrated solid ion powder into degassed MilliQ

water at RT to a final concentration of 100 mM, and used as stock solutions and their exact concentration was measured by ion chromatography.

8.2 Synthetic procedures

8.2.1 General precipitation polymerization procedure

Microgels were synthesized via free radical precipitation polymerization. The procedure was adapted from the literature.[50] Briefly, monomer, comonomer, crosslinker and surfactant were dissolve in filtered MilliQ water at RT, in a three neck round bottom flask equipped with a mechanical stirrer, a thermometer and an inlet for inert gas. The solution was left stirring at 300 rpm for 60 min, while heating up to 70 °C, and N_2 was bubbled through during the 60 min to ensure complete degassing of the solution. A solution of initiator in water (10 ml) was degassed for 10 min and then added in one shot to the degassed reaction mixture. The reaction was allowed to proceed for 3 h under inert atmosphere at 70 °C, and was subsequently quenched by allowing air in the solution and cooling the reaction crude down to RT. The formed gels were purified by dialysis (Spectra /Por(R)7 Dialysis Membrane, Pre-treated RC Tubing, MWCO: 50 kDa) with MilliQ water for where water was exchanged twice daily for 6 days. The gels were then collected and stored in water as stock solutions (PVCL-based microgels) or lyophilized (PNIPAm-based microgels) for further use.

For each microgel produced, 1 ml solution was freeze dried to determine the wt/V% for each sample, and the free dried sample was analyzed for characterization.

8.2.2 Molar amounts for each microgel

In this section are listed the amounts of reactants and volumes used for each produced microgel batch.

P(VCL-*co*-IADME microgels)

P(VCL-*co*-IADME) microgels were obtained following the procedure described in section 1.2.1. The reactant quantities used are listed in Table 8.1 below. Each sample was stored as an aqueous microgel suspension after use.

Table 8.1 Synthetic amounts for VCL-*co*-IADME microgels for a reaction volume of 150 ml.

VCL:IADME ratio	VCL (mmol)	IADME (mmol)	BIS	CTAB (mmol)	AMPA (mmol)
100:0	15	0	0.39	0.027	0.304
95:5	14.25	0.75			
90:10	13.50	1.50			
85:15	12.75	2.25			
80:20	12.00	3.00			

Microgels used in chapter 5, that have the same chemical composition but vary in size were obtained by changing the CTAB concentration, from 5 mg to 12 mg.

P(VCL-*co*-IA) microgels

P(VCL-*co*-IA) microgels that were obtained from direct copolymerization of VCL and IA, were obtained *via* the dispersion polymerization procedure described in section 1.2.1. VCL (1.87 g, 13.5 mmol), IA (0.195 g, 1.5 mmol), CTAB (0.010 g mmol)), AMPA (0.050 g, mmol) were reacted in 150 ml filtered MilliQ water. The reaction pH was adjusted to pH= 4 prior to initiation. The gels were stored as an aqueous solution.

P(VCL-*co*-GMA) microgels

P(VCL-*co*-GMA) microgels were obtained by following the procedure in section 1.2.1, to obtain microgels with 7.5 mol% of GMA and 2.5 mol% of BIS. In brief: VCL (1.548 g, 11.1 mmol), GMA (0.1177 g, 0.82 mmol), BIS (0.060 g, 0.4 mmol), 0.005 g of CTAB (mmol) and 0.027 g of AMPA (0.16 mmol) were solubilized in 150 ml of filtered MilliQ water. Microgels were stored as an aqueous solution after purification.

P(NIPAm-*co*-MAAc)

P(NIPAm-*co*-MAAc) microgels were obtained by following the procedure described in section 1.2.1. Microgels were synthetized to have 5.5 mol% of MAAc and 2.5 mol% of BIS as crosslinker. In brief: NIPAm (2.82 g, 25 mmol), MAAc (0.114 ml, 1.35 mmol), BIS (0.104 g, 0.674 mmol), SDS, and KPS (0.116 g, mmol) were reacted in 250 ml of filtered MilliQ water. Microgels were purified by ultracentrifugation cycles (282k RCF, 2h, 32 ml vessel) in milliQ water, were the supernatant was discarded and the formed pellet resuspended in fresh MilliQ water. The procedure was done 4 times, and the samples were

then freeze-dried for storage. In order to change the size of the resulting gel, SDS was varied. In Table 8.2, are listed the resulting D_H for each SDS amount.

Table 8.2 SDS concentrations used to obtain PNIPAm-based microgels used in Chapter 4.

Microgel	D_H in H_2 (nm)	SDS (mM)
NIPAm-350	267 ± 3	2.1
NIPAM-400	275 ± 4	1.8
NIPAm-450	328 ± 7	1.4

P(NIPAm-*co*-AlAm) microgels

P(NIPAm-*co*-AA) microgels were obtained by following the procedure in section 1.2.1, to obtain microgels with a 10 mol% of AlAm and 2.5 mol% of BIS crosslinker. The amount of SDS was varied to obtain microgels in different sizes. In brief: NIPAm (3.8 g, 33 mmol), AA (0.116 g, 3.3 mmol), SDS (0.066 g, 0.43 mmol) and KPS (0.166 g, 0.6 mmol) in 250 ml of filtered MilliQ water were used. SDS was varied. The resulting radii are listed in Table **??**.

Table 8.3 SDS concentrations used to obtain PNIPAm-AA microgels used in Chapter 5.

Microgel	D_H in H_2 (nm)	SDS (mM)
NIPAm-AA-300	297 ± 38	0.8
NIPAM-AA-400	390 ± 50	0.6
NIPAm-AA-600	580 ± 100	0.3

The resulting microgels were purified by diaylsis against MilliQ water, ver the period of 6 days (3L, 2x daily water exchange).. and then freeze dried for storage.

8.2.3 Postpolymerization approach to microgel modification

Synthesis of VCL-*co*-IA/IADME microgels

Microgels were left stirring for 3 to 7 days in 0.1 M NaOH solution to ensure the hydrolysis of the itaconate moieties to itaconic acid (IA), followed by dialysis (SpectraPor(R)7 Dialysis Membrane, Pre-treated RC Tubing, MWCO: 50 kDa) against MilliQ water for 4 days and left in water as stock solutions for further use. To determine the weight concentration 2 ml of microgel solution were freeze-dried and weighted on a high precision balance.

8.2.4 PMOxa-*b*-PDMS-*b*-PMOxa synthesis

The synthesis of PMOxa-*b*-PDMS-**b**-PMOxa was performed by Sven Kasper, following a previously optimized protocol. Commercial hydroxyl terminated PDMS (OH-PDMS-OH) was dried under high vacuum over night. AAfter bubbling, freshly destilled Triethylamine (TEA) was added and the mixture was cooled to -20 °C. PDMS was then reacted with Trifluoromethanesulfonic acid (Tfsa) for 3h at -20°C resulting in a bifunctional triflic PDMS macroinitiator. The reactionmixture was filterd through a cooled G4 filter under Argon. From the filtrate Hexane was removed under Vacuum and replaced by dry Ethylacetate. Adding destilled 2-Methyl-2-oxazolin resulted in a cationic ring opening polymerisation of Polymethyoxazolin (PMOXA) on the PDMS macroinitiator. Termination was performed after 60h at 40°C, by adding a 2:8 mixture of TEA:Water resulting in bifunctional OH terminal groups on the PMOXA blocks. Finally the solvent was removed by vacuum distillation. Purification was done by resolubilizing the polymer in Ethanol/Water 1:1 mixture and ultrafiltrating through a 5 KDa Membrane.

8.2.5 PDMS-*b*-PMOxa synthesis

The synthesis of PDMS-*b*-PMOxa was performed by Dr. Riccardo Wehr. The procedure described is adapated from his doctoral thesis, section 5.3.2, where the detailed syntheisis is described. In brief, Hexamethylcyclotrisiloxane (D_3) was dried over CaH_2 and distilled under vacuum. Freshly distilled D_3 was resuspended in anhydrous cyclohexane, followed by the drop-wise addition of *b*-butyllitium (BuLi). After 4 stirring at RT, the reaction mixture was diluted with dry THF and allowed to proceed for 38.5 h. Dimethylchlorosilane was then added to quench the reaction, and the unreacted monomer, togther with the solvent was removed under reduced pressure. The reulting hydryde terminated PDMS-H was dissolved in dry toluene and 2-allyloxyethanol was added to the solution, together with platinum(0)-1,-divynil-1,1,3,3-tetramethyldisiolaxane complex, and allowed to proceeed overnight at 110 °C. The crude was purified by evaporation of the solvent under reduced pressure and the resulting yellow oil was dissolved in dichloromethane. The solution was filtered through celite S and evaporated, yielding a colorless oil (PDMS-OH, M_n (NMR)= 2000 g/mol PDI (GPC)= 1.17). PDMS-OH was dried under high vacuum overnight at 100 °C. PDMS-OH was dissolved in anhydrous hexane and triethylamine, while being cooled down with an ice/NaCl azeotrope and stirred for 15 min. Triflic anhydride was added dropwise under cooling, and the mixture was left reacting for 4 h. The solution was filtered through a glas frit under inert atmosphere to remove the precipitate triflate salt. The solvent was evaporated and activated PDMS-OTf was dissolved in dried ethylacetate and freshly distllied MOXa was added to the

solution and left stirring at 40 °for 63. The crude was purified by precipitation of the PDMS in EtOH, and subsequent centrifugation (4000 rpm, 10 min). The supernatant was collected and the solvent evaporated under reduced pressure and the polymer was dialyzed against a 1:1 mixture of EtOH/Water, gradually increasing the water concentration to 100% water over 5 days. The precipitated polymer was lyophilized. The polymer was then resolubilized in MeOH and then extracted twice in hexane. The MeOH phase was evaporated and the polymer was obtained as a pale yellow wax (M_n= 2850 g/mol, PDI (GPC)= 1.19)

8.3 Characterization methods

8.3.1 NMR

NMR spectra were acquired in deuterated solvents (Chloroform−d or deuterated water) on a Bruker 400 MHz (^1H : 400 MHz; Bruker, USA) spectrometer at room temperature utilizing 256 scans with a 0.1 wt% microgel concentration. Chemical shifts (δ) are reported in ppm, whereas the chemical shifts are calibrated to the main solvent residual peaks. The collected spectra were analyzed using MestReNova (v9.1) (Mestrelab Research S.L).

8.3.2 FT-IR

Background corrected attenuated total reflection-Fourier transform infrared spectroscopy (ATR-FTIR) spectra were recorded on a Bruker spectrophotometer in the range of 4000−400 cm^{-1}, using 128 scans at a nominal resolution of 4 cm^{-1} using a diamond single reflection ATR. Atmospheric compensation and offset correction were applied on the collected spectra to determine the degree of hydrolysis by following the presence of the methyl groups relative the IADME monomer on freeze-dried samples. The ATR-FTIR spectra were evaluated with the use of OPUS spectroscopy software (v7.0) (Bruker Optics).

8.3.3 Potentiometric titration

The pH sensitivity, the determination of the acid groups of the resulting microgels were evaluated by potentiometric titrations and the pKa values were determined in the pH value range of 5−9 using a Zetasizer Nano ZsP (Malvern Instruments). For the titration and pH detection of 0.1 wt% microgel solutions, prepared by using Millipore pure water MPT−2 multi-purpose titrator (Malvern Instruments) with a MV114−SC Malvern Comb Glass Electrode were used. The aqueous solutions were titrated with NaOH solution (0.01 M) at increments with an interval of 0.5. The ζ potential as well as the change of the particle

size were determined at room temperature as the average of 3 measurements. The collected datasets were analyzed using Zetasizer Software (v7.0) (Malvern Instruments).

8.3.4 Gel Permeation chromatography (GPC)

GPC was measured using an HPLC grade DMF (Schalrlau, Germany) at 60 °C at a flow rate of 1 ml/min. Calibration was done prior to measurement, by using low dispersity molecular weight poly(methylmethacrylate) (PMMA). The viscotek TDA device was set up with three SDV Linear S colums (5 μm 8x300 mm, PSS, Germany), a PSS precolum (SDV, 5 μm 8x50 mm) and a refractive index detector. The instrument was controlled by a WinGPC UniCHrom software (version 8.20, PSS).

8.3.5 TEM

Microgel morphologies and group distribution were determined via TEM imaging with a Philips Morgagni 268D microscope (Philips., the Netherlands). Microgel solutions in water at 0.01 wt% were deposited on a carbon-coated copper grid. The samples were blotted, washed and negatively stained with a solution of 1% sodium phosphotungstic acid (PTA) solution. TEM images were acquired at an accelaration of 80 kV, and each grid was imaged in at least three different points.

8.3.6 SEM

Scanning electron microscopy was used to image micrometer-sized objects and microgels packed on surfaces. The samples (1 mg/ml) were deposited on a cleaned silicon wafer (2x isopropanol, 1x water, 1x acetone) and allowed to dry overnight. The samples were sputter-coated with 10 nm Au layer. SEM images were acquired with a XL30 FEG (XL series, Philips, The netherlands) microscope, with an acceleration of 5 kV.

8.3.7 DLS

Dynamic light scattering (DLS) was used to measure the hydrodynamic diameter (D_H) of the microgels by using a Zetasizer Nano ZsP (Malvern Instruments). Measurements were taken at 20 °C, after an equilibration time of 420 s with a back scattering angle of 173 °(NIBS technology, Malvern). The samples were filtered prior to measurement, placed in a PS microcuvette (Malvern Instruments), and measured after 7 in of equilibration time.

8.3.8 SLS

Static light scattering (SLS) measurements were performed with an LS spectrometer (LS Instruments, Switzerland) equipped with a HeNe laser (633 nm) with varying scattering angles in 2D/pseudo cross-correlation mode. All measurements were carried out at 20 °C and averaged over 3 measurements of 60 seconds each. Scattering data was measured between 30 and 120 °and fitted using the Guinier fitting to determine the radius of gyration R_g. The natural logarithm of the signal intensity (LnI) was plotted against the scattering vector (q^2) in the Guinier regime (30-55 °) and fitted with a linear fit. The R_g was calculated from the slope of the fit (slope= R_g/3).

8.3.9 Turbidimetry

Turbidimetry changes were measured with of an automatized injector coupled to a SpectraMax device. Datapoints were collected for 120 s, with a measurement interval of 0.5 s.

8.3.10 Ion chromatography

The metal cation uptake by the microgels was measured via ion chromatography with a 940 Professional IC Vario (Metrohm). 30 μl samples were eluted on a 250mm$x$40mm column with an elution flux of 0.8 ml/min in HNO_3 (7.25 mM) at 30 °C. Three independent measurements were used to evaluate one data point.

8.3.11 Confocal scanning microscopy (CLSM)

CLSM imaging was performed with a Zeiss 880 confocal laser microscope (Zeiss, Germnay), equipped with a Plan-Apochromat 20x/0.8 M27 objective and controlled by Zen Black software (Zeiss). Rhodamine was excited with a 633 HeNe laser. Images were recorded with an image size of 1024x1024 pixels, a bit depth of 16 bit and 1 Airy unit. Laser power and gain were adjusted depending on the measurements. Z-stacks and 3 D reconstructions were done by taking snaps along the focal plane, setting manually the lowest and highest z-height. The slices were taken at an equal distance from each other. Time measurements were used in Airyscan mode, to increase the time resolution of the images. Image processing was done using FiJi (ImajeJ, NIH, USA).

8.3.12 Oscillatory rheology

Oscillatory rheology of jammed microgels, soaked in AAm was performed on a DHR-3 TA Instrument (TA, USA), using an 8 mm diameter parallel plate steel geometry, and controlled by TRIOS software (TA, USA). All measurements were performed at RT, with a 800 μm gap. Amplitude sweep measurements were performed at 1.0 rad^{-1} oscilaltion. Frequency sweep measurements were made at 1% strain. Shear recovery (self-healing) measurements were performed at 1.0 rad^{-1}, alternating 300 s at 1% strain and 10% strain, with no soak time in between strain changes. Each sample was allowed to equilibrate for 300s before each measurement.

8.3.13 Macro Imaging

Macroscopic images were taken with an iPhone 12 (Apple, USA) equipped with a 12 MPixel camera and a RedMi Note 10 Pro (Xiaomi, China) equipped with a 8 MPixel camera.

8.4 Experimental methods

8.4.1 Metal cation triggered gel collapse.

The microgels were dispersed in a metal cation (chloride salt) solution at different dilutions (100, 10, 1, 0.5, 0.1, 0.05, 0.01 and 0.001 mM) to a final concentration of 0.02 wt% of microgels at pH= 7. The equilibration time of the microgels were set on 10 min under continous shaking and subsequently analyzed *via* DLS at RT and neutral pH.

8.4.2 Metal cation microgel loading

Microgels were dispersed in a metal cation (chloride salt) solution with a final microgel concentration of 0.1 wt% (5 ml water) at pH= 7, and left agitating on a shaker overnight. Microgels and blank cation solutions were centrifuged in a Vivaspin 20 centrifuge filter (Sartorius Stedim biotech, Vivaspin 20, MWCO PES: 10 kDa) at 2000 rpm for 40 min to obtain 4 mL of filtered sample. The filtrate was collected for further analysis. The concentrated metal cation loaded microgels (remaining 1 ml) were diluted back to 5 mL with acidic solution to obtain final pH of 2, 3, 4 and 5. The samples were left shaking for 1 h, followed by centrifugation (2000 rpm for 1h at 20 °C) and the filtrate was collected for further analysis.

8.4.3 Metal leaching

Microgels (0.1 wt% were loaded with a metal cation and washed once with Millipore pure water by centrifuging utilizing Vivaspin 20 centrifuge filters (Sartorius Stedim biotech, Vivaspin 20, MWCO PES: 10 kDa). The gels were left shaking for 30 minutes in Millipore pure water (5mL) at pH= 7, and centrifuged for 30 min. The procedure was repeated 10 times. The filtrate was analyzed via ion chromatography to determine the amount of metal cation released from the gels over time.

8.4.4 Metal cation release

Loaded microgels were transferred to solutions at pH 2, 3, 4 and 5, with an equilibration time of 10 minutes. The gels where then centrifuged in a Vivaspin 20 centrifuge filter (Sartorius Stedim biotech, Vivaspin 20, MWCO PES: 10 kDa) and the filtered water was analyzed via Ion Chromatography.

8.4.5 System reversibility

To determine whether the loading and unloading of a microgel system is reversible, reversibility test was performed. The reversibility experiment consisted in the Mg^{2+} loading ($MgCl_2$) into a 5 mL 0.1 wt% microgel solution at pH 7 and RT in a VIVASPIN 20 ®centrifuge filter (Sartorius Stedim biotech, Vivaspin 20®, MWCO PES: 10 kDa) and equilibration of the sample for 2 h. The sample was centrifuged and washed with MilliQ water, and redispersed to a final volume of 5 mL. The pH of the sample was subsequently lowered to 2 with 1M HCl, and the microgels solution was left equilibrating for 2 h at RT. The sample was then centrifuged (40 min, 2000 rpm), and subjected three times to dispersion in MilliQ water at pH 7 and RT for 2 h and centrifugation (40 min, 2000 rpm). Each microgel free filtrate was collected and analysed via ion chromatography. The abovementioned cycle was repeated three times.

8.4.6 Competition between metal cations

To describe the selectivity of the uptake of a certain ion M^{n+} (Mg^{2+}, Sr^{2+}, Cu^{2+} and Fe^{3+}) solutions containing the same amount of different metal ions were mixed with a microgel solution to a final volume of 5 mL, final M^{n+} concentration of 1 mM for each ion and a final microgel concentration of 0.1 wt%. The gels were left equilibrating overnight on a shaker at RT and neutral pH and subsequently centrifuged with a VIVASPIN 20®centrifuge filter

(Sartorius Stedim biotech, Vivaspin 20, MWCO PES: 10 kDa), and the filtrated was collected for analysis. The amount of M^{n+} bonded was determined by ion chromatography.

8.4.7 Microgels soaking and jamming procedure

General procedure

Solutions composed of 1 wt/V% of microgels, 10 wt/V% of AAm, 0.25 mol% BIS (in respect to AAm content) and 1 mol% of PI (in respect to AAm content) were left equilibrating in the dark at 4 °C over night, or at least fr 2 h. The sample (32 mL) was transferred into an Optiseal tube (polypropylene, 32 ml) (Beckmann Coulter, Switzerland), sealed with a stopper and equipped with an amber spacer. The sample was centrifuged at 50k rpm for 2 h (in a MLA-50 rotor) at RT. The sample was retrieved by slicing the tube open and scooping the sample out with a single use spatula, and tranferring the sample into a 3 ml Luer Lock syringe. The sample was kept in the dark at RT for further use.

8.4.8 3D printing procedure

General 3D printing procedure

The jammed microgel pellet in a Luer-lock syringe was transferred into a brown Luer-Lock syringe compatible with the 3D printer. Additive manufacturing was done by using a commercial 3D bioprinter (Inkredible+, Cellink, USA). The microgels were extruded from a 21 gauge syringe through a pressure driven piston with varying pressures, depending on the sample (30-140 kPa). Printing was controlled by G-code commands generated by a built in machine software (Cellink, HeartWare). Printing was performed on polystyrene substrate with a starting gap of 0.1 mm. Printed structures were crosslinked under UV light (UVP CL-1000, Analytik Jena, 365 nm, 2 mW/cm^2, for 10 min at RT.

Photocuring

Pellets, molded and extruded microgels, soaked in AAm and crosslinker were exposed to UV light for 15 min at RT. The UV lamp (CAMAG UV lamp 4, Switzerland) had a power of 2 mW/cm^2.

8.4.9 Vesicle self-assembly *via* "solvent switch" method

8 mg of PMOxa-*b*-PDMS-*b*-PMOxa were solubilised in 0.400 ml of THF, and left stirring for at least 1 h at 300 rpm. 1.6 ml of microgel solution in buffer (soaked overnight) was injected

via a syringe pump with a low rate of 0.1 ml/min. THF was removed by dialysis (SpectraPor 1 kDa MWCO) against MilliQ water or the adequate buffer. Buffers used: MilliQ (no added salts), PBS (without Ca^{2+} and Mg^{2+}) bicarbonate buffer pH=9 or Boric acid buffer pH=9.2. The sample was then kept as a suspension and diluted 1:10 for TEM anaylsis.

8.4.10 Vesicle self-assembly *via* "film rehydration" method

PMOxa-*b*-PDMS-*b*-PMOxa (6 mg/ml, 40 μl) were placed in a 2.5 ml vial, and dried under high vacuum overnight. A 1 wt/V% suspension of microgels was prepared and allowed to soak overnight. The dried film was rehydrated upon gentle addition of 200 μl of microgel containing buffer with a 200 μl pipette. The pipette tip was used to gently scrape the film and move the buffer around. The vila was then sealed and the film was left swelling overnight at RT and no shaking. The sample was diluted 1:10 in MilliQ water and imaged with CLSM.

8.4.11 GUVs self assembly *via* double emulsion-templated microfluidic

Microgles were encapsulated in monodisperse microscopic GUVs via double emulsion-templated microfluidics. Double emulsions were obtained as water/oil/water emulsions in a 6-way junction silicon microfluidic chip with 50 μm channels, with liquid flow rates regulated by a three-module precision syringe pump (low pressure, NEMESYS, Cetoni)

Microgels (1 or 5 wt/V%) were dispersed in a solution of 10 wt% of PEG (Mw 6000) in MilliQ water, and allowed to swell for at least 1 h. The dispersion was used as inner aquous phase (IA). IA was enveloped by an orgenic polymer phase (PO) containing 6 mg/ml of PDMS-*b*-PMOxa in a 3:2 Hexane:Chloroform solution (V:V), and periodically ruptured by an outer aqueous phase (OA), composed of 5 wt/V% of hydrolyzed poly(vinyl acohol) (PVA, 18-23 KDa), 400 mM NaCl in MilliQ water. Flow rates were used as follows: OA was set to 50 μl/min, PO to μl/min and IA to 2 μl/min. OA and PO were filtered on a 200 μm filter with adequate polarity prior to use.

The double emulsions were collected for 10 min, in a 2 mL eppendorf snapcap, filled with 100 μl OA at RT. The sample was then left equilibrating for 1 h prior to imaging, to allow the organic phase to evaporate and let the polymer assemble into GUVs.

References

[1] Felix A. Plamper and Walter Richtering. Functional microgels and microgel systems. *Accounts of Chemical Research*, 50:131–140, 2017.

[2] A. Lee, H.-Y. Tsai, and M. Z. Yates. Steric stabilization of thermally responsive n-isopropylacrylamide particles by poly(vinyl alcohol). *Langmuir*, 26:18055–18060, 11 2010.

[3] Susanne Wiese, Antje C. Spiess, and Walter Richtering. Microgel-stabilized smart emulsions for biocatalysis. *Angewandte Chemie*, 125:604–607, 1 2013.

[4] L. Andrew Lyon and Alberto Fernandez-Nieves. The polymer/colloid duality of microgel suspensions. *Annual Review of Physical Chemistry*, 63:25–43, 5 2012.

[5] Garima Agrawal and Rahul Agrawal. Stimuli-responsive microgels and microgel-based systems: Advances in the exploitation of microgel colloidal properties and their interfacial activity, 4 2018.

[6] A. Fernandez-Nieves, A. Fernández-Barbero, B. Vincent, and F. J. de las Nieves. Osmotic de-swelling of ionic microgel particles. *The Journal of Chemical Physics*, 119:10383–10388, 11 2003.

[7] Brian R. Saunders, Helen M. Crowther, and Brian Vincent. Poly[(methyl methacrylate)-co-(methacrylic acid)] microgel particles: swelling control using ph, cononsolvency, and osmotic deswelling. *Macromolecules*, 30:482–487, 2 1997.

[8] B R Saunders and B Vincent. Osmotic de-swelling of polystyrene microgel particles. *Journal of Colloid Science*, 275:9–17, 1997.

[9] Olga Mergel, Patrick Wünnemann, Ulrich Simon, Alexander Böker, and Felix A. Plamper. Microgel size modulation by electrochemical switching. *Chemistry of Materials*, 27:7306–7312, 10 2015.

[10] Liqiang Zhu, Chuanzhuang Zhao, Jiawei Zhang, and Dirong Gong. Photocontrollable volume phase transition of an azobenzene functionalized microgel and its supramolecular complex. *RSC Advances*, 5:84263–84268, 2015.

[11] Juan-Jose Lietor-Santos, Benjamin Sierra-Martin, Ronny Vavrin, Zhibing Hu, Urs Gasser, and Alberto Fernandez-Nieves. Deswelling microgel particles using hydrostatic pressure. *Macromolecules*, 42:6225–6230, 7 2009.

[12] Katja Nothdurft, David H. Müller, Sonja D. Mürtz, Anna A. Meyer, Luis P. B. Guerzoni, Alexander Jans, Alexander J. C. Kühne, Laura De Laporte, Thorsten Brands, André Bardow, and Walter Richtering. Is the microgel collapse a two-step process? exploiting cononsolvency to probe the collapse dynamics of poly-n-isopropylacrylamide (pnipam). *The Journal of Physical Chemistry B*, 125:1503–1512, 1 2021.

[13] Vittoria Chimisso, Simona Conti, Phally Kong, Csaba Fodor, and Wolfgang P. Meier. Metal cation responsive anionic microgels: behaviour towards biologically relevant divalent and trivalent ions. *Soft Matter*, 17:715–723, 1 2021.

[14] Jung Kwon Oh, Ray Drumright, Daniel J. Siegwart, and Krzysztof Matyjaszewski. The development of microgels/nanogels for drug delivery applications. *Progress in Polymer Science (Oxford)*, 33:448–477, 4 2008.

[15] Courtney D. Sorrell and Michael J. Serpe. Reflection order selectivity of color-tunable poly(n-isopropylacrylamide) microgel based etalons. *Advanced Materials*, 23:4088–4092, 9 2011.

[16] Yuta Koda, Takaya Terashima, Mikihito Takenaka, and Mitsuo Sawamoto. Star polymer gels with fluorinated microgels via star–star coupling and cross-linking for water purification. *ACS Macro Letters*, 4:377–380, 3 2015.

[17] Miguel Angel Fernandez-Rodriguez, Alberto Martín-Molina, and Julia Maldonado-Valderrama. Microgels at interfaces, from mickering emulsions to flat interfaces and back. *Advances in Colloid and Interface Science*, 288, 2 2021.

[18] Heather M. Shewan and Jason R. Stokes. Review of techniques to manufacture micro-hydrogel particles for the food industry and their applications, 2013.

[19] Fengyun Li, Danya Lyu, Shuo Liu, and Weiwei Guo. Dna hydrogels and microgels for biosensing and biomedical applications, 1 2020.

[20] Walter Richtering. Responsive emulsions stabilized by stimuli-sensitive microgels: Emulsions with special non-pickering properties. *Langmuir*, 28:17218–17229, 10 2012.

[21] Neil B Graham and Audrey Cameron. Nanogels and microgels: The new polymeric materials playground, 1998.

[22] Walter Richtering Andrij Pich. *Chemical Design of Responsive Microgels*. 2010.

[23] Clinton D. Jones and L. Andrew Lyon. Synthesis and characterization of multiresponsive coreshell microgels. *Macromolecules*, 33:8301–8306, 10 2000.

[24] Janine Dubbert, Katja Nothdurft, Matthias Karg, and Walter Richtering. Core-shell-shell and hollow double-shell microgels with advanced temperature responsiveness. *Macromolecular Rapid Communications*, 36:159–164, 1 2015.

[25] Anne C. Nickel, Timon Kratzenberg, Steffen Bochenek, Maximilian M. Schmidt, Andrey A. Rudov, Andreas Falkenstein, Igor I. Potemkin, Jérôme J. Crassous, and Walter Richtering. Anisotropic microgels show their soft side. *Langmuir*, 0, 9 2021.

[26] Agnieszka Natalia Ksiazkiewicz, L. Bering, F. Jung, Nadja Anna Wolter, Jörn Viell, Alexander Mitsos, and Andrij Pich. Closing the 1–5µm size gap: Temperature-programmed, fed-batch synthesis of µm-sized microgels. *Chemical Engineering Journal*, 379, 1 2020.

[27] Ethan Tumarkin and Eugenia Kumacheva. Microfluidic generation of microgels from synthetic and natural polymers. *Chemical Society Reviews*, 38:2161–2168, 2009.

[28] Andreas J.D. Krüger, Onur Bakirman, Luis P.B. Guerzoni, Alexander Jans, David B. Gehlen, Dirk Rommel, Tamás Haraszti, Alexander J.C. Kuehne, and Laura De Laporte. Compartmentalized jet polymerization as a high-resolution process to continuously produce anisometric microgel rods with adjustable size and stiffness. *Advanced Materials*, 31, 12 2019.

[29] Benjamin Kessel, Mihyun Lee, Angela Bonato, Yann Tinguely, Enrico Tosoratti, and Marcy Zenobi-Wong. 3d bioprinting of macroporous materials based on entangled hydrogel microstrands. *Advanced Science*, 7, 9 2020.

[30] Matteo Hirsch, Alvaro Charlet, and Esther Amstad. 3d printing of strong and tough double network granular hydrogels. *Advanced Functional Materials*, 31, 1 2021.

[31] M. Constantin, M. Cristea, P. Ascenzi, and G. Fundueanu. Lower critical solution temperature versus volume phase transition temperature in thermoresponsive drug delivery systems. *Express Polymer Letters*, 5:839–848, 10 2011.

[32] Luqin Hua, Manqing Xie, Yukun Jian, Baoyi Wu, Chongyi Chen, and Chuanzhuang Zhao. Multiple-responsive and amphibious hydrogel actuator based on asymmetric ucst-type volume phase transition. *ACS Applied Materials amp; Interfaces*, 11:43641–43648, 10 2019.

[33] Coro Echeverria, Daniel López, and Carmen Mijangos. Ucst responsive microgels of poly(acrylamideacrylic acid) copolymers: Structure and viscoelastic properties. *Macromolecules*, 42:9118–9123, 10 2009.

[34] Wenjuan Su, Kongshuang Zhao, Jingjing Wei, and To Ngai. Dielectric relaxations of poly(n-isopropylacrylamide) microgels near the volume phase transition temperature: Impact of cross-linking density distribution on the volume phase transition. *Soft Matter*, 10:8711–8723, 11 2014.

[35] Martina Keerl and Walter Richtering. Synergistic depression of volume phase transition temperature in copolymer microgels. *Colloid and Polymer Science*, 285:471–474, 1 2007.

[36] Daniel Crespy and René M. Rossi. Temperature-responsive polymers with lcst in the physiological range and their applications in textiles. *Polymer International*, 56:1461–1468, 12 2007.

[37] Alexander A. Steinschulte, Andrea Scotti, Khosrow Rahimi, Oleksii Nevskyi, Alex Oppermann, Sabine Schneider, Steffen Bochenek, Marie F. Schulte, Karen Geisel, Felicitas Jansen, Andre Jung, Sabrina Mallmann, Roland Winter, Walter Richtering, Dominik Wöll, Ralf Schweins, Nicholas J. Warren, and Felix A. Plamper. Stimulated

transitions of directed nonequilibrium self-assemblies. *Advanced Materials*, 29, 11 2017.

[38] Wenhui Sun, Zesheng An, and Peiyi Wu. Ucst or lcst? composition-dependent thermoresponsive behavior of poly(n-acryloylglycinamide-co-diacetone acrylamide). *Macromolecules*, 50:2175–2182, 3 2017.

[39] Zeeshan Ahmed, Edward A. Gooding, Konstantin V. Pimenov, Luling Wang, and Sanford A. Asher. Uv resonance raman determination of molecular mechanism of poly(n-isopropylacrylamide) volume phase transition. *The Journal of Physical Chemistry B*, 113:4248–4256, 3 2009.

[40] Andy C. W. Lau and Chi Wu. Thermally sensitive and biocompatible poly(n-vinylcaprolactam): synthesis and characterization of high molar mass linear chains. *Macromolecules*, 32:581–584, 1 1999.

[41] Larisa M. Mikheeva, Natalia V. Grinberg, Alexander Ya. Mashkevich, Valerij Ya. Grinberg, Le Thi Minh Thanh, Elena E. Makhaeva, and Alexei R. Khokhlov. Microcalorimetric study of thermal cooperative transitions in poly(n-vinylcaprolactam) hydrogels. *Macromolecules*, 30:2693–2699, 5 1997.

[42] Ainara Imaz and Jacqueline Forcada. N-vinylcaprolactam-based microgels for biomedical applications. *Journal of Polymer Science, Part A: Polymer Chemistry*, 48:1173–1181, 3 2010.

[43] Justin D. Debord and L. Andrew Lyon. Synthesis and characterization of ph-responsive copolymer microgels with tunable volume phase transition temperatures. *Langmuir*, 19:7662–7664, 7 2003.

[44] Courtney D. Sorrell, Matthew C.D. Carter, and Michael J. Serpe. Color tunable poly (n-isopropylacrylamide)-co-acrylic acid microgel-au hybrid assemblies. *Advanced Functional Materials*, 21:425–433, 2 2011.

[45] Molla R. Islam and Michael J. Serpe. Penetration of polyelectrolytes into charged poly(n-isopropylacrylamide) microgel layers confined between two surfaces. *Macromolecules*, 46:1599–1606, 2 2013.

[46] Helene Dalmont, Orawan Pinprayoon, and Brian R. Saunders. Study of ph-responsive microgels containing methacrylic acid: Effects of particle composition and added calcium. *Langmuir*, 24:2834–2840, 2008.

[47] Susann Schachschal, Andreea Balaceanu, Claudiu Melian, Dan E. Demco, Thomas Eckert, Walter Richtering, and Andrij Pich. Polyampholyte microgels with anionic core and cationic shell. *Macromolecules*, 43:4331–4339, 4 2010.

[48] Larisa V. Sigolaeva, Dmitry V. Pergushov, Marina Oelmann, Simona Schwarz, Monia Brugnoni, Ilya N. Kurochkin, Felix A. Plamper, Andreas Fery, and Walter Richtering. Surface functionalization by stimuli-sensitive microgels for effective enzyme uptake and rational design of biosensor setups. *Polymers*, 10, 7 2018.

[49] Sarah K. Wypysek, Andrea Scotti, Mohammed O. Alziyadi, Igor I. Potemkin, Alan R. Denton, and Walter Richtering. Tailoring the cavity of hollow polyelectrolyte microgels. *Macromolecular Rapid Communications*, 41, 1 2020.

[50] Andreea Balaceanu, Dan E. Demco, Martin Möller, and Andrij Pich. Microgel heterogeneous morphology reflected in temperature-induced volume transition and 1h high-resolution transverse relaxation nmr. the case of poly(n-vinylcaprolactam) microgel. *Macromolecules*, 44:2161–2169, 3 2011.

[51] Nicole Welsch, Matthias Ballauff, and Yan Lu. *Microgels as Nanoreactors: Applications in Catalysis*. 2010.

[52] Xianjing Zhou, Jingjing Nie, and Binyang Du. Functionalized ionic microgel sensor array for colorimetric detection and discrimination of metal ions. *ACS Applied Materials amp; Interfaces*, 9:20913–20921, 6 2017.

[53] Todd Hoare and Robert Pelton. Titrametric characterization of ph-induced phase transitions in functionalized microgels. *Langmuir*, 22:7342–7350, 7 2006.

[54] De Wei Yin, Ferenc Horkay, Jack F. Douglas, and Juan J. De Pablo. Molecular simulation of the swelling of polyelectrolyte gels by monovalent and divalent counterions. *Journal of Chemical Physics*, 129, 2008.

[55] Gabriel S. Longo, Monica Olvera de la Cruz, and I. Szleifer. Molecular theory of weak polyelectrolyte gels: The role of ph and salt concentration. *Macromolecules*, 44:147–158, 12 2010.

[56] Julien Es Sayed, Christophe Meyer, Nicolas Sanson, and Patrick Perrin. Oxidation-responsive emulsions stabilized by cleavable metallo-supramolecular cross-linked microgels. *ACS Macro Letters*, 9:1040–1045, 7 2020.

[57] Ferenc Horkay, Ichiji Tasaki, and Peter J. Basser. Effect of monovalentdivalent cation exchange on the swelling of polyacrylate hydrogels in physiological salt solutions. *Biomacromolecules*, 2:195–199, 12 2000.

[58] Shufu Peng and Chi Wu. Ca2+-induced thermoreversible and controllable complexation of poly(n-vinylcaprolactam-co-sodium acrylate) microgels in water. *The Journal of Physical Chemistry B*, 105:2331–2335, 3 2001.

[59] Gary M. Eichenbaum, Patrick F. Kiser, Dipak Shah, William P. Meuer, David Needham, and Sidney A. Simon. Alkali earth metal binding properties of ionic microgels. *Macromolecules*, 33:4087–4093, 2000.

[60] Qiang Matthew Zhang, Xue Li, Molla R. Islam, Menglian Wei, and Michael J. Serpe. Light switchable optical materials from azobenzene crosslinked poly(n-isopropylacrylamide)-based microgels. *Journal of Materials Chemistry C*, 2:6961–6965, 9 2014.

[61] Antonio Garcia, Manuel Marquez, Tong Cai, Rohit Rosario, Zhibing Hu, Devens Gust, Mark Hayes, Sean A. Vail, and Choong-Do Park. Photo-, thermally, and ph-responsive microgels. *Langmuir*, 23:224–229, 10 2006.

[62] Joachim Jelken, Se Hyeong Jung, Nino Lomadze, Yulia D. Gordievskaya, Elena Yu Kramarenko, Andrij Pich, and Svetlana Santer. Tuning the volume phase transition temperature of microgels by light. *Advanced Functional Materials*, 32, 1 2022.

[63] Michael Sommer. Substituent effects control spiropyran–merocyanine equilibria and mechanochromic utility, 1 2021.

[64] Meng Li, Qi Zhang, Yin-ning Zhou, and Shiping Zhu. Progress in Polymer Science Let spiropyran help polymers feel force ! *Progress in Polymer Science*, 79:26–39, 2018.

[65] Chaolei Hu, Wenjing Xu, Christian Martin Conrads, Jingnan Wu, and Andrij Pich. Visible light and temperature dual-responsive microgels by crosslinking of spiropyran modified prepolymers. *Journal of Colloid and Interface Science*, 582:1075–1084, 1 2021.

[66] Alexander K Chibisov and Helmut Gorner. Complexes of spiropyran-derived merocyanines with metal ions: relaxation kinetics, photochemistry and solvent effects, 1998.

[67] Jörg Kohl-Landgraf, Markus Braun, Cem Özçoban, Diana P. N. Gonçalves, Alexander Heckel, and Josef Wachtveitl. Ultrafast dynamics of a spiropyran in water. *Journal of the American Chemical Society*, 134:14070–14077, 8 2012.

[68] Matthew J. Feeney and Samuel W. Thomas. Tuning the negative photochromism of water-soluble spiropyran polymers. *Macromolecules*, 51:8027–8037, 10 2018.

[69] Pooyan Makvandi, Sidra Iftekhar, Fabio Pizzetti, Atefeh Zarepour, Ehsan Nazarzadeh Zare, Milad Ashrafizadeh, Tarun Agarwal, Vinod V T Padil, Reza Mohammadinejad, Mika Sillanpaa, Tapas Kumar Maiti, Giuseppe Perale, Ali Zarrabi, and Filippo Rossi. Functionalization of polymers and nanomaterials for water treatment, food packaging, textile and biomedical applications: a review. *Environmental Chemistry Letters*, 19:583–611, 12 2021.

[70] Fanyong Yan, Keqing Fan, Zhangjun Bai, Ruiqi Zhang, Fanlin Zu, Jinxia Xu, and Xiang Li. Fluorescein applications as fluorescent probes for the detection of analytes, 12 2017.

[71] Manuel Natali, Christer Aakeröy, John Desper, and Silvia Giordani. The role of metal ions and counterions in the switching behavior of a carboxylic acid functionalized spiropyran. *Dalton Transactions*, 39:8269–8277, 9 2010.

[72] Tao Liu, Jinming Hu, Jun Yin, Yanfeng Zhang, Changhua Li, and Shiyong Liu. Enhancing detection sensitivity of responsive microgel-based cu(ii) chemosensors via thermo-induced volume phase transitions. *Chemistry of Materials*, 21:3439–3446, 7 2009.

[73] Qiang Matthew Zhang, Wenda Wang, Ya-Qiong Su, Emiel J. M. Hensen, and Michael J. Serpe. Biological imaging and sensing with multiresponsive microgels. *Chemistry of Materials*, 28:259–265, 12 2015.

[74] Markus Stieger, Jan Skov Pedersen, Peter Lindner, and Walter Richtering. Are thermoresponsive microgels model systems for concentrated colloidal suspensions? a rheology and small-angle neutron scattering study. *Langmuir*, 20:7283–7292, 7 2004.

[75] Qing Wu, Teng Su, Yanjie Mao, and Qigang Wang. Thermal responsive microgels as recyclable carriers to immobilize active proteins with enhanced nonaqueous biocatalytic performance. *Chemical Communications*, 49:11299–11301, 11 2013.

[76] Della S. Shin, Emi Y. Tokuda, Jennifer L. Leight, Connor E. Miksch, Tobin E. Brown, and Kristi S. Anseth. Synthesis of microgel sensors for spatial and temporal monitoring of protease activity. *ACS Biomaterials Science amp; Engineering*, 4:378–387, 3 2017.

[77] Sarah Boesveld, Alexander Jans, Dirk Rommel, Matthias Bartneck, Martin Möller, Lothar Elling, Christian Trautwein, Pavel Strnad, and Alexander J. C. Kuehne. Microgels sopping up toxins—gm1a-functionalized microgels as scavengers for cholera toxin. *ACS Applied Materials amp; Interfaces*, 11:25017–25023, 6 2019.

[78] Angelo S. Mao, Jae Won Shin, Stefanie Utech, Huanan Wang, Oktay Uzun, Weiwei Li, Madeline Cooper, Yuebi Hu, Liyuan Zhang, David A. Weitz, and David J. Mooney. Deterministic encapsulation of single cells in thin tunable microgels for niche modelling and therapeutic delivery. *Nature Materials*, 16:236–243, 2 2017.

[79] Priti S. Mohanty, Sofi Nöjd, Kitty Van Gruijthuijsen, Jérôme J. Crassous, Marc Obiols-Rabasa, Ralf Schweins, Anna Stradner, and Peter Schurtenberger. Interpenetration of polymeric microgels at ultrahigh densities. *Scientific Reports*, 7, 12 2017.

[80] Susanne Wiese, Yoanna Tsvetkova, Nadine J.E. Daleiden, Antje C. Spieß, and Walter Richtering. Microgel stabilized emulsions: Breaking on demand. *Colloids and Surfaces A: Physicochemical and Engineering Aspects*, 495:193–199, 4 2016.

[81] Susann Schachschal, Hans Juergen Adler, Andrij Pich, Stefanie Wetzel, Anke Matura, and Karl Heinz Van Pee. Encapsulation of enzymes in microgels by polymerization/cross-linking in aqueous droplets. *Colloid and Polymer Science*, 289:693–698, 4 2011.

[82] Amir Erfani, Abanoub Hanna, Payam Zarrintaj, Saeed Manouchehri, Katie Weigandt, Clint P. Aichele, and Joshua D. Ramsey. Biodegradable zwitterionic poly(carboxybetaine) microgel for sustained delivery of antibodies with extended stability and preserved function. *Soft Matter*, 17:5349–5361, 6 2021.

[83] Randi Nordström, Lina Nyström, Oliver C.J. Andrén, Michael Malkoch, Anita Umerska, Mina Davoudi, Artur Schmidtchen, and Martin Malmsten. Membrane interactions of microgels as carriers of antimicrobial peptides. *Journal of Colloid and Interface Science*, 513:141–150, 3 2018.

[84] Sonal Deshpande, Smita Patil, and Neetu Singh. Enhancing gene-knockdown efficiency of poly(n-isopropylacrylamide) nanogels. *ACS Omega*, 3:8042–8049, 7 2018.

[85] Yu Hoshino, Hiroyuki Koide, Keiichi Furuya, Walter W Haberaecker, Shih-Hui Lee, Takashi Kodama, Hiroaki Kanazawa, Naoto Oku, and Kenneth J Shea. The rational design of a synthetic polymer nanoparticle that neutralizes a toxic peptide in vivo. *Proceedings of the National Academy of Sciences*, 109(1):33–38, 2012.

[86] Keiichi Yoshimatsu, Benjamin K. Lesel, Yusuke Yonamine, John M. Beierle, Yu Hoshino, and Kenneth J. Shea. Temperature-responsive "catch and release" of proteins by using multifunctional polymer-based nanoparticles. *Angewandte Chemie*, 124:2455–2458, 3 2012.

[87] Yang Wang, Jinshan Nie, Baisong Chang, Yangfei Sun, and Wuli Yang. Poly(vinylcaprolactam)-based biodegradable multiresponsive microgels for drug delivery. *Biomacromolecules*, 14:3034–3046, 8 2013.

[88] Yongzhi Men, Shaojun Peng, Peng Yang, Qin Jiang, Yanhui Zhang, Bin Shen, Pin Dong, Zhiqing Pang, and Wuli Yang. Biodegradable zwitterionic nanogels with long circulation for antitumor drug delivery. *ACS Applied Materials amp; Interfaces*, 10:23509–23521, 6 2018.

[89] Dennis Jgamadze, Li Liu, Steffen Vogler, Liang Yin Chu, and Sophie Pautot. Thermoswitching microgel carriers improve neuronal cell growth and cell release for cell transplantation. *Tissue Engineering - Part C: Methods*, 21:65–76, 1 2015.

[90] Yongqing Xia, Shuai Gao, Hua He, Xiaojuan Wang, Zhujun Zeng, Binghe Chen, Nianjun Zou, Meiwen Cao, and Shengjie Wang. A new and straightforward strategy to prepare an optical hydrogel film with dynamic structural colors. *The Journal of Physical Chemistry C*, 124:16083–16089, 6 2020.

[91] Yongfeng Gao, Xue Li, and Michael J. Serpe. Stimuli-responsive microgel-based etalons for optical sensing. *RSC Advances*, 5:44074–44087, 2015.

[92] Liang Hu and Michael J. Serpe. Controlling the response of color tunable poly(n-isopropylacrylamide) microgel-based etalons with hysteresis. *Chemical Communications*, 49:2649–2651, 3 2013.

[93] Wenwen Xu, Yongfeng Gao, and Michael J. Serpe. Electrochemically color tunable poly(n-isopropylacrylamide) microgel-based etalons. *Journal of Materials Chemistry C*, 2:3873–3878, 5 2014.

[94] Niels M.B. Smeets and Todd Hoare. Designing responsive microgels for drug delivery applications. *Journal of Polymer Science, Part A: Polymer Chemistry*, 51:3027–3043, 7 2013.

[95] Matthias Karg, Andrij Pich, Thomas Hellweg, Todd Hoare, L. Andrew Lyon, J. J. Crassous, Daisuke Suzuki, Rustam A. Gumerov, Stefanie Schneider, Igor. I. Potemkin, and Walter Richtering. Nanogels and microgels: From model colloids to applications, recent developments, and future trends. *Langmuir*, 35:6231–6255, 4 2019.

[96] Shivkumar V. Ghugare, Ester Chiessi, Barbara Cerroni, Mark T.F. Telling, Victoria García Sakai, and Gaio Paradossi. Biodegradable dextran based microgels: A study on network associated water diffusion and enzymatic degradation. *Soft Matter*, 8:2494–2502, 2 2012.

[97] Dinggeng He, Shuo Wang, Lei Lei, Zengtao Hou, Peng Shang, Xiaoxiao He, and Hemin Nie. Core-shell particles for controllable release of drug. *Chemical Engineering Science*, 125:108–120, 3 2015.

[98] Qi Wang, Xiangyu Zhang, Hongze Liao, Ying Sun, Li Ding, Yanwei Teng, Wei Hong Zhu, Zhirong Zhang, and Yourong Duan. Multifunctional shell–core nanoparticles for treatment of multidrug resistance hepatocellular carcinoma. *Advanced Functional Materials*, 28, 4 2018.

[99] Koen Raemdonck, Tinneke G. Van Thienen, Roosmarijn E. Vandenbroucke, Niek N. Sanders, Joseph Demeester, and Stefaan C. De Smedt. Dextran microgels for time-controlled delivery of sirna. *Advanced Functional Materials*, 18:993–1001, 4 2008.

[100] Gustavo Ramirez-Calderon, Hepi Hari Susapto, and Charlotte A. E. Hauser. Delivery of endothelial cell-laden microgel elicits angiogenesis in self-assembling ultrashort peptide hydrogels in vitro. *ACS Applied Materials amp; Interfaces*, 13:29281–29292, 6 2021.

[101] Pyung Hwan Kim, Hyun Gu Yim, Young Jin Choi, Byung Jae Kang, Joohyun Kim, Sang Mo Kwon, Byung Soo Kim, Nathaniel S. Hwang, and Je Yoel Cho. Injectable multifunctional microgel encapsulating outgrowth endothelial cells and growth factors for enhanced neovascularization. *Journal of Controlled Release*, 187:1–13, 8 2014.

[102] Amanda W. Bridges, Rachel E. Whitmire, Neetu Singh, Kellie L. Templeman, Julia E. Babensee, L. Andrew Lyon, and Andrés J. García. Chronic inflammatory responses to microgel-based implant coatings. *Journal of Biomedical Materials Research - Part A*, 94:252–258, 7 2010.

[103] J. Brijitta, B. V.R. Tata, R. G. Joshi, and T. Kaliyappan. Random hcp and fcc structures in thermoresponsive microgel crystals. *Journal of Chemical Physics*, 131, 2009.

[104] Senff H. and Richtering W. Influence of cross-link density on rheological properties of temperature-sensitive microgel suspensions. *Colloid and Polymer Science*, 278:830–840, 2000.

[105] L. Andrew Lyon, Justin D. Debord, Saet Byul Debord, Clinton D. Jones, Jonathan G. McGrath, and Michael J. Serpe. Microgel colloidal crystals. *The Journal of Physical Chemistry B*, 108:19099–19108, 8 2004.

[106] S. Franco, E. Buratti, B. Ruzicka, V. Nigro, N. Zoratto, P. Matricardi, E. Zaccarelli, and R. Angelini. Volume fraction determination of microgel composed of interpenetrating polymer networks of pnipam and polyacrylic acid. *Journal of Physics Condensed Matter*, 33, 4 2021.

[107] FA Jenkins and HE White. Fundamentals of optics, mcgraw-hill companies. 2001.

[108] Jess M. Clough, Christoph Weder, and Stephen Schrettl. Mechanochromism in structurally colored polymeric materials. *Macromolecular Rapid Communications*, 42, 1 2021.

[109] Mao Chen, Lin Zhou, Ying Guan, and Yongjun Zhang. Polymerized microgel colloidal crystals: Photonic hydrogels with tunable band gaps and fast response rates. *Angewandte Chemie*, 125:10145–10149, 9 2013.

[110] Siyu Jia, Zhuo Tang, Ying Guan, and Yongjun Zhang. Order–disorder transition in doped microgel colloidal crystals and its application for optical sensing. *ACS Applied Materials amp; Interfaces*, 10:14254–14258, 4 2018.

[111] Gun Ho Lee, Sang Hoon Han, Jong Bin Kim, Jong Hyun Kim, Jung Min Lee, and Shin-Hyun Kim. Colloidal photonic inks for mechanochromic films and patterns with structural colors of high saturation. *Chemistry of Materials*, 31:8154–8162, 9 2019.

[112] Benjamin Viel, Tilmann Ruhl, and Goetz P. Hellmann. Reversible deformation of opal elastomers. *Chemistry of Materials*, 19:5673–5679, 10 2007.

[113] P. Spahn, C. E. Finlayson, W. Mbi Etah, D. R.E. Snoswell, J. J. Baumberg, and G. P. Hellmann. Modification of the refractive-index contrast in polymer opal films. *Journal of Materials Chemistry*, 21:8893–8897, 6 2011.

[114] Liang Hu and Michael J. Serpe. Color-tunable etalons assembled from poly (n-isopropylacrylamide) based microgels. *Polymers*, 4:134–149, 2012.

[115] Qiang M.atthew Zhang, Darren Berg, Samuel M. Mugo, and Michael J. Serpe. Lipase-modified ph-responsive microgel-based optical device for triglyceride sensing. *Chemical communications (Cambridge, England)*, 51:9726–9728, 6 2015.

[116] Wenwei Tang and Cheng Chen. Hydrogel-based colloidal photonic crystal devices for glucose sensing, 3 2020.

[117] Molla R. Islam and Michael J. Serpe. Poly(n-isopropylacrylamide) microgel-based thin film actuators for humidity sensing. *RSC Advances*, 4:31937–31940, 2014.

[118] Shuai Li, Wei Wu, Kemao Xiu, Fujian Xu, Zhongming Li, and Jianshu Li. Doxorubicin loaded ph-responsive micelles capable of rapid intracellular drug release for potential tumor therapy. *Journal of Biomedical Nanotechnology*, 10:1480–1489, 2014.

[119] Miguel Angel Fernandez-Rodriguez, Alberto Martín-Molina, and Julia Maldonado-Valderrama. Microgels at interfaces, from mickering emulsions to flat interfaces and back. *Advances in Colloid and Interface Science*, 288, 2 2021.

[120] Jinglin Zhang, Lei Mei, Peihua Ma, Yuan Li, Yang Yuan, Qing-Zhu Zeng, and Qin Wang. Microgel-stabilized hydroxypropyl methylcellulose and dextran water-in-water emulsion: Influence of ph, ionic strength, and temperature. *Langmuir*, 37:5617–5626, 4 2021.

[121] Dana Akilbekova, Madina Shaimerdenova, Salimgerey Adilov, and Dmitriy Berillo. Biocompatible scaffolds based on natural polymers for regenerative medicine. *International Journal of Biological Macromolecules*, 114:324–333, 7 2018.

[122] Radislav A. Potyrailo. Polymeric sensor materials: Toward an alliance of combinatorial and rational design tools?, 1 2006.

[123] Christopher D. Spicer. Hydrogel scaffolds for tissue engineering: The importance of polymer choice. *Polymer Chemistry*, 11:184–219, 1 2020.

[124] Andy C. W. Lau and Chi Wu. Thermally sensitive and biocompatible poly(n-vinylcaprolactam): synthesis and characterization of high molar mass linear chains. *Macromolecules*, 32:581–584, 1 1999.

[125] Vittoria Chimisso, Miguel Angel Aleman Garcia, Saziye Yorulmaz Avsar, Ionel Adrian Dinu, and Cornelia G. Palivan. Design of bio-conjugated hydrogels for regenerative medicine applications: From polymer scaffold to biomolecule choice. *Molecules*, 25, 9 2020.

[126] S Ebasm and M Endo. Calcium ion and muscle contraction.

[127] C Takeguchi, E Kohno, C J Sih, C A Winter, E A Risley, and G W Nuss. A model of the nerve impulse using two first-order differential equations, 1978.

[128] TREVOR J Shuttleworth. Intracellular ca2+ signalling in secretory cells. *The Journal of experimental biology*, 300:303–314.

[129] Ana Rodríguez, Paul Webster, Javier Ortego, and Norma W Andrews. Lysosomes behave as ca 2-regulated exocytic vesicles in fibroblasts and epithelial cells, 1997.

[130] Ivana Y. Kuo and Barbara E. Ehrlich. Signaling in muscle contraction. *Cold Spring Harbor Perspectives in Biology*, 7, 2015.

[131] Ozana Onaca, Ramona Enea, David W. Hughes, and Wolfgang Meier. Stimuli-responsive polymersomes as nanocarriers for drug and gene delivery, 2 2009.

[132] Mallika Das, Sawitri Mardyani, Warren C.W. Chan, and Eugenia Kumacheva. Biofunctionalized ph-responsive microgels for cancer cell targeting: Rational design, 1 2006.

[133] Garg Sanjay Gupta Piyush Vermani Kavita. Hydrogels: from controlled release to ph-responsive drug delivery. *Drug discovery today*, 7:569–579, 2002.

[134] Xiaolin Cui, Junnan Tang, Yusak Hartanto, Jiabin Zhang, Jingxiu Bi, Sheng Dai, Shi Zhang Qiao, Ke Cheng, and Hu Zhang. Nipam-based microgel microenvironment regulates the therapeutic function of cardiac stromal cells. *ACS Applied Materials amp; Interfaces*, 10:37783–37796, 10 2018.

[135] Wing-Fu Lai, Andrei S. Susha, and Andrey L. Rogach. Multicompartment microgel beads for co-delivery of multiple drugs at individual release rates. *ACS Applied Materials amp; Interfaces*, 8:871–880, 12 2016.

[136] Melanie Bradley and Brian Vincent. Poly(vinylpyridine) core/poly(n-isopropylacrylamide) shell microgel particles: Their characterization and the uptake and release of an anionic surfactant. *Langmuir*, 24:2421–2425, 2 2008.

[137] Yongfeng Gao, Gustavo P. Zago, Zhanghu Jia, and Michael J. Serpe. Controlled and triggered small molecule release from a confined polymer film. *ACS Applied Materials amp; Interfaces*, 5:9803–9808, 9 2013.

[138] Arjan P.H. Gelissen, Andrea Scotti, Sarah K. Turnhoff, Corinna Janssen, Aurel Radulescu, Andrij Pich, Andrey A. Rudov, Igor I. Potemkin, and Walter Richtering. An anionic shell shields a cationic core allowing for uptake and release of polyelectrolytes within core-shell responsive microgels. *Soft Matter*, 14:4287–4299, 2018.

[139] Wenjing Xu, Andrey A. Rudov, Ricarda Schroeder, Ivan V. Portnov, Walter Richtering, Igor I. Potemkin, and Andrij Pich. Distribution of ionizable groups in polyampholyte microgels controls interactions with captured proteins: From blockade and "levitation" to accelerated release. *Biomacromolecules*, 20:1578–1591, 3 2019.

[140] Daryl Sivakumaran, Danielle Maitland, and Todd Hoare. Injectable microgel-hydrogel composites for prolonged small-molecule drug delivery. *Biomacromolecules*, 12:4112–4120, 10 2011.

[141] Victoria K. Switacz, Sarah K. Wypysek, Rudolf Degen, Jérôme J. Crassous, Marc Spehr, and Walter Richtering. Influence of size and cross-linking density of microgels on cellular uptake and uptake kinetics. *Biomacromolecules*, 21:4532–4544, 5 2020.

[142] George Eisenman. cation selective electrodes and their mode of opration. *Biophysics Journal*, pages 259–323, 1962.

[143] Shufu Peng and Chi Wu. Comparison of the ca2+/coo- complexation induced controllable aggregation of p(vcl-co-naa) spherical microgels and linear chains. *Macromolecules*, 34:6795–6801, 8 2001.

[144] Shishir D Gadam, Guhan Jayaraman, and Steven M Cramer. Characterization of non-linear adsorption properties of dextran-based polyelectrolyte displacers in ion-exchange systems, 1993.

[145] P M Byrne. Discontinuous Volume Transitions Induced by Calcium- Sodium Ion Exchange in Anionic Gels and Their Neurobiological Implications I , O o. *Biopolymers*, 34:209–215, 1994.

[146] Gustav Ferrand-Drake del Castillo, Rebekah L. N. Hailes, and Andreas Dahlin. Large changes in protonation of weak polyelectrolyte brushes with salt concentration—implications for protein immobilization. *The Journal of Physical Chemistry Letters*, 11:5212–5218, 6 2020.

[147] S J Stohs and D Bagchi. Mechanisms in the toxicity of metal ions, 1995.

[148] G. Papanikolaou and K. Pantopoulos. Iron metabolism and toxicity. *Toxicology and Applied Pharmacology*, 202:199–211, 1 2005.

[149] Alessandro Fulgenzi and Maria Elena Ferrero. Edta chelation therapy for the treatment of neurotoxicity. *International journal of molecular sciences*, 20, 2 2019.

[150] Heather A. Leitch and Norbert Gattermann. Hematologic improvement with iron chelation therapy in myelodysplastic syndromes: Clinical data, potential mechanisms, and outstanding questions. *Critical Reviews in Oncology/Hematology*, 141:54–72, 9 2019.

[151] Bruce R. Bacon Robert S. Britton Katherine L. Leicester. Iron toxicity and chelation therapy. *Progress in Hematology*, 2002.

[152] Mary Jean Brown, Teresa Willis, Bennet Omalu, and Richard Leiker. Deaths resulting from hypocalcemia after administration of edetate disodium: 2003-2005. *Pediatrics*, 118(2):e534–e536, 2006.

[153] Saketh R. Karamched, Nasim Nosoudi, Hannah E. Moreland, Aniqa Chowdhury, and Naren R. Vyavahare. Site-specific chelation therapy with edta-loaded albumin nanoparticles reverses arterial calcification in a rat model of chronic kidney disease. *Scientific Reports*, 9, 12 2019.

[154] Alan Dardik, Robert C Moesinger, Gershon Efron, Adrian Barbul, and Miles G Harrison. Acute abdomen with colonic necrosis induced by kayexalate-sorbitol. *Southern medical journal*, 93(5):511–513, 2000.

[155] Thomas R Scott, Scott M Graham, Eugene J Schweitzer, and Stephen T Bartlett. Colonic necrosis following sodium polystyrene sulfonate (kayexalate®)-sorbitol enema in a renal transplant patient. *Diseases of the colon & rectum*, 36(6):607–609, 1993.

[156] Sameer Varma and Susan B. Rempe. Coordination numbers of alkali metal ions in aqueous solutions. *Biophysical Chemistry*, 124:192–199, 12 2006.

[157] Marc-Oliver M. Piepenbrock, Gareth O. Lloyd, Nigel Clarke, and Jonathan W. Steed. Metal- and anion-binding supramolecular gels. *Chemical Reviews*, 110:1960–2004, 12 2009.

[158] Wengui Weng, J. Benjamin Beck, Alex M. Jamieson, and Stuart J. Rowan. Understanding the mechanism of gelation and stimuli-responsive nature of a class of metallo-supramolecular gels. *Journal of the American Chemical Society*, 128:11663–11672, 8 2006.

[159] Takashi Nakamura, Yoshinori Takashima, Akihito Hashidzume, Hiroyasu Yamaguchi, and Akira Harada. A metal-ion-responsive adhesive material via switching of molecular recognition properties. *Nature Communications*, 5, 8 2014.

[160] Babatunde O. Okesola and David K. Smith. Applying low-molecular weight supramolecular gelators in an environmental setting-self-assembled gels as smart materials for pollutant removal. *Chemical Society Reviews*, 45:4226–4251, 8 2016.

[161] Ayman M. Atta, Husein S. Ismail, and Ashraf M. Elsaaed. Application of anionic acrylamide-based hydrogels in the removal of heavy metals from waste water. *Journal of Applied Polymer Science*, 123:2500–2510, 2 2012.

[162] Jason Y.C. Lim, Shermin S. Goh, Sing Shy Liow, Kun Xue, and Xian Jun Loh. Molecular gel sorbent materials for environmental remediation and wastewater treatment. *Journal of Materials Chemistry A*, 7:18759–18791, 2019.

[163] Ting Chen Tseng, Lei Tao, Fu Yu Hsieh, Yen Wei, Ing Ming Chiu, and Shan Hui Hsu. An injectable, self-healing hydrogel to repair the central nervous system. *Advanced Materials*, 27:3518–3524, 6 2015.

[164] Liyang Shi, Pinghui Ding, Yuzhi Wang, Yu Zhang, Dmitri Ossipov, and Jöns Hilborn. Self-healing polymeric hydrogel formed by metal–ligand coordination assembly: Design, fabrication, and biomedical applications. *Macromolecular Rapid Communications*, 40, 4 2019.

[165] Shuai Li, Zhouxiang Zhao, Wei Wu, Chunmei Ding, and Jianshu Li. Dual ph-responsive micelles with both charge-conversional property and hydrophobic-hydrophilic transition for effective cellular uptake and intracellular drug release. *Polymer Chemistry*, 7:2202–2208, 2016.

[166] JY An, HS Yun, YP Lee, SJ Yang, JO Shim, Ji Hoon Jeong, CY Shin, JH Kim, DS Kim, and UD Sohn. The intracellular pathway of the acetylcholine-induced contraction in cat detrusor muscle cells. *British journal of pharmacology*, 137(7):1001–1010, 2002.

[167] Amor Royer and Tariq Sharman. Copper toxicity. 2020.

[168] Carlos G. Lopez and Walter Richtering. Influence of divalent counterions on the solution rheology and supramolecular aggregation of carboxymethyl cellulose. *Cellulose*, 26:1517–1534, 2 2019.

[169] WL Lindsay and WA Norvell. Equilibrium relationships of zn2+, fe3+, ca2+, and h+ with edta and dtpa in soils, 1969.

[170] Turash Haque Pial, Harnoor Singh Sachar, and Siddhartha Das. Quantification of mono- and multivalent counterion-mediated bridging in polyelectrolyte brushes. *Macromolecules*, 54:4154–4163, 4 2021.

[171] Michał Zabiszak, Martyna Nowak, Katarzyna Taras-Goslinska, Małgorzata T. Kaczmarek, Zbigniew Hnatejko, and Renata Jastrzab. Carboxyl groups of citric acid in the process of complex formation with bivalent and trivalent metal ions in biological systems. *Journal of Inorganic Biochemistry*, 182:37–47, 5 2018.

[172] George Maistralis, Nick Katsaros, Spyros P Perlepes, and Dimitra Kovala-Demertzi. Coordinating properties of isoorotic acid, 1992.

[173] Andrea Belluati, Sagana Thamboo, Adrian Najer, Viviana Maffeis, Claudio von Planta, Ioana Craciun, Cornelia G. Palivan, and Wolfgang Meier. Multicompartment polymer vesicles with artificial organelles for signal-triggered cascade reactions including cytoskeleton formation. *Advanced Functional Materials*, 30, 8 2020.

[174] Glenn S. Smith. Structural color of morpho butterflies. *American Journal of Physics*, 77:1010–1019, 11 2009.

[175] SV Teyssier and D Saenko. van der marel, and mc milinkovitch. *Nat. Commun*, 6:6368, 2015.

[176] J F Haw, P W Goguen, T Xu, T W Skloss, W Song, and Z Wang. Surface effects from nanostructure structural color and the lotus effect**. *Angew. Chem. Int. Ed*, 110:948–949, 1998.

[177] A A R El Agib. Structure of opal. *NATURE December*, 5, 1964.

[178] RD Alcock, CD Creasey, P Wileman, NA Halliwell, and JM Coupland. Remote detection of the pitch and orientation of a reflective diffraction grating: an optical strain gauge. *Proceedings of the Royal Society A: Mathematical, Physical and Engineering Sciences*, 461(2053):179–188, 2005.

[179] Lucas D. C de Castro and Osvaldo N. Oliveira. Silica nanoparticle/polymer film-based soft mechanochromic devices for detecting mechanical deformation and stress cycles in varied environments. *ACS Applied Nano Materials*, 5:2906–2911, 1 2022.

[180] Xiaohui Wang, Yichen Li, Jianyong Zheng, Xinyang Li, Guojin Liu, Lan Zhou, Wenlong Zhou, and Jianzhong Shao. Polystyrene@poly(methyl methacrylate-butyl acrylate) core–shell nanoparticles for fabricating multifunctional photonic crystal films as mechanochromic and solvatochromic sensors. *ACS Applied Nano Materials*, 5:729–736, 1 2022.

[181] Zhujun Zeng, Jinhui Liang, Ronghua Yu, Jiahui Liu, Meiwen Cao, Shengjie Wang, and Yongqing Xia. Programmable color in a free-standing photonic microgel film with ultra-fast response. *ACS Applied Materials amp; Interfaces*, 13:25563–25570, 5 2021.

[182] Goki Hattori, Mikihito Takenaka, Mitsuo Sawamoto, and Takaya Terashima. Nanostructured materials via the pendant self-assembly of amphiphilic crystalline random copolymers. *Journal of the American Chemical Society*, page jacs.8b03838, 2018.

[183] Andrij Pich, Anne Tessier, Volodymyr Boyko, Yan Lu, and Hans Juergen P Adler. Synthesis and characterization of poly(vinylcaprolactam)-based microgels exhibiting temperature and ph-sensitive properties. *Macromolecules*, 39:7701–7707, 2006.

[184] Alexander F. Routh, Alberto Fernandez-Nieves, Melanie Bradley, and Brian Vincent. Effect of added free polymer on the swelling of neutral microgel particles: A thermodynamic approach. *Journal of Physical Chemistry B*, 110:12721–12727, 6 2006.

[185] Andrea Scotti. Characterization of the volume fraction of soft deformable microgels by means of small-angle neutron scattering with contrast variation. *Soft Matter*, 17:5548–5559, 6 2021.

[186] Ri Hong, Yuqi Shi, Xiao Qiao Wang, Lu Peng, Xingjiang Wu, Hengyang Cheng, and Su Chen. Highly sensitive mechanochromic photonic gel towards fast- responsive fingerprinting. *RSC Advances*, 7:33258–33262, 2017.

[187] Chia-Hua Hsieh, Yi-Cheng Lu, and Hongta Yang. Self-assembled mechanochromic shape memory photonic crystals by doctor blade coating. *ACS Applied Materials amp; Interfaces*, 12:36478–36484, 7 2020.

[188] Yoshimitsu Sagara, Marc Karman, Ester Verde-Sesto, Kazuya Matsuo, Yuna Kim, Nobuyuki Tamaoki, and Christoph Weder. Rotaxanes as mechanochromic fluorescent force transducers in polymers. *Journal of the American Chemical Society*, 140:1584–1587, 1 2018.

[189] Judith Museh, Stefanie Schneider, Peter Lindner, and Walter Richtering. Unperturbed volume transition of thermosensitive poly-(n- isopropylacrylamide) microgel particles embedded in a hydrogel matrix. *Journal of Physical Chemistry B*, 112:6309–6314, 5 2008.

[190] Elia A. Guzzi and Mark W. Tibbitt. Additive manufacturing of precision biomaterials. *Advanced Materials*, 32, 4 2020.

[191] Dipankar Behera and Michael Cullinan. Current challenges and potential directions towards precision microscale additive manufacturing – part i: Direct ink writing/jetting processes. *Precision Engineering*, 68:326–337, 3 2021.

[192] Zhaoyao Zhan, Jianing An, Yuefan Wei, Van Thai Tran, and Hejun Du. Inkjet-printed optoelectronics. *Nanoscale*, 9:965–993, 1 2017.

[193] Fabian Niesler and Martin Hermatschweiler. Two-photon polymerization-a versatile microfabrication tool from maskless lithography to 3d printing. *Laser Technik Journal*, 3, 2015.

[194] Ilbey Karakurt and Liwei Lin. 3d printing technologies: techniques, materials, and post-processing. *Current Opinion in Chemical Engineering*, 28:134–143, 6 2020.

[195] Michael E. Mackay. The importance of rheological behavior in the additive manufacturing technique material extrusion. *Journal of Rheology*, 62:1549–1561, 11 2018.

[196] Gaurasundar M Conley, Philippe Aebischer, Sofi Nöjd, Peter Schurtenberger, and Frank Scheffold. Jamming and overpacking fuzzy microgels: Deformation, interpenetration, and compression. *Science advances*, 3(10):e1700969, 2017.

[197] Yue Ma, Peiyan He, Wanli Xie, Qiang Zhang, Weiling Yin, Jianming Pan, Miao Wang, Xin Zhao, and Guoqing Pan. Dynamic colloidal photonic crystal hydrogels with self-recovery and injectability. *Research*, 2021:1–11, 3 2021.

[198] Francis L C Morgan, Julia Fernández-pérez, Lorenzo Moroni, and Matthew B Baker. Tuning Hydrogels by Mixing Dynamic Cross-Linkers : Enabling Cell-Instructive Hydrogels and Advanced Bioinks. 2101576:1–15, 2022.

[199] Carlos G Lopez, Ferenc Horkay, Ralf Schweins, and Walter Richtering. Solution properties of polyelectrolytes with divalent counterions. *Macromolecules*, 54(22):10583–10593, 2021.

[200] Mi Zhou, Fubao Xing, Meilin Ren, Yan Feng, Yongqiang Zhao, Haixia Qiu, Xiaodong Wang, Chunjuan Gao, Feifei Sun, Yongqiang He, et al. A facile method to assemble pnipam-containing microgel photonic crystals. *ChemPhysChem*, 10(3):523–526, 2009.

[201] Cheng-Hsun Lu, Cheng-Hsuan Yu, and Yi-Cheun Yeh. Engineering nanocomposite hydrogels using dynamic bonds. *Acta Biomaterialia*, 130:66–79, 2021.

[202] M. Mario Perera and Neil Ayres. Dynamic covalent bonds in self-healing, shape memory, and controllable stiffness hydrogels. *Polymer Chemistry*, 11:1410–1423, 2 2020.

[203] Andrea Belluati, Ioana Craciun, Claire E. Meyer, Serena Rigo, and Cornelia G. Palivan. Enzymatic reactions in polymeric compartments: nanotechnology meets nature. *Current Opinion in Biotechnology*, 60:53–62, 12 2019.

[204] D. Kenzelmann, R. Chiquet-Ehrismann, and R. P. Tucker. Teneurins, a transmembrane protein family involved in cell communication during neuronal development. *Cellular and Molecular Life Sciences*, 64:1452–1456, 6 2007.

[205] Carla Bänziger, Davide Soldini, Corina Schütt, Peder Zipperlen, George Hausmann, and Konrad Basler. Wntless, a conserved membrane protein dedicated to the secretion of wnt proteins from signaling cells. *Cell*, 125:509–522, 5 2006.

[206] Pauline Van Nies, Ilja Westerlaken, Duco Blanken, Margarita Salas, Mario Mencía, and Christophe Danelon. Self-replication of dna by its encoded proteins in liposome-based synthetic cells. *Nature Communications*, 9, 12 2018.

[207] Pasquale Stano. Is research on "synthetic cells" moving to the next level? *Life*, 9, 3 2019.

[208] Wolfgang Meier. Polymer nanocapsules. *Chemical Society Reviews*, 29:295–303, 2000.

[209] Vittoria Chimisso, Viviana Maffeis, Dimitri Hürlimann, Cornelia G. Palivan, and Wolfgang Meier. Self-assembled polymeric membranes and nanoassemblies on surfaces: Preparation, characterization, and current applications. *Macromolecular Bioscience*, 20, 1 2020.

[210] Mihai Lomora, Fabian Itel, Ionel Adrian Dinu, and Cornelia G. Palivan. Selective ion-permeable membranes by insertion of biopores into polymersomes. *Physical Chemistry Chemical Physics*, 17:15538–15546, 6 2015.

[211] Michael Martin, Timothy Dubbs, and J. R. Fried. Planar bilayer measurements of alamethicin and gramicidin reconstituted in biomimetic block copolymers. *Langmuir*, 33:1171–1179, 1 2017.

[212] Andrea Belluati, Viktoria Mikhalevich, Saziye Yorulmaz Avsar, Davy Daubian, Ioana Craciun, Mohamed Chami, Wolfgang P. Meier, and Cornelia G. Palivan. How do the properties of amphiphilic polymer membranes influence the functional insertion of peptide pores? *Biomacromolecules*, 21:701–715, 12 2019.

[213] Tomaž Einfalt, Roland Goers, Ionel Adrian Dinu, Adrian Najer, Mariana Spulber, Ozana Onaca-Fischer, and Cornelia G. Palivan. Stimuli-triggered activity of nanoreactors by biomimetic engineering polymer membranes. *Nano Letters*, 15:7596–7603, 10 2015.

[214] Jens Gaitzsch, Stephan Hirschi, Sven Freimann, Dimitrios Fotiadis, and Wolfgang Meier. Directed insertion of light-activated proteorhodopsin into asymmetric polymersomes from an abc block copolymer. *Nano Letters*, 19:2503–2508, 3 2019.

[215] Manish Kumar, Mariusz Grzelakowski, Julie Zilles, Mark Clark, and Wolfgang Meier. Highly permeable polymeric membranes based on the incorporation of the functional water channel protein aquaporin z. 2007.

[216] Elena C. dos Santos, Andrea Belluati, Danut Necula, Dominik Scherrer, Claire E. Meyer, Riccardo P. Wehr, Emanuel Lörtscher, Cornelia G. Palivan, and Wolfgang Meier. Combinatorial strategy for studying biochemical pathways in double emulsion templated cell-sized compartments. *Advanced Materials*, 32, 12 2020.

[217] Kasper Renggli, Patric Baumann, Karolina Langowska, Ozana Onaca, Nico Bruns, and Wolfgang Meier. Selective and responsive nanoreactors. *Advanced Functional Materials*, 21(7):1241–1259, 2011.

[218] Mariusz Grzelakowski, Ozana Onaca, Per Rigler, Manish Kumar, and Wolfgang Meier. Immobilized protein–polymer nanoreactors. *Small*, 5(22):2545–2548, 2009.

[219] Sagana Thamboo, Adrian Najer, Andrea Belluati, Claudio von Planta, Dalin Wu, Ioana Craciun, Wolfgang Meier, and Cornelia G Palivan. Mimicking cellular signaling pathways within synthetic multicompartment vesicles with triggered enzyme activity and induced ion channel recruitment. *Advanced Functional Materials*, 29(40):1904267, 2019.

[220] Eva M Schmid, David L Richmond, and Daniel A Fletcher. Reconstitution of proteins on electroformed giant unilamellar vesicles. 128:319–338, 2015.

[221] Patrick F Kiser, Glynn Wilson, and David Needham. A synthetic mimic of the secretory granule for drug delivery. 1998.

[222] Meina Wang, Adriana M. Mihut, Ellen Rieloff, Aleksandra P. Dabkowska, Linda K. Månsson, Jasper N. Immink, Emma Sparr, and Jérôme J. Crassous. Assembling responsive microgels at responsive lipid membranes. *Proceedings of the National Academy of Sciences of the United States of America*, 116:5442–5450, 2019.

[223] Cornelia G. Palivan, Roland Goers, Adrian Najer, Xiaoyan Zhang, Anja Car, and Wolfgang Meier. Bioinspired polymer vesicles and membranes for biological and medical applications. *Chemical Society Reviews*, 45:377–411, 1 2016.

[224] Cornelia G Palivan, Roland Goers, Adrian Najer, Xiaoyan Zhang, Anja Car, and Wolfgang Meier. Bioinspired polymer vesicles and membranes for biological and medical applications. *Chemical society reviews*, 45(2):377–411, 2016.

[225] Corinne Nardin, Thomas Hirt, Jörg Leukel, and Wolfgang Meier. Polymerized aba triblock copolymer vesicles. *Langmuir*, 16:1035–1041, 11 1999.

[226] Riccardo Pascal Wehr. *Synthesis and Aqueous Self-assembly of Atactic and Isotactic Poly (butylene oxide)-block-poly (glycidol) Diblock Copolymers*. PhD thesis, University_of_Basel, 2021.

[227] Victoria K. Switacz, Sarah K. Wypysek, Rudolf Degen, Jérôme J. Crassous, Marc Spehr, and Walter Richtering. Influence of size and cross-linking density of microgels on cellular uptake and uptake kinetics. *Biomacromolecules*, 21:4532–4544, 5 2020.

[228] Débora F. do Nascimento, Laura R. Arriaga, Max Eggersdorfer, Roy Ziblat, Maria de Fátima V. Marques, Franceline Reynaud, Stephan A. Koehler, and David A. Weitz. Microfluidic fabrication of pluronic vesicles with controlled permeability. *Langmuir*, 32:5350–5355, 5 2016.

Chapter 9

Each microgel listed in the table below was synthesized with a 2.5 mol% of BIS (60 mg, 0.38 mmol) in respect to VCL, 50 mg of AMPA 10 mg CTAB (0.027 mmol).

Table 9.1 Synthetic conditions for the polymerization of neutral microgels with various N-vinylcaprolactam (VCL) and dimethylitaconate (IADME) ratios.

Sample ID	VLC:IADME	VCL		IADME	
		g	mol	g	mol
N0	100:0	2.087	15.00	0	0
N5	95:5	1.983	14.24	0.118	0.75
N10	90:10	7.879	13.50	0.237	1.50
N15	85:15	1.774	12.75	0.355	2.25
N20	80:20	1.670	12.00	0.474	3.0
N30	70:30	1.461	10.50	0.711	4.5

Table 9.2 Hydrolysis yield for each microgel sample determined by potentiometric titration.

Sample	COOH mol%	Hydrolysis yield
M6	57 %	
M8	51 %	
M10	47 %	
M14	36 %	
M22	50 %	
M19	57 %	
M26	52 %	
M30	51 %	

Table 9.3 R_g/R_H of P(VCL-*co*-IADME) (N*n*) microgels in pure water at pH 7 and P(VCL-*co*-IA) (M*n*) microgels in pure water at pH 7 and pH 3

Sample ID	R_g/R_H (pH=7)	Code	R_g/R_H (pH=7)	R_g/R_H (pH=3)
N0	0.55			
N5	0.52	**M8**	0.63	0.37
N10	0.61	**M14**	0.60	0.38
N15	0.61	**M22**	0.63	0.42
N20	0.66	**M26**	0.63	0.52
N30	0.74	**M30**	-	0.37

Table 9.4 Comparison of the D_H of P(VCL-*co*-IA) (M*n*) microgels in the presence of Ca^{2+} and at pH 3 at T = 20 °C

Sample ID	D_H [Ca^{2+}]= 10 mM (pH= 7)	R_g/R_H [Ca^{2+}]= 10 mM (pH= 7)	D_H [Ca^{2+}]= 0 mM (pH= 3)
M8	319 ± 18	0.66	244 ± 2
M14	320 ± 10	0.64	264 ± 4
M22	298 ± 8	0.62	230 ± 4
M26	308 ± 3	0.43	204 ± 2
M30	278 ± 4	0.53	NA

Table 9.5 R_g/R_H ratio of M5, M10 and M19 taken at 20 °C, at pH 7, 1 mM Mg2+ and pH=2.

Sample ID	R_g/R_H pH 7	R_g/R_H 1 mM [M^{2+}]	R_g/R_H pH 3
M6	0.44	0.59	0.56
M10	0.49	0.64	0.64
M19	0.45	0.66	0.65

Table 9.6 . ζ-potential of P(VCL-*co*-IA) (M*n*) microgels samples in pure water and loaded with Ca^{2+} ions.

	ζ-potential (mV)	
Sample ID	Empty gels	Loaded gels
M8	-16.2 ± 0.5	-11.9 ± 0.8
M14	-18.8 ± 0.4	-16.9 ± 0.3
M22	-19.8 ± 0.6	-18.4 ± 0.2
M26	-24.3 ± 0.6	-20.3 ± 1.0
M30	-28.9 ± 0.9	-26.6 ± 0.8

Table 9.7 Amount of Mg^{2+} ion bonded at ambient condition in PBS

Microgel	% Mg^{2+}	% Fe^{3+}
M6	0	100
M19	0	100

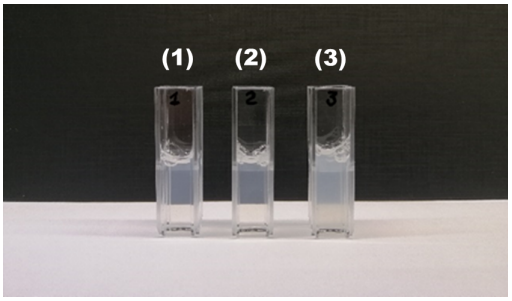

Fig. 9.1 Turbidity of 0.1 wt% P(VCL-*co*-IA) (*M*15) microgel samples in (1) water, (2) after the addition of 1 mM Ca^{2+} to the solution and (3) after the addition of acid to equilibrate to pH 3.

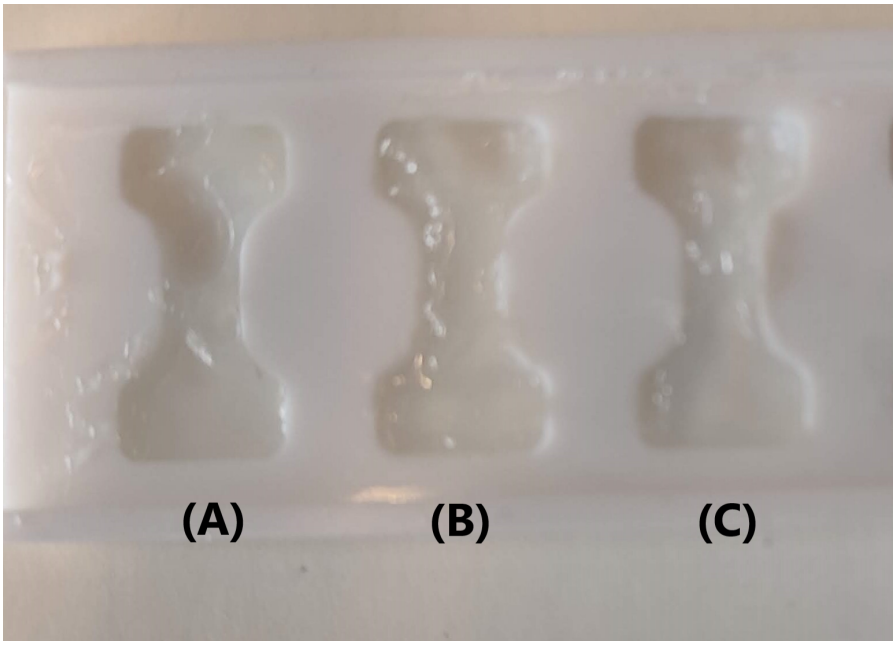

Fig. 9.2 Dogbone molds of (a) NIPAm-450, (b) NIPAm-400 and (c)NIPAm-350 crosslinked under UV light (60 mW/cm^2.

Fig. 9.3 Dogbone mold of PNIPAm-400 against black background under diffused light, cured with low intensity UV light.

Fig. 9.4 P(VCL-*co*-IA) microgels compressed by ultracentrifugation at RT.

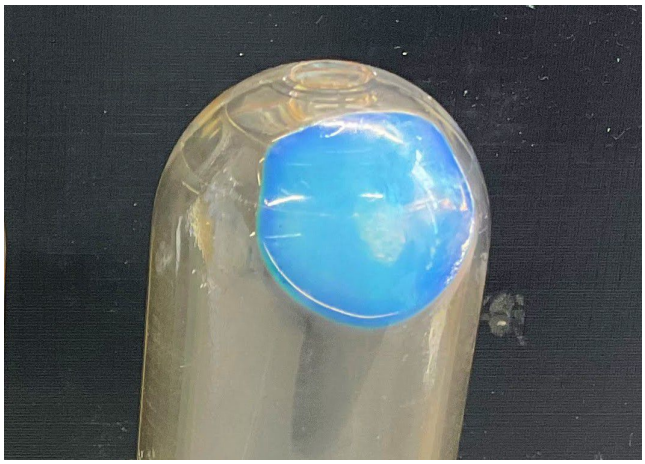

Fig. 9.5 P(VCL-*co*-GMA) microgels compressed by ultracentrifugation at RT in 10% AAm aqueous solution. The ink was printed in a 2 layer grid with a printing pressure of 70 kPa and 10 mm/s printing speed.

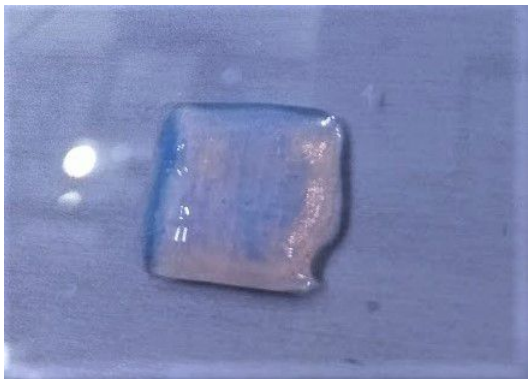

Fig. 9.6 PVCL microgels compressed by ultracentrifugation at RT in 10% AAm aqueous solution and 1% of CMC 90 kDa. The ink was printed in a 2 layer grid with a printing pressure of 70 kPa and 10 mm/s printing speed.

Fig. 9.7 Double network of PVCL-IA-15-400 crosslinked in 10 wt/V% of AAm in the presence of 50 mM of CaCl2.

Table 9.8 Molar constituents of microgels used in Chapter 6.

Microgel	P(NIPAm-*co*-MAAc) (mol%)	PNIPMAm (mol%)	P(NIPMAm-*co*MAAc) (mol%)
NIPAm	88.3		
NIPMAm		94.99	88.6
MAAc	5.7		4.8
BIS	5.00	5.00	4.7
MRB	1	0.01	1

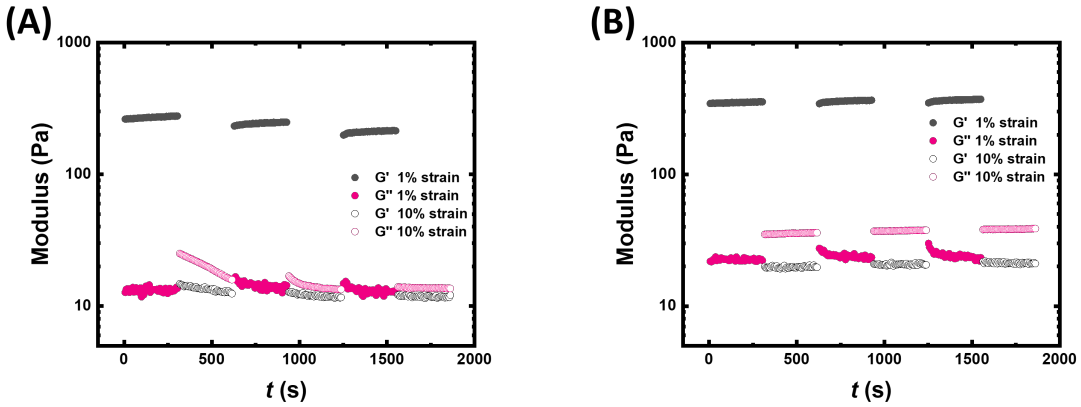

Fig. 9.8 Shear recovery plots of (a) PVCL-IA-15-500 and (c) PVCL-IA-15-550 containing 0.1 M $CaCl_2$ from dispersions centrifuged at 282k RCF at RT and neutral pH. G' (in black) and G" (in pink) are plotted against time, at 10% strain (filled dots) and 1% strain (hollow dots).

Fig. 9.9 PNIPAm-400 extruded by hand at RT into a PDMS bath.

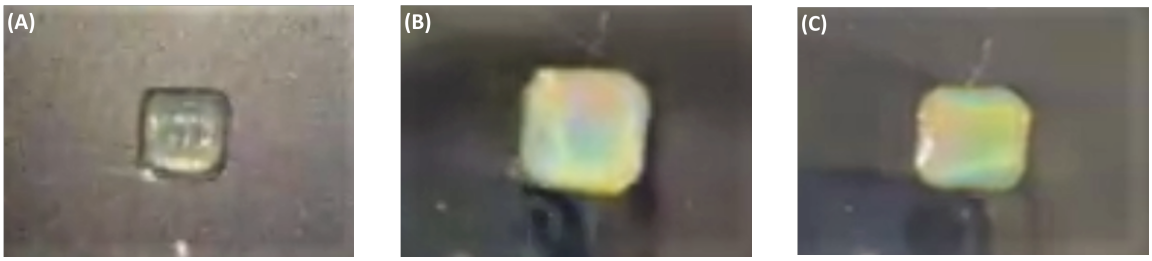

Fig. 9.10 NIPAm-AA-300 DNGH under (a) diffused light, (b) and (c) direct light.

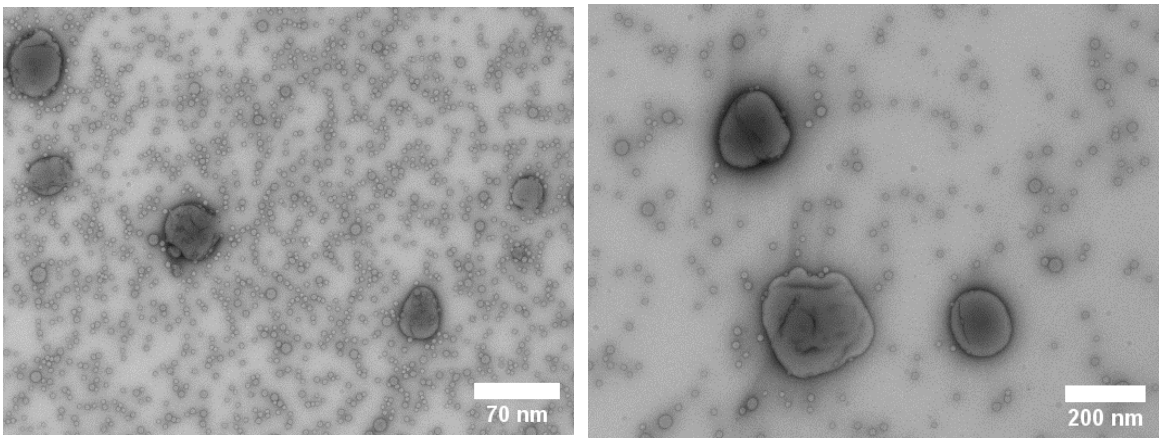

Fig. 9.11 TEM images of $PMOXa_8$-$PDMS_{45}$-$PMOxa_8$ based vesicles and micelles, assembled in PBS at RT with the film rehydration method.

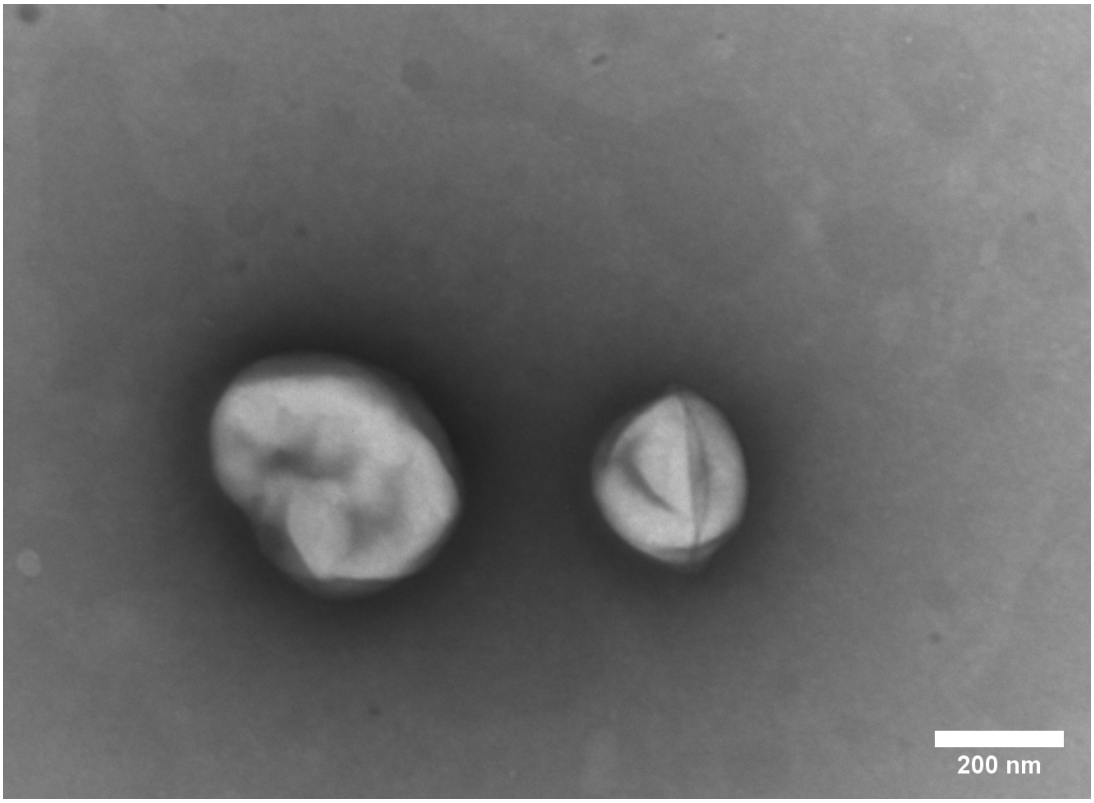

Fig. 9.12 TEM image of $PMOXa_8$-$PDMS_{45}$-$PMOXa_8$ based vesicles, assembled in PBS at RT with the solvent switch method.